Interannual and decadal variability of sea ice drift, concentration and thickness in the Weddell Sea

Dissertation zur Erlangung des Doktorgrades der Naturwissenschaften

- Dr. rer. nat. -

vorgelegt von

Sandra Schwegmann

am Fachbereich Physik der Universität Bremen

January 2, 2012

AWI Alfred-Wegener-Institut für Polar- und Meeresforschung in der Helmholtz-Gemeinschaft

Universität Bremen

1. Gutachter: Prof. Dr. Peter Lemke
2. Gutachter: Prof. Dr. Rüdiger Gerdes

Datum des Kolloquiums: 12. März 2012

Sandra Schwegmann
Alfred-Wegener-Institut (AWI) für Polar- und Meeresforschung
Bussestrasse 24
27570 Bremerhaven

Die vorliegende Arbeit ist die leicht veränderte Fassung einer Dissertation zur Erlangung des Doktorgrades der Naturwissenschaften (Dr. rer. nat.), die im Januar 2012 im Fachbereich Physik an der Universität Bremen eingereicht worden ist. Die Veränderungen betreffen einen Teilabschnitt im Kapitel 4 in Bezug auf die Netto-Gefrierraten.

Contents

Abstract

Sea ice concentrations in the Weddell Sea are subject to regional climate variability. The magnitude and origin of local trends in the sea ice coverage were studied using the bootstrap algorithm sea ice concentration data from the NSIDC for 1979-2006. The impact of atmospheric forcing such as air temperature, wind speed, sea level pressure and cloud coverage, gained from NCEP/NCAR reanalysis, was assessed by analyzing correlation coefficients between the respective atmospheric component and the sea ice concentrations. In addition, the variability of sea ice drift was analyzed using the Polar Pathfinder sea ice motion vectors, and the correlation with sea ice concentration was tested after an assessment of the product's uncertainties. The connection to the variability of sea ice thicknesses was derived by model simulations from the Finite Element Sea ice-Ocean Model (FESOM). It was found that sea ice concentrations increased in the eastern and decreased in the western Weddell Sea, predominantly in the marginal sea ice zone. There, and in coastal regions, temperatures are strongly negatively correlated to sea ice concentrations, whereas in the central Weddell Sea, mostly a positive correlation was assessed, especially during winter. From analyses of the wind field it was found that the prevailing westerlies at the Antarctic Peninsula frequently show a shift towards the south. The enhanced southward winds are expected to bring warmer air into the western and central Weddell Sea and are further expected to redistribute the sea ice from the west into the central and eastern regions. This would increase the sea ice concentrations in the central Weddell Sea due to enhanced compactness, although temperatures are increasing. The correlation between sea ice concentrations and sea ice drift is only robust for the central Weddell Sea, where both parameters are mainly anti-correlated. Hence, strong sea ice drift is connected to lower sea ice concentrations and vice versa. This finding is consistent with the connection to the wind fields, since stronger northerly winds would reduce the north-eastward drift of sea ice in this region and enhance the sea ice concentrations. From model simulations with FESOM it was found that sea ice thicknesses predominantly show the same tendencies for changes as the simulated sea ice concentrations, which are basically decreasing in the central Weddell Sea and increasing in the eastern Weddell Sea. The overall changes in sea ice thickness and concentration result in an increase of the total sea ice volume by

1 % per decade in the simulations. A sensitivity study with a free drift model, forced by 10-m wind speeds and ocean currents from FESOM showed that the trends in the modelled sea ice drift are driven by the atmospheric fields, since ocean currents show barely any trends. Further it was revealed that sea ice drift velocities in the model are overestimated, especially in the zonal direction. Nevertheless, despite the overestimation, the mean sea ice export rate of 22 x 10^3 m^3/s is only about half of the export rates found in previous studies, which is certainly an effect of underestimated sea ice thicknesses in the western Weddell Sea.

Zusammenfassung

In dieser Studie wurden die Stärke und der Ursprung lokaler Trends in der Meereiskonzentration im Weddellmeer für den Zeitraum 1979-2006 untersucht. Dazu wurden die Bootstrap-Algorithmus Konzentrationsdaten mit einer Auflösung von 25 km x 25 km vom NSIDC analysiert. Der Einfluss der Atmosphäre auf das Meereis, bedingt durch Lufttemperatur, Wind, Luftdruck und Wolkenbedeckung, u. a., wurde über Korrelationskoeffizienten zwischen den jeweiligen atmosphärischen Komponenten aus den NCEP/NCAR Reanalysedaten und der Meereiskonzentration ermittelt. Es hat sich gezeigt, dass die Meereiskonzentrationen im östlichen Weddellmeer zunehmen, während das westliche Weddellmeer eine Abnahme verzeichnet. Die Veränderungen treten überwiegend in der Eisrandzone auf. Dort, und auch in Küstenregionen, sind Temperaturen stark negativ mit der Meereiskonzentration korreliert, wohingegen das zentrale Weddellmeer eher eine positive Korrelation zwischen beiden Variablen zeigt, vor allem im Winter.

Die Analyse von Windgeschwindigkeiten hat aufgedeckt, dass die vorherrschenden Westwinde an der Antarktischen Halbinsel tendenziell eine Verschiebung zu Nordwestwinden aufweisen. Es kann angenommen werden, dass die verstärkten südlich gerichteten Winde warme Luftmassen ins westliche und zentrale Weddellmeer bringen und darüber hinaus zu einer Umverteilung von Eismassen aus dem Westen ins zentrale und östliche Weddellmeer führen. Das würde einen Anstieg der Meereiskonzentrationen im zentralen Weddellmeer in Verbindung mit ansteigenden Lufttemperaturen erklären.

Die Korrelation zwischen Meereiskonzentration und Meereisdrift aus den Polar Pathfinder Meereisdriftvektoren ist nur im zentralen Weddellmeer robust, wo beide Parameter negativ miteinander korrelieren. Das ist konsistent mit der Veränderung im Windfeld, da stärkere Nordwinde die nordostwärts gerichtete Drift reduzieren würden und somit die Meereiskonzentrationen ansteigen.

Die Variabilität der Meereisdicke wurde mit Hilfe eines Finite Elemente Meereis-Ozean Modells (FESOM) untersucht. Modellsimulationen mit FESOM zeigen, dass Meereisdicken tendenziell die gleichen Veränderungen zeigen wie die modellierten

Meereiskonzentrationen, welche im zentralen Weddellmeer ab- und im östlichen Weddellmeer zunehmen. Die Veränderungen in der Meereisdicke und der Konzentration führen zu einem Anstieg des Meereisvolumens um 1% pro Dekade in den Simulationen.

Eine Sensitivitätsstudie mit einem Modell der freien Drift, angetrieben durch 10-m Winde von NCEP und Ozeanströmungen modelliert mit FESOM zeigt, dass die modellierten Trends in der Meereisdrift von der Atmosphäre angetrieben werden, da die Ozeanströmungen kaum einen Trend aufweisen. Darüber hinaus konnte gezeigt werden, dass Driftgeschwindigkeiten in dem Modell zum Teil überschätzt werden, besonders in der zonalen Komponente. Trotz dieser Überschätzung ist der Netto-Eisexport von 22x10^3 m^3/s in etwa nur halb so groß wie der in früheren Studien ermittelte Eisexport, was vermutlich durch die Unterschätzung der Meereisdicken im westlichen Weddellmeer verursacht wird.

Chapter 1

Introduction

1.1 Motivation

Sea ice is an important indicator for climate change, since it reacts sensitively to changes in e.g. global temperatures or circulation processes. Although sea ice covers only a comparatively small part of the Earth's surface, it has in turn also an impact on the climate system of the Earth, because it significantly modifies the exchange of heat, momentum, moisture and matter between the ocean and the atmosphere in high latitudes (e.g. *Drinkwater et al.*, 2001; *Fichefet et al.*, 2006; *Owens & Lemke*, 1990; *Parkinson & Cavalieri*, 2002; *Semtner*, 1976; *Strass & Fahrbach*, 1998).

Due to the high albedo and the low heat conductivity of sea ice (*Fichefet et al.*, 2006), surface temperatures are much lower in ice covered regions than above the open ocean. About 50 to 70 % of the solar radiation are reflected at the bare sea ice surface, and even up to 90 % are reflected from a dry snow surface (*Perovich et al.*, 1998). The high reflectivity of sea ice and snow, in combination with the spherical geometry and declination of the Earth, generates strong meridional differences in the energy budget, since the high latitudes absorb much less energy than the tropics. These differences drive circulation systems in the atmosphere as well as in the ocean, which lead to an energy transport from the low and mid latitudes into the polar regions by winds and ocean currents. Despite this energy exchange, temperatures in the polar regions are frequently low enough to induce sea ice growth. The growing sea ice serves as habitat for different species, such as polar bears in the Arctic and penguins in the Antarctic (e.g. *Ferguson et al.*, 2000; *Wilson et al.*, 2001). Also other species depend on sea ice, such as algae or microorganism that live either within the sea ice or at the sea ice bottom in polar regions (*Ackley et al.*, 1979; *Schnack-Schiel et al.*, 2001). These organisms are part of the food chain, serving as food source for larger animals such as krill, which in turn are preyed by whales (*Atkinson et al.*, 2004; *Friedlaender et al.*,

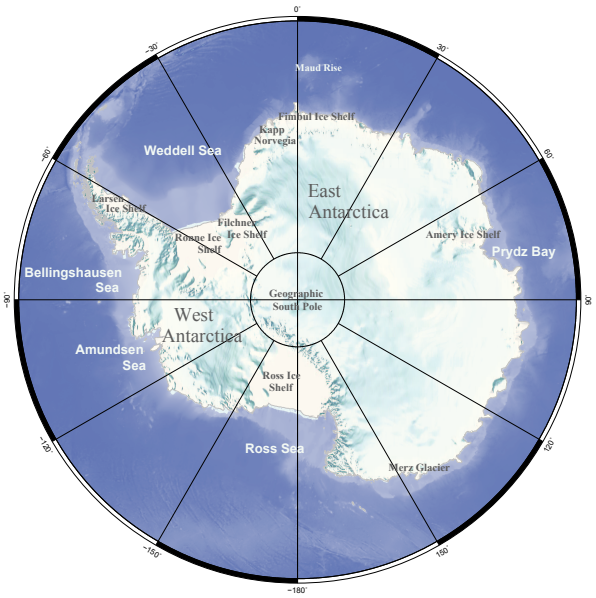

Fig. 1.1: *Map of the Southern Ocean including the Antarctic continent. Light blue areas in the ocean next to the coasts indicate the continental shelves.*

2008; *Loeb et al.*, 1997). Due to the interaction of sea ice with the other components of the climate system[1], it is crucial to understand the mechanisms driving the sea ice and its variations in a changing environment. For that reason, the following sea ice parameters are studied in this thesis, with focus on the Weddell Sea, Antarctica:

- **Sea ice extent and sea ice concentration**: The sea ice concentration (SIC) is the fraction of sea ice coverage per unit area, while sea ice extent (SIE) is defined as the cumulative area of satellite pixels covered by at least 15 % SIC. The distribution of sea ice modifies the state and variability of the regional as well as the global climate (*Liu et al.*, 2004) via the exchange of heat, moisture and momentum between the ocean and the atmosphere, through the surface albedo and by changing the density structure of the ocean by salt release in regions of sea ice growth and freshening of the surface layer in regions of ice melt (e.g. *Harms et al.*, 2001). Since SIE and SIC are in turn influenced by atmospheric changes, it is assumed that they are first indicators for climate change. Both parameters have been analyzed in several studies in both hemispheres (e.g. *Barreira & Compagnucci*, 2011; *Cavalieri et al.*, 1997, 2003; *Cavalieri & Parkinson*, 2008; *Liu et al.*, 2004; *Venegas & Drinkwater*, 2001; *Worby & Comiso*, 2004; *Zhang*, 2007; *Parkinson & Cavalieri*, 2002; *Rigor et al.*, 2000; *Stroeve et al.*, 2005). The studies based on large-scale satellite data indicate that the polar regions have been subject to strong changes during

[1] which includes next to the cryosphere the ocean, the atmosphere and the biosphere

the last decades. SIE has strongly decreased in the Arctic (Fig. 1.2 and, e.g., *Parkinson & Cavalieri*, 2002; *Cavalieri et al.*, 1997) by more than 4 % per decade for the period 1979 through 2010 and also the sea ice covered area (decrease of about 2 % per decade) as well as sea ice thicknesses (not shown) decreased notably (e.g *Rothrock et al.*, 1999). On the contrary, sea ice

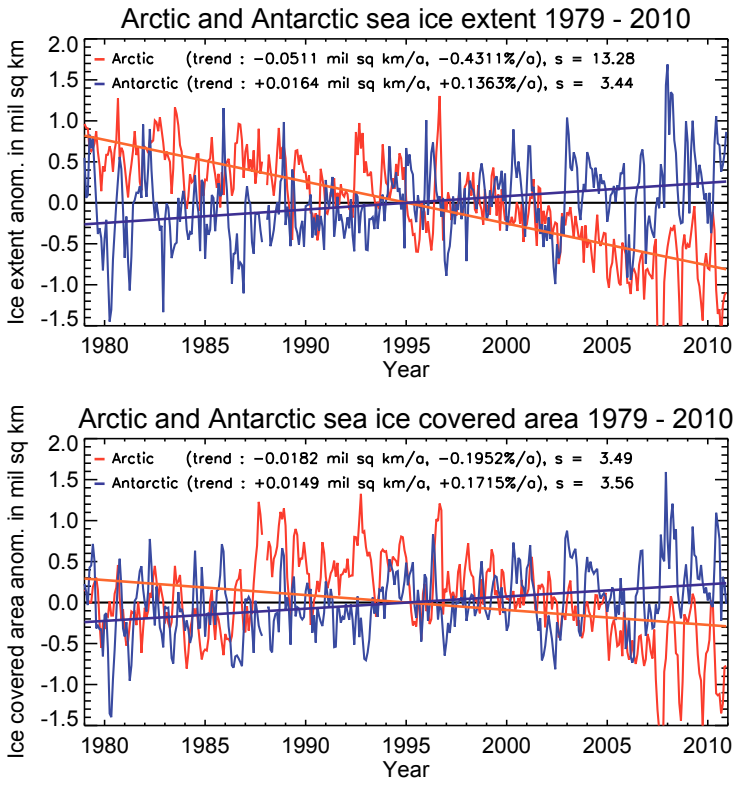

Fig. 1.2: *Anomalies of SIE (top) and ice covered area (bottom) in million km^2 for the Arctic and Southern Ocean, covering the period January 1979 through December 2010. Data from the NSIDC (Fetterer et al., 2002). s denotes the relative significance, with a value of above 1 indicating a statistically significant trend at the 95% level.*

coverage in the Antarctic has not changed notably during the last three decades. Actually, SIE increased slightly by about 1.4 % and the sea ice covered area even by 1.7 % per decade for the period from 1979 till 2010. Changes in the ice coverage and its reason have been analyzed in several studies for different Antarctic sectors (e.g. *Cavalieri & Parkinson*, 2008; *Liu et al.*, 2004; *Lefebvre & Goosse*, 2008; *Zwally et al.*, 2002a). For the Weddell Sea, *Zwally et al.* (2002a) found a positive trend for SIE for the period 1979 through 1998, with the largest changes detected in summer and autumn. Also *Cavalieri & Parkinson* (2008) found comparable positive trends of 0.8 % per decade for the SIE and 0.6 % for the sea ice covered area (cumulative area of actually ice covered ocean) for the period from 1979 till 2006. Both studies agree with the finding that changes are the strongest in summer and autumn. These positive trends, however, are

statistically not significant. This is certainly affected by the opposing trends in the sub-regions of the Weddell Sea. Since the Weddell Sea spans a large area, small-scale and regional differences in trends cannot be identified in a large-scale average, and regional features may be balanced in averages for the entire Weddell Sea. For instance, *Liu et al.* (2004) found a decrease of SIE in the western Weddell sector. On the other hand, parts of the eastern Weddell Sea exhibit increased SIE, as will be discussed later in this study. The decrease of SIE in the western Weddell Sea might be related to increasing surface air temperatures, as were found by e.g. *Kwok & Comiso* (2002a) and *Turner et al.* (2005). There are also studies analyzing the connection between atmospheric oscillations such as the Southern Annular Mode (SAM, e.g. *Lefebvre et al.*, 2004; *Liu et al.*, 2004; *Lefebvre & Goosse*, 2008; *Stammerjohn et al.*, 2008) and El Ninõ-Southern Oscillation (ENSO) (e.g. *Kwok & Comiso*, 2002b; *Lefebvre et al.*, 2004; *Liu et al.*, 2004; *Lefebvre & Goosse*, 2008, and *Stammerjohn et al.*, 2008). Recent sea ice changes are assumed to be connected to the increasing positive polarities in the SAM index in the mentioned studies. This trend in the SAM index is attributed to the ozone depletion in the stratosphere in the Southern Hemisphere (*Arblaster & Meehl*, 2006), which results in a strengthened Antarctic polar vortex with increasing zonal winds during summer and autumn (*Renwick*, 2004; *Thompson & Solomon*, 202; *Turner et al.*, 2009). However, a clear and consistent relationship between SAM and ENSO with SIE changes in the recent decades was not found in those studies and the causes for the contrary changes in both hemispheres are still not fully identified. For the future, however, it is expected that also the Southern Ocean will show a decline in the SIE (e.g. *Goosse & Renssen*, 2001; *Parkinson et al.*, 2006), due to the recovery of ozone concentrations in the stratosphere and further increasing greenhouse gas concentrations (*Bracegirdle et al.*, 2008; *Turner et al.*, 2009).

In this study, the changes of SIE, sea ice covered area and SIC are reconstructed for the years 1979 through 2006. Changes of SIE and sea ice covered area are analyzed for sub-regions of the Weddell Sea, to find out, whether the statistically insignificant trend of SIE is a product of averages for the entire Weddell Sea. In addition, correlation maps between SIC and surface air temperature, wind speed and divergence in the wind field as well as cloud coverage were calculated to estimate the impact that these atmospheric variables have on SIC, individually. It is also analyzed, whether these impacts changes seasonally. The correlation between SIC and SAM index as well as ENSO is also shown to demonstrate the connection between sea ice and these atmospheric oscillation patterns in the Weddell Sea for individual seasons.

- **Sea ice thickness**: Not only the coverage of sea ice, also the sea ice thickness distribution is an important variable, since both sea ice parameters together determine the volume of the ice. Analyzing the sea ice thickness distribution is also necessary to understand the physical processes of the polar oceans (*Zwally et al.*, 2008), since the sea ice thickness determines the amount of salt that is released to the ocean, the amount of freshwater, that can be advected to other regions and the heat transfer between the ocean and the atmosphere. Despite the need of large-scale and frequent data, satellite-based measurements of sea ice thickness have only recently been developed and are not conducted routinely yet (*Renner & Lytle*, 2007), which complicates the analysis of the sea ice thickness distribution. *Worby et al.* (2008) compiled available ship based sea ice thickness measurement for the Southern Ocean and analyzed the seasonal variability of sea ice thickness. They found the summer to be the season with the highest sea ice thickness variability. From the *in-situ* measurements they calculate a mean sea ice thickness distribution, which they interpret as sea ice thickness climatology, since the data set is a compilation and average over more than two decades. Due to the high spatial and temporal varying data distribution, long-term variability and trends could not be calculated from this data set (*Worby et al.*, 2008). Another data source, covering the northern Weddell Sea, is based on upward looking sonar data (ULS, e.g. *Harms et al.*, 2001; *Strass & Fahrbach*, 1998; *Strass*, 1998). These data have been measured between 1990 and today along a transect between Kapp Norvegia and Joinville Island as well as along the Greenwich Meridian. However, time series have many data gaps and measurements are restricted to some few regions. Therefore, an adequate analysis of the sea ice thickness distribution and its trends cannot be revealed from this data set.

  Large-scale space-borne sea ice thicknesses, based on measurements of sea ice surface elevations, have been measured during the period 2003 through 2009, by the Ice, Cloud, and Land Elevation Satellite (ICESat). However, measurements were only performed for distinct survey phases in February/March, May/June and October/November (*Yi et al.*, 2011), but unfortunately not consistently for every year. *Yi et al.* (2011) analyzed the sea ice thickness distribution and the sea ice volume changes for the ICESat surveys. Mean sea ice thicknesses in their study do not indicate any trend. To calculate the 6-year trend in sea ice volume, data were fitted to a seasonal cycle by *Yi et al.* (2011). They found a slightly positive, but statistically insignificant trend of 0.08 % per year. For the future, CryoSAT-2, is supposed to provide space-borne sea ice thickness data based on radar altimeter measurements

and changes in the sea ice thickness might be better detectable with an extended data set. However, so far, model simulation are mainly used for analyses of sea ice thickness variability and trends. *Zhang* (2007), e.g., found a positive trend for sea ice thickness in most sea ice covered regions in the Southern Ocean as well as a positive trend for the sea ice volume for the period 1979 through 2004. In this study, the sea ice thickness distribution and trends in the sea ice thickness for the Weddell Sea are simulated with a newly developed Finite Element Sea ice-Ocean Model (FESOM, *Timmermann et al.*, 2009). Furthermore, it is tested, whether proxies, such as the differentiation of the sea ice classes first and second year ice (FYI, SYI), can be used for an estimation of mean sea ice thickness and volume changes. *Johannessen et al.* (1999) and *Maslanik et al.* (2007), e.g., found a consistency between the decline in the general mean age and thickness of sea ice for Arctic sea ice. Furthermore, multi-year ice is generally much thicker than FYI (*Maslanik et al.*, 2007) and therefore, one might be able to estimate changes in the sea ice mass of a region by the differentiation between both ice classes. This would serve an independent data set for this sea ice parameter, which might be helpful for model validation.

- **Sea ice drift**: During sea ice formation, the sea water's salt is released into the ocean (e.g. *Harms et al.*, 2001; *Fichefet et al.*, 2006), since only a small amount of it is included in the crystal structure of sea ice. The salt release modifies the density structure of the surface water in the region of formation (e.g. *Harms et al.*, 2001; *Venegas & Drinkwater*, 2001). Due to sea ice drift, freshwater in form of sea ice is exported from the region of its formation and influences additionally the density structure in regions of melting, in particular when thermodynamical growth of sea ice usually does not take place in those regions. Melting of the sea ice results in a freshening of the surface layer, which decreases the density of the surface water. This leads to a stabilization of the ocean's stratification (*Harms et al.*, 2001) and therefore to a reduced vertical mixing (*Venegas & Drinkwater*, 2001). Therefore, the exchange of heat and matter between the water masses in different depths, e.g., is to some extent modified by sea ice drift. The movement of sea ice modifies in addition the sea ice parameters SIC and thickness (*Harder & Fischer*, 1999; *Venegas & Drinkwater*, 2001). Divergent drift opens the sea ice cover and increases therefore the exchange of heat between the ocean and the atmosphere. In winter, the relatively warm ocean loses a large amount of heat to the cold atmosphere, which results in new sea ice formation in such leads. This has an influence on the density structure of the ocean and additionally on the

meridional movement of the atmosphere. In summer, on the other hand, leads support a quick melting, since the albedo of the open water is much higher than that of the sea ice. Therefore, the ocean takes up a large amount of energy, which results in sea ice melt. When sea ice drift is convergent, as for example in the western Weddell Sea because of the obstruction of sea ice drift by the Antarctic Peninsula (*Turner et al.*, 2002), sea ice can become much thicker than by thermodynamic growth alone and may survive a summer melt period, becoming second year ice. Hence, sea ice motion influences the sea ice thickness distribution (*Harder & Fischer*, 1999) as well as the total sea ice volume significantly.

Sea ice drift has been observed and analyzed during the last decades by deploying sea ice drift buoys installed on ice floes (e.g. *Geiger et al.*, 1998; *Heil et al.*, 2001, 2008; *Kottmeier & Sellmann*, 1996; *Massom*, 1992; *Uotila et al.*, 2000). The buoys record regularly their position and from position changes, the velocity of the floe can be calculated (*Argos Collect Localisation Satellites Company*, 2008). Although buoys measure drift velocities only locally, a large-scale drift pattern can be obtained from the time series of their records. *Kottmeier & Engelbart* (1992), e.g., showed that the records of buoy data represent the well known large-scale Weddell Gyre circulation. Also deformation processes are calculated from arrays of buoys, but only locally on small scales. *Heil et al.* (2008), e.g., studied the sea ice deformation in a small part of the western Weddell Sea for austral summer 2004/2005 and found a general divergent drift field in the observation region between about 69 - 67^{o}S and 58 - 54^{o}W. This is comparable to the studies of *Vihma et al.* (1996), who studied the deformation in the central Weddell Sea, and to results of *Wadhams et al.* (1989). In both studies, mean sea ice drift was divergent in the observed regions of the Weddell Sea.

With the beginning of satellite observations, the possibility of sea ice drift determination on large scales became available. For an determination of sea ice drift, the cross correlation method (CCM, *Agnew et al.*, 1997; *Emery et al.*, 1986; *Ninnis et al.*, 1986) was developed and applied to different satellite data. This method compares the signal patterns of two subsequent satellite images and calculates then the displacement of these patterns between both images. Consequently, large-scale sea ice drift fields can be obtained for polar regions in both hemispheres. For the Southern Ocean, *Emery et al.* (1997), *Fowler et al.* (2001), and *Kwok et al.* (1998), e.g., showed for the first time the large-scale mean sea ice drift characteristics. They displayed the well known Weddell Gyre circulation, with an inflow near the eastern coast and a northward flow

in the western Weddell Sea, which is deflected to the east in the north-western Weddell Sea (*Emery et al.*, 1997).

Such satellite-based sea ice drift fields for the Antarctic have been compared to buoy-derived sea ice drift by, e.g., *Heil et al.* (2001) and *Schwegmann et al.* (2011). They found a generally good agreement of the broad-scale drift pattern in both data sets, with the exception, that satellite-based sea ice motion is too low in comparison with buoy data.

Based on satellite-derived sea ice drift fields in combination with buoy data, *Schmitt* (2005) analyzed the trend of sea ice drift in the Weddell Sea. She found a reduction of sea ice drift velocities in the entire Weddell Sea, except for the marginal sea ice zone and the inflow in the east for the period 1979 through 1997.

In the present study, monthly mean sea ice drift fields based on satellite observations are presented to show their seasonal variability. In addition, long-term and monthly trends are shown. It is discussed, whether trends observed by *Schmitt* (2005) are also identified in the drift product used here for the extended period till December 2006. To demonstrate the interannual and decadal variability of sea ice drift in the Weddell Sea, single grid points have been chosen for regions with both significant and non-significant trends near the coasts and in the central Weddell Sea. Correlation with SAM and ENSO is tested for these grid points to indicate the influence of these oscillation patterns on the sea ice drift variability. Moreover, maps of the divergence in sea ice drift are presented for the entire Weddell Sea. The correlation between SIC and both the sea ice drift as well as the sea ice deformation with respect to divergent drift behaviour is also demonstrated, to estimate their connection to SIC changes.

- **Sea ice export**: A net positive freshwater export out of a region results in a salinity enrichment of the water masses in this region, due to the fact that only a small amount of the sea water's salt is included in the crystal structure of sea ice during sea ice formation. The remaining salt is injected into the ocean and increases the density of the water, leading to vertical mixing. The effects of sea ice mass transport and a related salt release are believed to be of special importance in the Weddell Sea (*Harder & Fischer*, 1999) and may contribute to the thermohaline ocean circulation, because of the formation of deep and bottom water. These very cold and dense water masses mainly originate at the shelves (*Mosby*, 1934; *Foster & Carmack*, 1976) around the coast (light blue in Figure 1.1) and sink down to deep layers of the ocean. Hence, knowledge about the freshwater fluxes is important to obtain a realistic description of the ocean in climate models. The calculation of sea ice and freshwater exports

from the Weddell Sea is difficult, since regular sea ice drift as well as sea ice thickness data are required. In the Weddell Sea, especially sea ice thickness data are barely available. The ULS measurements provide only data for short periods. In addition, the transect between Kap Norwegia and Joinville Island, which is used for a calculation of sea ice export, is at no time covered completely by data. *Harms et al.* (2001) derived a correlation between the length of the sea ice season and the sea ice thickness and calculated yearly mean sea ice volume fluxes based on this proxy data set, combined with drift velocities from a free drift model for the period 1979 through 1998. *Uotila et al.* (2000) calculated sea ice volume fluxes based on ULS data measured in 1991/1992 and drift velocities from the free drift model and found comparable export rates as *Harms et al.* (2001). An alternative to measurements is provided by model simulations. *Harder & Fischer* (1999) and *Timmermann et al.* (2001) simulate net sea ice export rates with values comparable to the studies of *Harms et al.* (2001) and *Uotila et al.* (2000). In the present study, sea ice export rates were calculated from FESOM for the extended period 1979 through 2010. It is analyzed, whether export rates are comparable to the former studies and whether rates have changed significantly within the last decades.

Another aim of this thesis is the evaluation of FESOM simulations. *Timmermann et al.* (2009) developed a coupled sea-ice ocean model based on finite elements, which permits a refinement of the horizontal mesh in regions of special interest on e.g. dynamic processes. In their study, *Timmermann et al.* (2009) showed, that a representation of globally simulated aspects such as the transport of the Antarctic Circumpolar Current (ACC) is comparable to results from the traditional models using the finite-differences method. With respect to sea ice, they found a good agreement of simulated sea ice thicknesses with observations in the central Weddell Sea and along the Greenwich Meridian. In addition, mean winter SIE was found to be in good agreement with observations. Sea ice drift velocities, however, have not been tested in their study. In this thesis, the comparison of the simulated sea ice parameters SIC, thickness, and drift from FESOM with observations is extended, based on monthly averaged of these sea ice parameters. Model results are compared with small-scale *in-situ* and large-scale satellite data, where and when available, to estimate the model's uncertainties and to fill afterwards data gaps, especially concerning sea ice thickness data. These model results are afterwards used to calculate sea ice volume and its changes as well as the net transport of sea ice out of the Weddell Sea.

This study is focused on the Weddell Sea, because the Weddell Sea:

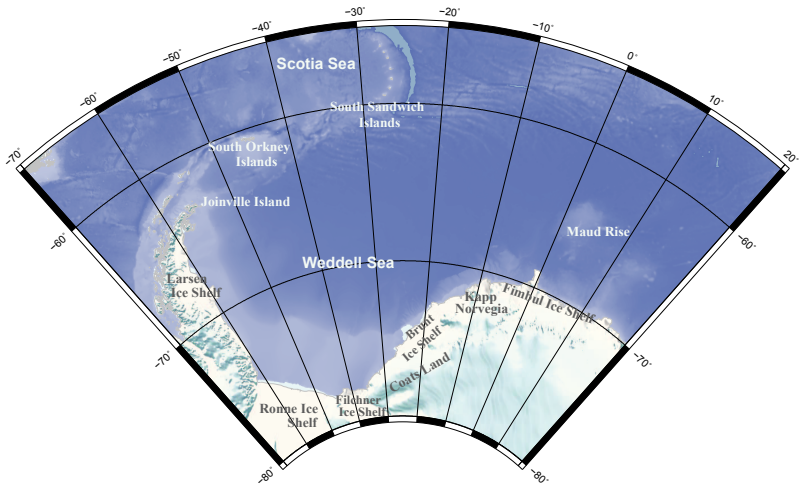

Fig. 1.3: *Map of the Weddell Sea.*

- has the largest SIE in the Southern Ocean in winter, with up to 2200 km from the coast (*Harms et al.*, 2001)
- has a special sea ice drift regime, because of the restriction of movements at the Antarctic Peninsula (*Turner et al.*, 2002), which permits the exchange of sea ice with the Bellingshausen Sea and forces high sea ice thicknesses due to deformation at the coasts
- is one of the few regions in the Southern Ocean, where some sea ice survives a summer melt period and becomes second year ice (*Worby et al.*, 2008), influencing the sea ice thickness distribution (due to deformation second year ice can grow much thicker than first year ice)
- is one of the most prominent regions for potential deep and bottom water formation (e.g. *Brennecke*, 1921; *Mosby*, 1934; *Foldvik et al.*, 1985)

It has been shown, that the different sectors of the Southern Ocean[2] show different and partly opposing trends for the SIE (e.g. *Cavalieri & Parkinson*, 2008). The Weddell Sea as a whole exhibits a slightly increasing trend, as the entire Southern Ocean. This trend can be divided into a reduction of SIE in the west and an increased SIE in the east, as was already mentioned above. Therefore, the Weddell Sea is ideal to study the factors that drive both positive as well as negative trends of the sea ice parameters. Their changes are mainly analyzed based on large-scale satellite products.

[2]The Antarctic can be divided into the Ross, Bellingshausen/Amundsen and Weddell Seas and the Indian and Pacific Ocean sectors (e.g. *Zwally et al.*, 2002a; *Lefebvre & Goosse*, 2008)

1.2 Structure of this thesis

The primary aim of this study was to assess the interannual and decadal variability of sea ice drift, thickness and concentration in the Weddell Sea. Moreover, it was tested, how much atmospheric boundary conditions and the sea ice drift are correlated to SIC changes. For this purpose, different data sets were analyzed. Small-scale data were used to validate the large-scale satellite products to achieve a reliability of calculated trends. A second goal was to validate FESOM and to use the model simulations for filling the gaps of observational data.

In Chapter 2, the atmospheric variables surface temperature, sea level pressure and 10-m wind speeds, provided by the National Center for Environmental Predictions (NCEP), are presented. A first perspective on the expected influences of the atmospheric fields on sea ice is given in this chapter. These influences might be seen in observations of the analyzed sea ice parameters, but certainly occur in FESOM simulations, since the model is forced with the NCEP reanalysis data. The general model setup and principles of FESOM are briefly described in Appendix B.

Chapter 3 discusses the changes in SIE and SIC as documented by satellite data. Passive microwave SIC is correlated with atmospheric components such as air temperature and wind speed to estimate their influence on the variability of SIC. In addition, the temporal evolution of SIE and SIC is compared to model simulations with respect to their interannual variability and trends.

The distribution and evolution of sea ice thickness is addressed in Chapter 4. Backscatter data were used to determine the distribution of the sea ice classes FYI and SYI, which is assumed to be a proxy for the sea ice thickness distribution. It is further assumed, that the sea ice class distribution from satellite data is connected to the sea ice age distribution in model simulations under specified aspects. Criteria for this connection are tested in this study and the interannual variability and trends of the sea ice class distribution obtained from backscatter data are compared to model simulations of the sea ice age. The model used for this comparison is the Bremerhaven Regional Ice Ocean Simulations (BRIOS) model, since this model already includes a routine after *Harder* (1996) to determine the sea ice age. Furthermore, sea ice thicknesses gained from FESOM simulations are analyzed with respect to the mean sea ice thickness distribution and its temporal variability. Comparisons of modelled sea ice thicknesses with the sparsely available *in-situ* data of upward looking sonars are made to verify model results.

Chapter 5 deals with sea ice drift velocities. Small-scale buoy data and large-scale satellite-based sea ice motion are compared and are used to reveal the general sea

ice drift regime and its trends in the Weddell Sea on a yearly and seasonal basis. Large-scale sea ice drift fields are correlated with SIC to assess their influence on the SIC. In addition, observations are compared to model results. It is discussed whether the atmospheric forcing data from NCEP or the oceanic circulation is the major contributor to simulated changes in the sea ice drift field. For this aim, simulations with a free drift model are performed with time-invariant climatologies of either the wind field or the ocean currents. Furthermore, a sensitivity study is performed to evaluate the influence of different model parameters such as the ice strength or the drag coefficients for the atmosphere and ocean stresses on the modelled sea ice drift velocities. The agreement of the simulated drift velocities from this sensitivity study with buoy data is additionally tested.

From model simulations, sea ice volume and salt fluxes over a flux gate crossing the Weddell Sea from Joinville Island to Kapp Norvegia are presented in Chapter 6. Model simulations are compared to observational-based volume fluxes, whose availability depends on the sparsely available sea ice thickness data from upward looking sonars, and to results of previous studies dealing with sea ice volume fluxes.

A summary of the most important results of this study as well as an outlook to future work is given in Chapter 7.

Chapter 2

Atmospheric boundary conditions

Atmospheric conditions for the period January 1979 to December 2006 for the Weddell Sea were derived from monthly mean fields of surface air temperatures (SAT), sea level pressure and 10-m winds, provided by the National Center for Environmental Predictions/National Center for Atmospheric Research Reanalysis Project (NCEP/NCAR, hereinafter referred to as NCEP data, *Kalnay et al.*, 1996). This time span was chosen because it covers the same period for which sea ice drift fields are available for the Weddell Sea. The NCEP data have a spatial resolution of 2.5^{o} x 2.5^{o} and are graded as class B, i.e. the respective mean fields are composites of observations - when and where available - and model simulations (where no observations are available, *Kalnay et al.*, 1996). Monthly mean anomalies of SAT and sea level pressure were calculated by subtraction of the monthly climatology to remove the signal of the seasonal cycle. Furthermore, geostrophic winds were derived from sea level pressure gradients. Sea ice drift is expected to be closely related to the geostrophic wind fields, since they explain more than 70 % of the variance in daily and monthly sea ice drift away from coastal boundaries (*Thorndike & Colony*, 1982; *Kwok & Comiso*, 2002b). On basis of several months, the geostrophic wind field still explains about half of the sea ice drift (*Thorndike & Colony*, 1982). Therefore, a first impression of sea ice motion can be obtained by examining geostrophic winds, also on monthly basis. For all variables, monthly as well as long-term trends were derived and statistical significance at the 95 % confidence level was assessed by a t-test (see Appendix E). From the analysis of these atmospheric parameters, a first perspective of expected changes of the SIC, drift and thickness can be derived.

2.1 Air temperature distribution

The mean SAT distribution over the study period and the distribution of the long-term trends along with their relative significance in the Weddell Sea are displayed in Figure 2.1. SAT increased in large parts of the Weddell Sea, except for the north-eastern

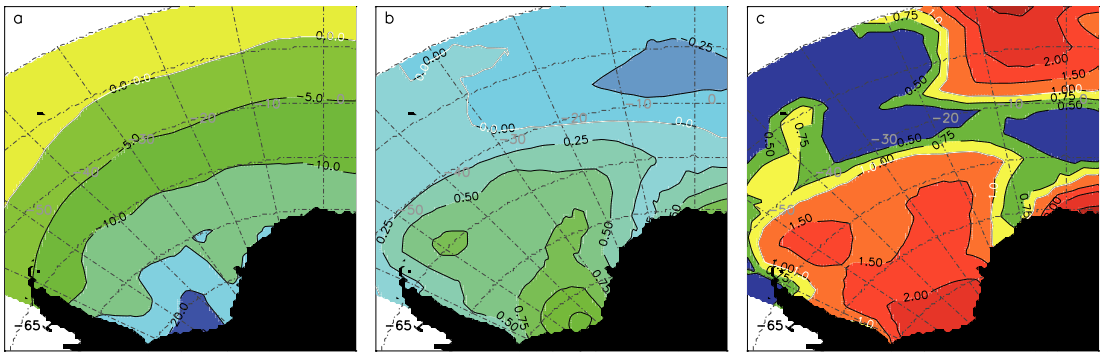

Fig. 2.1: *a) Mean SAT (in ^{o}C), b) long-term trend of SAT anomalies (in ^{o}C per decade) and c) relative significance (a value of at least one denotes a significant result at the 95% confidence level) from the NCEP data for the period from 1979 to 2006.*

region, where a slight cooling can be observed. The strongest warming occurred in the southern Weddell Sea with more than 1.0 ^{o}C per decade. At the Antarctic Peninsula, SAT also increased slightly, although the increase in this data set is not as strong as was observed for other time periods analyzed in previous studies (e.g. *Kwok & Comiso*, 2002a; *Turner et al.*, 2005). Most of the SAT trends in Figure 2.1b are statistically significant at the 95 % confidence level (see Fig. 2.1c). The warming at the Antarctic Peninsula has been associated with an increase in the occurrence of the positive phase of the Southern Annular Mode/Antarctic Oscillation (SAM/AAO) index, which is defined as the difference between the normalized zonal mean sea level pressures at 40^{o}S and 65^{o}S (*Gong & Wang*, 1999; *Lefebvre & Goosse*, 2008). A positive phase of the SAM is connected with an enhanced transport of warm air from the north into the western Weddell Sea (*Stammerjohn et al.*, 2008), which results in an increased SAT above the Antarctic Peninsula.

Seasonally, the SAT trends vary strongly (see Fig. 2.2). During summer (December - February), SAT predominantly decreased throughout the considered period. Only in few parts of the western Weddell Sea, especially near the tip of the Antarctic Peninsula, a warming of air masses can be observed. In autumn (March - May), SAT increased over the southern and western Weddell Sea, with a maximum warming of 3.5 ^{o}C per decade in the south-central basin. This warming expands to the central Weddell Sea, suppressing the prevailing cooling towards the east. In May, negative SAT trends occur only east of 20^{o}W. This cooling shifts to the northern regions in

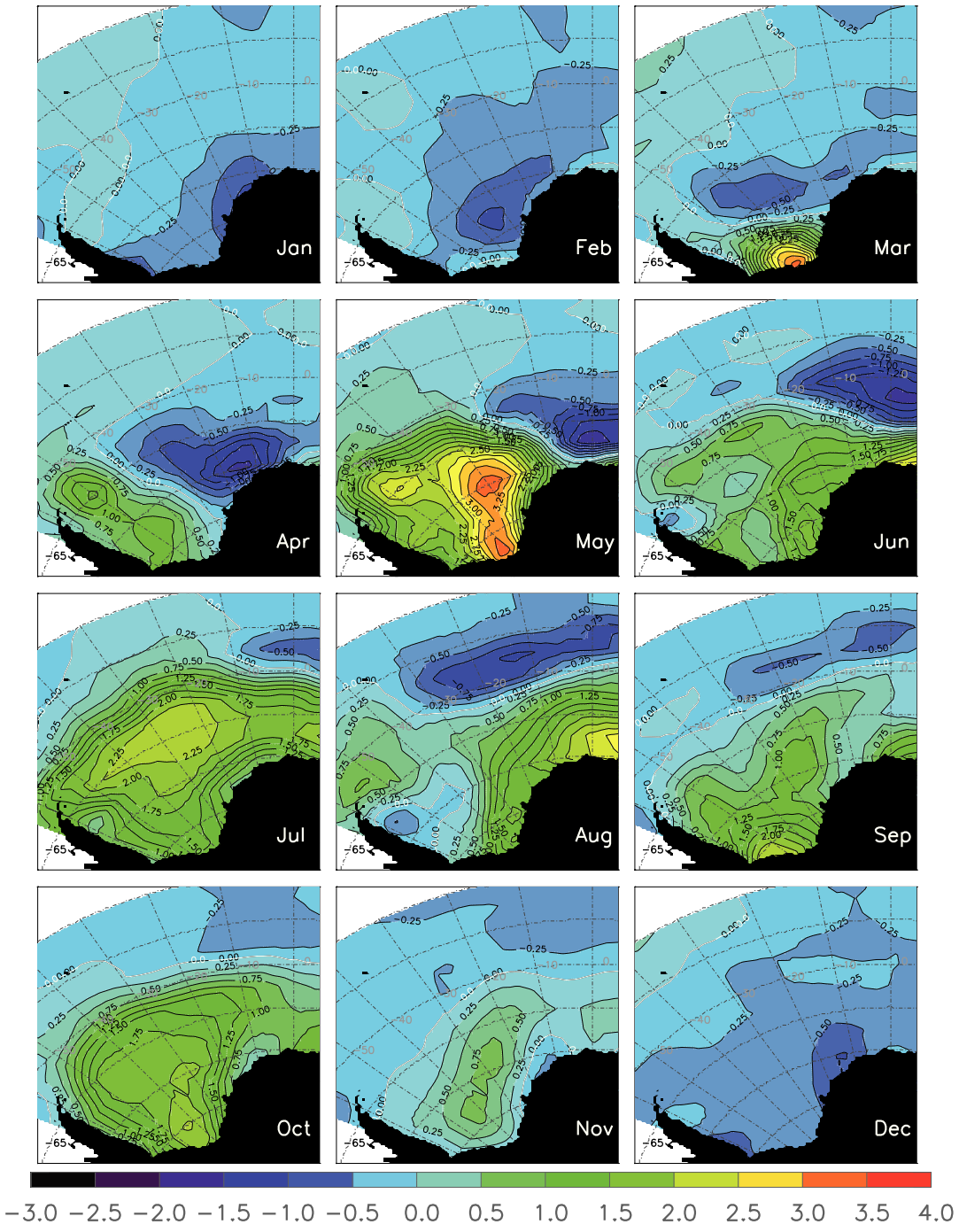

Fig. 2.2: *Monthly trends of SAT anomalies from the NCEP data for the period from 1979 to 2006 in ^{o}C per decade. White line indicates contour of no trend.*

austral winter (June - August) and starts to expand into the west, so that in spring (September - November), nearly all regions north of 60^{o}S reveal a slight cooling, except for October, when the warming of air expands to about 55^{o}S. The central Weddell Sea as well as the eastern-coastal regions still exhibit positive trends of up to 2.5 ^{o}C per decade, although these trends weaken towards the end of spring in November.

In summary, warming dominates in autumn, winter and spring, mainly in the central Weddell Sea. In the summer months, when sea ice melts and large parts of the Weddell Sea are ice free, the SAT trends are negative during the considered period. Especially the cooling in summer, but also most of the stronger positive SAT trends are statistically significant and had very likely a strong connection to sea ice changes, because of a modified heat exchange between the ocean and the atmosphere.

2.2 Sea level pressure and associated wind fields

The overall mean sea level pressure and trends of its anomalies over the Weddell Sea are illustrated in Figure 2.3 (coloured background). Additionally, the vectors of the corresponding geostrophic winds are depicted, which are - by definition - parallel to the isobars. Mean sea level pressure decreases overall from the north to the

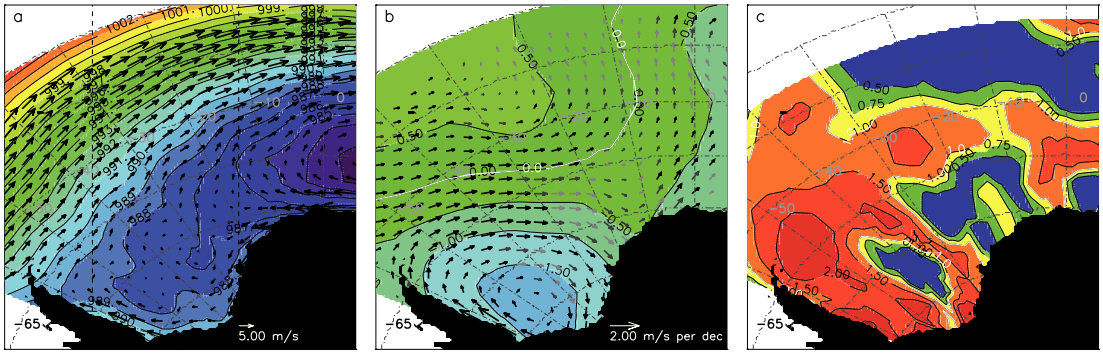

Fig. 2.3: *Mean sea level pressure in hPa (a), trends of its anomalies in hPa per decade (b) and relative significance (c) from the NCEP data for the period 1979 through 2006. Vectors show the corresponding mean geostrophic winds in m/s and their trends in m/s per decade. Black vectors in b) illustrate statistically significant geostrophic wind speed trends; grey vectors mark the non-significant trends.*

south, with the lowest sea level pressure occurring in the central and eastern Weddell Sea. Towards the Antarctic continent, the sea level pressure increases again very slightly. These feature induces a mean geostrophic wind field that is directed west- to south-westward in the south-east, parallel to the coast. The flow changes to the north, parallel to the Antarctic Peninsula, and is deflected to the west at the tip of the Antarctic Peninsula. Westerly winds are predominant in the north-western region. In the interior of the Weddell Sea, winds are weaker and mainly follow the circulation of the outer air masses.

Trends in the sea level pressure are negative in every region of the Weddell Sea south of 65 ^{o}S. The strongest negative trends occur in the central Weddell Sea basin.

These trends are formed like rings and expand towards the Antarctic Peninsula in the west. The predominant trends of the sea level pressure induce enhanced geostrophic winds parallel to the coast of the Antarctic Peninsula, and a stronger westerly flow at its northern tip. Trends of the geostrophic winds in the central Weddell Sea describe a circulation pattern, which intensifies the prevailing wind speeds. While in the eastern Weddell Sea the meridional wind component increases, the zonal wind component tends to be smaller. The result is a negative trend in the generally westward wind speeds next to the Fimbul Ice Shelf (see Fig. 1.3). Additionally, in the marginal sea ice zone, the prevailing westerlies get a stronger northward directed component, which might enhance a transport of sea ice to the north and might increase the ice extent in this region.

On a monthly basis, trends are fairly variable and lack a clear seasonal cycle. Figure 2.4 displays a subset of monthly trends to demonstrate their seasonal variability.

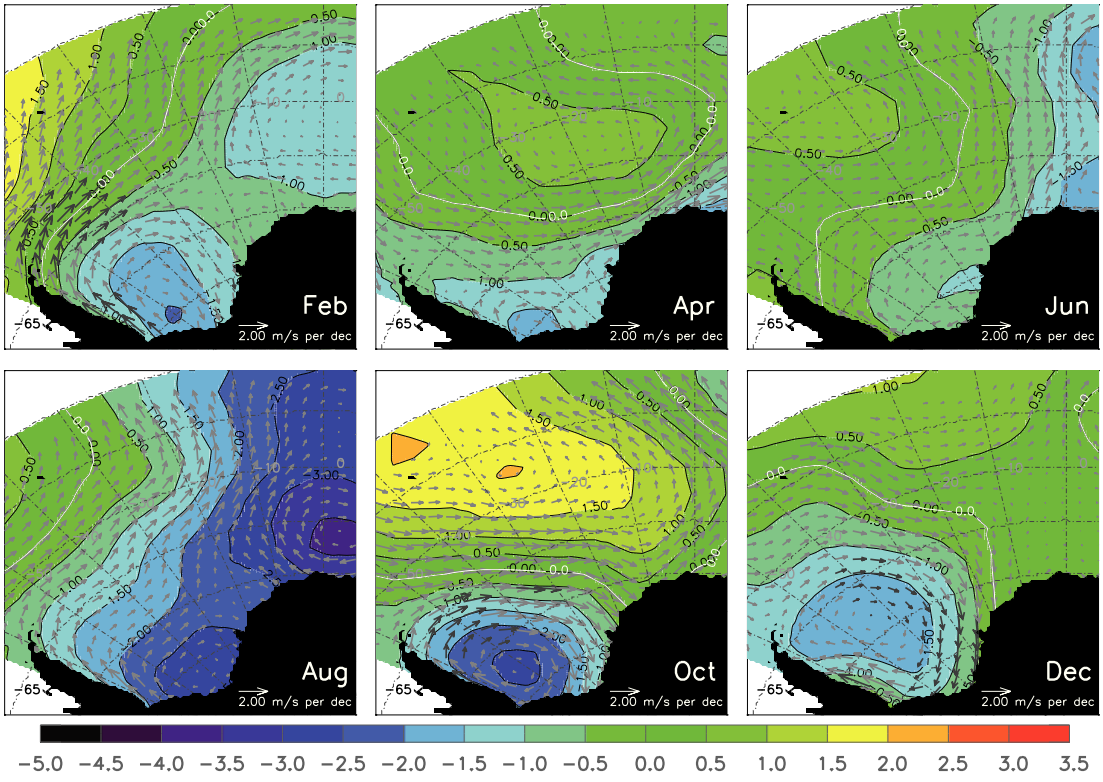

Fig. 2.4: *Subset of monthly trends of sea level pressure anomalies (hPa per decade) and geostrophic winds (m/s per decade) for the period from 1979 to 2006 from the NCEP data. The colour of arrows indicate the statistical significance of trends: black - significant, dark gray - trend is not significant, but exceed at least one standard deviation, light gray - not significant.*

In most months (e.g. April, May, August), sea level pressure trends are negative in the south-central Weddell Sea, which intensifies the winds in a southerly direction east of about 40°W and northward at the Antarctic Peninsula. In some occasions,

the sea level pressure changes force the geostrophic winds to be more eastward directed (east of 40^{o}W, e.g. May, June), which would result in a reduction of wind speeds. At the northern Antarctic Peninsula, an increasingly eastward direction of the geostrophic wind persists year-round. Moreover, next to the Fimbul Ice Shelf, the meridional geostrophic winds increased, which results in a tendency to stronger offshore instead of alongshore winds, weakening the westward flow of air masses in this region. Regarding the sea level pressure, trends of more/less than $\pm$ 1.5 hPa per decade exceed at least one standard deviation, and in most cases, trends higher/lower than $\pm$ 2 hPa per decade are statistically significant. For the geostrophic wind, most of the trends are statistically not significant at the 95 $\%$ level, but some of them are at least as high as one standard deviation, indicated by dark gray arrows.

Corresponding trends of the 10-m winds are illustrated in Figure 2.5. The coloured background shows the wind speed, vectors indicate the direction of the mean wind field as well as the trends. Geostrophic winds are deflected by about 20^o to the left, compared to the surface winds, and therefore, the 10-m wind will look slightly different. In coastal areas, strong offshore winds are visible in the 10-m wind data, except for

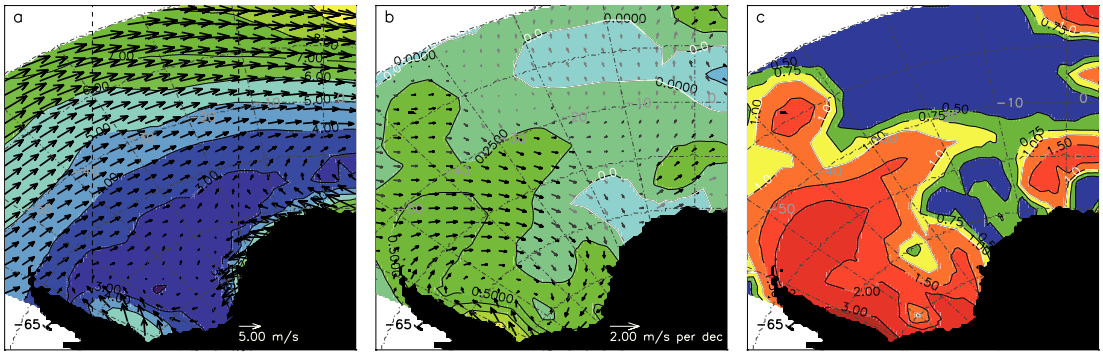

Fig. 2.5: *10-m mean wind speeds in m/s (a), their long-term trends in m/s per decade (b) and relative significance (c) for the period from 1979 to 2006 from the NCEP data. Black vectors in b) illustrate statistically significant wind speed trends; gray vectors mark the non-significant trends.*

the tip of the Antarctic Peninsula. This weak representation of strong offshore winds is potentially because of the poor representation of the Antarctic Peninsula's topography north of 69^{o}S in the NCEP data (*Windmüller*, 1997; *Timmermann et al.*, 2009).

The predominant pattern shows enhanced wind speeds over the entire Weddell Sea with two exceptions, where a reduction could be observed: 1. next to the Fimbul and Brunt Ice Shelves at the eastern coast, which is due to the trend to the eastward directed winds and 2. in the north-eastern Weddell Sea because of the tendency to a higher meridional wind component and a decreased zonal wind component. In most parts of the central and western Weddell Sea, trends for the 10-m winds are

significant. The enhanced wind speeds in the western Weddell Sea are consistent with strengthened positive SAM phases (*Stammerjohn et al.*, 2008). Furthermore, an increased southward component of the westerly winds might also have strengthened the advection of warmer maritime air over the colder Antarctic Peninsula and are a likely explanation for the increased SAT in this region (*Kwok & Comiso*, 2002b).

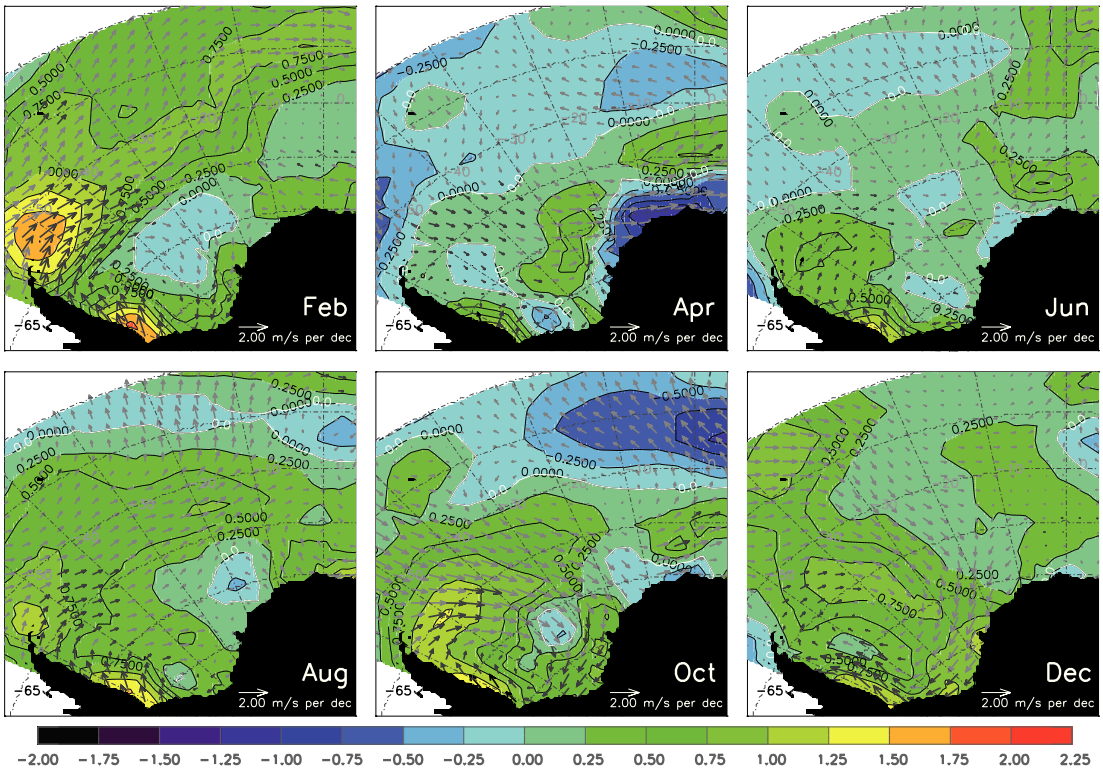

Fig. 2.6: *Subset of monthly trends of 10-m mean wind speeds in m/s per decade for the period from 1979 to 2006 from the NCEP data. The colour of arrows indicates the statistical significance of trends as described in Figure 2.4.*

On a monthly basis, the Weddell Sea shows strong changes in 10-m winds, but since these changes are partly contrary over the year, they are barely visible in the long-term trends. For example, at the tip of the Antarctic Peninsula, 10-m winds strongly increased in some months (e.g. in February, May) with up to 1.5 m/s per decade (about 37.5 % of the mean wind speed). In other months, like in April, these changes were only small and further north, they were even negative. In some occasions, trends are statistically significant near the Antarctic Peninsula and in some parts of the central Weddell Sea, and mostly, trends are at least as high as one standard deviation in these regions. For the rest of the Weddell Sea - except for some small regions in the east near the Antarctic continent - trends are lower than one standard deviation, indicating that the interannual variability is much higher than the trends.

2.3 Discussion

In this section, the described changes in SAT, in the sea level pressure and in the wind field are discussed with respect to their potential connections to the various sea ice parameters in the Weddell Sea.

A cooling or warming of air modifies the exchange of heat between the ocean and the atmosphere. As long as SAT are lower than those of the ocean, a cooling of the air would lead to an enhanced heat transport from the ocean to the atmosphere. Hence, the sea ice production would increase over open water (e.g. leads) or at the ice-ocean interface. On the contrary, when SAT are higher than sea surface temperatures (SST), which is mainly the case in the northern Weddell Sea in summer, a negative trend of the SAT would reduce the heat transport from the atmosphere to the ocean because of a decreased temperature gradient. This would reduce the melting of the sea ice. Since a cooling of SAT was observed in the NCEP data for summer, it is expected that summer SIC and sea ice thicknesses increased over the time period considered in this study. Together, both effects potentially resulted in an increased sea ice volume. Sea ice has a higher albedo than the open ocean, and therefore, increased coverage results in a positive feedback, since it induces further cooling. In winter, a warming, as can be observed in the western and central Weddell Sea, potentially reduced the sea ice thicknesses, since the temperature gradient between the sea ice - ocean and ice/snow - atmosphere interfaces decreases. Therefore, the ocean would lose less heat, which would result in a lower sea ice production at the bottom of the sea ice. A reduction of SIC in winter because of the observed warming, however, is unlikely, since SAT in the central Weddell Sea are still well below the freezing point during this season.

The correct assessment of temperature induced changes in the sea ice coverage and thickness is further complicated by dynamic factors. Such factors include the sea ice deformation and export due to a changed sea ice drift as a result of changes in the sea level pressure and associated wind speeds as well as changes in the oceanic circulation. Sea ice reacts strongly to changes in geostrophic winds (*Thorndike & Colony*, 1982; *Kwok & Comiso*, 2002b). This is confirmed by the fact that the observed sea ice drift in the Weddell Sea (e.g. shown in *Emery et al.*, 1997; *Kottmeier & Sellmann*, 1996; *Kwok et al.*, 1998; *Massom*, 1992) is similar to the patterns for the mean geostrophic wind field described above.

In the western Weddell Sea, the detected changes of the sea level pressure, and therefore of the wind, induce the assumption that SIC along the Antarctic Peninsula decreased. This is because the increased wind speeds force an enhanced transport from the southern to the northern Antarctic Peninsula, where the eastward wind

speeds have also intensified. An enhanced northward wind field is expected to force a higher deformation along the Antarctic Peninsula, and furthermore, may enhance the formation of a coastal polynya in the south-western Weddell Sea next to the Ronne Ice Shelf. Strengthened eastward wind speeds at the tip of the Antarctic Peninsula potentially result in a higher sea ice transport towards the central Weddell Sea, and thus, less SIC in the coastal regions of the western Weddell Sea. Therefore, SIC in the central Weddell Sea are expected to increase in turn. In combination with the increased SAT, the new sea ice formation might remain comparatively low at the tip of the Antarctic Peninsula and sea ice thicknesses potentially decreased in the western and also in the central Weddell Sea, except for the regions, where deformation processes play the major role for the sea ice thickness distribution. The enhanced export of sea ice from the west would lead to a redistribution of ice from the western Weddell Sea into the central and eastern Weddell Sea. Thus, when the redistributed sea ice collides with the sea ice in the eastern Weddell Sea, the compactness in this region is expected to increase.

At the eastern coast - next to the Fimbul Ice Shelf - drift velocities potentially decrease as a result of weakened wind speeds. Given that sea ice could hardly be replaced by sea ice from the East Antarctic sea ice zone in summer (which is barely present in this season), the SIC most likely decrease (increase), when the advection to the west into the Weddell Sea increases (decreases). Therefore, the SIC are expected to increase in this region in summer and autumn, when the advection of sea ice into the Weddell Sea decreases. On the other hand, in winter, the near coastal region is expected to show a decreased SIC, because of a strengthened northward sea ice transport, while coverage as well as sea ice thicknesses most likely increased further offshore due to enhanced deformation.

Taking all these aspects together, it is expected that SIC along with sea ice thicknesses decrease at the entire Antarctic Peninsula in summer and at least at the tip of the Antarctic Peninsula in winter, mainly because of the enhanced wind speeds, but also due to the mostly positive trends in SAT. In the central Weddell Sea, SIC are expected to increase partly, in consequence of the redistribution of sea ice from the west. Contrary to that, sea ice thicknesses are expected to decrease due to the positive trend in SAT during the considered period. SIC and sea ice thicknesses in the eastern Weddell Sea most probably increase in consequence of the redistribution of sea ice from the west and potentially decreasing drift velocities, induced by weaker wind speeds. Whether these hypothesized changes in SIC, drift and thickness can actually be observed, is shown and discussed in the following chapters by using various data sources, such as *in-situ* data, satellite-based sea ice observations and model simulations.

Chapter 3

Sea ice extent and concentration

Large-scale sea ice observations have been performed, starting with the first satellite observations in the early 1970s. Since November 1978, consistent measurements of sea ice extent (SIE) and sea ice concentration (SIC) are available. SIC is the fraction of sea ice coverage per unit area. SIE is defined as the cumulative area of satellite pixels covered by at least 15 % SIC. Both sea ice variables are first indicators for climate change and have been subject to several studies in both hemispheres (e.g. *Barreira & Compagnucci*, 2011; *Cavalieri et al.*, 1997, 2003; *Cavalieri & Parkinson*, 2008; *Liu et al.*, 2004; *Venegas & Drinkwater*, 2001; *Worby & Comiso*, 2004; *Zhang*, 2007; *Parkinson & Cavalieri*, 2002; *Rigor et al.*, 2000; *Stroeve et al.*, 2005). On the one hand, the sea ice system is influenced by atmospheric changes, as can be observed in the Arctic, where SIE has been shrinking dramatically over the last decades (e.g. *Serreze et al.*, 2007). On the other hand, sea ice also modifies the state and variability of the regional as well as the global climate (*Liu et al.*, 2004) via the exchange of heat, moisture and momentum between the ocean and the atmosphere, through the surface albedo and by changing the density structure of the ocean by salt release in regions of sea ice growth and freshening of the surface layer in regions of ice melt. These water mass modifications are believed to drive the global thermohaline circulation (*Venegas & Drinkwater*, 2001). Therefore, a better understanding of the causes for sea ice variability is necessary (*Liu et al.*, 2004; *Zwally et al.*, 2002a) to unravel and interpret current and possible future effects of climate change.

This chapter deals with trends of SIE and SIC from passive microwave data and relates both variables to the variations of atmospheric forcing. Subsequently, these trends are compared to FESOM simulations.

3.1 Trends of sea ice extent derived from passive microwave data and model simulations

SIE in the Weddell Sea was calculated by summing up all pixel areas lying between the Antarctic Peninsula and about 6^{o}E[1], which have a SIC of at least 15%. This threshold is widely used and is expected to eliminate noise and fluctuations due to wind and weather influences (e.g., rapid changes in the wind intensity can cause daily sea ice edge variations of up to 1^o latitude, *Worby et al.*, 1998; *Worby & Comiso*, 2004). Figure 3.1 compares the seasonal cycle of SIE and ice covered area (cumulative area of actually ice covered ocean) from observations (blue) with FESOM simulations (red).

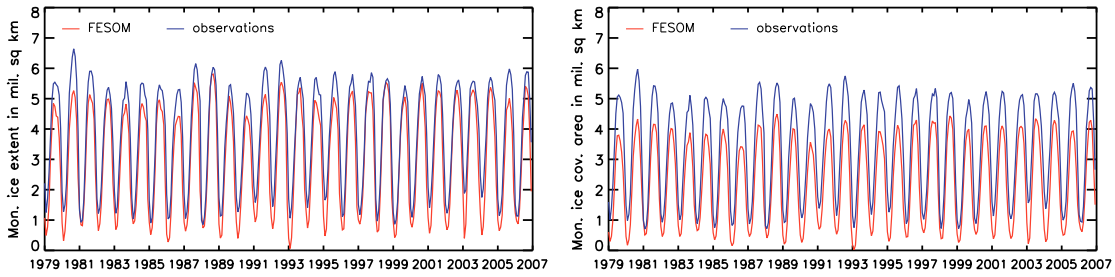

Fig. 3.1: *Monthly SIE and ice covered area in million km^2 from passive microwave data (bootstrap, blue, provided by the NSIDC) and FESOM (red) from January 1979 till December 2006.*

Generally, modelled SIE matches the satellite-based observations, although winter maxima and summer minima are mostly underestimated by FESOM. Summer sea ice disappears nearly completely in the model. Discrepancies in summer minima and winter maxima of the ice covered area are even higher, indicating that SIC are also too low in FESOM, which will be discussed in Section 3.2.2. The interannual variability of summer minima is barely represented in both sea ice parameters in the model, but that of winter maxima fits the observations well. In Figure 3.2 it is shown, how this behaviour influences the trends; it displays the monthly anomalies and the long-term trends of SIE as well as those of the ice covered area for both observations and model simulations.

Figure 3.2 indicates that the annual SIE increased slightly in the satellite-based observations for the period January 1979 through December 2006. However, the

[1] In this study, the boundaries for the Weddell Sea were defined using Cartesian grid coordinates. The actual range for the study area includes the grid points 50 to 170 in x-direction and 185 to 331 in y-direction for the calculation of SIE and the sea ice covered area. This selection corresponds to a longitude of about 6^{o}E at latitude 65^{o}S.

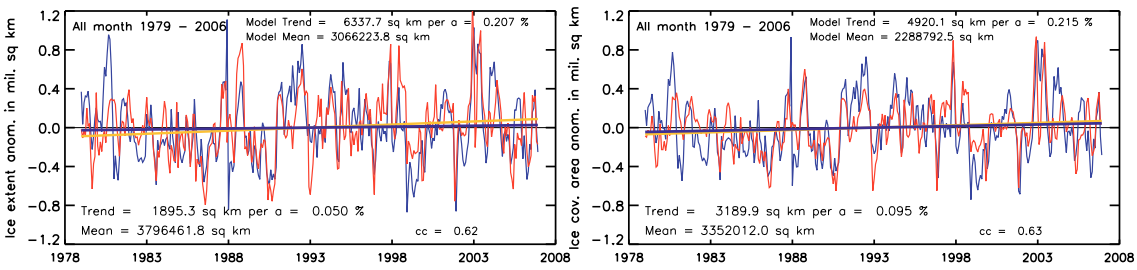

Fig. 3.2: *Monthly anomalies of SIE and ice covered area in million km^2 and their long-term trends in million km^2 per year for the period January 1979 through December 2006 from passive microwave data (bootstrap, blue, trend: black, provided by the NSIDC) and FESOM (red, trend: orange). cc: correlation coefficient.*

trend of about 0.050 % or 1895.3 km^2 per year is statistically not significant. This is because of the high seasonal and interannual variability of the SIE, with alterations of about $\pm$ 1 x 10^6 km^2. With 3189.9 km^2 (0.095 %) per year, the ice covered area shows a slightly stronger, but also statistically insignificant positive trend. These changes are comparable to those found by *Cavalieri & Parkinson* (2008), who determined non-significant trends of 0.8 % (SIE) and 0.6 % (ice covered area) per decade for the same period, even though their study area was slightly larger than in this study and they used the NASA Team algorithm SIC.

Figure 3.2 also indicates that FESOM captures the interannual variability of SIE and ice covered area quite well. The correlation between observations and model simulations is 0.62 for SIE and 0.63 for ice covered area. However, trends are overestimated by the model. Both simulated SIE and ice covered area increased by more than 0.2 % per year. Hence, the trend for modelled SIE (ice covered area) is more than four (two) times higher than the respective trend derived from satellite observations. In contrast, the trend for the entire Antarctic SIE of 1 % per decade from observations (*Cavalieri & Parkinson*, 2008) is well represented by FESOM, which simulates a trend of 1.2 % per decade (*Timmermann et al.*, 2009).

The seasonal cycle of trends in SIE and ice covered area is shown in Figure 3.3 for satellite-based observations and model simulations. Satellite-based SIE and ice covered area follow the same pattern, with trends of the ice covered area being slightly higher. In austral summer, trends were the strongest with up to about 0.8 % (SIE) and 1 % (ice covered area) per year in February. In autumn, this increase diminishes and in the winter months, both sea ice variables show no trend over the last decades. In November and December, SIE as well as ice covered area decreased slightly over the study period. Hence, the major changes appear during summer and autumn. This agrees with the findings of *Cavalieri et al.* (1997, 2003) and *Cavalieri & Parkinson*

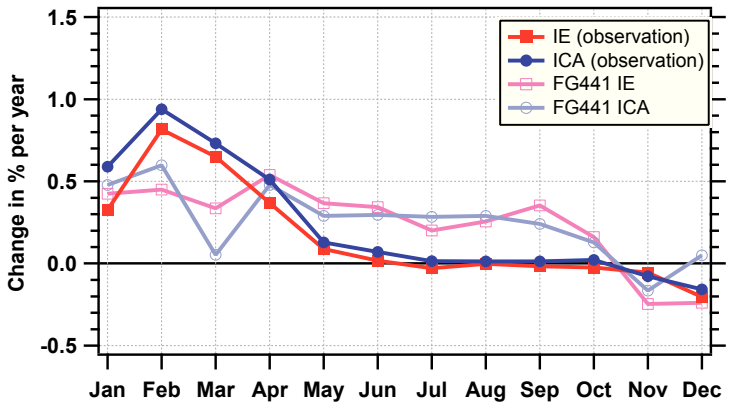

Fig. 3.3: *Monthly trends of SIE as well as from the ice covered area in % per year from 1979 to 2006 from passive microwave data and FESOM. IE: SIE, ICA: ice covered area, FG441: standard model run*

(2008), who also observed the strongest changes in summer and autumn, although - in their studies - March showed the strongest increase of SIE and ice covered area.

Model simulations from FESOM reproduce only a small part of the seasonal variations of trends observed by the satellite data. Trends in January, February and April are higher than over the rest of the year, but the magnitude of the trend from the satellite observations is reached neither in February, nor in March. Additionally, the differences between summer and winter trends are not very high in FESOM. The SIE changes for November and December follow the observed trends, but the ice covered area in the model already increases in December. However, all these changes from the satellite-based observations as well as from the simulations are generally very small and statistically insignificant so that slight differences in the modelled SIE and in the ice covered area may lead to differences in the trend calculation. One has to keep in mind that model simulations are not able to reproduce the observations perfectly, and furthermore, that the summer ice coverage in the FESOM simulations is consistently too small (*Timmermann et al.*, 2009).

Most of the previous sea ice studies analyzed changes in the sea ice parameters for the entire Weddell Sea and found insignificant trends (e.g. *Cavalieri & Parkinson*, 2008 and *Zwally et al.*, 2002a). Since the Weddell Sea spans a large area, small-scale and regional differences cannot be identified in a large-scale average and small-scale features may disappear in averages for the entire Weddell Sea. Therefore, three sub-regions, covering the western, eastern and central Weddell Sea (see Fig. 3.4), were analyzed.

In the western Weddell Sea (the area next to the Antarctic Peninsula), the SIE along with the ice covered area decreased statistically significant by more than 0.5 % per

year, which is one order of magnitude higher than the overall long-term trend over the entire Weddell Sea. This trend is comparable to the findings of *Liu et al.* (2004) for the period from 1979 till 2002. Both sea ice parameters show reductions in all seasons.

In the central Weddell Sea, seasonal trends are comparable to those of the entire Weddell Sea, with an increased SIE and ice covered area until May, nearly no trend between June and November, and only a slight decrease in December. Trends were usually slightly higher than those for the entire Weddell Sea, but in general, statistically insignificant. However, in summer and autumn, most of them are at least as high as one standard deviation.

The eastern part of the Weddell Sea shows an increased SIE and ice covered area throughout the year, except for December and January. The positive trend in February is relatively strong with more than 2 $\%$ per year. Although these trends are not statistically significant at the 95$\%$ confidence level, many of them exceed at least one standard deviation. Additionally, the annual long-term trend for this region is higher than 0.2 $\%$ per year and statistically significant for both variables.

The regional separation of SIE trends indicates that the large-scale summer signal is a combination of reduced SIE in the west and of increased SIE in the central and eastern Weddell Sea. Because of these regional combined trends, the mean changes for the entire Weddell Sea were found to be very low and statistically not significant, especially in winter, although there are some pronounced alterations in the different sub-regions. These will be described in the next section.

3.2 Sea ice concentration

3.2.1 Sea ice concentration distribution and trends from passive microwave data

In the Southern Ocean, most of the sea ice is seasonal, i.e. it melts during summer, and is newly formed each winter. Exceptions only arise in some parts in the Weddell and Ross Seas, where temperatures are low even in summer and the sea ice thickness is high enough to allow for a persistent sea ice coverage. In the Weddell Sea, these areas have a relatively high mean SIC with more than 90 $\%$ mean coverage, which decreases from south-west to north-east as illustrated in Figure 3.4. Noticeable is the southward shift of the sea ice edge between 25^{o}W and 30^{o}W. This

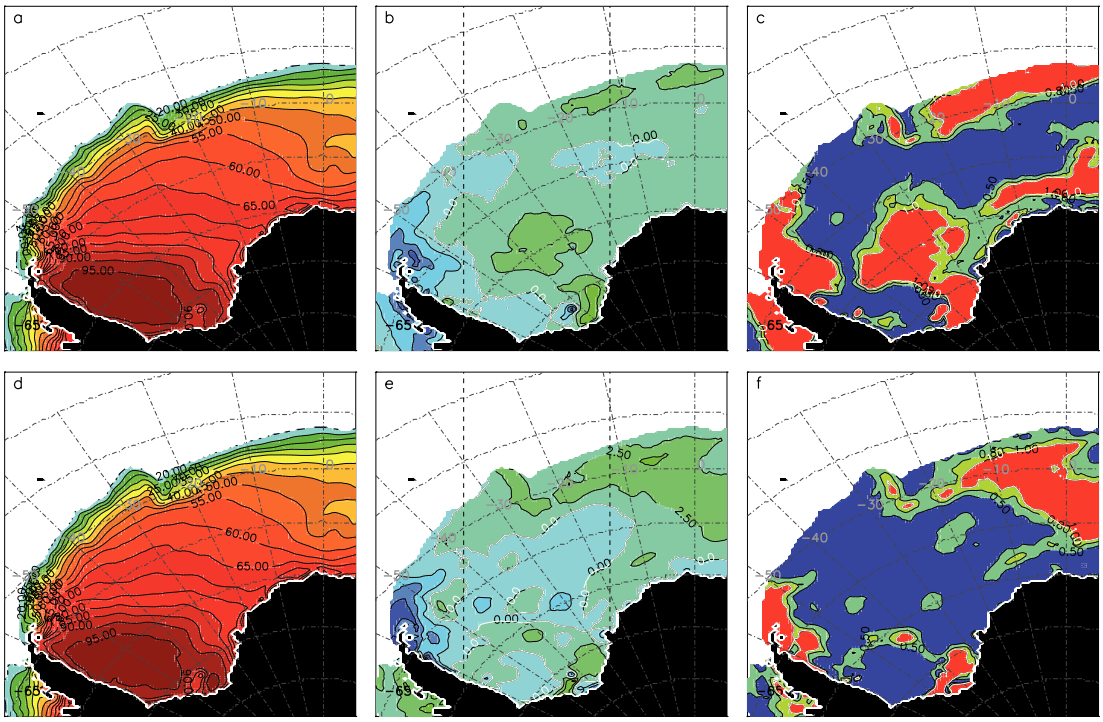

Fig. 3.4: *Long-term mean SIC in %, linear trends of SIC anomalies in % per decade and their respective relative significance for the observation periods 1979-2006 (a, b, c) and 1988-2006 (d, e, f) from the NSIDC bootstrap data. Vertical, dashed lines in panels b and e divide the Weddell Sea into three sub-regions described in Section 3.1.*

is potentially due to the South Sandwich Islands, that are located in this region and act as obstacles, preventing an unhindered transport of sea ice.

SIC changes were analyzed based on monthly anomalies according to their variances. Linear trends and their relative significance were derived for the periods from January 1979 till December 2006, and additionally, from January 1988 till December 2006 to be comparable to the results from sea ice drift fields, which are only available for the latter period. Furthermore, a division into these periods allows for a separation of data influenced by the SMMR data from those including only SSM/I retrievals, as spatial resolution of the sensors is different and might have an impact on the long-term trend analysis (*Worby & Comiso*, 2004). Additionally, this allows for an analysis of differences in SIC trends for different time scales.

For both time spans, SIC changes arise mainly in the outer pack ice, where wind forcing is known to highly influence the sea ice (*Stammerjohn et al.*, 2008). Basically, these changes consist of an increase in SIC at the north-eastern sea ice edge and a decrease at the tip of the Antarctic Peninsula. Additionally, in some parts of the central Weddell Sea, some stronger positive trends of 2.5 % per decade can be observed (only in Fig. 3.4b). Although all the trends are fairly small with increases of up to 5

% and decreases of as much as 7.5 % per decade, most of the stronger trends are statistically significant (Fig. 3.4c, f). For the more recent period, both the reduction of SIC at the Antarctic Peninsula as well as the increase at the north-eastern marginal sea ice zone increased in strength. Contrary to these amplified trends, SIC trends in the eastern part along the Fimbul Ice Shelf and in some parts of the central basin changed from slightly positive (green, Fig. 3.4b) to slightly negative (blue, Fig. 3.4d). Nevertheless, changes in this region were generally very small and the choice of the start year might be responsible for this reversal: starting the analysis in 1996 yield again increased SIC in the central Weddell Sea, but not next to the Fimbul Ice Shelf.

Figure 3.5 depicts the monthly mean SIC in the Weddell Sea. In summer, large parts of the region are ice free, but in the western and in the central Weddell Sea, ice persists throughout summer and becomes second year ice. The sea ice coverage at the Antarctic Peninsula remains high year-round with at least 80 to 90 % SIC. In the eastern Weddell Sea, nearly all the sea ice melts during summer.

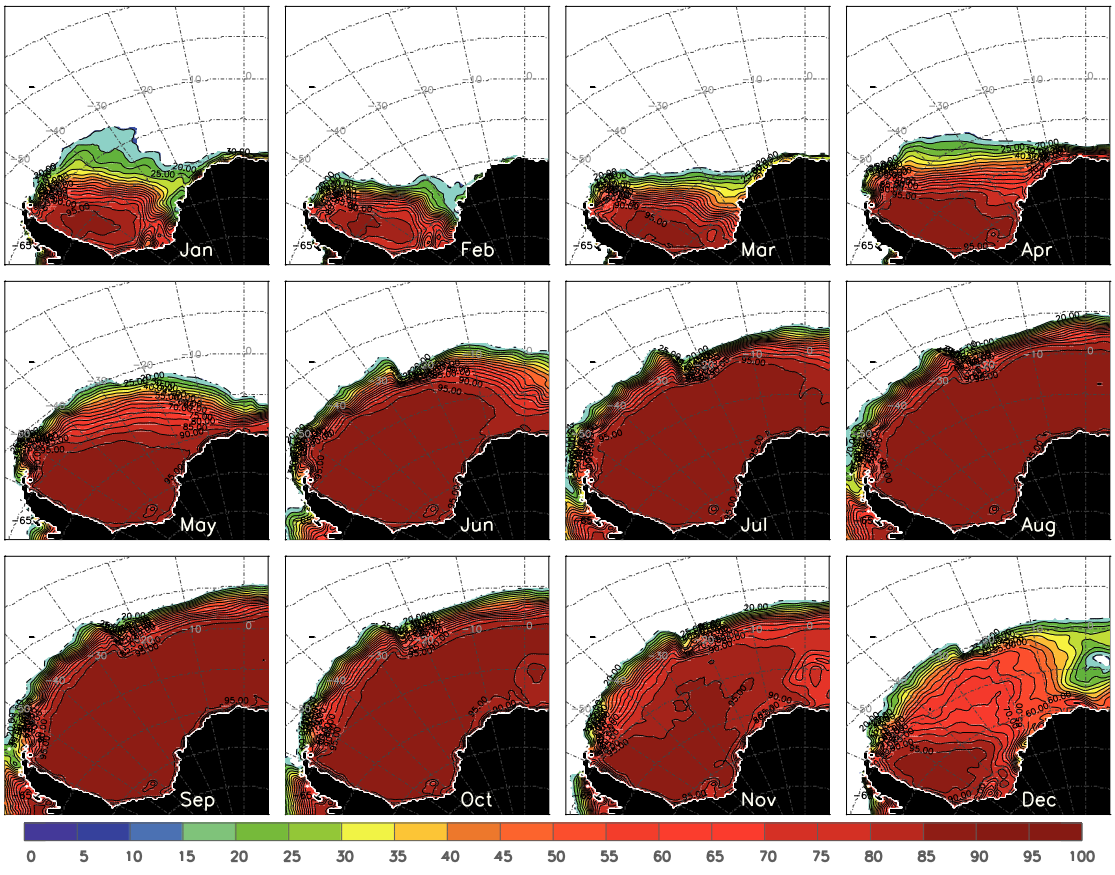

Fig. 3.5: *Monthly mean SIC in % averaged over the period January 1979 to December 2006 from the NSIDC bootstrap data (Comiso, 1999).*

The strongest changes in the mean sea ice coverage occurred during summer and autumn (Fig. 3.6). From January till April, the SIC decreased along the Antarctic Peninsula, but increased in the north-western areas, mainly at the sea ice edges.

These findings are consistent with the trends of SIE and the ice covered area for the sub-regions described in Section 3.1.

The interannual variability of the SIC is generally high and trends are rarely statistically significant. During winter and spring, the decrease of SIC at the southern Antarctic Peninsula is weaker than in summer or even turns into an increase. However, near

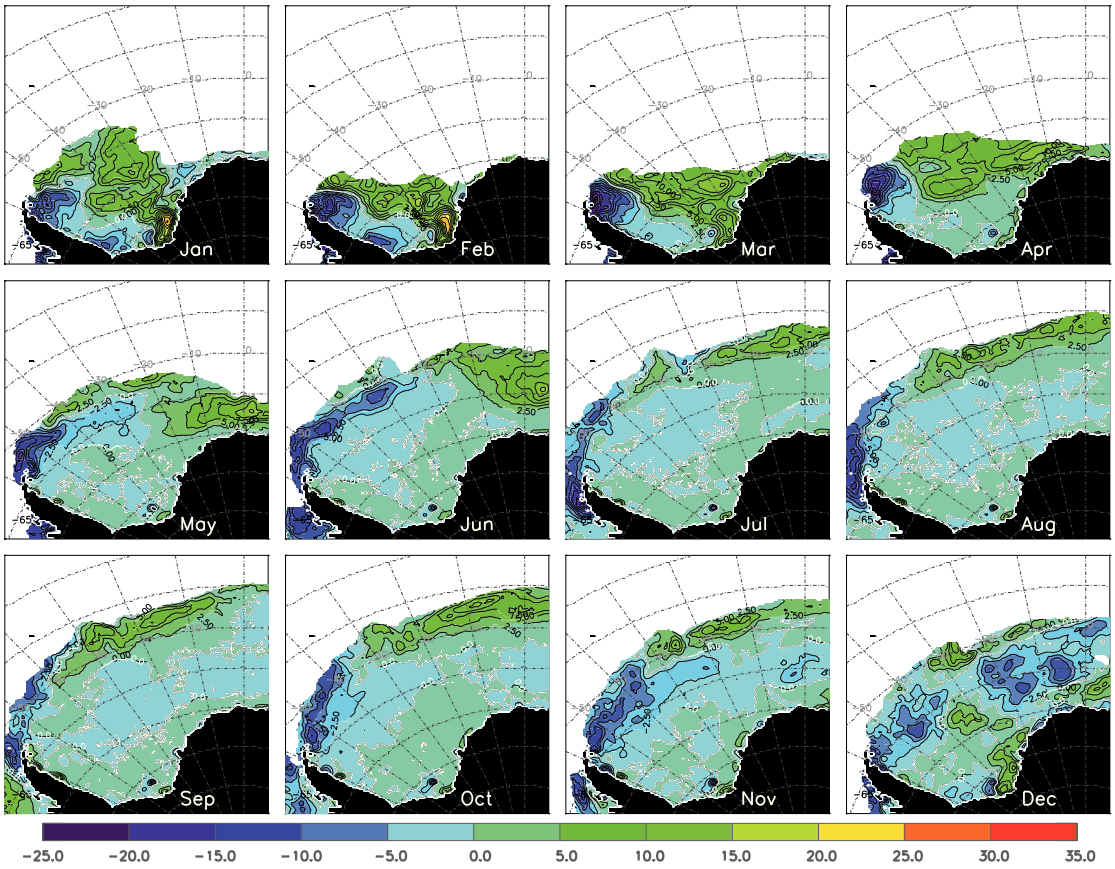

Fig. 3.6: *Monthly trends of SIC anomalies in % per decade from January 1979 till December 2006 from the NSIDC bootstrap data.*

the tip of the Antarctic Peninsula, SIC decreased strongly and statistically significant throughout the year. The region of decreasing SIC extends further to the east in winter and spring, while SIC in large parts near the sea ice edge show an increase during these seasons. The negative trend of the SIC in December, especially in the north-eastern Weddell Sea, is consistent with the negative trend of the SIE in this month (Fig. 3.3) and might indicate that sea ice retreat starts earlier in the season. *Stammerjohn et al.* (2008) actually found an earlier start of sea ice retreat in the western Weddell Sea and in some parts of the eastern Weddell Sea south of 60°W. For the period from 1988 till 2006, seasonal trends of SIC mainly show the same patterns as for the period from 1979 till 2006, but often they have increased in strength: especially at the tip of the Antarctic Peninsula SIC decreased much stronger, in particular during autumn.

To isolate the seasonally varying impact of atmospheric changes on sea ice, correlation coefficients between the individual detrended atmospheric components, such as air temperature, wind speeds and cloud coverage and detrended SIC, were derived and are depicted in Figures 3.7 to 3.12.

Temperatures

Overall, SAT in January are positively correlated with SIC, except for some parts in the southern-central Weddell Sea and in the marginal sea ice zone (Fig. 3.7). In the central basin, the positive correlation is statistically significant. This is interesting, since one would expect an anti-correlation between SAT and SIC. Nevertheless, in this month both parameters increase and decrease consistently, which indicates that temperatures are not the driving mechanism for SIC changes in January. From

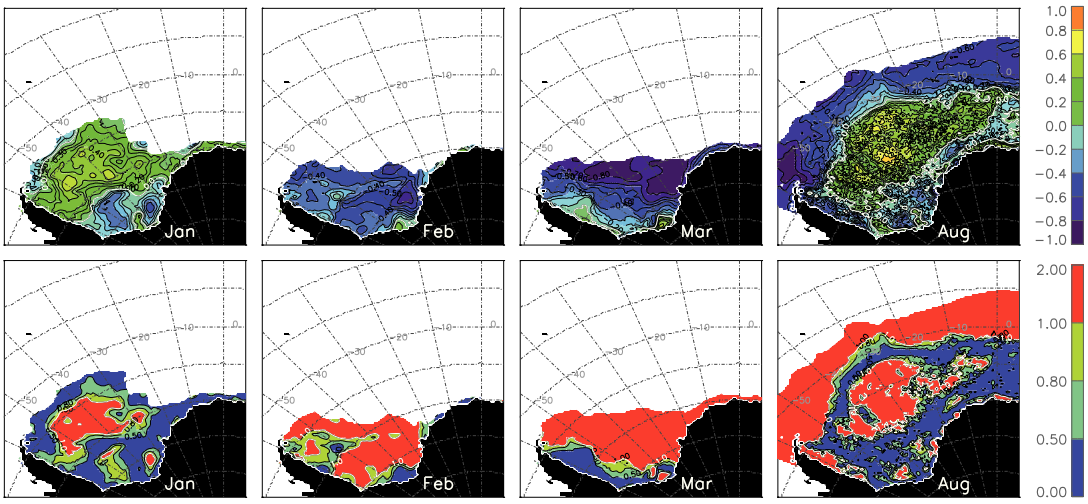

Fig. 3.7: *Correlation between detrended monthly SIC (bootstrap) and air temperature (NCEP) anomalies and their respective relative significance, exemplarily for January through March as well as for August 1979 through 2006.*

February on, both parameters are anti-correlated in the marginal sea ice zones through the remaining part of the year, which indicates that SAT changes may be responsible for the observed SIC changes there. In winter, SAT are positively correlated to the SIC in the central Weddell basin, indicating that the variability of SAT does not account for the variability in SIC in this region. Other effects, like dynamic forcing, is more likely changing SIC in winter.

Wind speed and divergence

To describe the influence of the atmospheric dynamics on sea ice, correlations between SIC and geostrophic wind speeds ($|\vec{w}| = \sqrt{u_g^2 + v_g^2}$) were calculated. A subset of monthly correlations between both is demonstrated in Figure 3.8. Throughout the year, wind speeds at the northern Antarctic Peninsula are anti-correlated with SIC. Stronger wind forcing seems to reduce the sea ice coverage in this region. Lower correlation coefficients are found in summer and early autumn, potentially because of the stronger impact that temperatures might have in these months. In winter, the connection is much stronger and correlation coefficients of as much as -0.7 can be observed in the north-western Weddell Sea.

Along the coast of the Antarctic Peninsula, the summer SIC decreased and the anti-correlation with the geostrophic wind speeds is consistent with the assumptions discussed in Chapter 2, i.e. that increased wind speeds lead to an enhanced export of sea ice, which is not totally replaced by, for example, newly grown ice. In winter, when the sea ice compactness is generally much higher and low air temperatures force a quick refreezing of any ice-free ocean (ice-free due to sea ice export and deformation processes) so that new ice formation can replace the exported sea ice, geostrophic winds and the SIC are positively correlated along the coast of the Antarctic Peninsula (a stronger wind leads to higher compactness rather than less sea ice). An exception arises near the tip of the Antarctic Peninsula, where ice is continuously and strongly advected towards the east without a replacement of sea ice from the west.

The eastern-coastal region next to the Fimbul and Brunt Ice Shelves shows varying correlation between geostrophic wind speeds and SIC. In summer, the anti-correlation implies that the increasing SIC arise because of the lower winds. This was already suggested in Chapter 2: When wind, and therefore drift velocities, decrease, sea ice advection into the central Weddell Sea decreases, which leads to a more compact sea ice coverage at the eastern coastal sea ice zone. On the contrary, stronger winds would export the little sea ice that is persistent in summer into the Weddell Sea basin. Neither gradually refreezing, nor the sea ice import from the East Antarctic sea ice zone (which is barely existent in summer) can replace the amount of advected sea ice so that the SIC decreases. However, in winter, the varying correlation coefficients are rather unexpected. It is noteworthy that the correlation coefficients are very low in this region, indicating that other effects play a more important role for SIC changes here in winter. Also no consistent correlation was found at the north-eastern sea ice edge. In some months (e.g. July, August), the correlation is positive, in other months, it is negative (e.g. September) and the magnitude of the coefficients varies too. The anti-correlation might mean that the compactness in the eastern Weddell

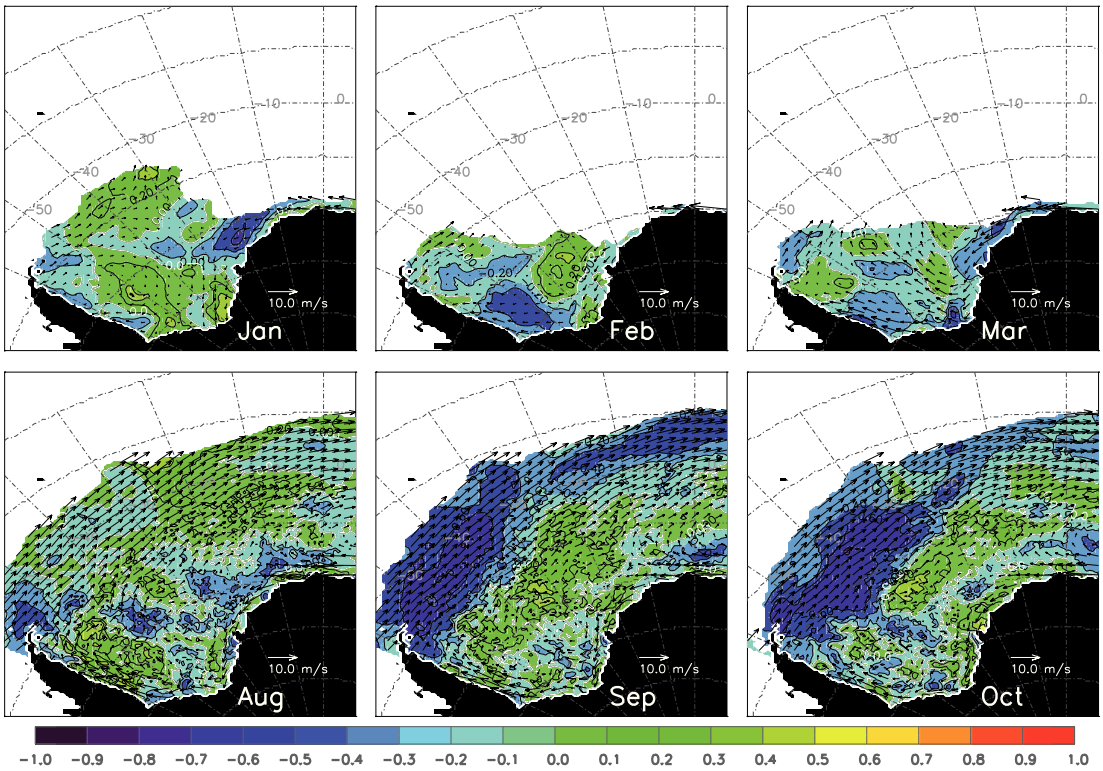

Fig. 3.8: *Geostrophic wind speeds correlated with detrended monthly SIC from 1979 through 2006. Additionally, vectors of the mean geostrophic wind field are shown.*

Sea increased due to the enhanced wind forcing in the western Weddell Sea and the related redistribution of sea ice. Sea ice coming from the west may collide with the sea ice located in the central Weddell Sea, leading to a higher compactness in this region. On the other hand, the positively correlated fields might describe the enhanced freezing of the open ocean parts (e.g. leads). However, the inconsistency of the correlation implies that the wind forcing on its own is not the main contributor to the SIC changes in this region during winter.

Also, the correlation between SIC and divergences in the wind field indicate that the wind has an impact on the sea ice, but is potentially not the main contributor. In summer and autumn, the enhanced divergence in the wind field comes together with the decreasing SIC at the southern central and western Weddell Sea. This feature is expected at least for the summer months, when comparatively high temperatures prevent new sea ice formation in the ice free ocean. On the contrary, the marginal sea ice zone generally shows a positive correlation between the wind divergence and SIC, which indicates that the SIC increases with the increasing divergence. In autumn, this feature might be related to new sea ice formation in the leads, but during summer, this feature is unexpected. During winter, the eastern marginal sea ice zone shows an anti-correlation with SIC, with values up to -0.6. This indicates that opened leads do not close by new ice formation. However, the major part of

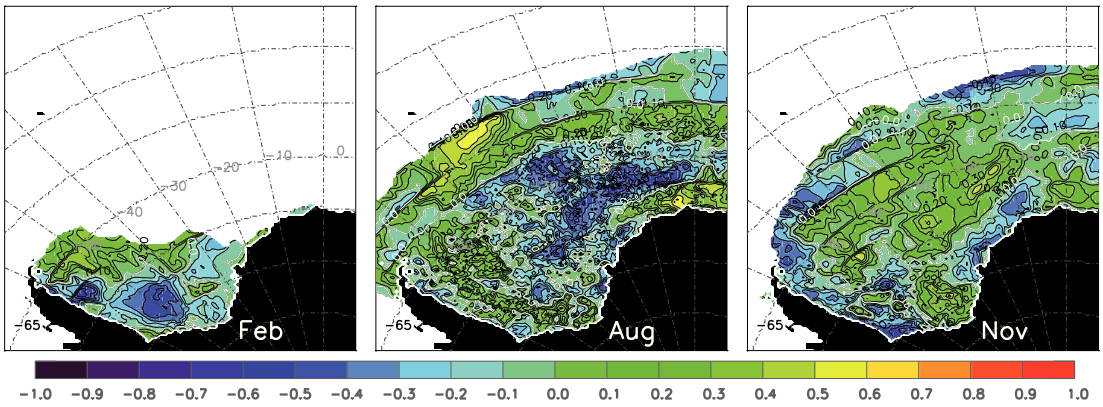

Fig. 3.9: *Monthly mean wind divergences derived from the NCEP data correlated with SIC (from the NSIDC), exemplarily for February, August and November from 1979 till 2006. A statistical significance is generally given for correlation coefficients larger/lower than ±0.4.*

the central and western marginal sea ice zone shows further a positive correlation between divergence and the SIC. In spring, larger regions show an anti-correlated relation between both variables. Nevertheless, only very few of the features show a statistical significance.

ENSO and SAM related changes

The correlation between SIC and the atmospheric oscillation patterns SAM and the El Ninõ-Southern Oscillation (ENSO) have been tested by using the SAM index provided by *Marshall* (2003) and the Niño 3.4 index[2] (iridl.ldeo.columbia.edu/SOURCES/.Indices/.nino/.EXTENDED/.NINO34). During summer and autumn, the correlation between ENSO and the SIC is generally positive, except for the western and some parts of the eastern Weddell Sea. Generally, positive values of the Niño 3.4 index are connected to El Niño events and negative indices are connected to La Niña events. The positive correlation of up to 0.5 indicates that ENSO has an impact on the SIC, i.e. an increase in the ENSO index comes together with a higher SIC in the central Weddell Sea, while a decrease in the ENSO index in turn is associated with a tendency to lower SIC. This behaviour is expected, since during La Niña (negative index) events, a strengthening of the polar front jets leads to a higher storm activity with warmer air temperatures, which are expected to decrease SIC in the western Weddell Sea (*Kwok & Comiso*, 2002a). EL Niño events (positive indices), on the other hand are associated with increasing SIC. However, the anti-correlation

[2]The Niño 3.4 index describes the sea surface temperature difference of the zonal averages (170^{o}W-120^{o}W) between 5^{o}N and 5^{o}S and is also entitled as the East Central Tropical Pacific SST Index (*Barreira & Compagnucci*, 2011).

near the Antarctic Peninsula indicates that ENSO is generally not related to sea ice changes in this region. During winter and spring, the central Weddell Sea partly shows a negative correlation, while the western Weddell Sea, near the Antarctic Peninsula exhibits more often a positive correlation. Throughout the year, summer and autumn show most of the statistically significant or almost significant patterns. This is more or

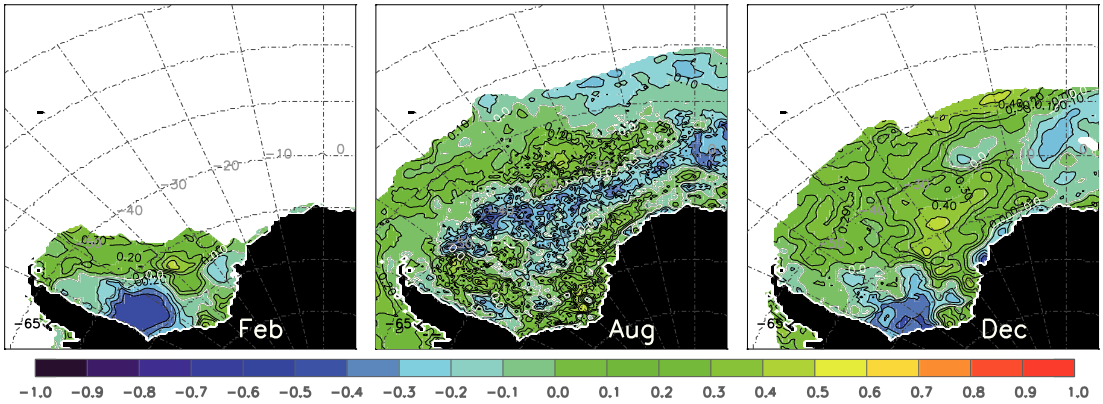

Fig. 3.10: *Monthly Niño 3.4 index correlated with SIC (from the NSIDC), exemplarily for February, August and December from 1979 till 2006. Statistically significant at the 95% level are generally correlation coefficients of about ± 0.4 and higher/lower. Coefficients of more/less than 0.2 mostly exceed one standard deviation.*

less consistent with the findings of *Fogt & Bromwich* (2006), who found out that the sea ice response to ENSO is the highest during spring and summer.

The correlation between SAM and SIC is very inconsistent, even on seasonal basis. In the marginal sea ice zone, e.g., a positive correlation occurs in June, which is statistically significant. In August, this positive correlation has turned into a statistically significant anti-correlation. Furthermore, in March and April, the anti-correlation in the central Weddell Sea is also significant, but turned into a generally positive correlation during winter and spring. It has been expected that the correlation at the Antarctic Peninsula and the western marginal sea ice zone is negative, since a positive phase of the SAM index is associated to stronger northerly, warm winds, which are expected to result in a reduction in SIC. Another inconsistency is that, according to *Marshall* (2003) and *Marshall et al.* (2006), the strongest impact of SAM on SIC is expected to occur during summer and autumn, while the highest correlation coefficients in this study happen during winter and spring.

Hence, there is obviously a correlation between these atmospheric patterns and the SIC, but as already stated by *Liu et al.* (2004) and *Stammerjohn et al.* (2008), SAM and ENSO do not show a consistent relation to the recent sea ice changes.

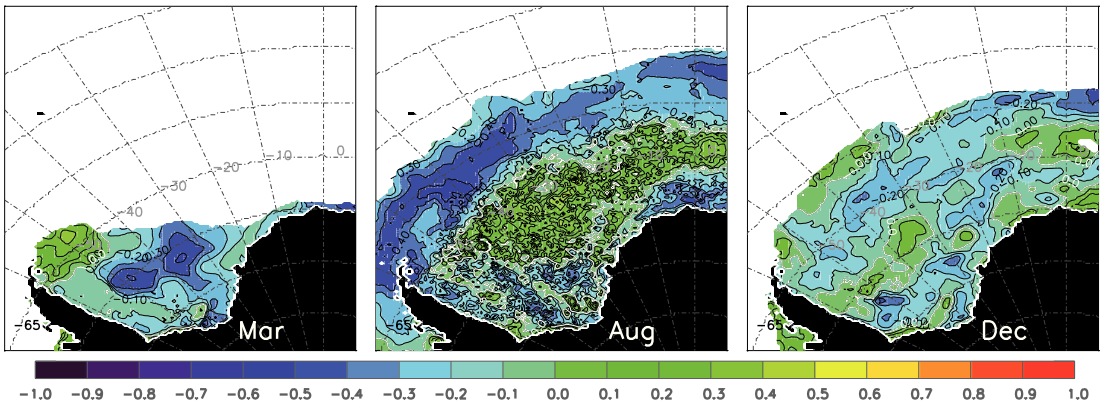

Fig. 3.11: *Monthly SAM index correlated with SIC (from the NSIDC), exemplarily for March, August and November from 1979 till 2006. Statistically significant at the 95% level are generally correlation coefficients of about ± 0.4 and higher/lower. Coefficients of more/less than 0.2 mostly exceed one standard deviation.*

Cloud coverage

Another component that may influence the sea ice is the cloud coverage, which modifies the surface energy balance (*van den Broeke*, 2000). On cloud-free days (outside the polar night), sun light is directly penetrating the sea ice, which results in surface melting. In leads or polynyas, where sea ice is missing, ocean temperatures rise because of the enhanced energy absorption, and can melt the surrounding sea ice, while persistent cloud coverage would weaken this effect. In this season, one would expect a positive correlation (more clouds, more SIC and vice versa for less clouds). In winter, when only little or even no sun light is present, missing cloud coverage would lead to an enhanced cooling, whereas persistent cloud coverage would reflect parts of the longwave radiation coming from the sea ice surface so that the energy - to some extent - remains in the lower atmosphere and would support a warming. Hence, one would expect a negative correlation (less clouds, more sea ice and vice versa for increased cloud coverage). Therefore, a separation of processes for different seasons is necessary. As found by *van den Broeke* (2000), annual mean temperatures and cloud coverage measured at different Antarctic stations correlate positively. Especially the winter correlation at Halley station (eastern Weddell Sea, near the Brunt Ice Shelf) is very high. This implies that the impact of cloudiness on SAT is also visible in the correlation between cloud coverage and SIC. However, analyzing the correlation of NCEP cloud coverage and passive microwave based SIC does not yield any robust relationship (Fig. 3.12). In summer, most of the southern parts show a positive correlation between clouds and sea ice coverage. This is consistent with the ideas discussed before. However, most areas of the marginal sea ice zone show an anti-correlated behaviour, with SIC decreasing with increasing

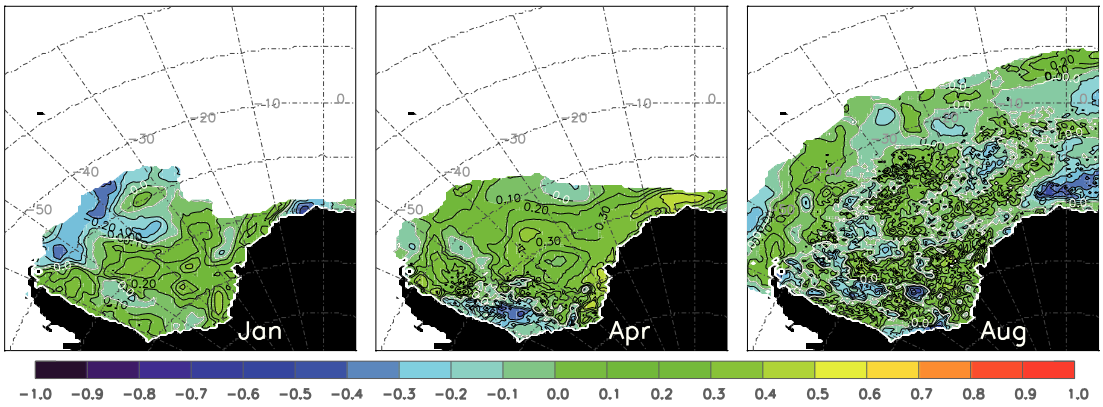

Fig. 3.12: *Monthly mean NCEP-based cloud coverage correlated with SIC from the NSIDC, exemplarily for January, April and July from 1979 till 2006.*

cloud coverage and the other way round. This is not against physical circumstances, since less sea ice coverage would result in more evaporation, and therefore, in more clouds, i.e. cloud coverage would be more affected by SIC than the other way around. Additionally, the sea ice thickness is most probably more affected by cloud coverage than the SIC.

Analyzing the pure effect of the incoming longwave radiation results in a very similar weak correlation with the SIC as the cloud coverage by itself [3]. This study indicates that regional changes of the SIC in the Weddell Sea are not likely to be forced by downward radiation fluxes on their own. Given that most of the correlation coefficients are not very high (and only few are statistically significant), it is concluded here that wherever a connection to cloud coverage was found, other effects account for the observed changes as well. It is highly likely that all the atmospheric components interplay with each other in driving the sea ice changes, which is not detectable by computing the correlation of only one single atmospheric component with the SIC.

3.2.2 Modelled sea ice concentration

One of the goals of this thesis is to evaluate the Finite Element Sea ice-Ocean Model (FESOM). Model simulations are necessary for different aspects, such as for filling gaps of *in-situ* and satellite data or for a prolongation of time series to prior periods, which have not been subject to large-scale satellite observations. In addition, model simulations can help to understand the physical processes, which

[3] The longwave radiation was calculated by the Stefan-Boltzmann law: $Q^{\downarrow}_{LW} = \epsilon_a \sigma T_a^4$ with the Stefan-Boltzmann constant $\sigma = 5.67 \cdot 10^{-8} W m^{-2} K^{-4}$ and ϵ being the emissivity of the atmosphere: $\epsilon = 0.765 + 0.22 \cdot c^3$ (after *König-Langlo & Augstein*, 1994). c is the cloud coverage (ranging from 0 to 1) and T_{air} is the SAT in K.

might drive changes in the sea ice system, since a model allows for a systematically change of boundary conditions. Therefore, one can test the climate response based on hypothesized changed for future boundary conditions, such as air temperature rise. However, before applying a model, an evaluation of the model simulations is necessary to determine its uncertainties and eventually eliminate some of them. For that reason, monthly mean model simulations of the sea ice parameters from FESOM were compared to observations to estimate the model's uncertainties and to fill data gaps afterwards, especially concerning sea ice thickness data. Here, SIC are compared to examine, whether the model simulations represent the same spatial characteristics as observations.

Figure 3.13 displays the averaged simulated SIC, trends and their relative significance over the period from January 1979 as well as from January 1988 till December 2006. As can be found in the satellite-based observations, modelled SIC are high along the Antarctic Peninsula and decrease slightly from the west to the east. However, modelled mean SIC are underestimated by about 10%, especially in the north-western Weddell Sea. There both the simulated sea ice coverage as well as the simulated SIE are strongly underestimated compared to satellite-based observations. Furthermore, the highest SIC occur in the south-eastern part in the model instead of the western part of the Weddell Sea. These shortcomings in FESOM may be due to model deficiencies concerning summer processes (*Timmermann et al.*, 2009), potentially also strongly induced by errors in the forcing data (*Zhang*, 2007). Most of the modelled sea ice disappears in summer, which affects the sea ice distribution in every month and in the annual mean. According to *Timmermann et al.* (2009), the underestimation of sea ice coverage at the Antarctic Peninsula is probably due to the poor representation of the topography in the NCEP reanalysis simulations, which affects the atmospheric forcing and influences the sea ice drift and melt in this area.

For the observational data, there is generally no big change in the long-term mean SIC maps for the time periods from 1979 as well as from 1988 till 2006. The distribution of the modelled trends for the SIC, depicted in Figure 3.13, differs from that. For the period from 1979 till 2006, the SIC mainly increased, except for the central Weddell Sea, where partly strong negative trends of up to 4% per decade are simulated. In contrast, observations show increasing SIC in this region. Time series from 1988 till 2006 match the satellite-based SIC observations much better. They illustrate a decrease of the sea ice coverage from the Antarctic Peninsula to about 30^{o}W. Although the magnitude is higher, the patterns of change are comparable, considering that the model resolution is much coarser than that of the observations[4]. The entire

[4]Since the model resolution is fairly coarse with 1.5^{o}, smaller scale features cannot be resolved. Therefore, the areal averaged trend covers a larger region for model simulations than for the satellite

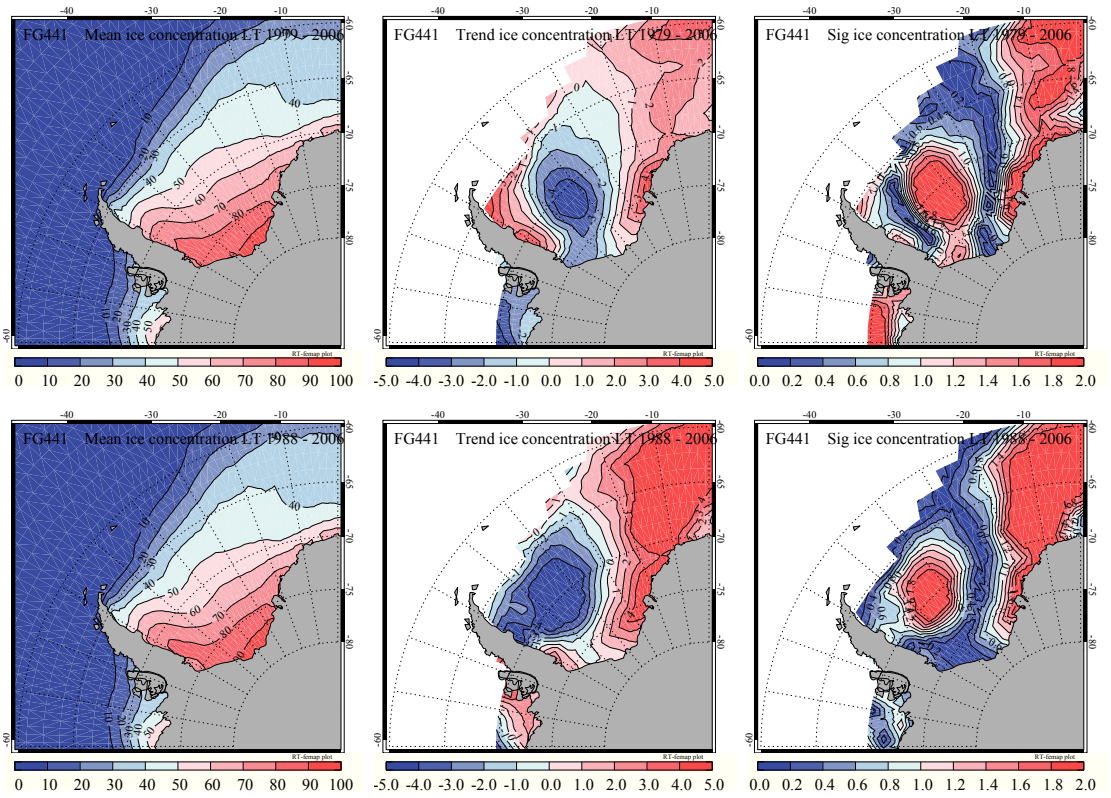

Fig. 3.13: *Averaged SIC (in %), long-term trends of anomalies (% per decade) and respective relative significance (a value of at least 1 describes a significant result) from 1979 till 2006 (top) as well as from 1988 till 2006 (bottom) from FESOM.*

eastern Weddell Sea reveals an increase in SIC in the model simulation. Basically, this is consistent with the satellite-based observations, except for the overestimation of trends by few percent per decade (only few regions have a long-term trend of more than 2.5% per decade in the observations, while model simulations show large regions with more than 2.5 % increase of ice coverage). All trends have the same order of magnitude, namely in general a few % per decade with maxima of up to about 7.5 % in the observations.

On a seasonal basis, the positive trends in the eastern Weddell Sea are fairly well described by the model for the period from 1979 till 2006, but the increasing SIC at the western marginal sea ice zones clearly contradict satellite-based observations. Actually, the observed reduction of SIC in this region lies mostly outside the simulated ice edge. Therefore, sea ice and its variability are totally underestimated by FESOM in this region. Almost all of the model trends are statistically insignificant. The only exceptions are some positive trends in the north-eastern and some negative trends in the central Weddell Sea.

based data, which have a resolution of 25 x 25 km^2.

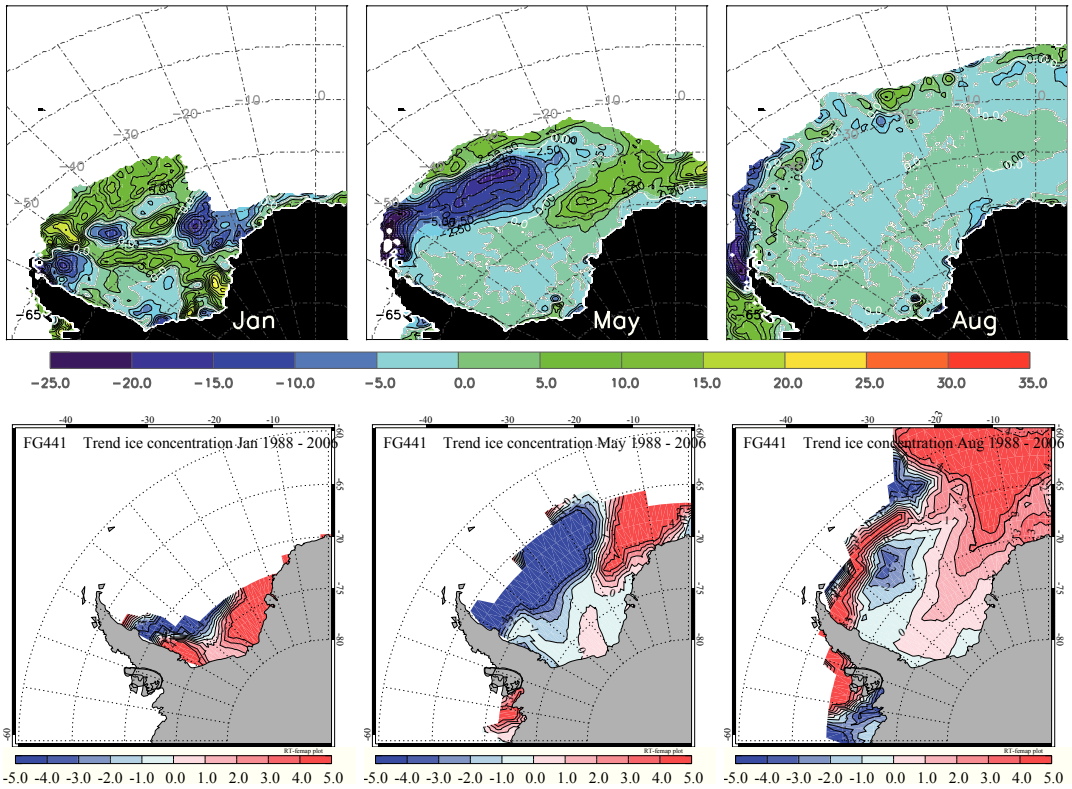

Fig. 3.14: *Comparison between satellite-based (top) and modelled (bottom) monthly SIC trends in % per decade, exemplarily for January, May and August from 1988 till 2006.*

Comparing monthly averaged trends for the period from 1988 till 2006 with observations reveals a much better result. As for the year-round long-term trends, decreased SIC are simulated near the Antarctic Peninsula for most months. Trends at the east coast are positive, but these positive trends cover a much too large region, compared to the observational estimates. Figure 3.14 shows a subset of monthly trend distributions of SIC taken from FESOM in comparison with satellite-based observations. Even though long-term trends in SIC match the satellite-based observations well, some months, such as January, show distinct differences in both data sets. However, as mentioned above, summer sea ice simulations cause problems, and therefore, disagreements are to be expected. In other months (e.g. May), the agreement is fairly good. The long tongue of decreasing SIC, beginning at the Antarctic Peninsula and extending to about 20^{o}W, as well as the tongue of increasing sea ice further south, match the observations remarkably well. The agreement between modelled and observed SIC trends is also quite high in August. In the observations, the SIC show a negative trend north of the Antarctic Peninsula and a slightly positive trend somewhat further south. This is also modelled by FESOM, and additionally both observations and simulations agree concerning the negative trend in the central Weddell Sea. On the other hand, trends in the eastern region are negative in the observations, especially along the coast, but positive in the model simulations.

3.3 Discussion and conclusion

As was shown in this section and was also observed by several other authors using different time periods, data and methods (e.g. *Cavalieri et al.*, 1997; *Cavalieri & Parkinson*, 2008; *Zwally et al.*, 2002a), SIE, ice covered area and SIC have changed in the Weddell Sea over the last decades. This change features a distinct pattern: a decrease of SIC in the western and an increase in the eastern Weddell Sea. In this study, various possible atmospheric forcings, such as SAT and wind speeds, have been considered and compared to the variability in SIC. Due to the interplay between these atmospheric components on the one hand and the interplay of each component with the sea ice on the other hand, it was difficult to determine, whether atmospheric forcing has driven the changes in the SIC or have been forced by changes in the SIC themselves. For example, it was found that air temperature changes can be related to changes in the SIC in the marginal sea ice zones. However, despite this high anti-correlation between temperatures and the SIC, it could not be identified from this study, whether modified air temperatures cause the SIC changes or whether they are changed by a modified sea ice coverage. True observations are sparse in the Southern Ocean and SIC are prescribed as boundary conditions in the assimilation system for the NCEP reanalysis data. Therefore, near-surface temperatures are bonded to the SIC distribution and the question, whether higher temperatures force sea ice melt, and therefore a reduction in SIC, or whether a decreased SIC force a local warming due to enhanced ocean-to-air heat flux cannot be answered clearly. A correlation analysis with time lags of $\pm$ 1 month (SIC were correlated with temperatures of one month in advance or one month behind) was also not sufficient to answer this question, since the coefficients often do not vary significantly between both time lags. It was found that the correlation is slightly higher in most cases, when SIC changes follow those of temperatures. However, the highest correlations were found for zero lag. Hence, this study can only show that temperatures and SIC are strongly connected, but which variable forces the other one remains unclear, like in the most recent study of *Barreira & Compagnucci* (2011).

The finding that SAT and SIC are positively correlated in the central Weddell Sea indicates a dominating impact of wind speeds there. In the western Weddell Sea, a shift to more frequent northerly winds over the year could be observed in the NCEP data. These winds most likely force a redistribution of sea ice from the western into the central Weddell Sea, which would increase the SIC in the central Weddell. Furthermore, these winds are expected to transport warmer air masses from the north into the southern regions (*Stammerjohn et al.*, 2008), increasing the prevailing temperatures. Hence, it is most likely that the SIC increase parallel to the increasing

SAT, and not as a response to them. It might also be that the increasing SAT have an effect on the precipitation (*Liu et al.*, 2004), i.e. would result in more snow-fall. This would increase the ice-albedo effect because of the higher albedo of snow (*Perovich et al.*, 1998). However, more realistically is that the sea ice thickness is more affected by the snow rather than the SIC. This point will be reviewed in Chapter 4.

In fact, the correlation between (geostrophic) wind speeds and the SIC indicates that this atmospheric component is not able to explain the observed changes by its own. Varying correlation coefficients in all parts of the Weddell Sea made it difficult to depict the influence of wind speed changes on SIC. Only the anti-correlation between SIC and wind speeds at the eastern coast in summer and the year-round anti-correlation at the tip of the Antarctic Peninsula were found to be robust.

Particularly the observed changes at the Antarctic Peninsula have been related to the positive trend of the SAM by various authors (e.g. *Lefebvre & Goosse*, 2008; *Kwok & Comiso*, 2002a). A positive phase of the SAM index leads to warm northerly winds, which potentially influence the sea ice because of the thermal and dynamic effects (*Stammerjohn et al.*, 2008). A similar effect has La Niña, when a strengthening of the polar front jets leads to a higher storm activity, warmer air conditions, and hence, less sea ice in the western Weddell Sea (*Kwok & Comiso*, 2002b). *Barreira & Compagnucci* (2011) analyzed the changes of Antarctic summer and autumn SIC by using a T-mode principal component analysis (PCA)[5] for the period from 1979 till 2009 applied to the NASA Team algorithm SIC data from the NSIDC. Similar to the above mentioned studies they found out that changes in the sea level pressure field lead to more southward directed winds with higher temperatures that are both associated with a decrease of SIC in the north-western Weddell Sea. On the other hand, the southerly and south-westerly winds coming from the continent, together with decreased temperatures in the central Weddell Sea are expected to account for the increased SIC in summer and partly in autumn in this region (*Barreira & Compagnucci*, 2011). In addition, *Liu et al.* (2004) stated that a positive anomaly of the SAM/AAO leads to less sea ice in the northern Weddell sector and that El Niño events force an opposite change. The time series of SIC used in this study have only four more years but indicate that only the north-western Weddell Sea shows decreasing trends. This is consistent with the findings of *Liu et al.* (2004), who demonstrated that SAM/AAO and ENSO are not able to explain the most recent sea ice changes and that there might be other large-scale processes influencing the sea ice. Also *Stammerjohn et al.* (2008) stated that SAM and ENSO do not show a consistent relation to sea ice changes (except for the western Antarctic Peninsula/southern Bellingshausen Sea

[5] provides temporal clusters of variable fields, while the standard S-mode PCA deviates spatial clusters of temporal series (*Barreira & Compagnucci*, 2011)

and the western Ross Sea, which are the regions, where the wind pattern related to the SAM has a strong non-annular component *Lefebvre et al.*, 2004). Furthermore, they found out that the correlation between summer Niño 3.4 index and the wind in the western Weddell Sea reversed its sign between the 1980s and 1990s, from which they explain the inability to connect the changes to the sea ice. In this study too, a clear relationship between the SIC and these atmospheric oscillation patterns could not be obtained.

The relation of SIC changes to the Southern Oscillation (SO, difference of standardized sea level pressures at Tahiti and Darwin; includes the evolution of the ENSO cycle (*Turner*, 2004)) was analyzed by e.g. *Kwok & Comiso* (2002b). They found that the climatic anomalies (such as the sea level pressure, air temperature as well as zonal and meridional wind) covaried with the SO index, especially in the Weddell Sea. A positive phase is connected with the low sea level pressure and lower temperatures (and vice versa for a negative phase), and therefore, is expected to be dynamically and thermodynamically associated to sea ice changes.

In addition to atmospheric forcing, also oceanic currents have an impact on the sea ice due to the fact that they influence the sea ice drift. Hence, an analysis of drift velocities is important, either by using the modelled sea ice drift, which depends in case of FESOM on the NCEP data and/or by independent satellite-based sea ice motion vectors. Both sea ice drift fields are discussed in Chapter 5.

In addition to the question, which factors drive the changes in the SIC distribution, it is also important to analyze, how much of the SIC changes are associated with sea ice thickness changes and, how much variability in the sea ice is hidden in cases, where sea ice thickness changed, but SIC remains constant. This point is especially important during winter, when temperature trends are positive in the central Weddell Sea, but also SIC partly increased. Since air temperatures are low enough in winter, a rise by few tens of ^{o}C would not result in a reduction of SIC, but might result in a thinning of sea ice thickness. This topic will be discussed in Chapter 4. Unfortunately, a regular coverage of sea ice thicknesses is only given by model simulations. Therefore, to assess the reliability of model simulations, each prognostic sea ice variable simulated by FESOM is first compared to *in-situ* and satellite-based data. For SIE, an underestimation was found in the Weddell Sea, which is mainly a product of the underestimated summer SIE. This is a typical feature in sea ice-ocean models, which are forced by atmospheric reanalysis data and neglect, according to *Semtner* (1976), the internal heat storage in the sea ice (so-called zero-layer approach, R. Timmermann, *personal communication*, 2011). To improve the model simulations, an implementation of a more complete

formulation of the thermodynamics of the sea ice in FESOM is currently work in progress (R. Timmermann, *personal communication*, 2011). For SIC, a relatively good agreement was found on a year-round and large-scale basis, although there are some disagreements between model simulations and observations on a monthly basis. Despite these shortcomings, it seems to be quite reasonable to use the model for further studies. It was found that the agreement between the data sets is improved, if only data from 1988 onwards are taken into account. This is probably due to the improving quality of atmospheric forcing data, which increasingly uses SIC data from satellites as lower boundary conditions. Since daily SSM/I data became available in 1987, the atmospheric field is likely to become more realistic for the more recent period. The underestimation of SIC will be kept in mind, when drawing conclusions in the relevant chapters.

Chapter 4

Sea ice thickness distribution

One of the most important sea ice properties is the sea ice thickness. Knowledge about this parameter is not only needed to determine sea ice mass changes and sea ice volume transport, it is also necessary to understand the physical processes of the polar oceans (*Zwally et al.*, 2008). While satellite-based observations of SIC, SIE and sea ice drift have become available more than three decades ago, satellite-based measurements of sea ice thickness have only recently been developed and are not conducted routinely yet (*Renner & Lytle*, 2007). For the period from 2003 till 2009, the Ice, Cloud, and Land Elevation Satellite (ICESat) provided space-borne sea ice thicknesses based on measurements of sea ice surface elevations. However, measurements were only performed for distinct survey phases during this period (*Yi et al.*, 2011). Regarding the future, CryoSAT-2, launched in April 2010, is supposed to provide space-borne sea ice thickness data based on radar altimeter measurements. Other data sources are sparse so far; the longest data set is based on *in-situ* upward looking sonar (ULS) data from 1990 until today. These data are spatially restricted, and measurements were not conducted consistently in every region. An alternative for sea ice thickness measurements might be the usage of proxy data, such as sea ice classes. *Johannessen et al.* (1999) and *Maslanik et al.* (2007), e.g. found that in the Arctic, the area of multi-year ice (MYI) and the general mean age of sea ice has declined in combination with sea ice thicknesses. Furthermore, MYI is generally much thicker than first year ice (FYI) (*Maslanik et al.*, 2007), and therefore, one might be able to estimate the changes in the sea ice mass of a region by the differentiation between the sea ice classes FYI and second/multi-year ice (SYI/MYI). Contrary to the Arctic, MYI is sparse in the Southern Ocean, but in a few regions, some sea ice survives the summer melt period and is converted into SYI. The Weddell Sea is one of those regions, and it contains furthermore a large percentage of the SYI in the Southern Ocean (*Lange & Eicken*, 1991; *Worby et al.*, 2008). In this study, QuikSCAT data are used to distinguish between FYI and SYI/MYI. Since August 1999, data are

continuously available on large scales with a daily resolution. With this time series, changes in sea ice mass for at least the most recent decade might be identified, which is discussed in Section 4.1. For longer periods, model simulations are a valuable data source. Here, FESOM is used to show results for simulated sea ice thickness and volume changes for the period from 1979 till 2006 (Section 4.2). A verification of these model results is given in Section 4.3, where the available data from ULS and ICESat as well as the results from Section 4.1 are compared to the model results.

4.1 Sea ice class distribution

The SeaWinds instrument on-board QuikSCAT provides a tool to distinguish between FYI and SYI and allows for an analysis of recent changes in their areal distribution. The scatterometer data used for this analysis are provided by the Centre ERS d'Archivage et de Traitement (CERSAT). A detailed instrument and data description can be found in *Ezraty & Piollé* (2001), which is briefly summarized here. The QuikSCAT (Quick Scatterometer) satellite was launched on June 19, 1999 into a sun-synchronous orbit with an altitude of 802 km above the equator. The local equator passing time is 6:00 a.m. $\pm$ 30 min for the ascending node and the recurrent period is four days. The SeaWinds instrument on-board the QuikSCAT is an active specialized microwave radar (scatterometer), which transmits microwave pulses at a frequency of 13.4 GHz (Ku-band) and receives the electromagnetic backscatter signal. The power of the received signal depends on the roughness of the observed surface. Measurements are independent of weather and cloud conditions, and the observations are possible during day and night. The SeaWinds instrument has a rotating dish antenna that covers the observed region with a 1400 km (inner beam) and 1800 km (outer beam) swath, respectively (*Spencer et al.*, 2000). Due to the pencil-beam, the instrument has a high signal-to-noise ratio; it is small with its single 1-meter parabolic antenna and provides a high spatial coverage. Measurements are provided for horizontal and vertical polarization with incident angles of 46^o (inner beam, horizontal-polarization, H-pol) and 54^o (outer beam, vertical polarization, V-pol). The footprint is approximately 25 km in azimuthal and 37 km in range direction. The large swath allows for a daily coverage of the entire polar regions. Figure 4.1 shows a sketch of the measurement principle.

Measurements are projected onto the same 12.5 km and 25 km polar stereographic grids as the passive microwave SIC from the NSIDC, which eases the comparisons of active and passive microwave data (*Ezraty & Piollé*, 2001). To convert geographical coordinates into grid coordinates, a Hughes ellipsoid is assumed with an Earth radius

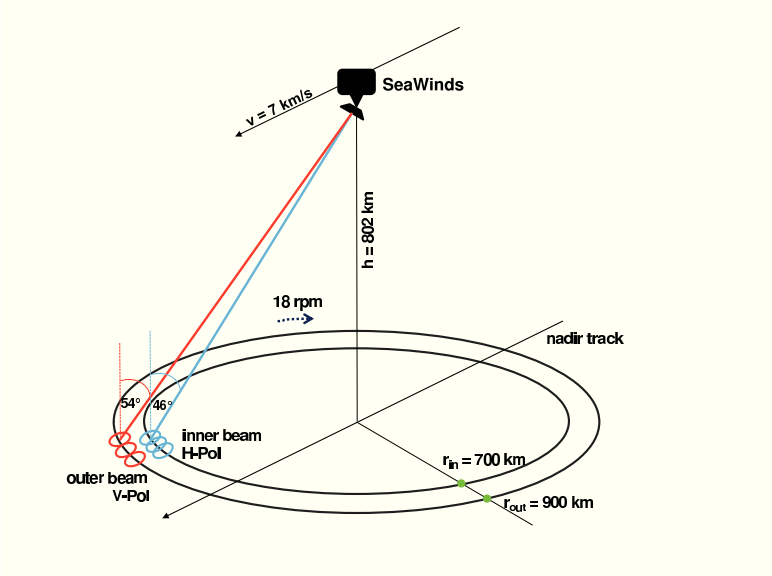

Fig. 4.1: *Measurement principle of the SeaWinds instrument on-board QuikSCAT (after Spencer et al. (2000) and Ezraty & Piollé (2001)).*

of 6378.273 km and an eccentricity (e) of 0.081816153. For more information about the polar stereographic grids, refer to the NSIDC Polar Stereographic Projection and Grid documentation (http://nsidc.org/data/polar_stereo/ps_grids.html).

Besides the measurement of backscatter power, noise power measurements from internal calibration pulses can be converted into apparent brightness temperatures due to the very stable receiver gain and careful calibration (*Ezraty & Piollé*, 2001). These brightness temperatures do not have the same quality as those from passive microwave imagery, but they are useful for the location of rain cells over the open ocean (important for wind speed determination) and for the discrimination of open water and sea ice covered areas, so that this discrimination can be done using only one single satellite product. This eliminates inconsistencies produced by different overpass times and locations. The differentiation between open water and sea ice with brightness temperatures is necessary because the electromagnetic backscatter power is not very different between thin ice and open water, so that a differentiation between both is not possible with backscatter measurements. Data are provided with and without a water mask based on the brightness temperatures. For this study, data including the water mask are used, since they fit well with the SIE observed by SSM/I passive microwave data at 40% SIC (*Ezraty & Piollé*, 2001).

To distinguish between FYI and SYI, backscatter signals (σ^0) were converted into decibel (dB):

$$\sigma = log_{10}(\sigma^0) \cdot 10. \tag{4.1}$$

Studies from *Ezraty & Piollé* (2001) showed that FYI has backscatter signals lower

than -12 dB (H-pol) and -15 dB (V-pol), while SYI backscatter is higher than -10 dB for both polarizations (for data measured in the Arctic in January). In this study, the differentiation between both sea ice classes was done for several backscatter coefficients within a range of -13 dB to -10 dB to test the sensitivity of the results to the chosen threshold. Trends of sea ice classes from different backscatter ranges were compared to each other to evaluate, how the distribution of sea ice classes varied and how these variations depend on the accuracy of the chosen backscatter power threshold for the determination of both sea ice classes.

Figure 4.2 displays an example for measured backscatter signals for May and June 2001 as well as July and August in 2004. The yellow and red areas show the region covered by SYI, while the green and blue regions were mainly covered by FYI. The

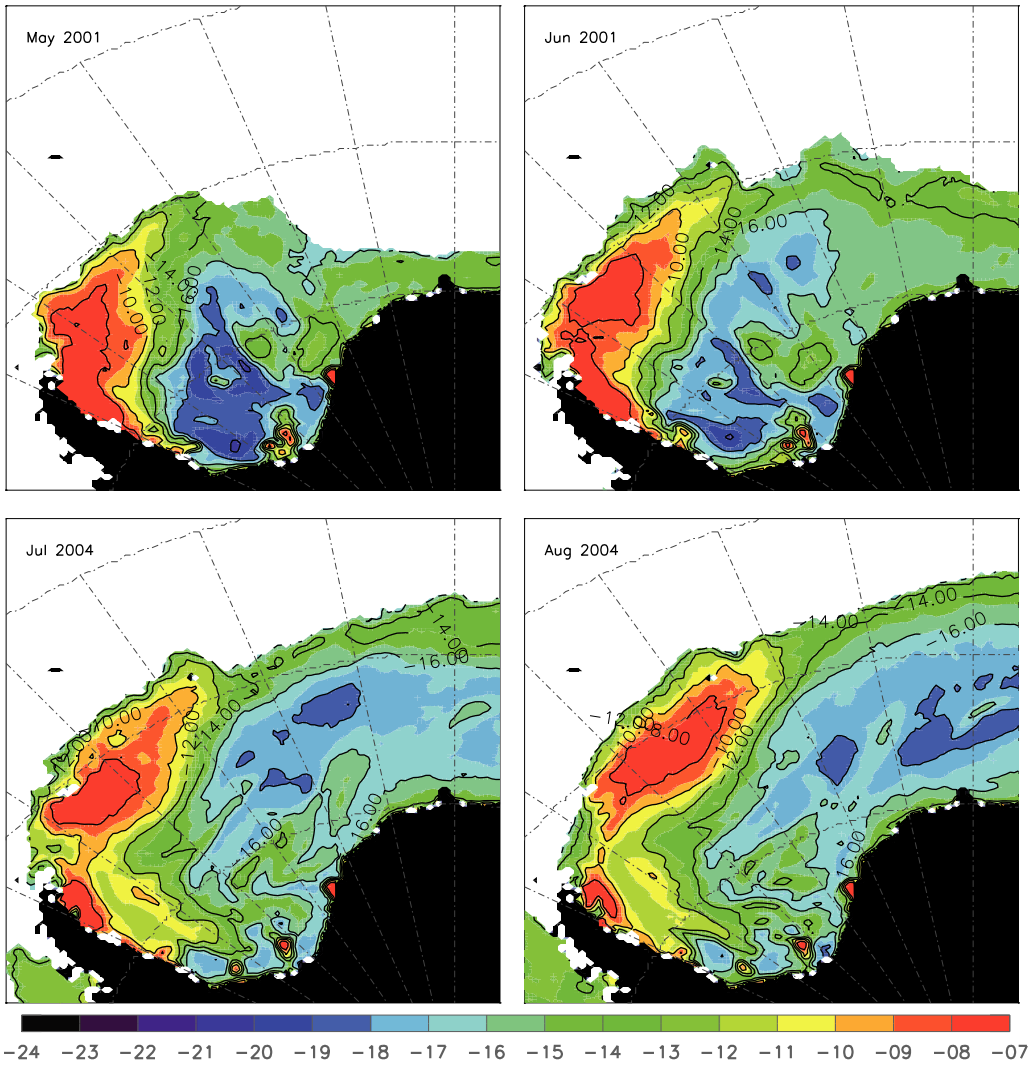

Fig. 4.2: *Example for backscatter maps in dB used to distinguish between FYI and SYI from the QuikSCAT scatterometer data for May and June 2001 (top) and July and August 2004 (bottom).*

movements of SYI from the south-western region to areas further to the north-east are visible for both years. The SYI drifts out of the Weddell Sea until summer or it melts in the northern regions (not shown).

For eight years of QuikSCAT scatterometer data, monthly areas of FYI and SYI were calculated by summing all pixel areas of the respective sea ice class. The monthly trends of FYI and SYI distribution are displayed in Figure 4.3 for the various backscatter power thresholds for the discrimination between both sea ice classes. FYI decreased in austral summer and autumn, and shows a slight increase in winter (July - October, Fig. 4.3a). Particular precaution is demanded for the months of October through January, since sudden atmospheric warming can modify the sea ice surface properties, including emissivity, and therefore backscatter signals (*Willmes et al.*, 2006, 2009). Signals during this period are often ambiguous, and a determination between both sea ice classes becomes difficult.

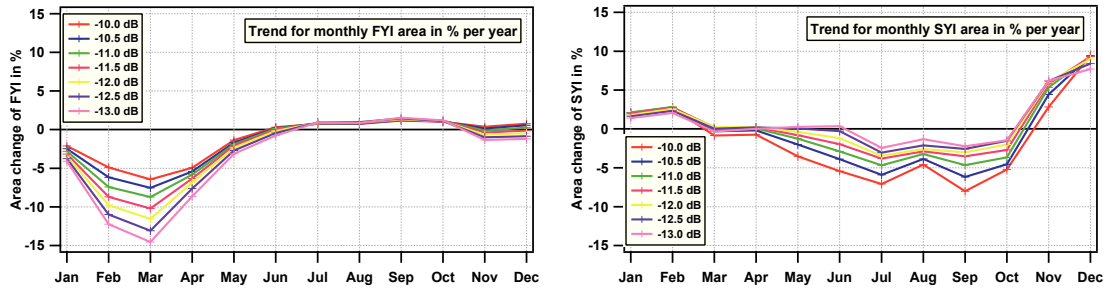

Fig. 4.3: *Monthly trends of FYI and SYI extent in % from 2000 till 2007 from the QuikSCAT scatterometer data.*

Figure 4.3b shows the monthly trends for SYI for the different backscatter power thresholds. SYI decreased in winter and has a slightly positive trend in summer for the observation period, contrary to the FYI. Interestingly, the general behaviour of FYI and SYI is nearly the same for all backscatter thresholds shown in this study. Except for some months, where trends slightly alternate around zero, the general tendencies are the same for the different thresholds, they vary only in strength. From trends in summer one would expect that the areal averaged sea ice thickness over the Weddell Sea became higher, since less first year ice is found. On the other side, areal averaged winter sea ice thickness potentially decreased, since more FYI and less SYI is found. Furthermore, from the data one would expect that sea ice volume shows either only a small change or decreases in general. These points are revisited, when the variability of sea ice thicknesses and sea ice volume from model simulations are analyzed in the next section. The increased FYI in winter might be related to a changed sea ice drift, which may lead to changed deformation processes. More divergent sea ice drift can open leads, and in winter, more thin ice would be produced.

Unfortunately, the Polar Pathfinder Sea Ice Motion fields used later in this study are only available through 2006. To explain the changes of FYI and SYI, time series of the same length are needed, ideally for periods longer than from 2000 till 2007, to assess interannual and interdecadal variability in a reliable way. Nevertheless, QuikSCAT scatterometer data are not available for a longer period, and therefore, model simulations may be helpful to hindcast sea ice class distributions. However, it turned out that model results are very different to observations and that a robust interpretation of them is not possible (see Appendix C for details). Nevertheless, the short QuikSCAT time series still give a first impression on sea ice class and thickness distribution and the results are compared to the sea ice thickness changes obtained from FESOM in the next section.

4.2 Modelled sea ice thickness and volume variability

In this section, sea ice thicknesses and the total sea ice volume in the Weddell Sea were analyzed regarding their interannual variability. Figure 4.4 shows the interannual variations of the areal averaged[1] effective[2] sea ice thickness within areas of at least 15 % SIC for the period from January 1979 till December 2006.

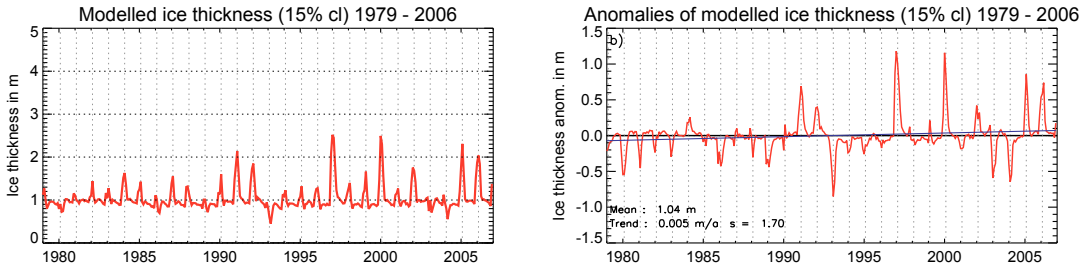

Fig. 4.4: *Interannual variability of the effective sea ice thicknesses (a) and their anomalies (b) in m simulated by FESOM for the period 1979 till 2006. Vertical grid marks the February of each year. s = relative significance. cl = minimum SIC, which is used for averaging.*

The modelled effective sea ice thickness varies between about 1 m and 2 m with some extrema up to about 2.5 m. The years 1991, 1997, 2000, 2002, 2005 and 2006 show relatively high sea ice thicknesses. In 1991, the areal averaged wind speeds north of 70^{o}S were comparatively low, which might have reduced divergent drift, and hence, the occurrence of leads in which new thin sea ice can be formed. Temperatures do not show extrema, which might force higher sea ice thicknesses in

[1] Data were averaged over the sea ice covered area between longitudes 298^o and 360^{o}E.

[2] Effective means that the sea ice thickness is averaged over the whole area of a grid cell, including the open water fraction.

this year, but in 1997, the areal averaged temperature was comparatively low in the Weddell Sea. Nevertheless, a clear relationship between areal averaged wind speeds and/or temperatures cannot be gained for the years with comparatively high sea ice thicknesses.

The areal averaged sea ice thickness had a slightly (statistically significant) increasing trend of 0.5 cm per year. This is consistent with the findings of *Zhang* (2007), who also simulated increasing sea ice thicknesses for most of the ice covered areas in the Southern Ocean for the period from 1979 till 2004. On a seasonal basis, the areal averaged sea ice thickness increased throughout summer until May with up to 1.4% per year, but the winter months show a slight decrease (not shown). None of the monthly trends are statistically significant at the 95 % confidence level. In fact, winter areal averaged sea ice thicknesses vary only little; on an interannual basis, variabilities barely exceed $\pm$ 10 cm. In summer, the interannual variances can rise to more than 1 m, and therefore, the variability is much higher than the trends. The positive summer trend may be related to a decreasing FYI and increasing SYI coverage and the negative winter trends to the opposite sea ice class changes, as described in Section 4.1. But the observed sea ice class trends are only valid for the period from 2000 till 2007. Comparing trends of modelled areal averaged sea ice thicknesses for the same period results in a poorer correlation, since for the shorter time period, modelled areal averaged sea ice thicknesses decrease in January and February and increase for the rest of the year. However, this is not a complete disagreement with results from scatterometer data, since an increased sea ice thickness in winter is not necessarily correlated with a trend of FYI or SYI. It might also be that the sea ice thicknesses of FYI just grow thicker in winter and melt faster in summer for this period without a change in the coverage of this sea ice class.

Figure 4.5 displays the modelled seasonal mean sea ice thickness distribution, its trend and the relative significance. During all seasons, mean sea ice thicknesses decreased in the central Weddell Sea. Only the trends in spring are not significant. Furthermore, also the increase along the south-eastern coast can be observed from the model for all seasons. Trends along the western coast are also mostly positive, except for some regions in winter (JJA), but they are not as high as those from the east-coast. In addition, the west-coast trends are not significant in most areas.

A comparison with the atmospheric forcing implies that the modelled trends over the Weddell Sea are a combination from mainly increasing temperatures, which might have affected the sea ice thicknesses in the central Weddell Sea, and increasing wind speeds in most parts of the Weddell Sea, which might force a stronger deformation in the coastal areas.

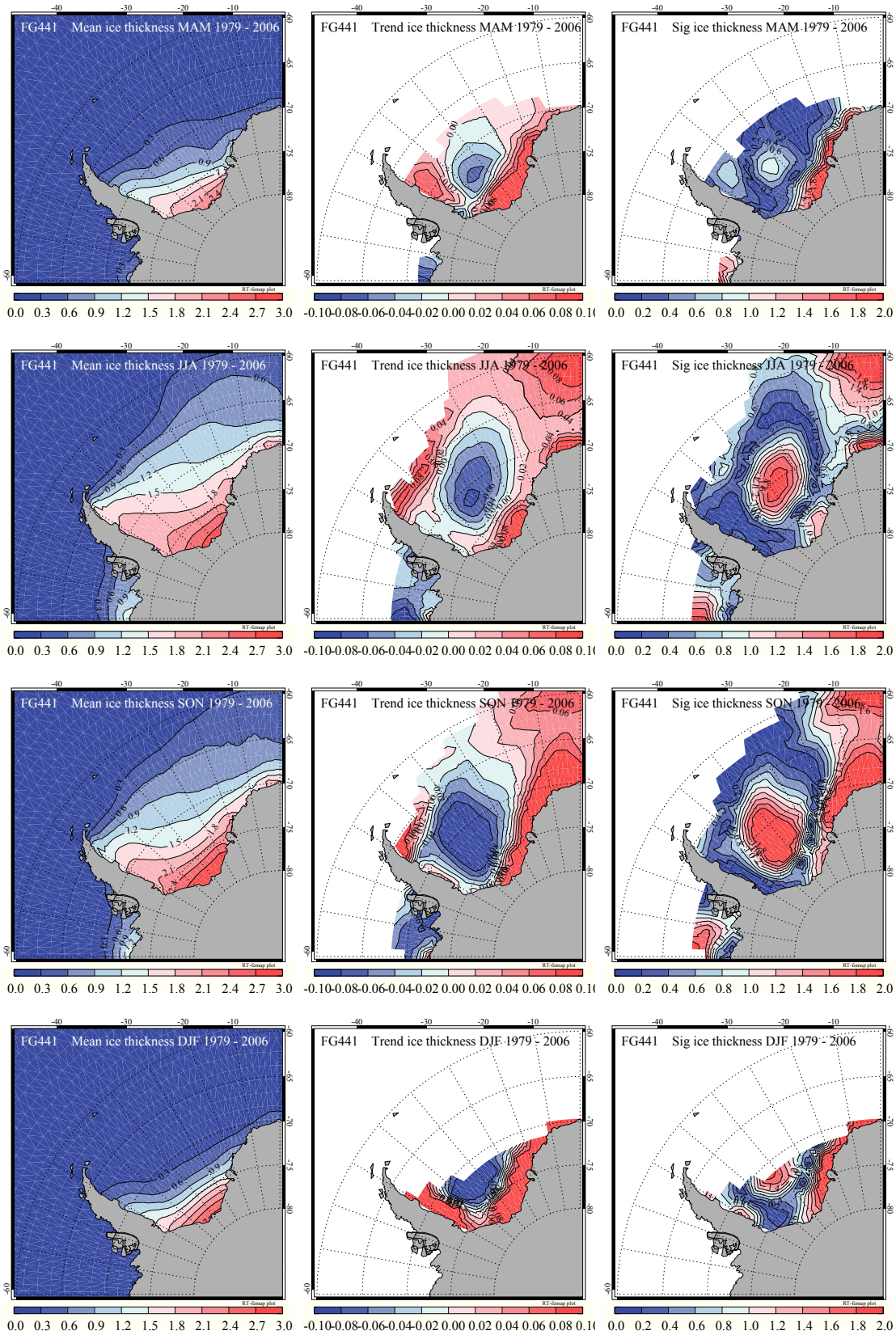

Fig. 4.5: *Seasonal mean sea ice thickness distribution in m, trends in m per year and their statistical significance from 1979 till 2006 simulated by FESOM. A value of at least 1 in c) means that the trend is statistically significant.*

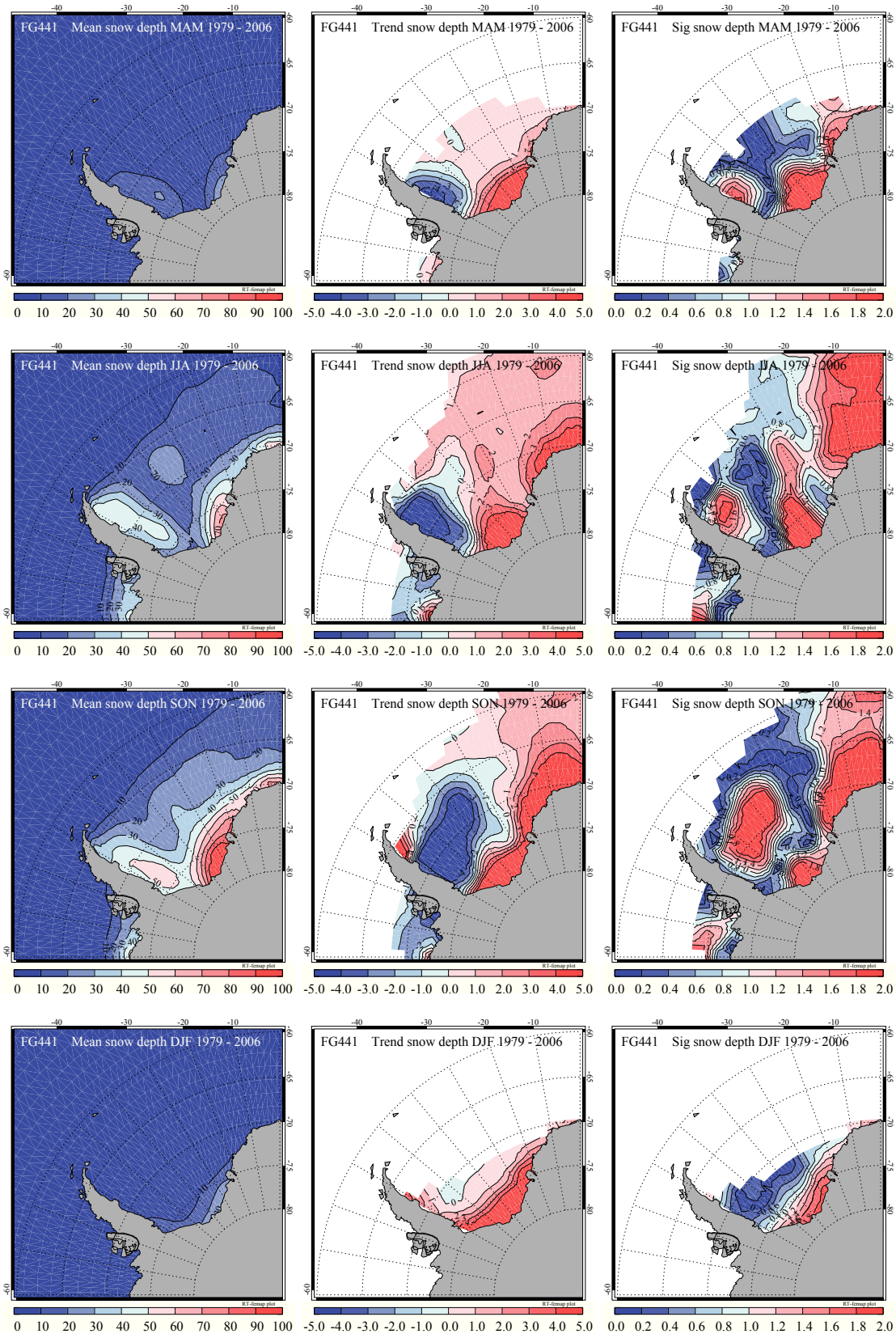

Fig. 4.6: *Seasonal mean snow depths in cm, trends in cm per decade and their statistical significance from 1979 till 2006 simulated by FESOM. A value of at least 1 in c) means that the trend is statistically significant.*

In addition, according to *Liu et al.* (2004), increasing SAT might also force higher sea ice thicknesses due to their potential effect on precipitation: more snow-fall would increase the ice-albedo effect due to the higher albedo of snow. Furthermore, more precipitation into the open ocean would reduce the salinity of the sea water, resulting in a stabilization of the surface layer. This would prevent the mixing of cold surface water with warmer water masses from below and hence reduce the basal melting of sea ice. Hence, increased snow coverage would also result in increased sea ice thickness, even though temperatures are increasing. Actually, snow depths in the Weddell Sea, shown in Figure 4.6, illustrate such a behaviour: in most occasions, trends in sea ice thickness and snow depth are positive or negative at the same time. Deficiencies might occur when the low heat conductivity of snow influences the thermodynamic growth of sea ice (*Massom et al.*, 1997), which is predominantly in autumn and winter the case, or when other effects, like dynamic processes, are the major drivers for sea ice thickness changes.

Sea ice thicknesses in the model generally increased in regions, where the model computes increasing SIC. This is true for most areas of the Weddell Sea in every season. Deviations mainly occur in the southern regions: In winter at the south-eastern and in summer at the south-western coast, where sea ice thicknesses in both cases increase, but SIC decrease over the study period. An explanation may be a changed drift field that might have reduced or strengthened the deformation processes in the respective regions. Increasing wind speeds in coastal regions, observed in the 10-m wind fields from NCEP reanalysis data, support this hypothesis.

For an illustration of the thermodynamical sea ice growth, Figure 4.7 displays the seasonal mean net freeze rates (left), their trend (middle) and relative significance (right) for the Weddell Sea. The mean net freeze rates underlie a well visible seasonal cycle with prevailing freezing (red) during autumn and winter and net melting (blue) in spring and summer in most parts of the Weddell Sea. Net freeze rates are lower in winter than in autumn, certainly because thick sea ice grows slower than the thin new formed sea ice that can be found in the beginning of the freeze period. In addition, snow on top of the ice might reduce the ocean-ice-atmosphere heat fluxes and dampens further the sea ice growth in winter.

In addition to the seasonality, two distinct regional features arise in the figures for the net freeze rates: The first one is the prevailing melting in the north-western Weddell Sea during winter, which potentially results from the warm water masses transported by the ACC into this region in the model simulation. The other feature is that parts of the southern Weddell Sea show still a net freezing during spring.

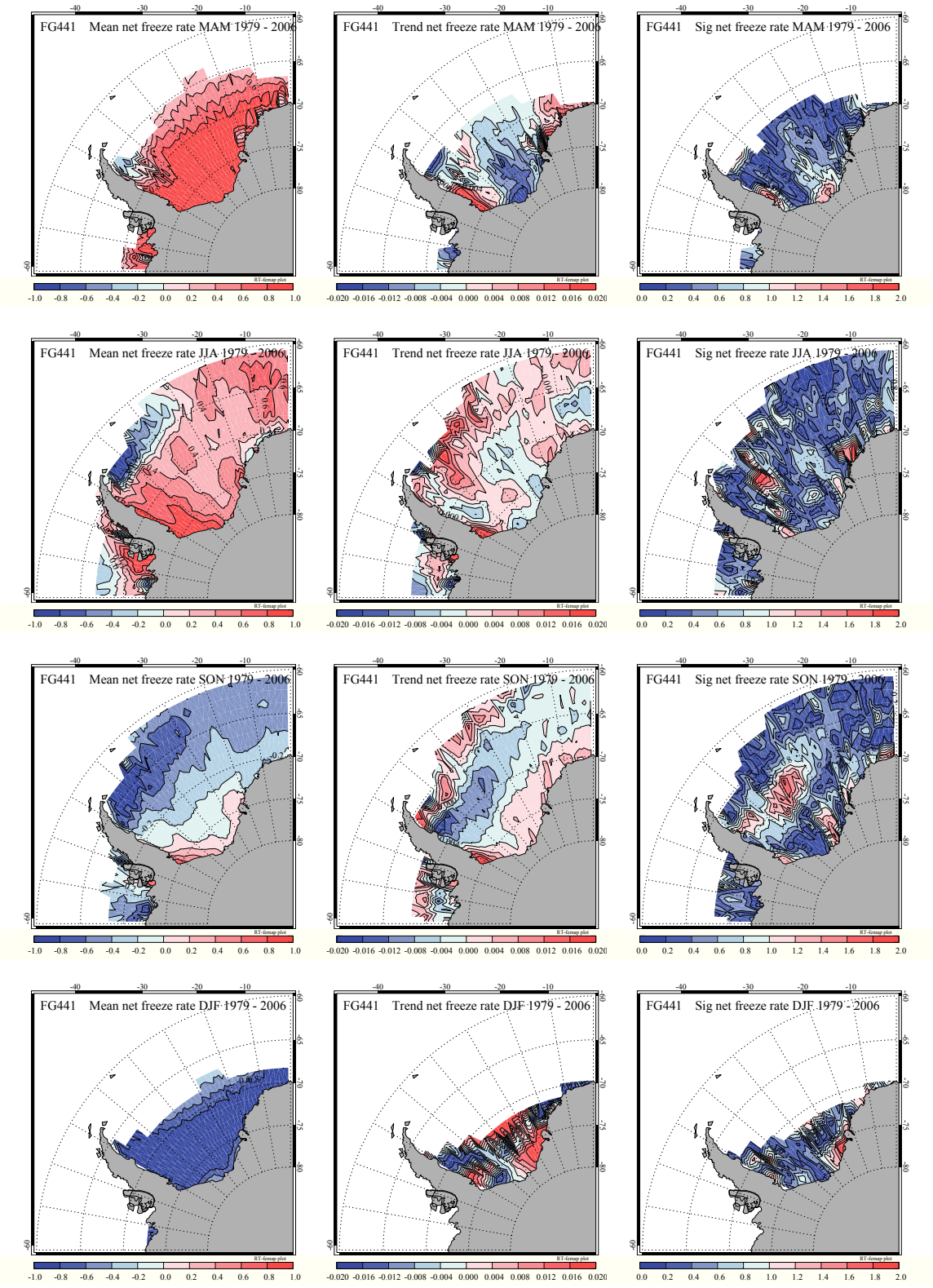

Fig. 4.7: *Seasonal mean net freeze rates (cm/day), trends (cm/day per year) and relative significance in the Weddell Sea for the period 1979 through 2006. Positive values (red) show net freezing, negative values (blue) are associated to net melting.*

This is potentially due to the year-round fairly low mean SAT in combination with the prevailing offshore winds in this region, which transport cold continental air northward and advect sea ice offshore. The latter might result in a formation of a polynya, where net freeze rates can keep high due to the direct exchange of heat between the relatively warm ocean and the cold atmosphere.

For the period 1979 through 2006, trends are seasonally and regionally very different. The only robust signal is the tendency to increasing net freeze rates in the south-western Weddell Sea near the Ronne Ice Shelf, which persists nearly year-round. This trend is consistent with the positive trend in the offshore wind speeds in this region, which might increase the freeze rates by the formation and maintenance of a polynya. Actually, sea ice thicknesses show a slight decrease in the south-western near-coastal region and partly an increase further north, which supports the assumption that sea ice production has increased by a polynya in front of the Ronne Ice Shelf.

In addition, the general tendency to less freezing in autumn as well as the tendency to less melting in the Weddell Sea in summer is well correlated with the trends in the SAT, which show increasing SAT in autumn and decreasing SAT in summer. However, most of the trends in the net freeze rates are statistically not significant, as is indicated by Figure 4.7 on the right site. This holds also for the long-term average shown in Fig. 4.8. The strongest signals are the statistically significant increase in net freeze rates in the south-western and a non-significant decrease in the north-western Weddell Sea, i.e. increased freezing near the Ronne Ice Shelf and increased melting in the north-western parts. The other regions exhibit only small and generally statistically insignificant changes.

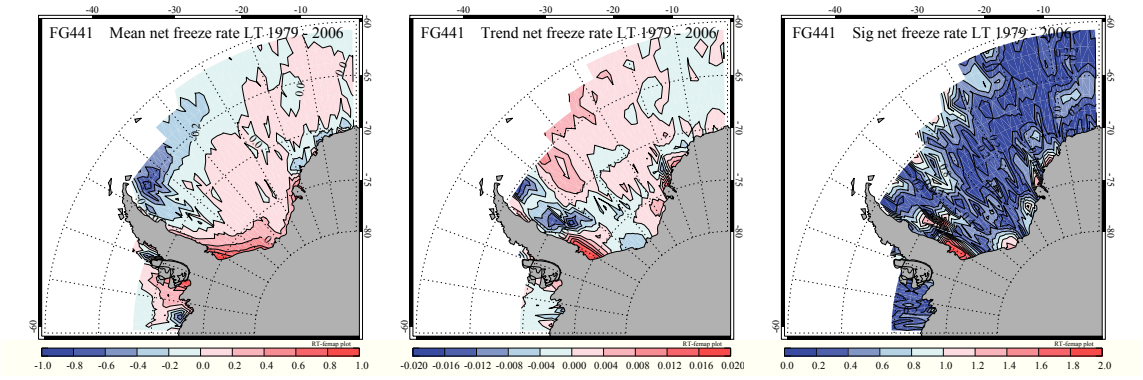

Fig. 4.8: *a) Mean net freeze rate in cm/day, b) its long-term trend in cm/day per year and c) its relative significance in the Weddell Sea for the period 1979 through 2006.*

In general, the growth of sea ice is an interplay of thermodynamic as well as dynamic effects. Processes like deformation and flooding as well as the isolating effect of snow

influences the sea ice thickness next to the thermodynamical growth. First analysis of the impact of sea ice deformation reveals that sea ice growth due to deformation is of special importance in the western Weddell Sea, in particular near the Antarctic Peninsula, which might explain the increase in sea ice thicknesses in this region despite of increasing SAT. However, further investigation are necessary to connect changes in thermodynamical and dynamical sea ice growth with trends in sea ice thicknesses. Also the impact of snow on the sea ice thickness changes needs further investigations, especially with respect to flooding.

The small and varying trends in the net freeze rates, and actually also in the growth rates by deformation processes (not shown), indicate that the sea ice volume certainly does not show a strong trend. Figure 4.9a and b display the total sea ice volume and its anomalies for the ice covered region in the Weddell Sea for the period 1979 through 2006. As expected, the simulated total sea ice volume shows only a small trend for this period, with an increase of 5.35 km^3 (0.11$\%$) per year. This trend is not significant at the 95$\%$ confidence level due to the high seasonal and interannual variability over the study period, but it is significant at the 90$\%$ confidence level. Large positive anomalies occur in 1991 and 1997, when the areal averaged sea ice thickness is very high, and in 2003, when the areal averaged sea ice thickness is indeed low, but instead sea ice covered area is very large. In 1993, the sea ice volume is the lowest, when both the areal averaged sea ice thickness as well as the ice covered area is quite low.

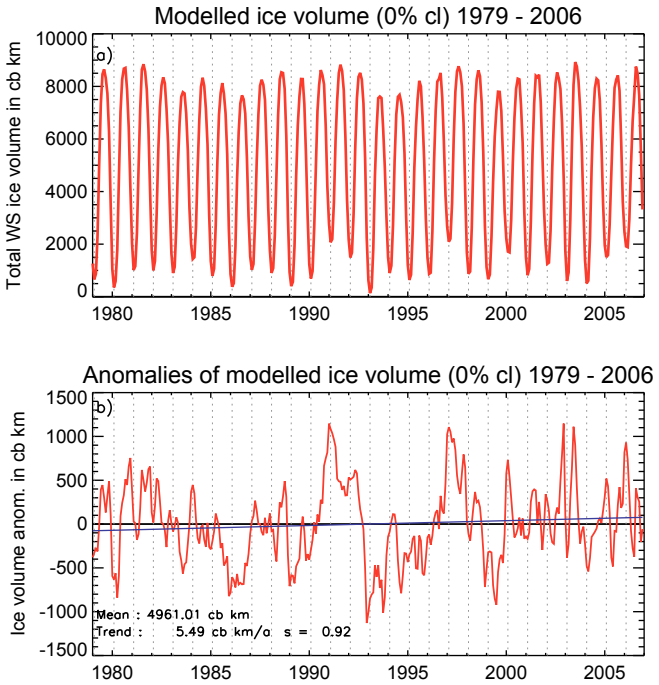

Fig. 4.9: *Simulated monthly mean sea ice volume (a) and its anomalies (b) in km^3 from 1979 through 2006. cl = minimum SIC, which is used for calculation of the sea ice volume.*

In the following, sea ice volume variability is here analyzed with respect to some characteristic regions. One of these regions is the north-western Weddell Sea (WWS). As is shown in Figure 4.5, sea ice thicknesses increased in this region despite increasing SAT. Comparisons with SIC maps showed that also the SIC increased in this region over the period from 1979 till 2006. It was discussed that this feature might be forced by inaccuracies in the early NCEP data, since the SIC trends for the period from 1988 till 2006 are negative, as is expected for increasing temperatures. Also the sea ice thicknesses in the shorter period (1988-2006) decreased. To show the interannual and decadal variability of sea ice volume in this region, it is demonstrated for an area spanning the coordinates 50-60^{o}W/65-67.5^{o}S. Another region is defined as the central Weddell Sea (CWS), where the volume is calculated between 40-50^{o}W and 70-75^{o}S. Moreover, an area in the eastern Weddell Sea was selected (EWS): 10-20^{o}W/70-72.5^{o}S. The anomalies of the sea ice volume for these regions as well as their trends are shown in Figure 4.10 for both periods, from 1979 till 2006 and from 1988 till 2006.

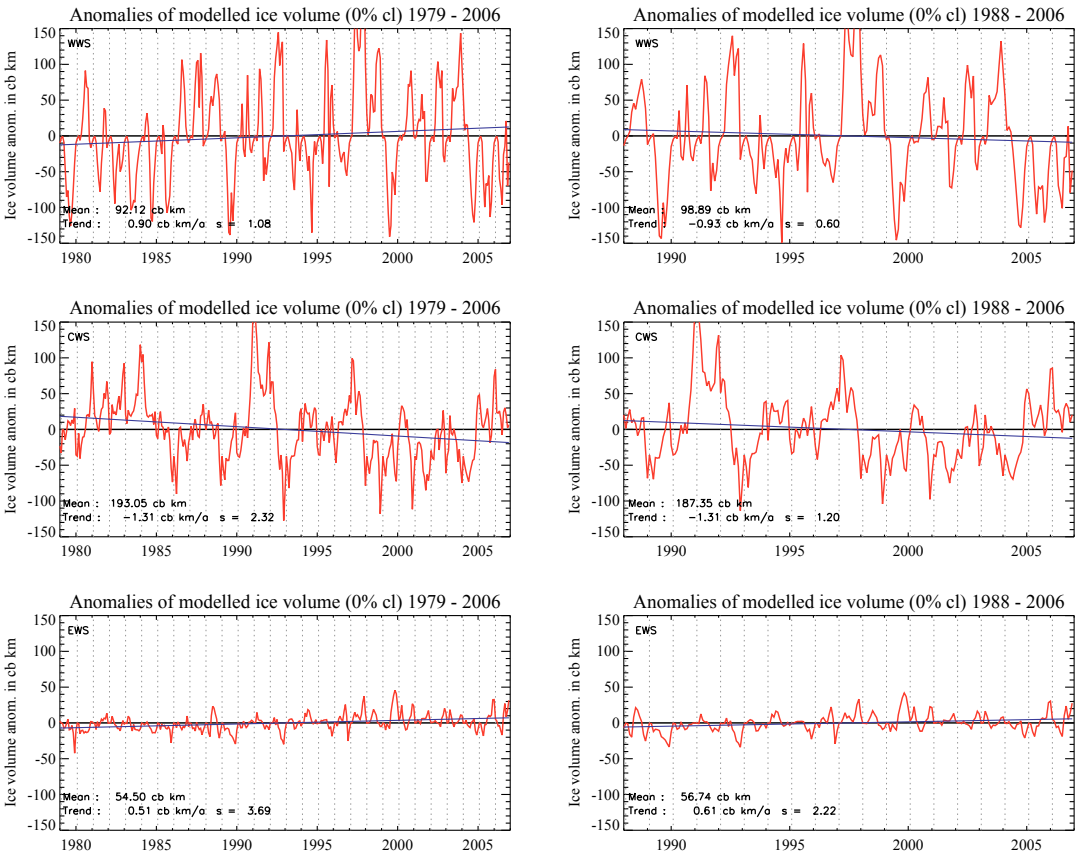

Fig. 4.10: *Modelled sea ice volume in km^3, averaged for distinct regions. WWS: 50-60^{o}W/65-67.5^{o}S, CWS: 40-50^{o}W/70-75^{o}S, EWS: 10-20^{o}W/70-72.5^{o}S. cl = minimum SIC, which is used for calculation of the sea ice volume.*

In the WWS, sea ice volume is highly variable, but the trend of 0.9 km^3 per year for the period 1979 through 2006 is statistically significant. For 1988 through 2006, however, this trend becomes negative and insignificant. Trends in this region are potentially forced by the very low sea ice volume in the early 1980's. For the other regions (CWS and EWS), such a change of the trend is not detected. In the central Weddell Sea, the negative trend can be observed for both observation periods and in both cases the trend is statistically significant. In the EWS, the positive trend becomes even slightly stronger and also here, trends are statistically significant.

Summarized, areal averaged sea ice thickness as well as sea ice volume increased for the period from 1979 till 2006 in FESOM for the Weddell Sea. The highest trends are calculated for the summer months, but the model has some deficiencies in this season. Nevertheless, simulated SIE changes are the highest in summer as well, which is generally comparable to observations. In addition, increased sea ice thicknesses and volume in summer are consistent with the decrease of mean SAT in the Weddell Sea.

4.3 Comparison of modelled sea ice thickness and volume with observations

To evaluate the model results, simulated sea ice thicknesses are compared to sea ice draft measurements from upward looking sonar data. In addition, ICESat data are used to assess the accuracy of the simulated sea ice thickness distribution and volume changes in the Weddell Sea. Finally, a sensitivity study was performed to test, whether different model setups might improve results.

4.3.1 Upward looking sonars

Upward looking sonars (ULS) have been deployed in the Weddell Sea since 1990 on top of moorings, at depths between 100 m and 175 m (*Harms et al.*, 2001; *Strass & Fahrbach*, 1998). They transmit an acoustic signal of 300 kHz with a pulse width of 66 ms and measure the travel time to the ice-ocean interface and back to the instrument (*Strass & Fahrbach*, 1998). The instrument additionally measures the temperature and pressure at the deployment depth as well as the tilt of the instrument. From the sound pulse travel time and the sound velocity, which is assessed from a dynamic-thermodynamic sea ice mixed layer model for the Weddell

Sea (*Timmermann et al.*, 1999), the distance to the reflecting surface is calculated (*Harms et al.*, 2001). Together with the known depth of the instrument, sea ice draft is obtained, i.e. the portion of sea ice underneath the sea surface. The footprint of the transmitted acoustic signal depends on the deployment depth and the beam opening angle. Considering a depth of 150 m and an angle of 2^o (*Harms et al.*, 2001; *Strass & Fahrbach*, 1998), the footprint is about 5 m. The temporal resolution of the draft measurements is 4 to 8 minutes (*Strass & Fahrbach*, 1998).

The ULSs provide local point measurements with high temporal resolution over several months up to few years. After the deployment phase, they are recovered and the stored data become available. The spatial and temporal distributions of the

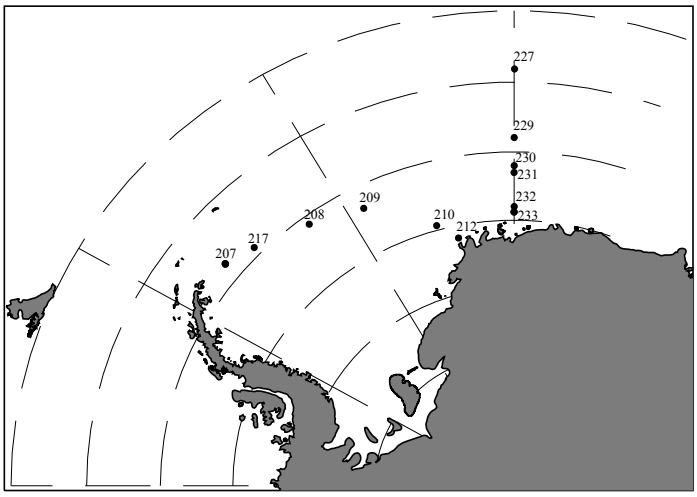

Fig. 4.11: *Map of ULS positions in the Weddell Sea.*

deployed ULS are shown in Figure 4.11 and Figure 4.12. Unfortunately, data from different positions do not span the same time periods and, in addition, new data are only available for ULS 207 and for those moorings that are deployed along the Greenwich Meridian. Data coverage in the central Weddell Sea is very low.

Since original data of the ULSs have too many gaps, an analysis of trends is not possible, but they can be used for model validation. *Timmermann et al.* (2009) showed a comparison of modelled sea ice thicknesses with ULS measurements for the period from 1990 till the beginning of 1998. In their study they used the ULS data processed after *Strass* (1998) and *Harms et al.* (2001) and they found a good agreement between ULS measurements and model simulations for the positions along the Greenwich Meridian, but underestimations in near-coastal regions. The ULS data set used here[3] differs from that in *Timmermann et al.* (2009) in the way

[3]Data were processed and provided by H. Witte and Dr. W. Dierking from the Alfred Wegener Institute.

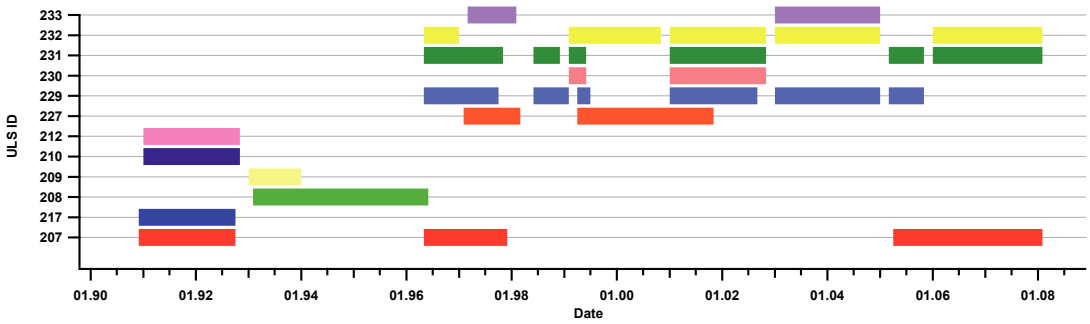

Fig. 4.12: *Upward looking sonar operation periods.*

that for this study no bias correction[4] for the ULS draft measurements (as described in *Strass*, 1998, *Strass & Fahrbach*, 1998, and *Harms et al.*, 2001) was used and icebergs were removed by a cut-off value of 30 m instead of 10 m. Furthermore, the time series were extended until 2008. The influence of excluding the bias correction is assessed in the discussion.

For a qualitative study of model accuracy, differences as well as correlation coefficients were calculated from monthly averages with respect to regional and seasonal dependencies. ULS drafts were converted into sea ice thickness using the empirical relationship from *Harms et al.* (2001):

$$h_{ice} = 0.028 + 1.012d \tag{4.2}$$

with d as sea ice draft and h_{ice} as sea ice thickness.

Figure 4.13 shows the simulated sea ice thicknesses (solid line, red) compared to those obtained from ULS draft measurements (dashed-dotted line, blue) for the Weddell Sea moorings. ULS 207 (at the tip of the Antarctic Peninsula) demonstrates a strongly varying seasonal cycle, but also a pronounced interannual variability. During the first period (1991/1992), sea ice thicknesses rarely fell below 1.5 m. The thickest sea ice is observed in October 1991, with more than 4 m. In the second period (1996/1997), sea ice disappeared almost completely during summer. The minimum monthly averaged sea ice thickness was 0.028 m in summer and did not exceed 3.5 m in winter. Finally, during the third period, which covers the years from 2005 till February 2008, sea ice was on average notably thinner than in the measurement phases before; maxima barely exceeded 2 m. The ULS data clearly indicate that

[4] According to *Strass* (1998), the spreading of the acoustic beam results in a footprint, which depends on the opening angle and the depth of the ULS. This spreading influences the measured signal as within this footprint sea ice draft can vary significantly. The returning echo is measured at the time when the echo signal reaches a fixed threshold value (approximately 1/4 of the overall mean of the signals amplitude, *Strass*, 1998), and therefore, signals, which are used to determine the travel time potentially come from higher drafts as the modal one would describe.

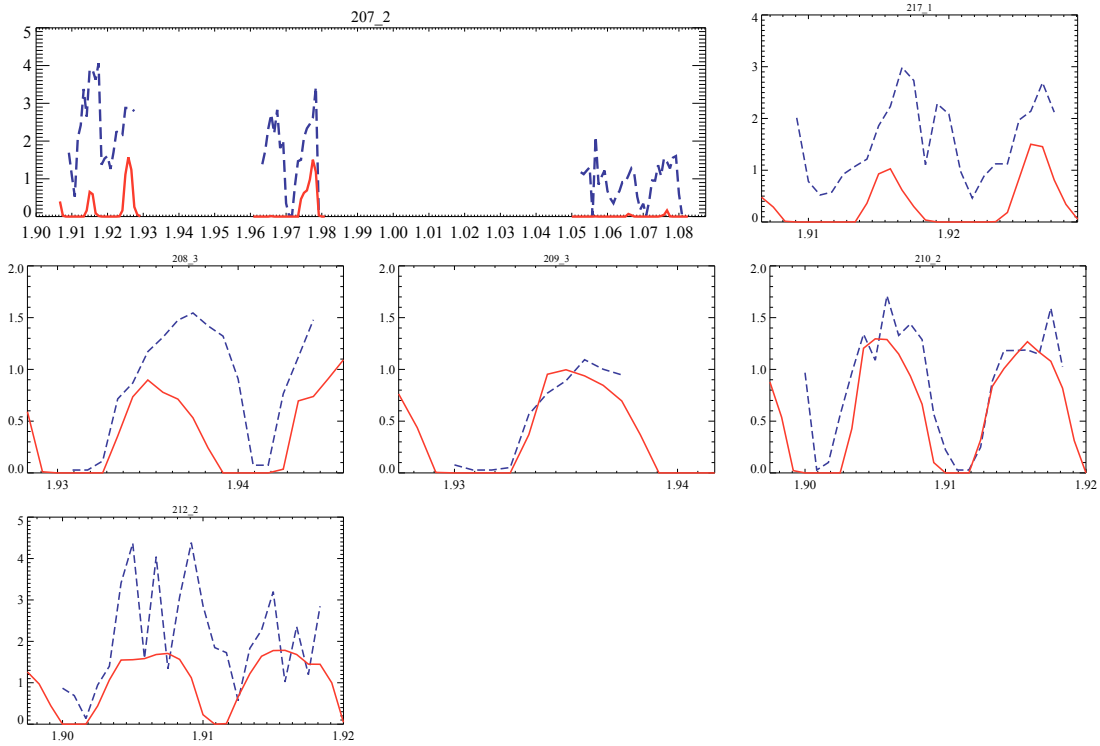

Fig. 4.13: *Comparison between monthly mean sea ice thicknesses (in m) obtained from ULS draft measurements (blue dashed-dotted line) and model simulations from FESOM (red solid line) in the Weddell Sea basin. Note the different ordinate scales.*

a decrease in sea ice thicknesses occurred near the Antarctic Peninsula over the covered periods. A comparison with model data also shows a decrease in sea ice thicknesses from the 1990s till the most recent years. However, FESOM strongly underestimates the sea ice thicknesses and their seasonal amplitude by 90% on average in this region during all deployment phases. This strong and statistically significant underestimation is attributed to the poor representation of the Antarctic Peninsula in the NCEP reanalysis data (*Timmermann et al.*, 2005; *Windmüller*, 1997), which affects the wind forcing and temperature distribution, and therefore dynamical processes as well as the thermodynamic growth of the sea ice in the model. Consequently, the model underestimates the sea ice cover in summer and the formation of thick multi-year ice in this region (*Timmermann et al.*, 2009).

At the position of ULS 217, about 400 km offshore, the influence of sea ice deformation is still visible. On average, sea ice grew up to 2 - 3 m in winter and also summer sea ice had a thickness of about 0.5 m. Similar to ULS 207, but less strong, the model underestimates the sea ice thicknesses (about 1 m for yearly means) and their seasonal amplitude (several dm). Furthermore, sea ice growth starts with a delay of about 1.5 months and the melt season starts too early in the model. The same feature arises at ULS 208. For both positions, differences are statistically significant.

At ULS 209, located in the central Weddell Sea, and ULS 210, the model represents the measured sea ice thicknesses well. The seasonal cycle and its amplitude are well captured. Differences are generally low and statistically insignificant, even though the melt period starts too early. Further to the east, next to the coast, ULS 212 shows highly variable sea ice thicknesses of up to 4.4 m and barely a seasonal cycle. These high variations occurred potentially because of the high sea ice deformation rates at the coast, which are not well simulated by FESOM. *Timmermann et al.* (2009)

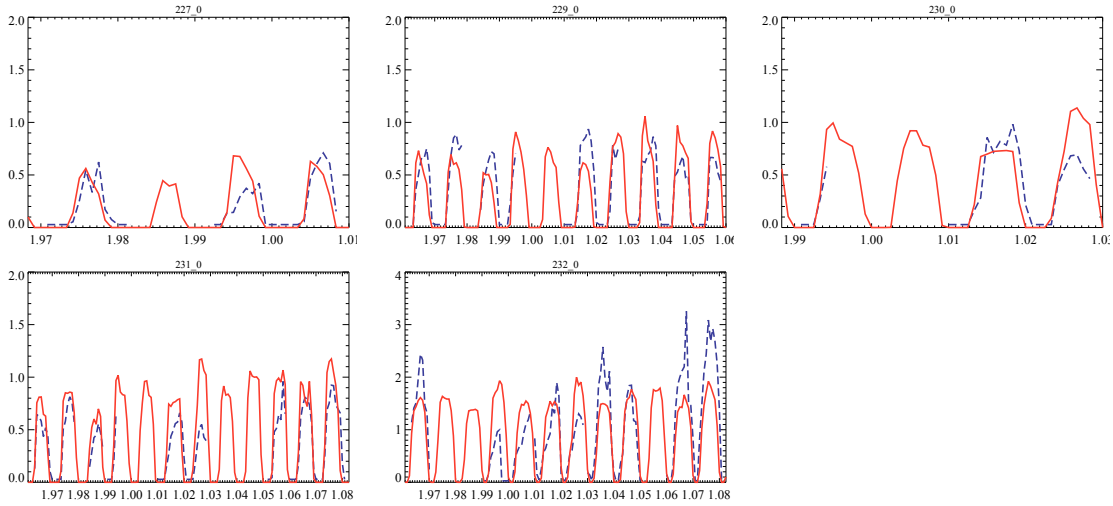

Fig. 4.14: *Comparison between monthly mean sea ice thicknesses (in m) obtained from ULS draft measurements (blue dashed-dotted line) and model simulations from FESOM (red solid line) along the Greenwich Meridian. Note the different ordinate scales.*

argued that these coastal deformation processes occur on spatial scales that are much smaller than the model resolution, and therefore, the model cannot capture them.

Comparisons with data from the Greenwich Meridian are shown in Figure 4.14. Measurements were performed more frequently in this region and allow for comparisons for several years with only small data gaps. At all ULS positions at the Greenwich Meridian, the seasonal cycle in modelled sea ice thicknesses is in a good agreement with measurements, and differences between the observations and model simulations are in most cases statistically not significant. However, FESOM does not capture the high interannual variability in all cases, and therefore, the interpretation of the trends in this region has to be done carefully.

Interestingly, sea ice thicknesses near the coast of the eastern Weddell Sea (ULS 233) are captured quite well by the model, contrary to the western Weddell Sea near the Antarctic Peninsula, where ULS obtained sea ice thicknesses are strongly underestimated. In 2002, the general thicker sea ice is represented in the model to some extent, since the simulation produce thicker sea ice in that year, compared to

the other two years. As mentioned before, the high variation of observed sea ice thicknesses due to deformation processes on small scales cannot be captured in the model simulations.

To assess the model's reliability, the correlation between both data sets was calculated. Table 4.1 lists the results for every ULS position as well as the differences

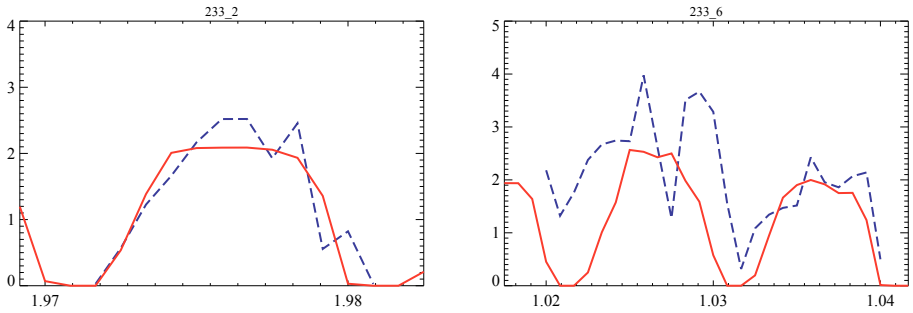

Fig. 4.15: *Comparison between monthly mean sea ice thicknesses (in m) obtained from ULS draft measurements (blue dashed-dotted line) and model simulations from FESOM (red solid line) near the coast at the Greenwich Meridian. Note the different ordinate scales.*

(diff) between both data sets in % of the mean ULS-derived sea ice thickness. Furthermore, the number of compared data points (n) is shown, which is unfortunately very low for the Weddell Sea basin.

The correlation coefficients indicate that the agreement between model and ULS data becomes better with increasing distance to the coast. From ULS 207 to ULS 209, the correlation increases from 0.509 up to 0.956 and decreases again down to 0.484 near the eastern coast at ULS 212. Also for the Greenwich Meridian, correlation coefficients are higher, when the moorings were located away from the coast (ULS 232 and 233, r = 0.725 and 0.573, respectively) or the sea ice edge at ULS 227 (r = 0.746). The correlation is statistically significant for all ULS positions.

The differences between both data sets also decrease from the western coastal region from -90.3 % down to -12.0 % at ULS 209 and increase again towards the eastern coastal boundary of the Weddell Sea basin (ULS 212, diff = -49.6 %, where a negative sign means that ULS thicknesses are underestimated by model simulations). At the Greenwich Meridian, sea ice thicknesses are mainly underestimated except for ULS 231 and 230, where overestimations of 31.1 % and 14.3 % were found.

Seasonal correlation and differences between both data sets are listed in Table 4.2. The highest correlation occurs in January with r = 0.621, but overall there is no clear seasonal dependency, as there is a strong month to month variation for the correlation coefficients. This indicates that regional effects play the major role for the occurrence of disagreements.

Table 4.1: *Correlation coefficients (r) and differences (diff) in $\%$ of mean ULS sea ice thickness between model simulation and ULS measurements at all ULS positions. n is the number of coincident sea ice thicknesses and r^2 is the stability index. Values in italic font are statistically not significant.*

ULS	207	217	208	209	210	212	227	229	230	231	232	233
n	78	23	17	10	23	23	34	87	28	89	105	37
r	0.509	0.626	0.676	0.956	0.855	0.484	0.746	0.812	0.822	0.889	0.725	0.573
r^2	0.259	0.392	0.457	0.914	0.731	0.234	0.557	0.659	0.676	0.790	0.526	0.328
diff $\%$	-90.3	-77.5	-60.3	*-12.0*	*-26.9*	-49.6	*-1.0*	*-8.5*	*14.3*	31.1	*-7.0*	-32.6

Table 4.2: *Seasonal correlation coefficients (r) and differences (diff) between both data sets. In addition the correlation was computed without ULS 207 and without 207 and 217. Values in italic font are statistically not significant.*

Month	Jan	Feb	Mar	Apr	May	Jun	Jul	Aug	Sep	Oct	Nov	Dec
n	45	46	44	46	50	52	49	48	48	47	44	35
r	0.621	0.000	0.429	*0.208*	0.389	0.406	0.385	0.463	0.350	*0.061*	0.573	0.474
r^2	0.386	0.000	0.184	0.043	0.151	0.165	0.148	0.214	0.123	0.004	0.328	0.225
diff $\%$	-89.4	-100.0	-99.9	-83.3	-50.5	*-21.5*	*-20.4*	*-21.1*	-30.0	-28.6	-34.3	-64.7
r (o 207)	0.674	0.000	0.650	0.470	0.782	0.728	0.683	0.773	0.675	0.367	0.695	0.563
r (o 207/217)	0.751	0.000	0.677	0.536	0.862	0.780	0.724	0.797	0.773	0.521	0.714	0.679

Correlation coefficients strongly increase, when ULS 207 is excluded and there is another increase, when ULS 217 is excluded as well. A seasonal dependency of the correlation is not apparent in any case. In contrast, the differences between both data sets show a clear seasonal dependency. From December to April/May, differences are the highest with 50 % to 100 %, while they decrease down to 20.4 % in June. In winter, the differences are not significant. During the rest of the year, the statistically significant differences occur potentially due to the fact that melting starts early and sea ice grows with a delay in the model simulations.

Figure 4.16 summarizes ULS data from specific regions defined as Coastal/High Deformation Zone, Weddell Sea and Greenwich Meridian. Comparing the Coastal/High Deformation ULS positions with model simulations result in a correlation of only 0.436. The slope, which should ideally be equal to one, is only 0.326. This means that the modelled sea ice thicknesses are systematically too low. As Figure 4.16a shows, modelled sea ice thicknesses do not exceed 2.6 m, while ULS data show sea ice that grew up to 4.4 m for these regions. The strongest underestimation occurs

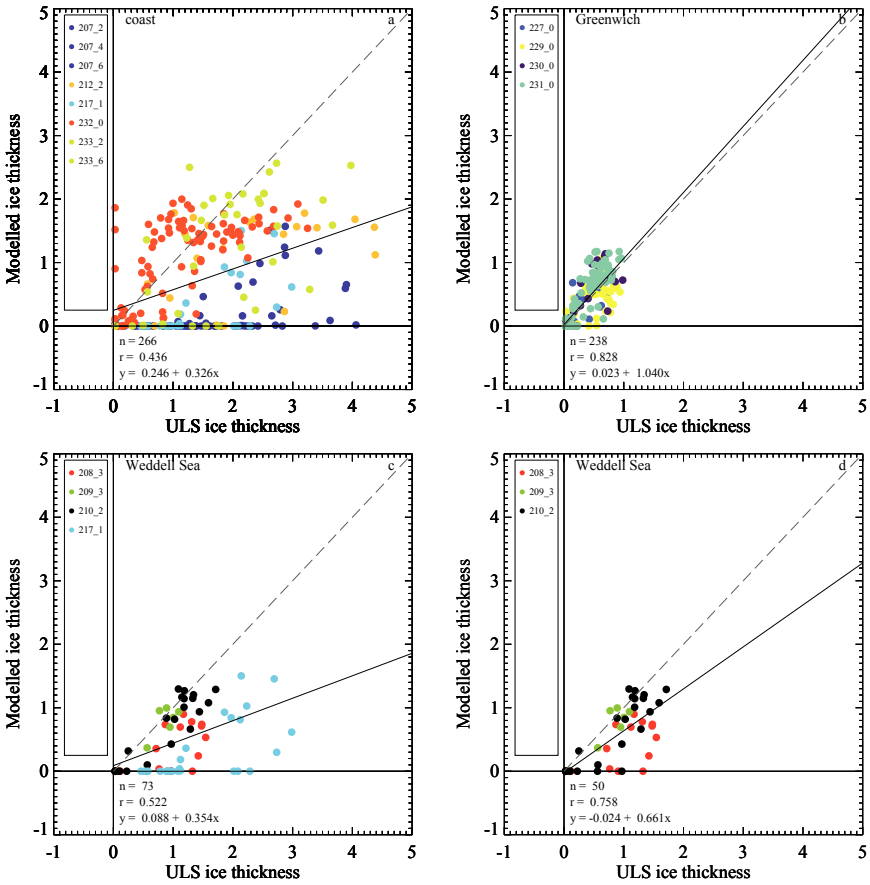

Fig. 4.16: *Regional correlation between model simulations and ULS sea ice thickness measurements at a) the coast, b) the Greenwich Meridian and in the Weddell Sea with (c) and without ULS 217 (d). Dashed lines indicate a slope of one.*

at the Antarctic Peninsula at ULS 207 and ULS 217. The situation is very different at the Greenwich Meridian, where the correlation is fairly high with r = 0.828 (without ULS 232) and r = 0.803 (with ULS 232, not shown). The slope is 1.04 (Fig. 4.16b). Hence, sea ice thicknesses in this region are well represented by FESOM. However, sea ice is generally not thicker than 1 m on average in both data sets, indicating that deformation plays a minor role here. In the central Weddell Sea, the correlation is r = 0.522, when ULS 217 is included (Fig. 4.16c). Sea ice measured by the ULS grew up to 3 m on average, which is not captured by FESOM. The slope of 0.354 is comparable to that in Figure 4.16a for the coastal regions. If data from ULS 217 are excluded, the correlation becomes r = 0.758 and the slope increases to 0.661.

This study indicates that sea ice thicknesses above 2 m are not well captured by FESOM. In fact, a comparison of slopes for all ULS data of a special sea ice thickness shows that the best representation of sea ice thicknesses in the model is given, when sea ice is not thicker than about 0.8 m (sl = 1.028, Fig. 4.17). When the measured sea ice thicknesses are lower, sea ice is in general slightly overestimated. Slopes for sea ice thicker than 0.8 m fall below 1. For example, the slope of sea ice not thicker than 1 m is 0.822 and that one of sea ice up to 2.5 m thickness is only 0.451. This indicates that the higher the sea ice thickness is, the worse is the general representation in the model. The correlation coefficients for the different cases overall show a similar behaviour: they become lower with increasing sea ice thicknesses. A

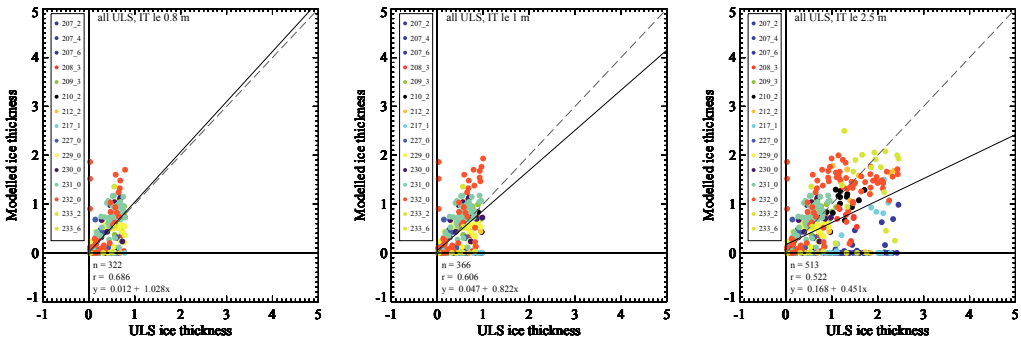

Fig. 4.17: *Agreement between simulated and ULS-based sea ice thicknesses with a predefined upper boundary of 0.8 m (left), 1 m (centre) and 2.5 m (right) for the measurements. ULS data are from every station without regional or temporal separation.*

possible reason for the underrepresentation of thick sea ice might be that the model's sea ice deformation is underestimated or that the forcing data are not good enough to initiate adequate dynamical processes, e.g. due to a weak representation of the katabatic wind in the NCEP data (*Windmüller*, 1997).

4.3.2 Comparison with satellite-based sea ice thickness data

Since 2003, the Ice, Cloud, and Land Elevation Satellite (ICESat) provides information on sea ice freeboard for distinct periods. The Geoscience Laser Altimeter System (GLAS) instrument on-board ICESat measures the travel time of emitted laser pulses to determine the distance between the satellite and the Earth's surface. The distances are corrected for atmospheric scattering from e.g. clouds. In addition, instrumental as well as tidal correction are applied to the data (*Zwally et al.*, 2002b, 2008). From the distance satellite-Earth, surface elevation is calculated using the height of the satellite and the Earth's geoid. This surface elevation is a mean over the footprint area of approximately 70 m (*Zwally et al.*, 2008; *Yi et al.*, 2011). Afterwards, a relative elevation is derived from the difference between the measured surface elevation and its 20 km running mean. This procedure avoids the contamination of the signal by inaccuracies of tide models and the geoid. Finally, the sea ice freeboard is the difference between the relative elevation and the ocean reference level, computed from the 2 $\%$ of lowest elevations, which are considered as leads or thin ice (*Zwally et al.*, 2008). From the calculated freeboard (F) and the snow thickness (h_S), which is derived from AMSR-E (Advanced Microwave Scanning Radiometer for Earth Observing System) data[5], sea ice thicknesses (h_I) are determined by using Archimedes buoyancy principle:

$$h_I = \frac{\rho_W}{\rho_W - \rho_I} F - \frac{\rho_W - \rho_S}{\rho_W - \rho_I} h_S \tag{4.3}$$

with ρ_W = 1023.9 kg/m^3 as water density, ρ_S = 300 kg/m^3 as snow density and ρ_I = 915.1 kg/m^3 as sea ice density, respectively (*Zwally et al.*, 2008). Data are available for regions with SIC higher than 60 $\%$ to avoid difficulties with the occurrence of open ocean and with the low accuracies of snow measurements in regions with little sea ice. In addition, freeboards higher than 1 m are excluded from the calculation of gridded sea ice thicknesses to eliminate the influence of icebergs on the data (*Zwally et al.*, 2008). Furthermore, freeboards are interpolated onto a 50 x 50 km^2 grid by averaging all the data within a 35 km radius around the grid cell. If there are no data points within this radius, it is increased to 100 km (*Zwally et al.*, 2008). Finally, sea ice thicknesses are calculated on this grid.

Zwally et al. (2008) showed some first results of estimated sea ice thickness distributions from ICESat freeboard data in the Weddell Sea for areas with more than 60 $\%$ SIC. Figure 4.18 shows their results for data gained from survey periods during

[5]According to *Zwally et al.* (2008), snow depth on sea ice is derived by using an algorithm after *Markus & Cavalieri* (1998), applied on AMSR-E data by *Comiso et al.* (2003).

May/June (MJ) and October/November (ON) in 2004 and 2005. For the MJ phase, sea ice with up to 6 m was mainly situated in the western region adjacent to the coast of the Antarctic Peninsula. It was transported to the north-eastern boundaries of the ice covered areas so that thick sea ice is also found along the sea ice edge. Since it was mixed with the thinner sea ice from the central Weddell Sea and was transported to areas with less than 60 % SIC, the thick sea ice does not appear as dense and as thick as it is observed in the western Weddell Sea. In the south and along the eastern coast, sea ice with thicknesses of about 2 m can be observed. The central Weddell Sea and the northern parts had less thick sea ice with values between 0 and 1.5 m. In both years, the distribution was fairly similar. Areal averaged sea ice thicknesses

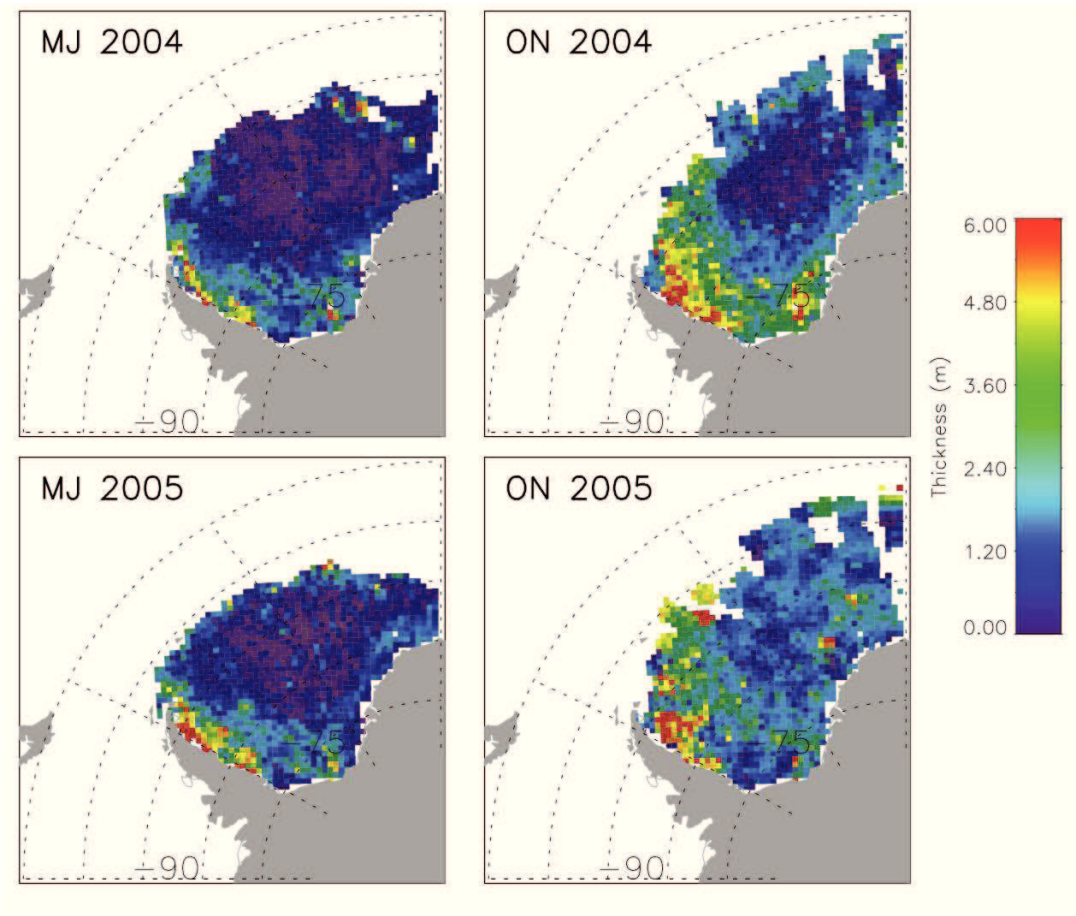

Fig. 4.18: *Mean May/June (MJ) and October/November (ON) sea ice thickness distribution for 2004 and 2005 from ICESat freeboard measurements on a 50 x 50 km^2 grid. Figure from Zwally et al. (2008), published in 2008 and modified by permission of American Geophysical Union.*

were 1.33 and 1.52 m for 2004 and 2005 for the sea ice covered area between 298^o and 360^{o}E, and the mean sea ice volumes were 5069 and 5095 km^3, respectively.

The ON distributions in both years were not as similar as the MJ ones. In 2004, the central Weddell Sea had a clear thin-ice signature, while the thick sea ice was situated

in the southern and western parts of the Weddell Sea, adjacent to the coast and near the sea ice edge. In 2005, the thickest sea ice still occurred along the coast of the Antarctic Peninsula, but also the rest of the Weddell Sea was covered by fairly thick sea ice. Areal averaged sea ice thicknesses were 2.23 and 2.31 m, respectively. With an ice covered area of 3.82 and 3.78 million km^2, this resulted in a volume of 8574 and 8758 km^3. The study of *Zwally et al.* (2008) showed that ON sea ice volumes are about 70 % higher than those in MJ.

Figure 4.19 shows the modelled sea ice thickness distributions for MJ and ON 2004 and 2005 to compare it with the satellite-based sea ice thickness data. The thickest sea ice in the model simulation occurs at the southern coast, with sea ice of up to 3 m thickness. In MJ, the thicker sea ice expands slightly to the Antarctic Peninsula, but it is far away from the regions, where satellite data show the thickest sea ice. Areal

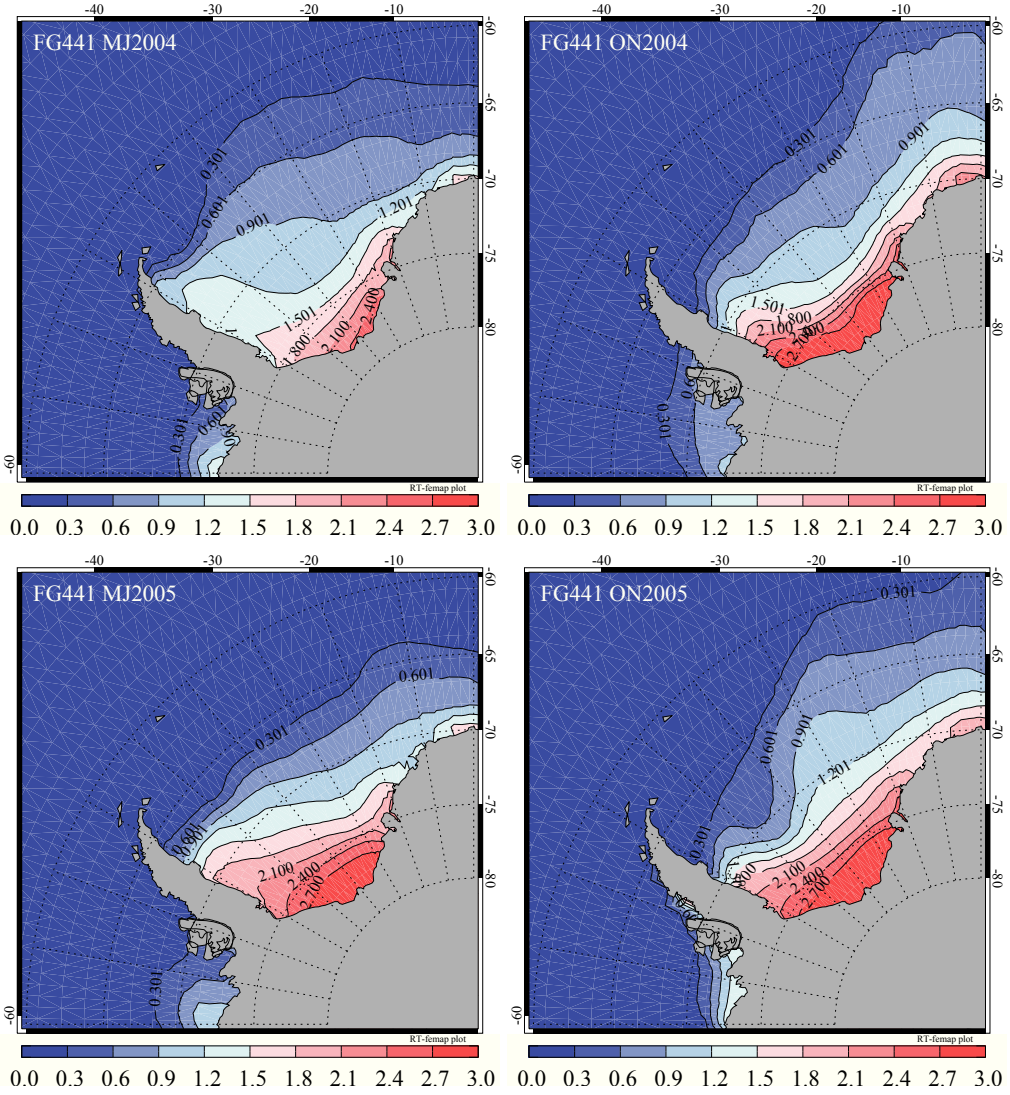

Fig. 4.19: *Modelled mean May/June (MJ) and October/November (ON) sea ice thickness distributions in m for 2004 and 2005 from FESOM.*

averaged MJ sea ice thicknesses are with 1.43 and 1.58 m for 2004 and 2005 a bit higher than those from ICESat data. Together with an ice covered area of 3.54 and 3.14 million km^2, a sea ice volume of 5053 and 4978 km^3 is simulated in those years, respectively. This is in a good agreement with the sea ice volumes observed by *Zwally et al.* (2008) for the MJ period. The year to year tendency is also well represented by the model: while the areal averaged sea ice thickness increase from 2004 till 2005, ice covered area shrinks for the same time. The major difference is that the ice covered area decreases much stronger in FESOM than observations indicate. Therefore, the observed slight increase of the sea ice volume is not captured by the model; it shows a decrease of sea ice volume from 2004 till 2005.

Modelled ON areal averaged sea ice thicknesses for both years (1.32 m and 1.63 m) are underestimated, and in addition, the increase of sea ice thicknesses from MJ to ON indicated by ICESat observations is not represented by FESOM. Due to this fact, sea ice volume is strongly underestimated, it is only 6602 and 5438 km^3, respectively, and therefore only about 30 % (2004) and 10 % (2005) higher than in MJ. The reduction of ice covered area from ON 2004 till ON 2005 and the ice covered area in 2005 itself are captured by FESOM, while the sea ice coverage in 2004 is strongly overestimated. For that reason, changes in sea ice volume from ON 2004 till ON 2005 show the opposite direction.

More recently, *Yi et al.* (2011) analyzed the sea ice thickness distribution from ICESat freeboards for the period from 2003 till 2009. The methods to calculate sea ice thicknesses are generally the same as described in *Zwally et al.* (2008), but the grid resolution is a bit finer with 25 x 25 km^2 in the study of *Yi et al.* (2011). These ICESat data show a seasonal cycle for the areal averaged sea ice thickness with generally low values in the beginning of winter (MJ). Until spring (OND), the areal averaged sea ice thickness grows up but decreases again in summer (FM)[6]. Model simulations show a seasonal cycle for the areal averaged sea ice thickness too, which is comparatively low in winter, as for ICESat data, but shows the highest value in summer (FM) instead of spring (ON). Areal averaged sea ice thickness starts to rise in November and reach its maximum in February, when only little thin sea ice is present in the model simulations and most of the sea ice is the thick ice that is located in the south of the Weddell Sea and becomes second-year ice. Discrepancies in the seasonal cycle appear because of different reasons, depending on the season. In FM, FESOM shows only very little thin sea ice within the 60% SIC boundary, while the

[6]Summer areal averaged sea ice thicknesses are higher than those in winter (*Worby et al.*, 2008). This is because most of the thin sea ice melts during summer and only the thick sea ice survives during this period (*Worby et al.*, 2008; *Yi et al.*, 2011). Averaged over the ice covered area, which is comparatively low in summer, sea ice thicknesses are therefore high in summer and lower in winter.

ICESat data still indicate the presence of much more thin sea ice (see *Yi et al.*, 2011 Fig. 4). The ON discrepancies occur certainly due to two different effects. On the one hand, winter sea ice growth is often delayed in the model, as already described in Section 4.3.1. Therefore, sea ice thickness reached by thermodynamic growth is smaller than it would be with an earlier start of the growth season. Another reason might be the underestimated deformation in coastal regions (also discussed in Section 4.3.1). Consequently, areal averaged sea ice thickness in October is dominated by the thin, newly formed as well as by only thermodynamically grown sea ice, resulting in an underestimation of its thickness. However, the increase from October over November and December is also present in the ICESat data indicated by the ND 2008 areal averaged sea ice thickness in *Yi et al.* (2011), which is with 2.86 m higher than all ON areal averaged values for all the years before.

The comparison of sea ice volumes between FESOM and ICESat data for the years 2004 and 2005 revealed that FESOM's winter sea ice volume is represented well for these years, despite the differences in the areal averaged sea ice thickness. *Yi et al.* (2011) analyzed sea ice volume changes for the entire ICESat data period from 2003 till 2009. They found a slightly increasing (but not significant) trend of 7 $\pm$ 92 km^3 per year for their data with peak-to-peak amplitudes of 7000 km^3 for the seasonal cycle. The maximum peak-to-peak amplitude of the seasonal cycle in FESOM is about 8000 km^3 for the same time period, as displayed in Figure 4.20a. The variability

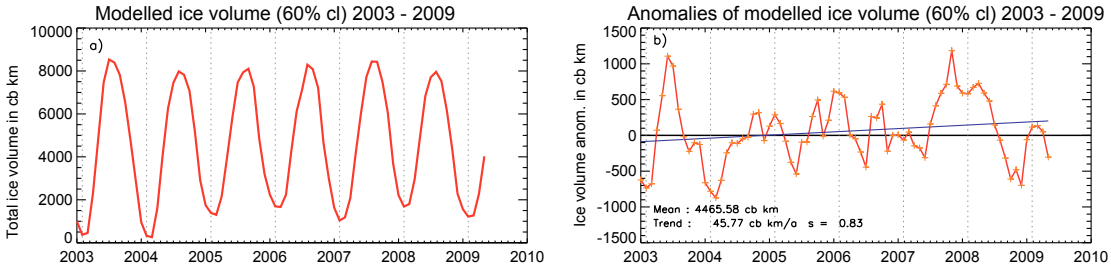

Fig. 4.20: *Monthly mean simulated sea ice volume and its anomalies in km^3 for the period from January 2003 till May 2009, corresponding to the ICESat period.*

of the modelled seasonal cycle is much stronger than that of the sinusoidal fit[7] in the study of *Yi et al.* (2011). Minima and maxima vary by several hundreds of km^3 over the years in the model simulation, while the function fitted volume in *Yi et al.* (2011) shows only very small variations from year to year in both maxima as well as minima. FESOM indicates a slightly positive trend of 46 $\pm$ 28 km^3 (about 1$\%$) per year for the

[7]Since ICESat measurements are only performed during distinct observation periods, there is no year-round coverage of sea ice thickness data and therefore, *Yi et al.* (2011) used a sinusoidal function to fit the sea ice volume time series.

sea ice volume for the 6 year period from 2003 till 2009, but as for ICESat data, the trend is statistically not significant at the 95 $\%$ confidence level.

4.3.3 Sensitivity studies

To improve the results from the standard model run (conducted with NCEP reanalysis data), tests were performed to analyze the effect of the ice strength parameter P^* and the lateral melting of the ice, individually. For the ice strength parameter test, P^* was set to 15000 N/m^2 instead of its standard value of 20000 N/m^2. Due to this change, sea ice is generally thicker in the simulations. In most cases, a comparison with ULS data results in slightly but not notably higher slopes in the scatterplots comparable to Figure 4.16. Varying the lateral melting of the sea ice also reveals only very small changes, which are not able to present a general solution. To test the effect of the lead closing parameter, which is set to h_0 = 1.0 m in the standard model run, two experiments were additionally performed: (i) h_0 = 0.5 m and (ii) h_0 = 1.5 m. In the first case (h_0 = 0.5 m), model simulations underestimate the sea ice thicknesses stronger than in the standard run. The underestimation is developed even along the Greenwich Meridian, where sea ice thicknesses are generally well represented in the standard model run. The second experiment, using a lead closing parameter of h_0 = 1.5 m, generally results in much thicker sea ice in the Weddell Sea, especially in the southern parts. Near the Antarctic Peninsula, differences between the modelled and the measured sea ice thicknesses decrease slightly from -90.3 $\%$ and -77.5 $\%$ at ULS 207 and ULS 217, respectively, to -88.6 $\%$ and -72.7 $\%$. However, at the Greenwich Meridian, simulated sea ice thicknesses overestimate the *in-situ* data by up to 80 $\%$. Furthermore, the sea ice thickness distribution did not change significantly compared to the standard model run. Hence, increasing the lead closing parameter results only in a slight improvement of sea ice thicknesses in the western Weddell Sea, but not in a general improvement in the sea ice thickness distribution. Additionally, at the Greenwich Meridian, an increased lead closing parameter might degrade the good agreement between ULS-based measurements and model results, i.e. a strong overestimation of sea ice thicknesses by model simulations might occur.

To investigate whether the specific configuration of the standard model run with FESOM is responsible for the observed shortcomings, results from another model version with a finer grid resolution (1.3^o x 1.3$^o cos\phi$), CORE-2 forcing data[8] instead

[8]The CORE-II reanalysis data are based on NCEP reanalyses, but include some adjustments with respect to air temperature, wind speed, humidity and solar radiation, following comparisons with observational data (*Large & Yeager*, 2008).

of NCEP reanalysis, and different details of the numerical implementation of the ocean component (Q. Wang, *personal communication*, 2011) were analyzed. Two experiments with lead closing parameters (h_0) of 0.5 m and 1 m were performed. For some years, actually, results are slightly better. However, these better results only occur sporadically and for some years results also differ much more from observations than results from the standard model run. Although the thickest sea ice is still located in the south-eastern region, the finer resolution leads to a more structured sea ice thickness distribution. This distribution differs from results of the standard model run and represents the satellite-based sea ice thickness distribution actually sometimes better, but in most cases it is only different and still does not describe the observed distribution. Furthermore, sea ice thicknesses are in most cases lower than those modelled with the NCEP reanalysis data. Especially at the northern part of the Antarctic Peninsula, the CORE-II runs often show less or even no sea ice, which is not observed in the ICESat data and is not shown in the standard run. For both forcings, SIE is often not well represented, compared to satellite-based data and therefore there is potentially very little difference between both model realizations with respect to sea ice volume fluxes.

Additionally, also results from BRIOS were analyzed, but it was found that thickness distributions are nearly the same with the thick sea ice situated in the south-eastern regions and too little (thick) sea ice along the Antarctic Peninsula, especially in summer. However, BRIOS uses the same forcing data and a similarly coarse resolution as FESOM. Hence, the right realization of the sea ice thickness distribution in the Weddell Sea seem to be a general challenge for the present models and still needs improvements. At the tip of the Antarctic Peninsula, deficiencies might especially be forced by the weak representation of the topography of the Antarctic Peninsula in the reanalysis data (*Windmüller*, 1997). An improvement of the simulated sea ice thickness distribution in this region would then require an improved atmospheric forcing data set.

4.4 Discussion

The last section showed the inaccuracies and uncertainties of modelled sea ice thicknesses from FESOM and models with similar physics. Simulated sea ice thicknesses are underestimated in many cases, especially near the tip of the Antarctic Peninsula. As explained in Section 4.3.1, ULS data might be biased towards higher thicknesses because of the beam spreading and the timing of the echo signal. Therefore, *Strass* (1998) suggested a bias correction of -11.5 %, based on

comparisons of sea ice draft measurements through bore holes, performed in 1989 and 1992 in the Weddell Sea, near the ULS sides. The comparison was based only on few sea ice thickness measurements, but is supposed to be representative for the entire Weddell Sea. Nevertheless, to avoid undefined uncertainties, no bias was considered for the comparison with the model data in this study. Since a bias to higher values in the ULS data is actually most likely, a comparison between the standard run output and ULS measurements with bias correction of -11.5 % was performed to gain the influence that a correction would have. The tests proved that correlation coefficients for the different regions discussed in Section 4.3.1 are the same, but slopes are (as expected) a little bit higher. Nevertheless, the bias correction does not change results significantly. The highest improvement occurred for the Greenwich Meridian (excluding ULS 233), where the slope increased from 0.731 to 0.826, i.e. sea ice thicknesses are less strongly underestimated. However, when excluding the near-coast data of ULS 232, the slope increased from 1.04 to 1.176. This means that in cases of a slight overestimation of simulated sea ice thicknesses, a bias correction of the ULS data would lead to a stronger overestimation on the side of the simulated sea ice thicknesses.

A related point that has to be considered, when comparing ULS data and model simulations is that the ULSs measure the modal sea ice draft, which is translated into a modal sea ice thickness. This means that an ULS stores the most frequent sea ice thickness within the footprint. The model, on the other side, calculates mean sea ice thicknesses. Therefore, it cannot be expected that the comparison between both data sets results in an optimal agreement. However, here we suggested that the mean and the modal value can be compared, since the difference between both is not expected to be high enough within the given footprints to change the results (see Appendix D for detailed description).

ULS data cannot be used to validate trends assessed from model simulations, since their time series have too many gaps. But also with the longer and sinusoidal fitted ICESat time series of *Yi et al.* (2011), an evaluation of trends is not easy, since only the ON measurements are consistent over all years. In general, there are some agreements between model simulations and data, but there are also serious discrepancies. For example, the general interannual variability of the areal averaged sea ice thicknesses in ON is captured by the model, but their magnitudes are strongly underestimated. However, for a statistical analysis of discrepancies between model simulations and satellite-based sea ice thickness data, the time span of the ICESat data is too short. This comparison only gives an estimation of model accuracy. Winter areal averaged sea ice thicknesses are in a good agreement and at least spring variability is captured, but the general distribution of thick sea ice is not represented

well in FESOM.

Anyway, one has to consider that ICESat data suffer from inaccuracies. The fact that the ocean reference level is analyzed by using the values of the 2 % lowest elevation measurements, assuming that these represent leads, might result in an underestimation of sea ice thicknesses in regions with no leads (*Zwally et al.*, 2008). Furthermore, snow wetness influences the backscatter signals and biases the measured snow thickness to smaller values (*Zwally et al.*, 2008). This means that a higher portion of the total (snow + sea ice) freeboard is expected to be sea ice, and therefore, spring and summer sea ice thickness might be overestimated, since the snow wetness occurs mainly during those months. This may partly explain the huge differences of the areal averaged sea ice thickness between ICESat data and model simulations for the ON periods. *Yi et al.* (2011) assumed a general uncertainty of about 58 cm for their sea ice thicknesses due to uncertainties in snow depth (about 5 cm), freeboard measurement (about 5 cm) and due to the fixed densities for water, sea ice and snow.

Very interesting is the fact that areal averaged sea ice thicknesses for 2004 and 2005 differed in the studies of *Zwally et al.* (2008) and *Yi et al.* (2011), although the data processing was generally the same (aside from the grid resolution). The differences are only few cm except for MJ 2005, when it is 15 cm. Either way, this discrepancy in the ICESat data does not change the general results in a comparison with FESOM simulations.

In terms of areal averaged sea ice thicknesses, the MJ areal averaged sea ice thicknesses are best represented in the model. Before and after, i.e. in MA and OND, results are worse, but the lowest agreement occurs for the FM period, when ICESat areal averaged sea ice thicknesses are much smaller than those simulated by FESOM and the interannual variability of the model does not follow that indicated by the ICESat data. Also the winter (MJ) sea ice volume is in a good agreement for the years 2004 and 2005, while the ON volume is strongly underestimated, compared to the ICESat data. However, the overall tendency of the variability is reproduced in FESOM and also some extrema are given correctly, as for example the winter maximum in 2003 and the very low winter maximum in 2007. For both ICESat data as well as model simulations, an insignificant positive trend of sea ice volume was found, with the trend in FESOM being somewhat larger than the ICESat trend.

Chapter 5

Sea ice drift

Sea ice dynamics influences the state of the atmosphere - sea ice - ocean system and is therefore an important factor that has to be considered when analyzing sea ice changes. For example, during sea ice formation, salt is released into the ocean and modifies its density structure in the region of formation (*Venegas & Drinkwater*, 2001). Since sea ice can get advected from these regions, freshwater is exported and influences additionally the density structure in regions of melting, in particular, when thermodynamical growth of sea ice usually does not take place in those regions. Moreover, the heat exchange between the ocean and the atmosphere and the regional albedo are modified due to the movement of sea ice. When divergent drift opens leads in winter, these openings in the sea ice cover experience a growth of new sea ice due to the high exchange of heat between the relatively warm ocean and the cold atmosphere. In summer, in turn, divergent sea ice drift induces faster melt of sea ice due to the absorption of energy, since the water in the leads has a much lower albedo than sea ice and snow. When sea ice drift is convergent, like in the western Weddell Sea due to the obstruction of sea ice drift by the Antarctic Peninsula (*Turner et al.*, 2002), sea ice can become much thicker than by thermodynamic growth alone and may survive a summer melt period, becoming second year ice. Hence, sea ice motion influences the sea ice thickness distribution (*Harder & Fischer*, 1999) as well as the total sea ice volume. Therefore, the dynamics of sea ice has to be known to better understand its influence on sea ice distribution and related climatic impacts. This chapter discusses sea ice drift velocities derived from drifting buoys (Section 5.1) and satellite data (Section 5.2). Satellite-based large-scale sea ice drift was validated by the small-scale buoy data and results are shown in Section 5.2 together with the general drift regime as well as its trends. In addition, also FESOM model simulations are compared to small-scale buoy drift. Furthermore, the simulated drift regime as well as its trends are compared to the Polar Pathfinder sea ice motion vectors from the NSIDC (Section 5.3). The chapter closes with a sensitivity study of modelled sea ice drift (Section 5.3.3) and a discussion.

5.1 Buoy-derived sea ice drift velocities

In the Weddell Sea, floatable, ice-strengthened drift buoys have been deployed on sea ice floes for several years between 1986 and 2005 in conjunction with different projects, such as the Winter Weddell Sea Project in 1986 or the Winter Weddell Gyre Studies in 1989 and 1992 (*Kottmeier et al.*, 1996), to investigate the motion of sea ice. Sea ice buoys are generally equipped with different sensors to measure various physical properties such as air pressure, air temperature and wind speed. The sketch in Figure 5.1 shows an example of a sea ice buoy. It includes an anemometer at a height of about 2 m to measure both wind speeds and their directions as well as radiation-shielded sensors (thermistors) for air and surface temperature measurements in a self-aspirated housing (*Kottmeier & Hartig*, 1990; *Kottmeier et al.*, 1996). Also included in this housing is a pressure-sensitive quartz crystal resonator (*Kottmeier & Hartig*, 1990; *Hoeber & Gube-Lehnhardt*, 1987) for detecting air pressure changes. For the determination of ocean currents underneath the sea ice, a current meter in about 10 m depth can be deployed.

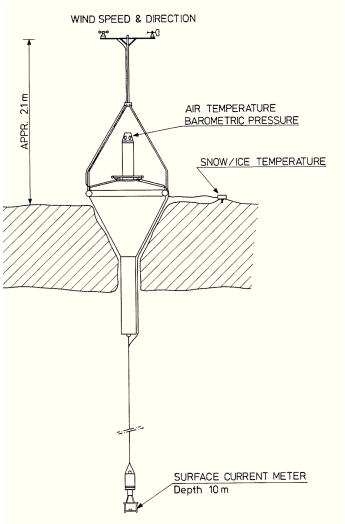

Fig. 5.1: *Scheme of a drift buoy from Hoeber & Gube-Lehnhardt (1987)*

The measured data are collected and transmitted as packages to the Argos satellite communication system (*Argos Collect Localisation Satellites Company*, 2008), usually several times per day. The transmitted signal is dated and the received frequency is recorded. This information is necessary to determine the position of a buoy, which is calculated by using Doppler range finding. Due to the Doppler effect, the frequency that is received by the satellite has changed compared to the transmitted signal, because of the movements of the satellite itself and the buoy. When the satellite (receiver) is moving towards the buoy (transmitter) position, the frequency of the signal reaching the satellite is higher than the transmitted

frequency and it is lower, when the receiver is moving away. The frequency ν' of the electromagnetic wave, that is received by the satellite, moving towards the buoy, is given as

$$\nu' = \frac{\nu_0}{1 - v/c} \cdot \frac{1}{\gamma} = \frac{\sqrt{1 - v^2/c^2}}{1 - v^2/c^2}\nu_0 = \sqrt{\frac{1 + v/c}{1 - v/c}}\nu_0 \tag{5.1}$$

γ is the time dilation and v the relative velocity between satellite and buoy. If the satellite moves away from the buoy, the received frequency ν' is given as

$$\nu' = \frac{\sqrt{1 - v^2/c^2}}{1 + v^2/c^2}\nu_0 = \sqrt{\frac{1 - v/c}{1 + v/c}}\nu_0. \tag{5.2}$$

Since the relative velocity is much smaller than the velocity of light, the time dilation can be neglected and Equations 5.1 and 5.2 can be simplified to:

$$\nu' = \frac{\nu}{1 - v/c} \quad \text{(B and S converge)} \tag{5.3}$$

$$\nu' = \frac{\nu}{1 + v/c} \quad \text{(B and S depart)} \tag{5.4}$$

Because of the known transmitted and received frequencies, possible positions for the buoy can be calculated. These positions are described by a cone defined by a vertex, whose angle depends on the difference between the frequencies (*Argos Collect Localisation Satellites Company*, 2008). After four received data packages, the location calculation process starts and the positions of the buoy are derived. These positions are provided to the users, together with information of the different meteorological sensors. For further details on the position processing and used plausibility tests see *Argos Collect Localisation Satellites Company* (2008).

The accuracy of the buoy positions is approximately 150 to 500 m (*Kottmeier & Hartig*, 1990; *Emery et al.*, 1997; *Heil et al.*, 2001; *Argos Collect Localisation Satellites Company*, 2008), depending on buoy properties such as its movements as well as the oscillator stability of its transmitter, but also on satellite properties such as its pass geometry and inaccuracies of its ephemeris (*Kottmeier & Hartig*, 1990; *Kottmeier et al.*, 1996). Newer buoys are equipped with GPS receivers, resulting in spatial inaccuracies of less than 50 m (*Kottmeier & Sellmann*, 1996; *Heil et al.*, 2001). GPS receivers have the advantage that they are independent of transmitter quality and that they are collected at a higher rate per day (*Argos Collect Localisation Satellites Company*, 2008). From the given range of precision for buoy positions, *Heil et al.* (2001) and *Harder & Fischer* (1999) calculated accuracies of approximately 0.005 to 0.006 m/s for daily sea ice drift velocities derived from drifting buoy position changes.

With the calculated position data and the corresponding times it is possible to determine sea ice drift vectors between two sequential position records. 17 years of sea ice drift buoy data from the Alfred Wegener Institute, available on the Pangaea webpage (http://www.pangaea.de/search?count=108Jq=Buoy+Weddell+sea++) and from the International Program of Antarctic Buoys (IPAB) were used in this study over the period from 1989 till 2005. Data with irregular temporal resolution were projected onto a regular hourly time grid, with the exception for data since 2001, which are available for a temporal resolution of only 3 hours. Smaller data gaps in the position recordings were linearly interpolated for this study.

Figure 5.2a shows the start positions for all operation years between 1989 and 2005, which are colour-coded regarding the year of deployment. In most years, at least 3 buoys were deployed, which drifted for several months up to a few years, depending on the sea ice conditions, and followed the general sea ice drift regime. Additionally, in Figure 5.2b the same data are colour-coded regarding the start month of their deployment, to indicate the seasonal bias for specific regions. For example, buoys in the southern Weddell Sea were deployed only during the summer months (January - March), when the region was accessible by ships. The spatial distribution of the

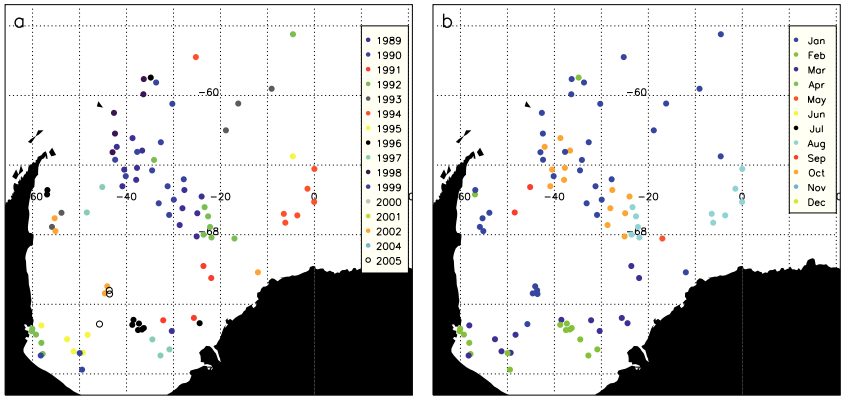

Fig. 5.2: *Buoy start positions separated according to a) years and b) months. Data from IPAB and Pangaea (Haas & Kottmeier, 2003).*

buoys seems to be fairly balanced across the study area (Fig. 5.2), but since the measurements were conducted at different parts of the Weddell Sea in different years, the observation of any trends in sea ice drift or the variability in specific regions is difficult. However, to give a first impression on the general sea ice drift regimes in different sections of the Weddell Sea, buoy tracks are shown in Figure 5.3 for all deployments between 1989 and 2005.

Generally, the buoy data indicate that sea ice drift is dominantly directed to the north in the south-western Weddell Sea (see e.g. 1992, 1995 and 1999). When buoys were

deployed in the central (e.g. in 1989, 1996 and 1997) or south-eastern Weddell Sea (e.g. in 1996 and 2004), they followed a c-shape with initial westward sea ice drift in the southern-most regions, followed by northward sea ice drift and a deflection to the north-east, when they reached the northern parts of the Weddell Sea. Deployments

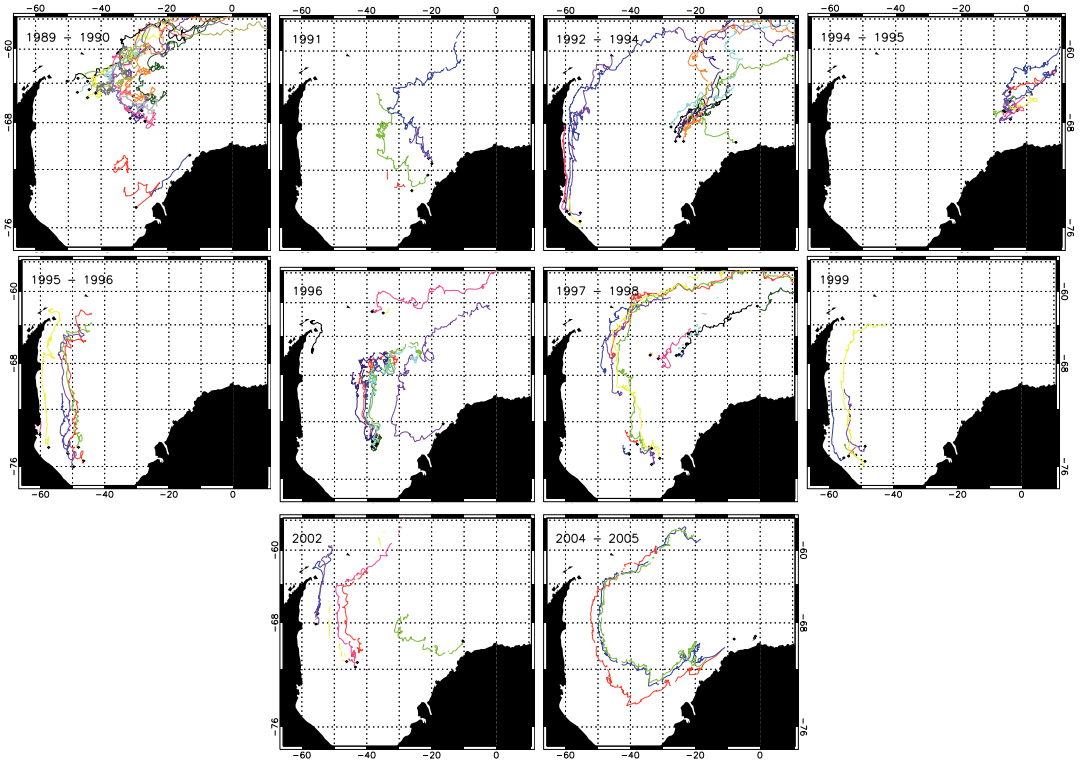

Fig. 5.3: *Yearly buoy distribution with sea ice drift tracks. Data from IPAB and Pangaea.*

in the north-eastern part of the Weddell Sea result in north-eastward drift, as can be seen in Figure 5.3 for the year 1994. The prevailing drift regime found here agrees with the geostrophic wind patterns described in Chapter 2 and shows, how strong the mean sea ice drift depends on the wind field, as mentioned by several authors (e.g. *Kwok & Comiso*, 2002b; *Serreze et al.*, 1989).

Although buoys can describe the general sea ice drift regime and some areas have been repeatedly investigated, interannual, seasonal or long-term variations cannot be studied by using these buoy data, since the coverage is too sparse and too variable in space and time. For an analysis of the mean sea ice drift behaviour, the variability and the sea ice drift changes, basin wide and regular coverage of the area of interest is necessary. Satellite-based data and model simulations meet these requirements. The buoy data, however, can be used to evaluate the drift of the large-scale products from satellite observations and model simulations to determine the reliability of these products.

5.2 Satellite-derived sea ice drift

Satellite-derived Polar Pathfinder sea ice motion vectors, obtained from the NSIDC (http://nsidc.org/data/nsidc-0116.html, *Fowler*, 2003) are presented in this section. First of all, a short explanation is given, how sea ice drift velocities were derived before they have been provided by the NSIDC. Afterwards, it is shown, how the accuracies of the sea ice motion fields were tested by comparing them to the satellite-based raw data and to the Lagrangian tracks of drifting-buoys. The section closes with an interpretation of the changes in sea ice drift velocities and their potential relation to SIC trends in different regions and seasons in the Weddell Sea.

5.2.1 How to determine sea ice drift velocities from satellites

Sea ice drift velocities were calculated by using the maximum cross correlation (CCM) method described by *Ninnis et al.* (1986) and *Emery et al.* (1991). The basic principle is to divide two sequential images into smaller areas spanning a couple of pixels, whereas the former image (template) is divided into smaller areas with less pixels than the subsequent image (search window). Afterwards, a search for the highest cross-correlation between each template and search window is performed. The center of the search window with the highest correlation is taken as the end position of a drift vector (*Emery et al.*, 1991). For the calculation of the cross-correlation, the means of the template $f(x, y)$ and search window $g(x, y)$ are subtracted from the respective function and the variances

$$\sigma_f^2 = r_{ff}(0, 0) \tag{5.5}$$

$$\sigma_g^2 = r_{gg}(0, 0) \tag{5.6}$$

are computed with the auto-covariance function

$$r_{ff}(x', y') = E[(f(x, y) - m_f)(f(x + x', y + y') - m_f)] \tag{5.7}$$

(E[ ] is the expectation value) and the signal means

$$m_f = E[f(x, y)] \tag{5.8}$$

$$m_g = E[g(x, y)], \tag{5.9}$$

whereby a vector lag relates $f(x, y)$ and $g(x, y)$:

$$f(x, y) = g(x + x_0, y + y_0). \tag{5.10}$$

Former versions (e.g. in *Ninnis et al.*, 1986) used as next step the Fast Fourier Transformations (FFT) of $f(x, y)$ and $g(x, y)$ to reduce computation time. Since this processing step can only be performed with constant and rectangular windows, coastal regions and cloud contaminated images could not be used for the maximum cross-correlation method (*Emery et al.*, 1991). Therefore, for newer sea ice drift products the cross-correlation

$$\rho(x, y) = \frac{r_{fg}(x, y)}{\sqrt{\sigma_f^2 \sigma_g^2}} \tag{5.11}$$

is calculated directly, without FFT, with r_{fg} being the cross-covariance function

$$r_{fg}(x', y') = E[(f(x, y) - m_f)(g(x + x', y + y') - m_g)]. \tag{5.12}$$

This approach allows for excluding coastal regions and also for masking out cloud coverage in AVHRR data (*Emery et al.*, 1991).

At the position (x_0, y_0) the cross-covariance is given as

$$r_{fg}(x_0, y_0) = E[(f(x, y) - m_f)(g(x + x_0, y + y_0) - m_f)] \tag{5.13}$$

and with equation 5.10 this leads to

$$r_{fg}(x_0, y_0) = E[(f(x, y) - m_f)^2] = r_{ff}(0, 0) \tag{5.14}$$

and finally to the cross correlation

$$\rho(x_0, y_0) = \frac{r_{fg}(x_0, y_0)}{\sqrt{\sigma_f^2}\sqrt{\sigma_g^2}}, \tag{5.15}$$

where σ_g^2 at lag (x_0, y_0) is equal to σ_f^2 for the ideal case. In this case, $\rho(x_0, y_0)$ would be equal to one, but since the signals are only partly correlated, this value is lower in reality. Finally, the part of the cross-correlation from $f_w(x, y)$ positions, which lie entirely inside the window of $g_w(x, y)$ is extracted and the highest value is located (*Ninnis et al.*, 1986). Displacements with a correlation of less than 0.4 are disregarded to avoid statistically insignificant drift velocities. *Emery et al.* (1986) stated that all correlation coefficients higher than 0.393 are statistically significant at the 99 $\%$ confidence level for 40 degrees of freedom so that the value of 0.4 is well chosen. Because of an overlap of the search windows, the grid resolution of sea ice drift vectors can be increased, although this means, that the independence of neighbouring sea ice drift vectors is not any longer given (*Emery et al.*, 1991).

The size of the search windows is a crucial point. Too small search windows lead to a lack of statistical significance, while too large windows increase the value of smallest drift motion that can be detected (*Emery et al.*, 1991).

The data product used for this study is provided by the NSIDC as daily, weekly and monthly mean motion fields. It is a combination of sea ice drift vectors derived from the brightness temperature fields from both polarizations of the 37 GHz channel of the SMMR (January 1979 - July 1987) and the 37 GHz and 85.5 GHz channels of the SSM/I (August 1987 - December 2006), as well as from the thermal and visible channels of the Advanced Very High Resolution Radiometer (AVHRR, July 1981 - December 2000) (*Fowler*, 2003). For each sensor, daily composites of all satellite overpasses are created. The resulting mosaics are expected to give the mean daily values of the detected signal, which are centered at noon of each day. Then, after applying the maximum cross-correlation method to all sensors and polarizations, the derived sea ice drift vectors are merged to one sea ice drift field product and are interpolated via optimal interpolation (OI) methods to all areas with SIC higher than 50 % (*Fowler et al.*, 2001). For the calculation of monthly averages, at least 20 drift vectors of the OI daily sea ice motion have to be available (*Fowler*, 2003). Daily as well as monthly sea ice drift fields have a resolution of 25 x 25 km^2 and are georeferenced to an azimuthal equal area projection with positions given in Cartesian grid coordinates (*Fowler*, 2003). Differently to the data product for the Arctic, the Southern Ocean sea ice drift fields do not include any buoy data. So, the sea ice drift product is independent of them and therefore, buoy data can be used for the validation of the satellite-based sea ice motion.

5.2.2 Validation of the satellite-based sea ice drift vectors

To assess the reliability and the uncertainties of the OI sea ice motion fields, the velocity grids were compared to the original, not interpolated SSM/I, SMMR and AVHRR derived vectors and to drifting-buoy data. Figure 5.4 shows examples of the Polar Pathfinder sea ice motion fields. The original satellite-based sea ice drift vectors, derived via the CCM and used to calculate the OI sea ice drift fields, are added as monthly averages. However, since there are often only few original data points in one grid cell for one month, these averages can be more or less averages over only few days, and therefore, some large discrepancies between original data and OI vectors can occur (Fig. 5.4). As explained in Section 5.2.1, each monthly averaged grid cell of the combined data product is an average of at least 20 sea ice drift vectors of the daily mean sea ice drift fields. Indeed, these 20 drift vectors are

not necessarily derived from the original data but can come from the OI sea ice drift vectors, which are present at every grid cell with SIC higher than 50%. Consequently, large sea ice drift fields can be calculated based on only few original data points. As a result, differences between the original data points and the OI drift vectors can arise due to the fact that

1. an **original data point** might represent more or less daily variability instead of a monthly mean.
2. an **OI drift vector** has strongly been influenced by original data points from other regions, hence is more or less a product of spatial interpolation.

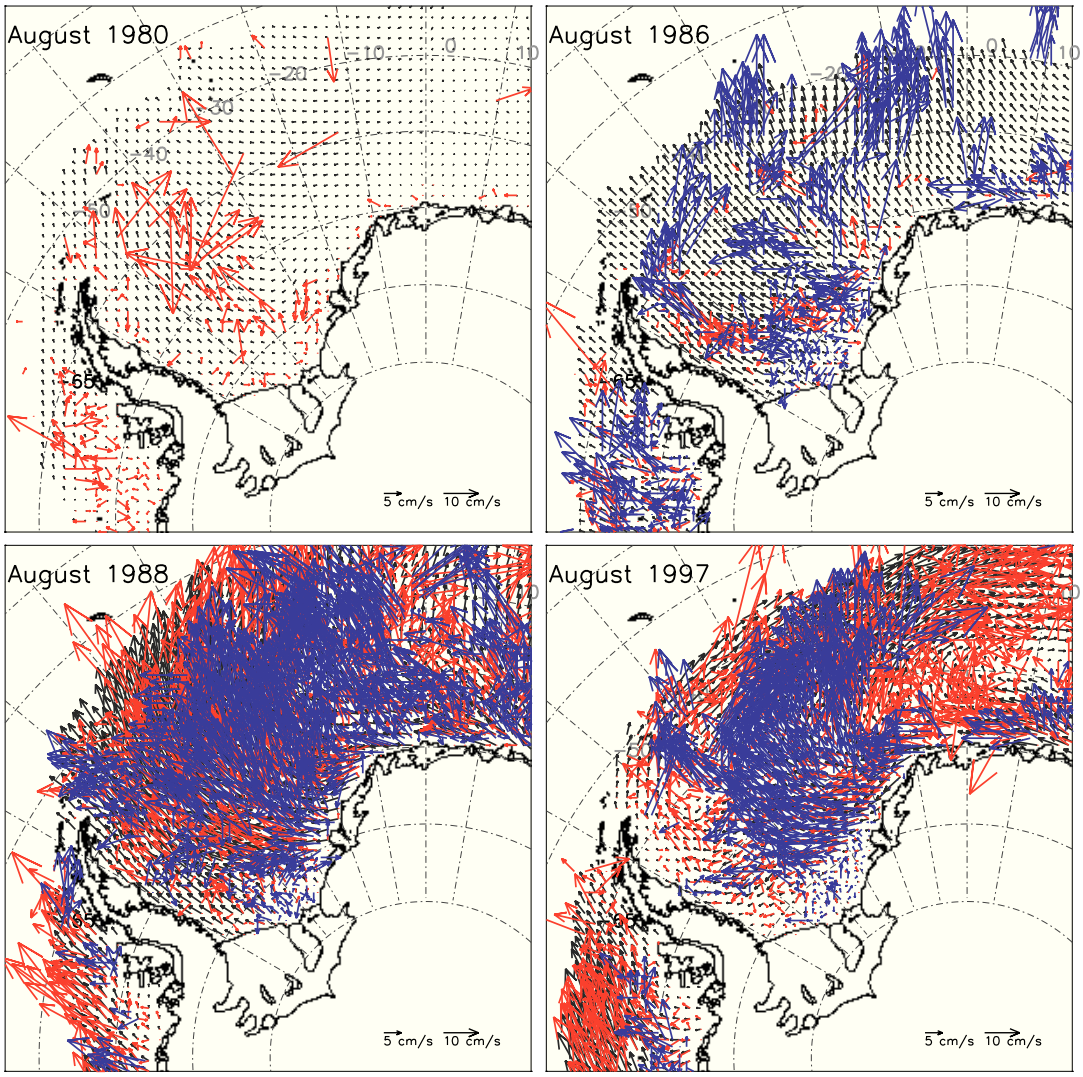

Fig. 5.4: *Example for satellite-based OI sea ice drift fields from the NSIDC in August 1980, 1986, 1988, and 1997 with overlying original monthly mean SSM/I (green) and AVHRR (blue) vectors.*

Figure 5.4 illustrates that the data coverage was very low in the beginning of the satellite era, even in austral winter, when less atmospheric disturbance such as

moisture or clouds and less changes in sea ice surface properties due to, e.g., melting perturb the measurements. In 1980, the August has only few original data points for the entire Weddell Sea. In the eastern regions, nearly no data are available and the sea ice drift field is a product of interpolated velocities from the western and central Weddell Sea. The OI vectors deviate often from the original data, since the original data are mostly averages over only a few days and additionally might be spatially interpolated over large-scales across the entire Weddell Sea. From Figure 5.5 can be seen that only some data points near the coast are averages of at least three days of original data. Smaller dots indicate that original data points were available for only one or two days throughout a month. Since austral winter 1981, AVHRR was able to fill some gaps of the SMMR fields and data coverage became much better (Fig. 5.5, August 1986). Nevertheless, since AVHRR data were mostly available for less then

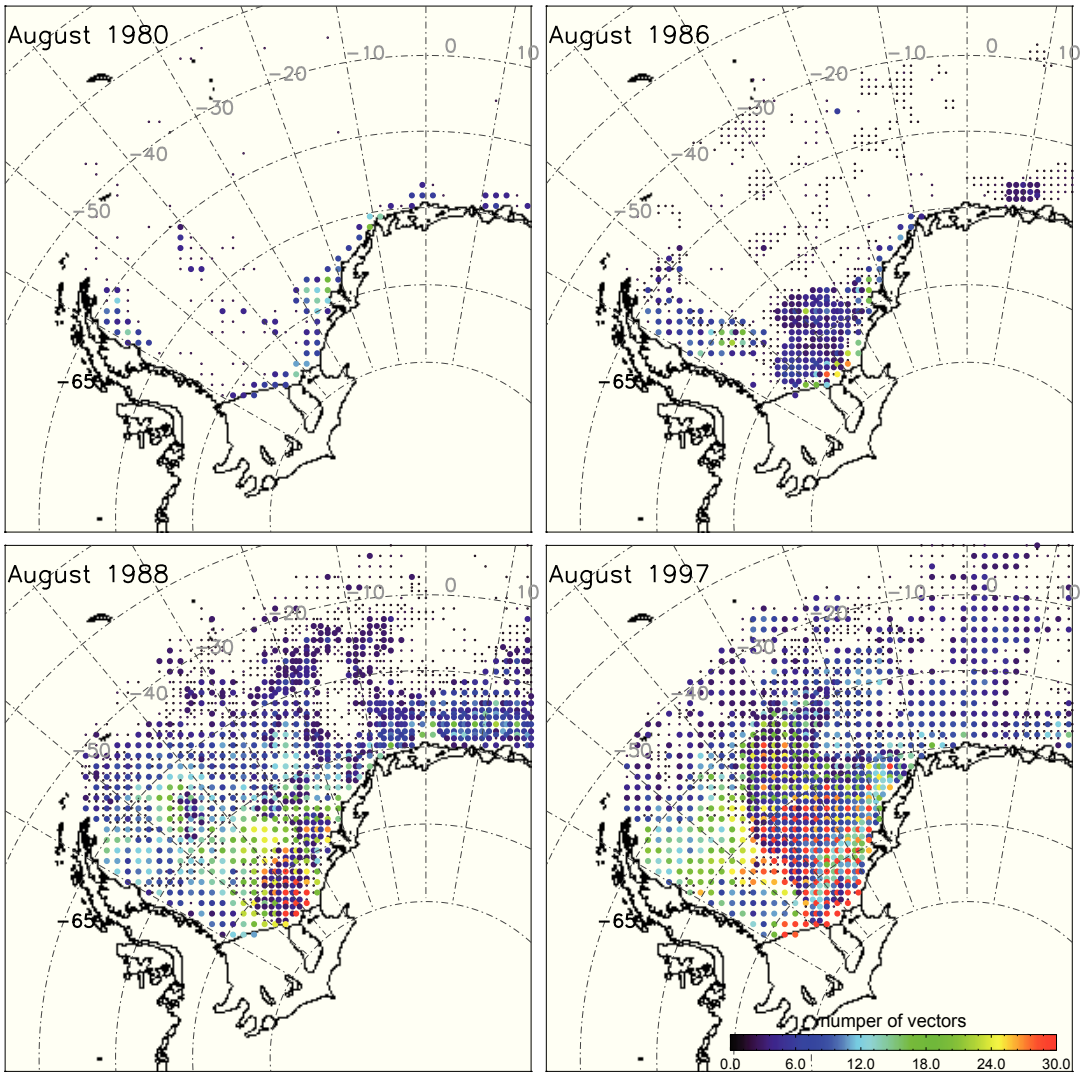

Fig. 5.5: *Example for original data coverage of the satellite-based sea ice motion in vectors per month for August 1980, 1986, 1988, and 1997 from SMMR-SSM/I and AVHRR data provided by the NSIDC.*

three days per grid cell (Fig. 5.4 and 5.5), high interpolations were still necessary.

As for 1980, in August 1986, only the coastal regions are covered with vectors which occur at least three times per month. At all other positions, OI drift velocities were calculated from the sporadically available original data points and their interpolation onto the sparsely covered regions. Since July 1987, when SMMR was replaced by SSM/I, daily data became available and in the following years, data coverage has expanded to nearly every region of the Weddell Sea and had a much higher repetition frequency (see Fig. 5.5, August 1988). In some regions, monthly averages are obtained from 30 days of original sea ice drift vectors. An improvement is hereby, that SSM/I covers the regions daily and has additionally the 85.5 GHz channel, which has a higher resolution than the 37 GHz channels. Unfortunately, austral summer data coverage is still low, and therefore, a usage of the summer sea ice drift velocities should be done carefully.

Figure 5.6 shows the temporal data coverage of the different satellites for the time 1979 (only SMMR), over the early 1980s (SMMR/AVHRR) and late 1980s through 2000 (SSM/I and AVHRR) and shows additionally the time 2001 through 2002, when only SSM/I data were used for this sea ice drift product. The total number of original SMMR-derived vectors (red, until 1987, Fig. 5.6a) was very low, although vectors were spread to daily data points so that their appearance is comparable to the daily data of SSM/I and AVHRR. Only the occurrence of AVHRR data (blue) since 1981 was able to fill some gaps, but in total, a data coverage of 4000 points per month was rarely obtained. The change from SMMR to SSM/I can be seen very well, since there is a sudden increase of data points per month in 1987. Noteworthy is that years with a generally low coverage since 1987 still had a higher amount of SSM/I data points than

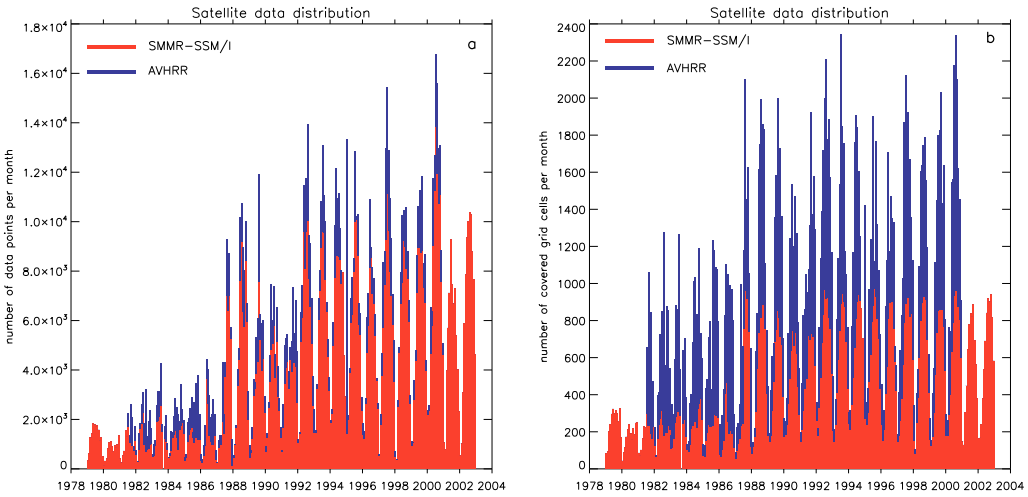

Fig. 5.6: *Total data coverage (a) and number of covered grid cells (b) from SMMR-SSM/I and AVHRR data provided by the NSIDC for the period January 1979 through December 2002.*

the combination of SMMR and AVHRR data in the years before. In addition to SSM/I, AVHRR data were available through December 2000, so that the winter months show a high original data coverage between the years 1987 through 2000.

The amount of grid cells covered by original vectors of the respective sensor per month is shown in Figure 5.6b. As in Figure 5.6a, the change from SMMR to SSM/I is clearly visible by a sudden increase in data coverage. The amount of grid cells covered by drift vectors obtained from AVHRR (blue) images is always fairly high in winter months, since the resolution of approximately 5 km is much higher than that of SMMR and SSM/I with 12.5 to 25 km. In addition, AVHRR data are mostly available for less than three days for individual grid cells but frequently over different areas of the Weddell Sea throughout a month. Thus, the small number of data points is distributed to a large number of grid cells. The reason for the low coverage in summer is that AVHRR is strongly affected by clouds (*Emery et al.*, 1991). Contrary to AVHRR data, the large amount of SSM/I data is distributed to less grid cells, but temporally more frequently. Therefore, it is unlikely that the quality of the satellite-based product has decreased after the withdrawal of AVHRR data in 2001, since AVHRR data gave only sporadic information.

The analysis of the data coverage indicates that sea ice drift fields before 1982 (the first year with complete AVHRR coverage) have high uncertainties, because of the interpolation of only few drift vectors onto large regions. In addition, data for 1983 look very unrealistic for some months, since drift velocities were very high in the entire Southern Ocean and they were all in the same direction in the Cartesian grid (not shown). Hence, the drift velocities from this data product seem to have very high uncertainties before 1984. However, also the years 1984 until 1987 have a low data coverage, even in winter. Since 1988 (the first year with complete SSM/I coverage), data coverage increased and a comparison with original vectors indicates that satellite-based sea ice drift fields are more reliable. Nevertheless, the data coverage does not show how reliable the sea ice drift fields in fact are and for that reason, daily sea ice motion is compared to Lagrangian buoy tracks for the years from 1989 till 2005, when the last sea ice drift data from buoys are available in the Weddell Sea for the considered period (1979-2006).

To compare the Lagrangian sea ice drift trajectories of the buoy data with the Eulerian sea ice drift fields from satellites (and later with model simulations), daily and monthly averages of both the zonal and the meridional sea ice drift component were computed. For daily means, all the buoy data between 0:00 and 23:59 were averaged for each day. Monthly means were created by averaging all the daily data files for the respective month. The satellite-derived sea ice drift velocity components of each available day

were interpolated onto the daily mean buoy positions and were rotated based upon their longitude (*Schwegmann et al.*, 2011). The last step was necessary, because the satellite-derived sea ice drift components are valid for a Cartesian coordinate system and therefore have to be transformed into vectors related to a geographic coordinate system. After that, daily satellite-derived sea ice drift components were subtracted from the daily averaged buoy-derived components. Statistical significance of differences and correlation coefficients was tested by using the students t-test described in Appendix E.

Figure 5.7a and b show the comparison of daily mean satellite- and buoy-derived zonal and meridional sea ice drift and the mean differences between both data sets on a yearly basis. Additionally, Figure 5.7b displays the number of coincident drift vectors for every year, from which the mean values have been calculated. Attached vertical bars indicate the 95 % confidence interval for the mean differences. *Schwegmann*

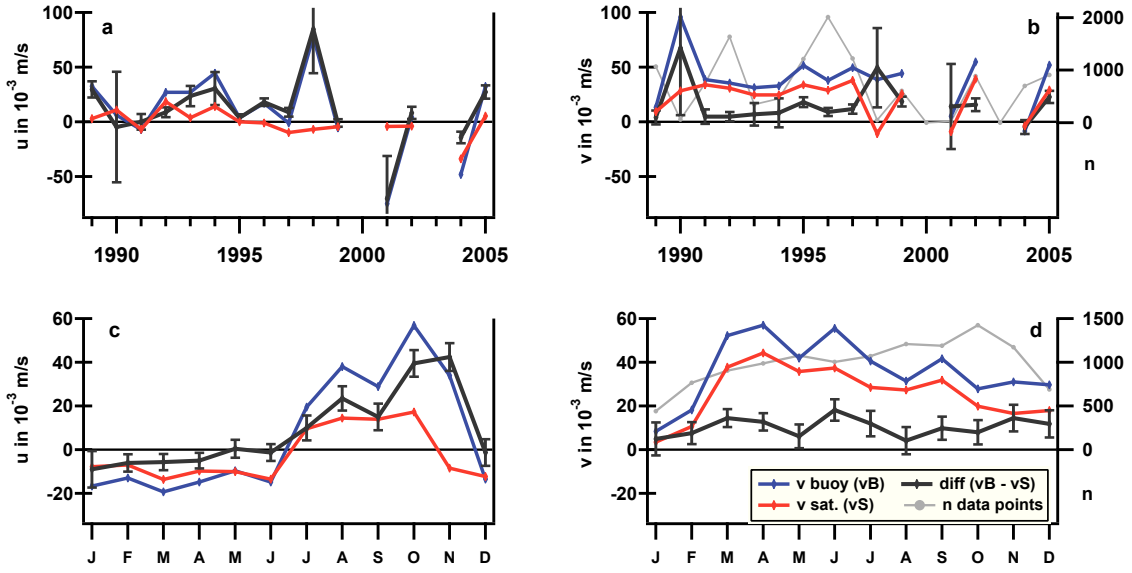

Fig. 5.7: *Comparison of mean values for zonal (left) and meridional (right) drift velocities derived from buoys (blue) and satellites (red), the average difference between both data sets (gray) with attached 95% confidence interval. The number of corresponding sea ice drift vector pairs (n) is shown in light gray (only in Fig. b and d). Upper figures display yearly and lower figures monthly distribution. Figures after Schwegmann et al. (2011).*

et al. (2011) found that the satellite-derived meridional sea ice drift component follows the characteristics of the buoy data quite well with deviations lower than 50 % in most years. On the contrary, the satellite-derived zonal sea ice drift component has most often deviations of more than 50 % (not shown). Furthermore, they found that correlation coefficients between satellite- and buoy-derived sea ice drift components (displayed in Fig. 5.8a) are generally located between 0.4 and 0.7 except for the

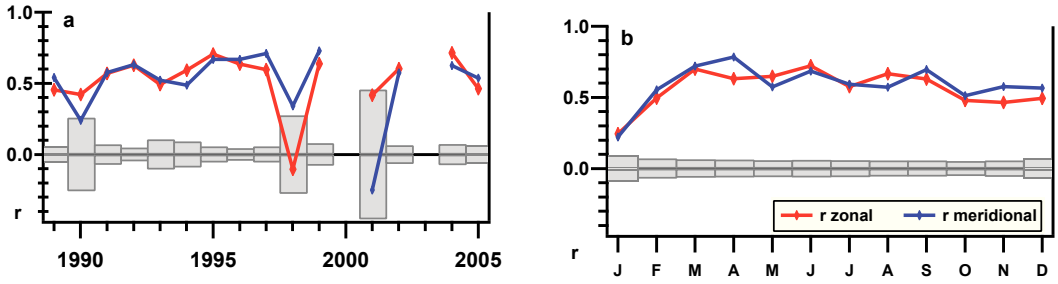

Fig. 5.8: *Correlation (r) between zonal (red) and meridional (blue) sea ice drift components of buoy- and satellite-derived data. a) shows yearly and b) monthly distribution. Regions of less than 95 % confidence for the correlation coefficients are displayed by gray bars. Figure after Schwegmann et al. (2011).*

years 1990, 1998 and 2001, when they are either lower or even negative. However, in those years, the correlation is statistically not significant, as indicated by the gray bars. There is evidence that the low number of corresponding drift vectors is one reason for this different behaviour of correlation coefficients in those years. Unfortunately, the interannual behaviour of discrepancies and correlation between both data sets could not be identified with the buoy data, since regular spatial and temporal coverage of these data is not given (*Schwegmann et al.*, 2011).

The monthly discrepancies of mean satellite- and buoy-derived sea ice drift are displayed in Figure 5.7 (c,d) for the zonal and meridional sea ice drift component, respectively. As found by *Schwegmann et al.* (2011), the prevailing drift direction changes in July from westward to eastward drift. This change of the drift direction represents the seasonal shift of buoy data coverage, since it only occurs in the northern Weddell Sea, as shown in Figure 5.9. Most of the buoy data available in winter are located in the northern Weddell Sea, while data from summer months are well distributed across the entire sea ice zone in the Weddell Sea. For all three northern sub-regions (listed in Tab. 5.1), a persistent change from westward to eastward sea ice drift can be observed over the year. For the southern sub-regions, this change cannot be detected; the monthly averaged sea ice drift is in westward direction for all seasons (not shown).

After the change of direction in June/July, the zonal sea ice drift is the highest for the period from July through November (see Fig. 5.7) with a mean maximum of 0.057 m/s (buoy) and 0.017 m/s (satellite) in October (*Schwegmann et al.*, 2011). Discrepancies are the highest during this time too. *Schwegmann et al.* (2011) argued that this is because of the general underestimation of sea ice drift velocities on the part of the satellite-derived data, on the one hand, which rises when velocities become

Table 5.1: *Definition of Weddell Sea sub-regions for local comparisons (after Schwegmann et al., 2011)*

Region	Longitude	Latitude
North-west (NW)	65^o - 45^{o}W	57^o - 70^{o}S
South-west (SW)	65^o - 45^{o}W	70^o - 76^{o}S
Central-north (NC)	45^o - 25^{o}W	57^o - 70^{o}S
Central-south (SC)	45^o - 25^{o}W	70^o - 76^{o}S
North-east (NE)	25^{o}W - 10^{o}E	57^o - 70^{o}S
South-east (SE)	25^{o}W - 10^{o}E	70^o - 76^{o}S

higher. On the other hand, additionally surface changes in spring can influence satellite signals so that the agreement between buoy- and satellite-derived data might decrease. Both effects together might result in very high differences for the zonal drift in October and November (*Schwegmann et al.*, 2011).

Regarding the meridional sea ice drift component, discrepancies are fairly low all over the year. The general seasonal variation is represented quite well for both satellite-based sea ice drift components. Correlation coefficients for the zonal and meridional sea ice drift are fairly similar between the data sets and lie between 0.5 and 0.8, except for January, when correlation for both sea ice drift components is only about 0.2 (*Schwegmann et al.*, 2011). In addition, the satellite-based zonal sea ice

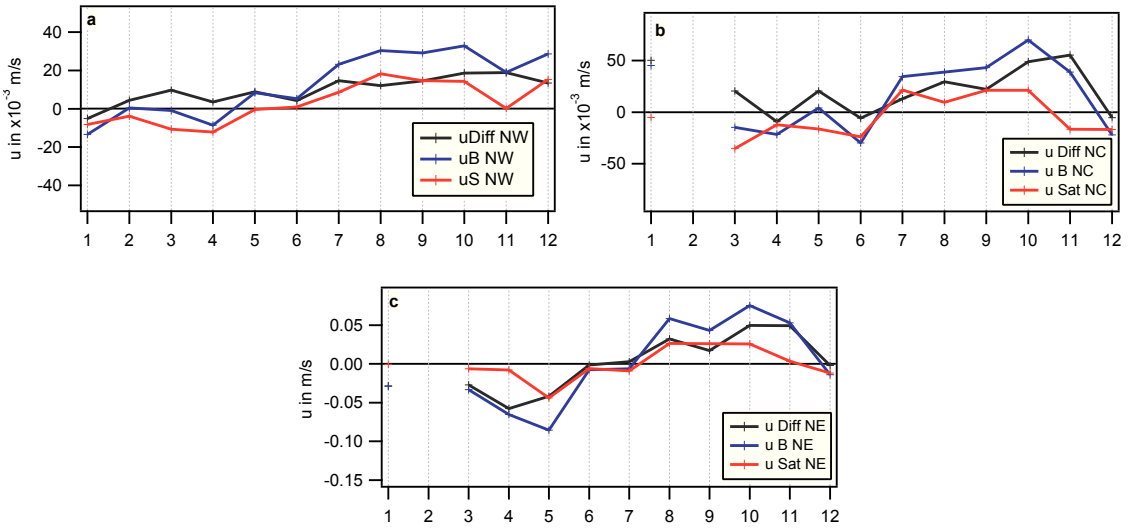

Fig. 5.9: *Seasonal change of zonal sea ice drift for the Weddell Sea sub-regions a) north-west (NW), b) north-central (NC) and c) north-east (NE) for buoy (blue) and satellite data (red). Note the difference in ordinate scales.*

drift correlates less well with buoy data during spring.

Mean sea ice drift velocities for both data sets are shown in Figure 5.10 for the sub-regions listed in Table 5.1. In all cases, the mean satellite-derived sea ice drift is lower compared to the buoy-derived one. Drift velocities seem to increase from the west to the east, especially for the northern parts.

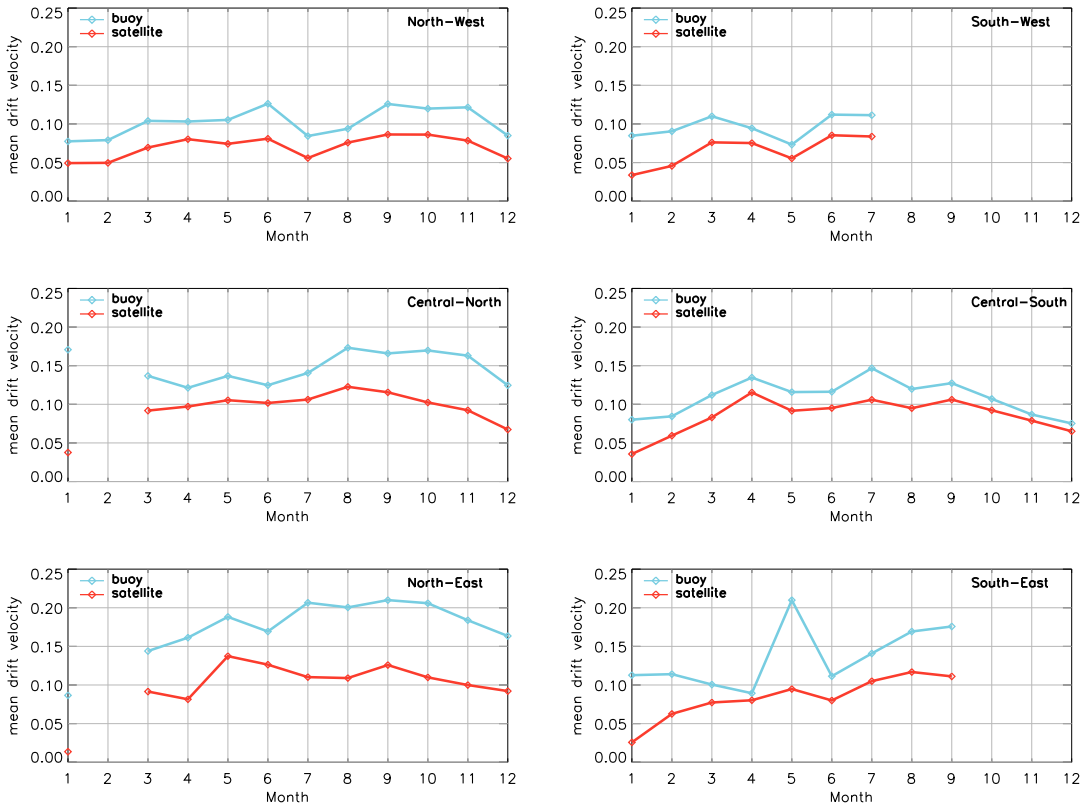

Fig. 5.10: *Comparison of satellite- (red) and buoy-derived (blue) sea ice drift velocities for different sub-regions of the Weddell Sea.*

In the western Weddell Sea, drift velocities do not exceed 15 cm/s on average and fluctuate in most months around 10 cm/s (buoy data). In the central regions, the northern part shows sea ice drift velocities of more than 15 cm/s in some months and the southern part has also mostly higher velocities than the south-western region. The highest velocities occur in the north-eastern region with more than 20 cm/s in some months. The described behaviour of monthly mean buoy drift is generally captured by the satellite data. The regional dependency is not as strong as for buoy data but the increase of mean velocities from west to east is also indicated.

The overall sea ice drift velocities in the Weddell Sea, displayed in Figure 5.11, lie between 8 cm/s (4 cm/s) in summer and more than 16 cm/s (less than 12 cm/s) in winter and spring for buoy (satellite) data. Over all 11928 coincident data points, the

mean daily buoy- and satellite-derived sea ice drift velocities were (13.5 $\pm$ 9.5) cm/s and (8.8 $\pm$ 6.5) cm/s (*Schwegmann et al.*, 2011), respectively. This agrees with mean sea ice drift velocities of 10-15 cm/s found by, e.g., *Fischer* (1995); *Harder & Fischer* (1999) and *Kottmeier & Hartig* (1990). As described before, mean satellite-derived sea ice motion is generally lower than the buoy-derived sea ice drift. *Schwegmann et al.* (2011) found a general underestimation for more than two-thirds of the compared data points in the Weddell Sea and also *Heil et al.* (2001) reported an underestimation of satellite-derived drift velocities, found by a comparison with buoy data in the East Antarctic sea ice zone. There are different reasons for the general lower sea ice

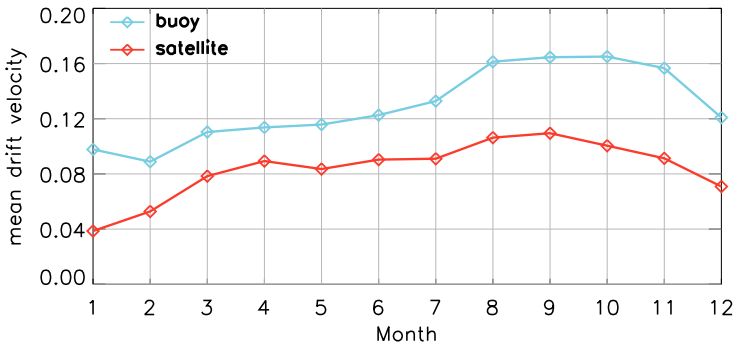

Fig. 5.11: *Comparison of monthly mean sea ice drift velocities determined from satellites and buoys, averaged for all data from the Weddell Sea.*

drift velocities. First, sea ice motion from the satellite product is derived via cross correlation. This means, that distinct patterns of one image have to be found again in the next image. When sea ice movements are high, these patterns can change quite strongly so that they might not be detected in the second image. Therefore, sea ice drift velocities are biased low (*Heil et al.*, 2001). Additionally, satellite images are composites of different satellite overpasses per day, which means that data records of different regions at different imaging times are combined. *Kwok et al.* (1998) found that this can lead to a drift-speed-dependent blurring or smearing of the satellite signal. Furthermore, the interpolation of only few, low biased sea ice drift velocities onto large areas influences the mean sea ice drift (*Schwegmann et al.*, 2011). This effect is especially present in the early years of the observation period and in summer months, as described before (see Fig. 5.4, 5.5, and 5.6). The low summer coverage occurs most probably due to changing snow and sea ice properties, such as snow melting and flooding, which affect the emissivity of the surface (*Willmes et al.*, 2006, 2009). In addition, an increased atmospheric water vapour content would be an explanation for the low data coverage in summer, since the SSM/I 85.5 GHz channel as well as the AVHRR are especially affected by atmospheric moisture (*Heil et al.*, 2001).

Despite all these shortcomings, satellite-derived sea ice drift gives an adequate overview of the sea ice circulation regime. Keeping in mind, that mean drift velocities are about one-third too low for data from 1989 till 2005 (*Schwegmann et al.*, 2011), they can be used for analyses of interannual variability and long-term changes. When analyzing data before the SSM/I period, inaccuracies might be higher and the interpretation of results have to consider this.

Since daily data have lots of uncertainties, monthly fields were used for further studies, so that daily discrepancies were smoothed by the averaging. In addition, this allows for a comparison between satellite-based sea ice drift velocities and simulated monthly sea ice drift fields from FESOM.

5.2.3 Variability of sea ice drift velocities

In this section, the variability of the Polar Pathfinder sea ice drift velocities is analyzed from data for the period 1988 through 2006. Prior to 1988, this data set has undefined uncertainties and therefore, trends for the period from 1979 till 2006 are considered only in some special cases. From all data, the mean long-term sea ice drift distribution, its trends and statistical significance were calculated and are displayed in Figure 5.12 for the period from 1988 till 2006. Near the coasts, sea ice drift velocities are relatively low with about 2 cm/s, but they increase towards the central Weddell Sea, where they are the highest with about 4.5 cm/s on a long-term and year-round average. In addition, the north-eastern coastal region, next to the Fimbul Ice Shelf shows fast sea ice movements. There is a strong westward directed coastal inflow of sea ice in the east heading into the Weddell Sea. From there, sea ice drifts into the south-west and displays the Weddell Gyre circulation with a northward drift near the Antarctic Peninsula. This feature is generally similar to the sea ice drift derived from buoys and follows the patterns of the geostrophic winds.

The sea ice drift speed in the eastern coastal current increased over the years. In the central Weddell Sea changes were overall very small with only a slight decrease of sea ice drift velocities. According to the satellite data, sea ice drift along the Antarctic Peninsula decreased by about 0.75 cm/s per decade. Only these sea ice drift trends near the Antarctic Peninsula and those along the eastern coast are statistically significant (see Fig. 5.12c). Compared to the trends derived from NCEP 10-m wind speeds, shown in Chapter 2, the observed trends of the sea ice drift near the eastern and western coasts are reversed. A possible explanation is that the changes in the wind field, as are shown for the long-term trends in Figure 2.5 and for monthly trends in Figure 2.6 (e.g. in May, October, December), strengthened the circulation system

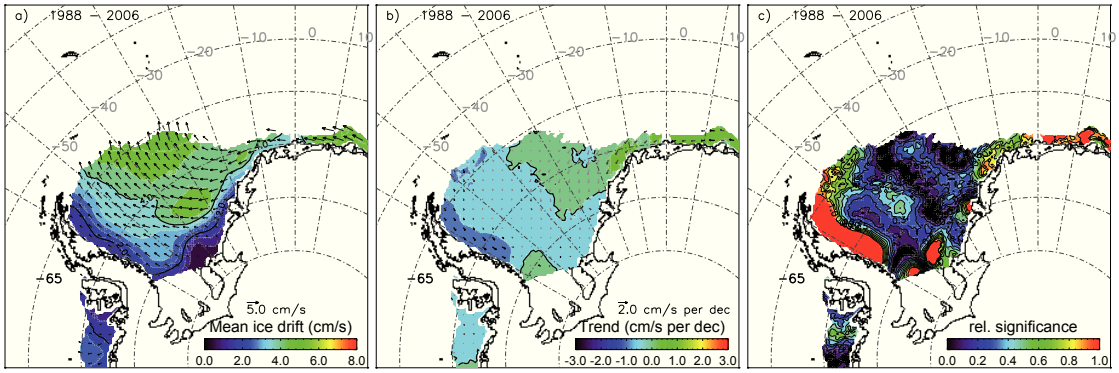

Fig. 5.12: *Satellite-derived OI a) mean sea ice drift velocities in cm/s, b) drift trends in cm/s per decade, and c) relative significance of trends for January 1988 through December 2006 from Polar Pathfinder sea ice motion vectors.*

in the central Weddell Sea. The increased wind speeds at the Antarctic Peninsula might lead to higher deformation along the coast of the Antarctic Peninsula, which would decrease drift velocities in this region. In the eastern inflow region, sea ice traction due to an intensified Weddell Gyre circulation might result in increased sea ice drift velocities despite of decreasing wind speeds. Considering only the year-round long-term trends for the sea ice drift divergence from the Polar Pathfinder sea ice motion (Fig. 5.13b), sea ice drift at the Antarctic Peninsula actually tend to be more convergent over the period from 1988 till 2006. Also the negative trend at the eastern inflow region is consistent with the assumptions made before, since decreasing wind speeds reduce the generally high divergence in this region. However, except for the eastern inflow region, mean divergence is low and the strongly varying trends are generally statistically insignificant (Fig. 5.13c).

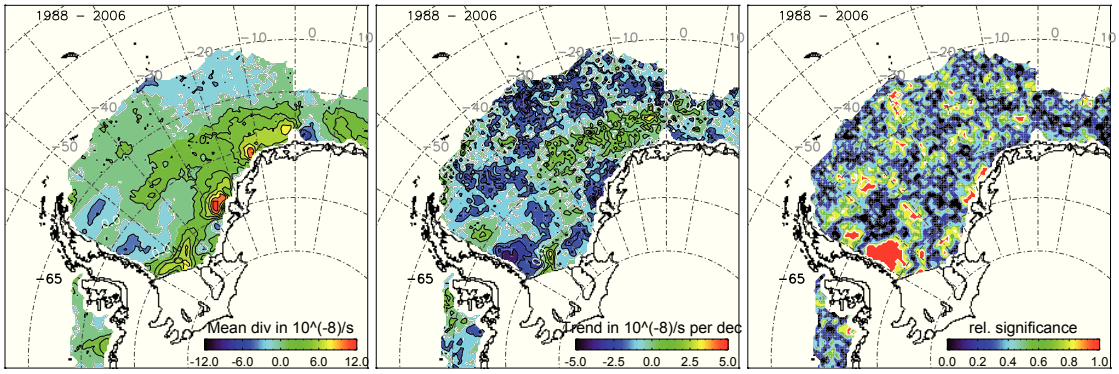

Fig. 5.13: *Satellite-derived OI a) mean sea ice drift divergence in s^{-1}, b) trends of divergence in s^{-1} per decade, and c) relative significance of trends for January 1988 through December 2006 from Polar Pathfinder sea ice motion vectors.*

The generally decreasing sea ice drift velocities in the satellite data are comparable to findings of *Schmitt* (2005), who calculated sea ice drift velocity fields based on OI

satellite- and buoy-derived sea ice motion vectors for the period 1979 through 1997. In her study, the entire Weddell Sea reveals decreasing sea ice drift velocities, although the trends in coastal regions are less strong as in the central Weddell Sea, contrary to findings of the present study.

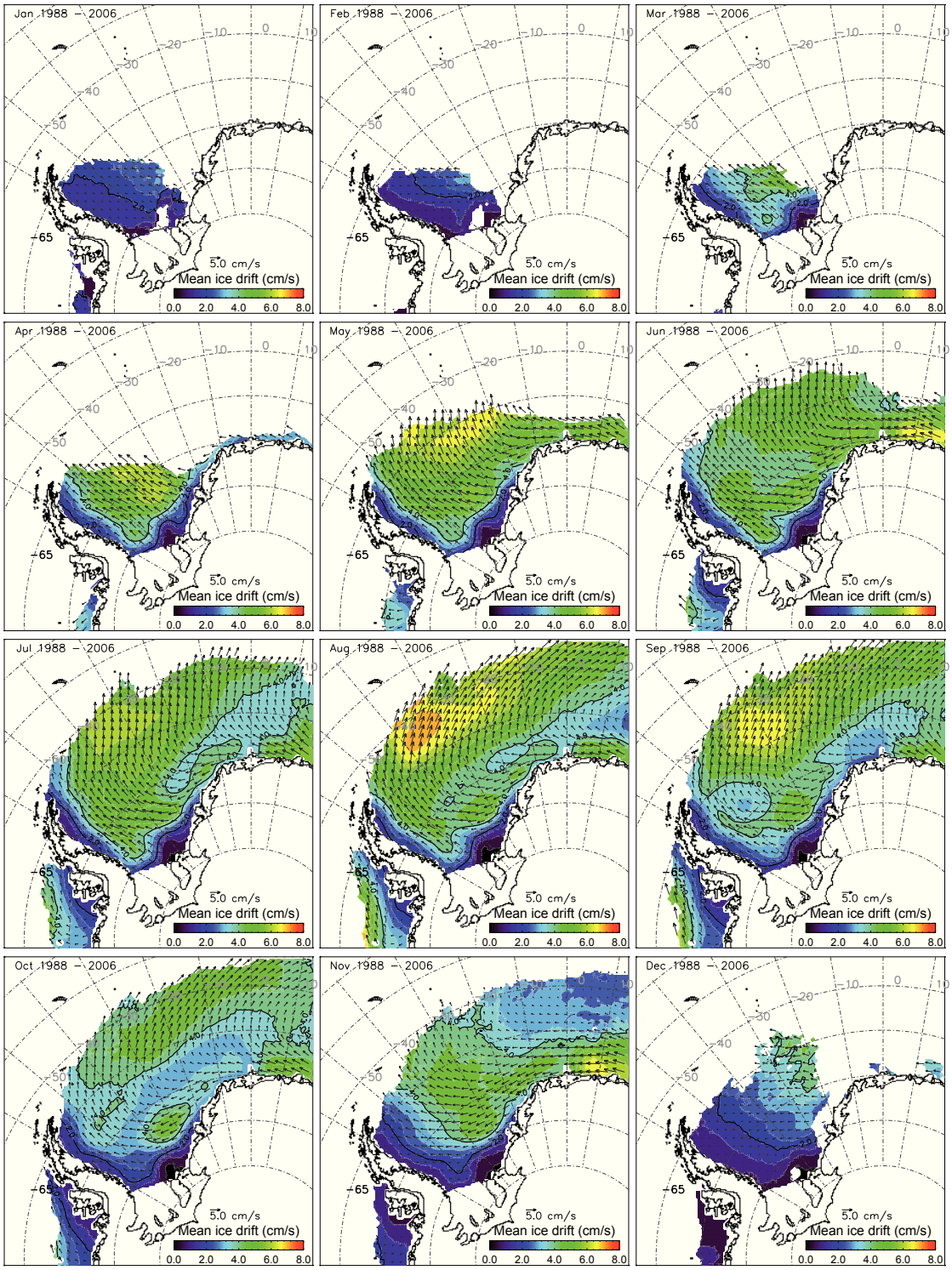

Fig. 5.14: *Monthly mean satellite-derived sea ice drift velocities in cm/s for 1988 through 2006.*

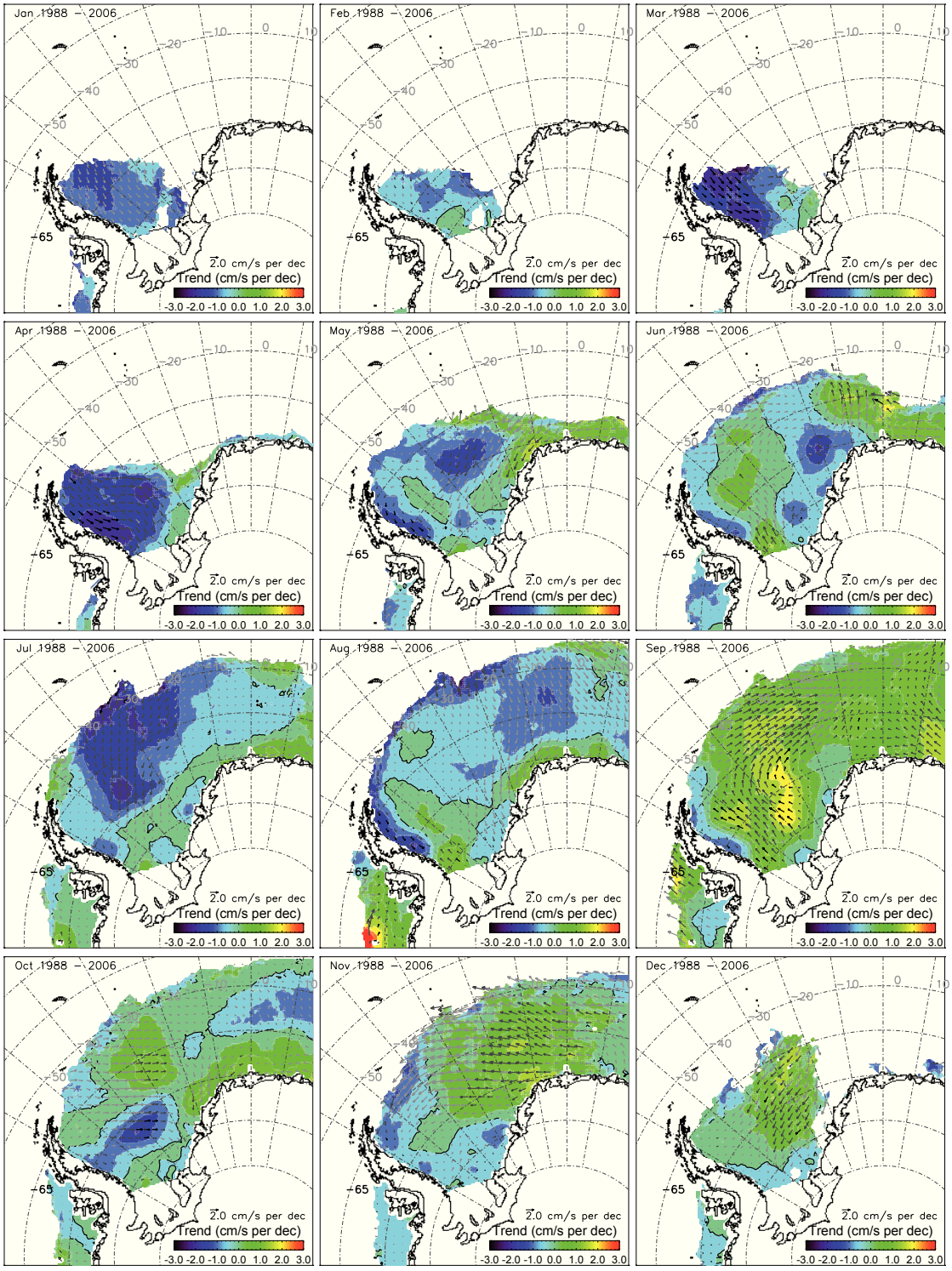

Fig. 5.15: *Trends of monthly mean satellite-derived sea ice drift velocities in cm/s per decade from 1988 till 2006, derived from the Polar Pathfinder sea ice motion. Black arrows indicate statistically significant trends. Trends in regions with dark gray arrows exceed at least one standard deviation and light gray arrows show statistically insignificant trends.*

To demonstrate the seasonal variability of the sea ice drift, Figure 5.14 and 5.15 display monthly mean sea ice drift velocities and their trends. For all months, the velocities increase from the coastal areas towards the northern-central Weddell Sea

(Fig. 5.14). The summer mean sea ice drift is orientated towards the west/north-west, pushing the sea ice towards the Antarctic Peninsula. Mean sea ice drift varies between 0.5 cm/s near the coast and 3 cm/s near the sea ice edge, while in December the north-eastern region reveals velocities of even up to 4 cm/s.

In autumn, sea ice drift velocities increase and become higher than 4 cm/s in the central basin. Lower sea ice motion with less than 3 cm/s on average appears only in a small band along the coast. The general direction of the sea ice drift is oriented towards the north/ north-west until May. In this month, the Weddell Gyre circulation is visible in the sea ice drift data for the first time during the year and it remains visible throughout winter.

In spring, the band of slower mean sea ice drift velocities in coastal regions start to expand into the Weddell Sea basin. Higher velocities (larger than 4 cm/s) only arise in the northern regions and in the inflow areas along the eastern coast. The Weddell Gyre circulation is visible in the sea ice drift data until October, although in November, the sea ice shows still a gyre-like circulation in the central basin to some extent. The south-western as well as the north-eastern sea ice fields in contrast start already to move towards the west at the end of spring, the same direction as sea ice drift has in summer.

Figure 5.15 illustrates the trends of the monthly mean sea ice drift fields. Except for December, summer sea ice drift decreased. As explained before, inaccuracies in summer are large and correlation between buoy data and satellite-based sea ice drift is weak. For that reason and due to mostly statistically insignificant trends, these results are not accurate enough for interpretation. In autumn and winter, most parts of the Weddell Sea exhibit a decreasing trend of sea ice drift velocities, comparable to trends in summer. Positive trends occur mainly in the eastern regions along the coast, indicating a strengthened inflow of sea ice from the East Antarctic sea ice zone, but also in some parts of the central Weddell Sea in winter. Statistically significant are in general only the decreasing trends in the western Weddell Sea, indicated by the black arrows in Figure 5.15. However, trends in the Weddell Sea basin exceed to some extent at least one standard deviation, indicated by the dark gray arrows.

Contrary to all other seasons, drift velocities in spring increased in general. Especially in September, nearly the entire Weddell Sea reveals accelerated sea ice motion with statistically significant trends of up to 1.75 cm/s per decade in the central basin. Only the coastal areas at the Antarctic Peninsula deviated from this pattern.

Both the decreasing velocities along the Antarctic Peninsula as well as the accelerated drift next to the Fimbul Ice Shelf occur nearly throughout the year, whereby the eastern

coastal sea ice drift can only be analyzed from April through November because of the lack of sea ice in the other months. This was already indicated by the overall long-term trend from 1988 till 2006 (Fig. 5.12).

The analyses of shorter time periods, e.g., the calculation of trends for the period from 1992 or 1996 till 2006, yielded different sea ice drift trends (not shown) than those for the period 1988 through 2006. It was found that trends next to the Fimbul Ice Shelf especially underlie alterations in sign. To demonstrate this interannual and decadal variability of sea ice drift velocities in the regions of interest, which are the coastal parts of the Weddell Sea and the central basin, time series of single grid points were generated. In total eight positions were selected, which are shown in Figure 5.16: three of them are located next to the Fimbul/Brunt Ice Shelves in the inflow region of the sea ice, further three lie along the Antarctic Peninsula and the remaining two positions are located in the central Weddell Sea. The positions next to the coasts have been selected since they represent statistically significant long-term trends for the period 1988 through 2006 (except for position 7, see Fig. 5.12). In the central Weddell

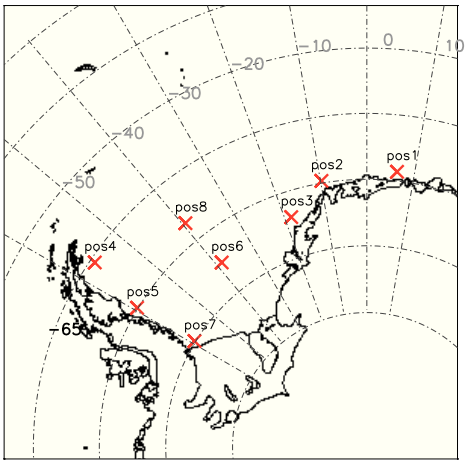

Fig. 5.16: *Map of grid points used for time series analysis of sea ice drift velocities.*

Sea, positions were chosen due to statistically significant trends in distinct months, such as the strong decrease in sea ice drift in the northern-central Weddell Sea in autumn and winter and the strong positive trend in the southern-central Weddell Sea in September. Since such features might be smoothed in areal averaged over larger regions and statistical significance might disappear, time series of single grid points are shown here instead of areal averages. Time series start in 1979 and linear trends are calculated for different periods starting between 1979 and 1996 and ending all in December 2006.

Considering the longer time periods[1], the eastern coastal inflow current (positions

[1] i.e. trends for a start year in 1979, 1984 and 1988

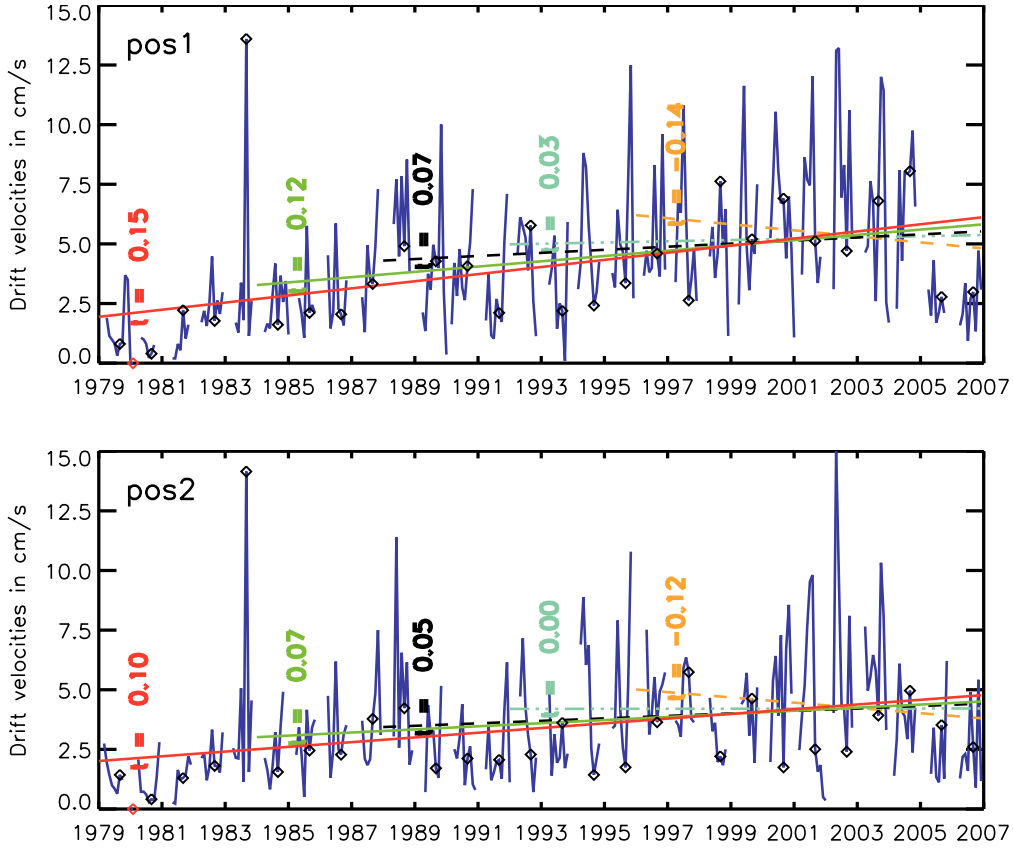

Fig. 5.17: *Time series (blue) of sea ice drift in cm/s at the eastern-coastal inflow region, exemplarily for position 1 and 2 from the Polar Pathfinder sea ice motion vectors. Coloured lines show the trend of the respective observation period. Solid line: trends are statistically significant, dashed line: trends are at least as high as one standard deviation, dashed dotted line: trends are lower than one standard deviation. Red diamonds mark February and black ones September drift of each year.*

1-3, exemplarily shown for positions 1 and 2) reveals statistically significant (Fig. 5.17, indicated by a solid line) and partly strong positive trends between 0.04 and 0.15 cm/s per year (see coloured trend lines in Fig. 5.17). Time series of all three positions have in common that drift velocities increased from 1979 until 2003. Sea ice drift strongly weakened since then. In consequence of the strong interannual variability, trends varied depending on the start year, which influenced especially the shorter periods (e.g. 1996 through 2006). The strong decrease of sea ice motion in the early 2000s, especially in the years 2005 and 2006, force the trends of all three grid points to be negative for the period 1996 to 2006. At position 1 and 2, this trend in the sea ice drift is not quite significant (indicated by the dashed line), while at position 3 (not shown), this negative trend is strong enough to be statistically significant. In the last years of the time series, sea ice drift velocities tend to have a stronger north-eastward component in this region, which is a feature that was already observed in the NCEP

wind speed, but for the entire observation period (1979-2006).

For the west Antarctic region, Figure 5.18 exemplarily shows the sea ice drift time series for position 5 and 7. Sea ice drift at position 4 (not displayed) shows similar features as drift at position 5. First of all, velocities are basically lower as in the eastern Weddell Sea, which was already mentioned in Chapter 5.2.2, where it was shown that buoy- and satellite-based sea ice drift increase from the west to the east. The relatively high drift velocities in 1980, 1983, 1989, and 1995 at position 4 and 5 are also visible at the positions 1 to 3. Trends in the western Weddell Sea (position 4 and 5) are generally negative and statistically significant. The south-western position (position 7) behaves in a different way. Here, mean sea ice drift velocities did not reveal any statistically significant trend (indicated by the dashed-dotted lines). In contrast to the eastern Weddell Sea, velocities in 2005 and 2006 were not remarkably low in this region compared to previous years.

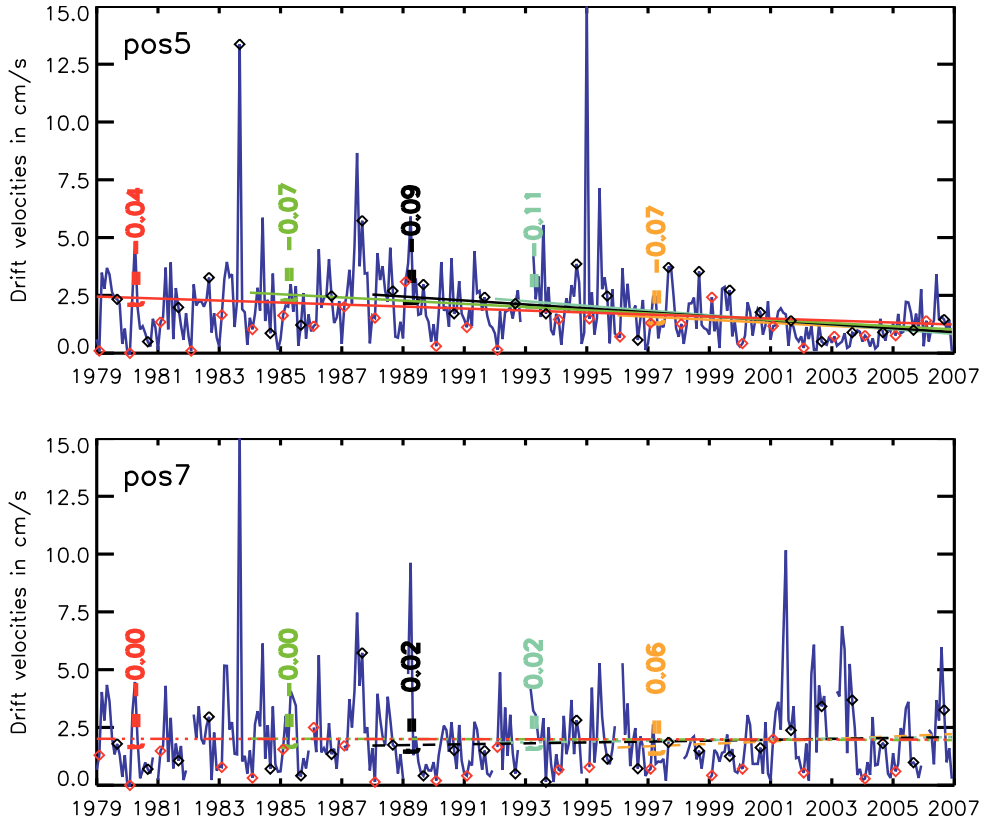

Fig. 5.18: *Time series of sea ice drift in cm/s at position 5 and 7 at the western coastal region, at the northern (pos5) and southern (pos7) Antarctic Peninsula from Polar Pathfinder sea ice motion vectors. Red diamonds show February and black ones September drift of each year.*

Sea ice drift in the central Weddell Sea (position 6 and 8, Fig. 5.19) has a high seasonal variability and the low trends are generally not statistically significant. The

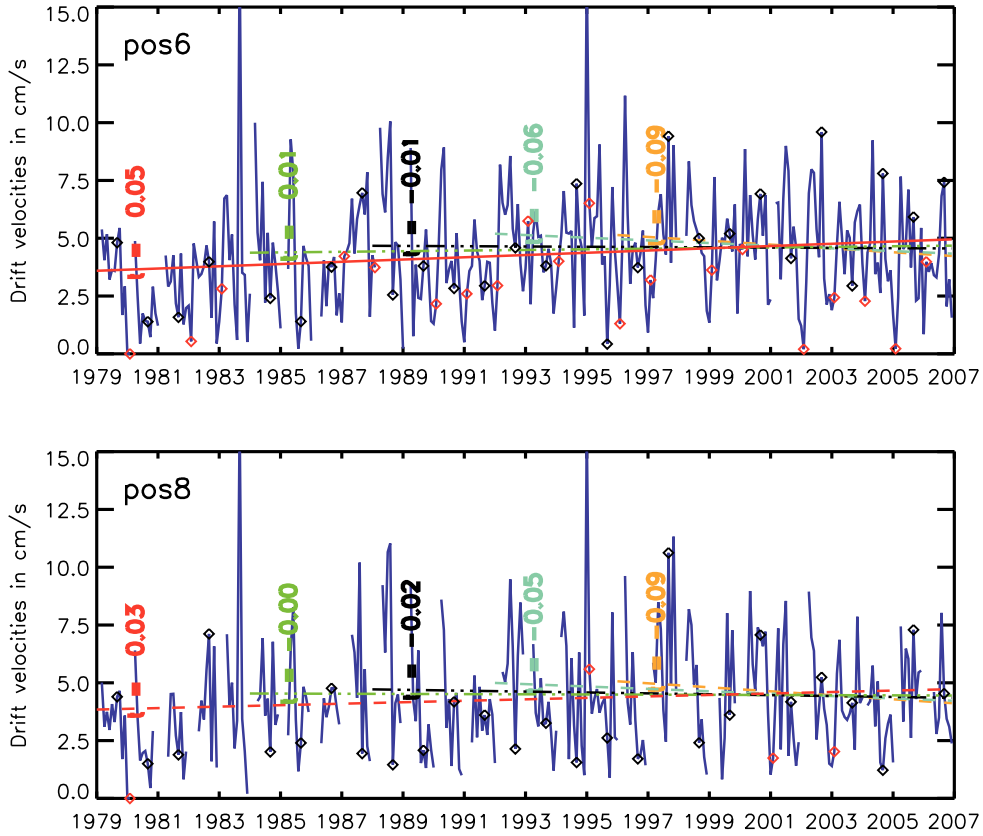

Fig. 5.19: *Time series (blue) of sea ice drift in cm/s at position 6 and 8 in the central Weddell Sea from Polar Pathfinder sea ice motion vectors. Coloured lines indicate the trends for the respective observation period. Red diamonds show February and black ones September drift of each year.*

pronounced increase of sea ice drift at position 6 is only visible in September and does not significantly influence the year-round long-term trend. The same holds for the decreasing trend in the northern-central Weddell Sea (position 8, July).

None of the above described extrema and special features can be consistently related to SAM or ENSO. Correlation coefficients between sea ice drift and the SAM as well as the Niño 3.4 index are only weak and rarely statistically significant. Only at the eastern coast, a statistically significant anti-correlation of at most -0.2 between sea ice drift and the SAM index can be obtained. ENSO reveals the highest positive correlation at the positions in the western Weddell Sea (positions 4, 5, and 7). This indicates that the impact of both atmospheric patterns on the sea ice is regionally dependent. An analysis of the regional and seasonal dependency could be a task for future work, especially since *Fogt & Bromwich* (2006) found a seasonal varying response of the atmosphere in high latitudes to the oscillation patterns. Furthermore, only spectral analyses can clearly identify the presence and periodicity of any oscillation pattern in

the data. This analysis could also be a task for future work. For this, it would be helpful to have updated sea ice drift velocity fields up to the most recent years to have longer, only SSM/I-based time series, since analyses of the entire period (SMMR + SSM/I) potentially will not show a clear signal due to uncertainties in the early years of the time series. Due to these uncertainties in the data of former years, the interpretation of the interannual variability and trends of the sea ice drift time series for the periods 1979 and 1984 through December 2006 should be done carefully, even though some of the trends are statistically significant. Sea ice drift trends for periods starting in 1988 and later are expected to be more reliable. However, the high interannual variability of sea ice drift is often much higher than the trends and therefore, trends for the shorter periods are often insignificant.

Correlation of SIC with sea ice drift and its divergence

The potential influence of the satellite-based sea ice drift speed on SIC changes is discussed here by means of correlation maps between the detrended monthly anomalies of both variables. A subset of correlation maps is shown in Figure 5.20.

On a monthly basis, signals are very difficult to interpret since they barely follow a robust relationship. The correlation in the central Weddell Sea is the most robust one. Except for January and November, sea ice drift and concentrations are mainly anti-correlated. Hence, strong (weak) sea ice drift is generally associated with reduces (increased) SIC in all seasons. This feature might be related to high divergent drift induced by strong winds, which can open leads and polynyas. Those leads and polynyas in the ice coverage are only closed again, when a reduction of divergent sea ice drift results in a permanent overfreezing of the open water, and hence, in increased SIC. Actually it was found that the westerlies in the north-western and -central Weddell Sea exhibit a stronger southward component. This would also result in a decrease of the meridional sea ice drift velocity and might reduce divergent drift in the central Weddell Sea. This in turn might decrease the SIC in this region. From an analysis of deformation rates of the sea ice drift and their correlation with SIC, however, no clear relationship was obtained, although there are some anti-correlated patterns visible, more than e.g. in the marginal sea ice zone. Nevertheless, results are very noisy and do not allow for a general interpretation. Also the analysis of divergences in the wind field does not result in a robust relationship. Wind divergence indeed tends to be regularly anti-correlated with SIC in the central Weddell Sea, but in most occasions only in smaller, regularly changing sub-regions.

For the marginal sea ice zone, sea ice drift and concentrations correlate basically in

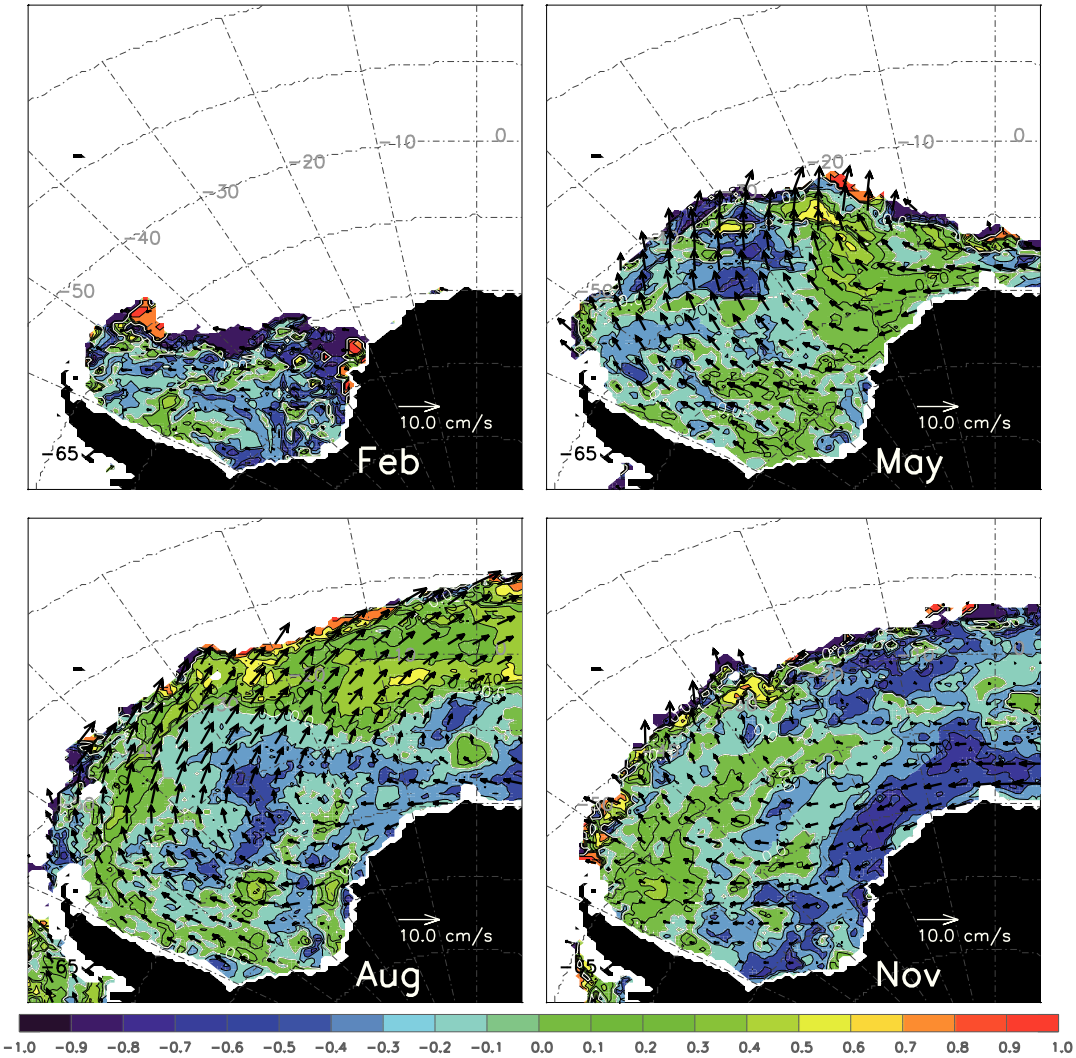

Fig. 5.20: *Correlation between SIC from the NSIDC bootstrap data and satellite-based sea ice drift velocities from the Polar Pathfinder sea ice motion vectors.*

winter. Stronger drift velocities result in higher SIC, indicating that convergent drift prevails. In spring, on the contrary, both sea ice parameters are anti-correlated. This indicates that ice coverage remains fairly compact when wind forcing is weak. Therefore, atmosphere-to-ocean heat flux is reduced, since sea ice absorbs much less energy than the open ocean, and sea ice melting is reduced. In summer and autumn, no robust signal was found for the correlation between sea ice drift and SIC in the marginal sea ice zone. In these months, temperature changes and cloud coverage might also have a strong impact on sea ice changes and might exceed the influence of sea ice drift on the SIC. In addition, the satellite-based sea ice drift in summer months does not well correlate with buoy data. It might be that the impact of sea ice motion on SIC disappears in the uncertainties in the sea ice drift fields. The correlation between the sea ice drift divergence and SIC is mostly high in this region, but with changing sign. Hence, an interpretation of the correlation between SIC and

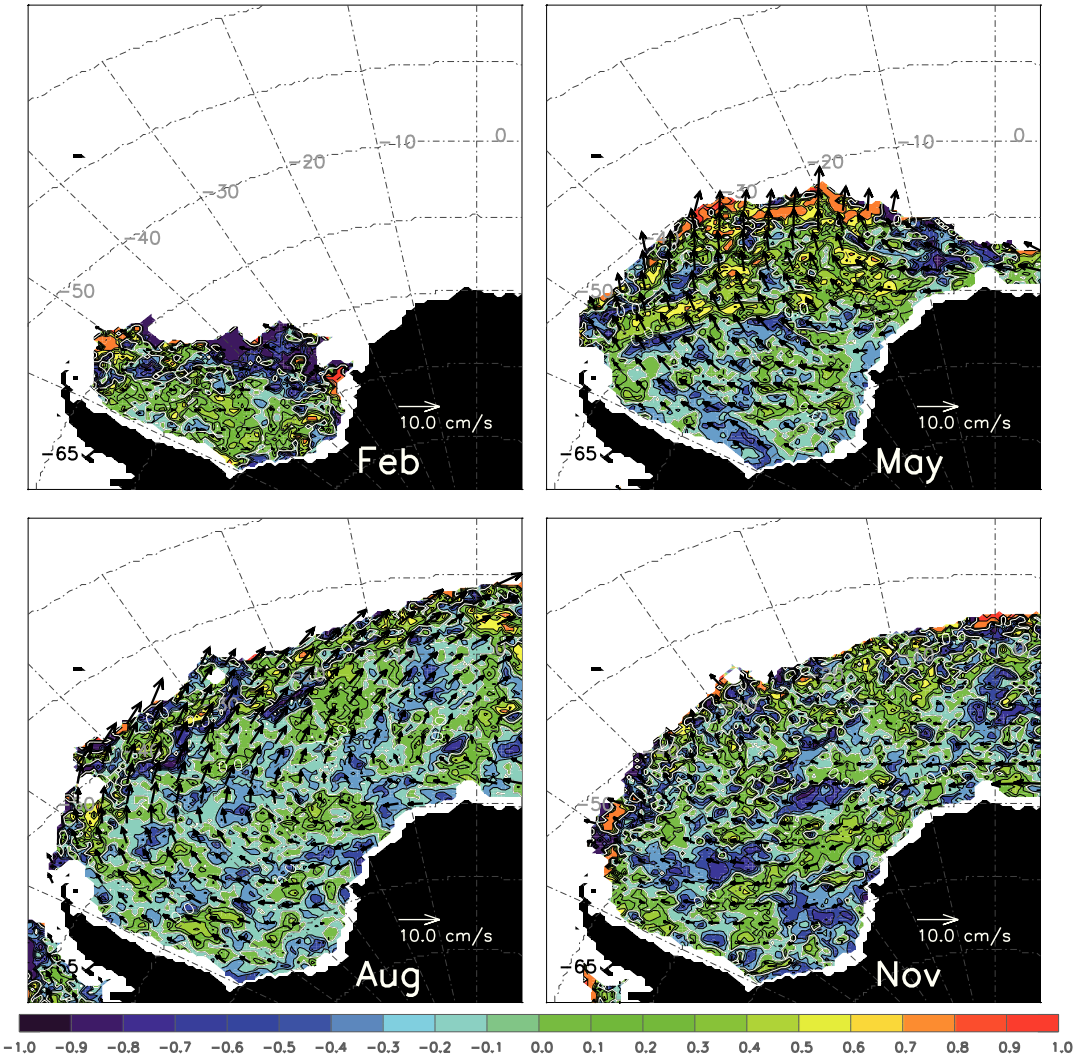

Fig. 5.21: *Correlation between SIC from NSIDC bootstrap data and satellite-based sea ice drift divergence derived from the Polar Pathfinder sea ice motion vectors.*

sea ice drift divergence derived from the Polar Pathfinder sea ice motion is apparently not useful.

Unfortunately, relationships between SIC and sea ice drift in the western-coastal sea ice zone cannot be revealed, since correlation coefficients are inconsistent throughout all seasons. However, SIC are often, but not consistently, anti-correlated with the satellite-based sea ice divergence. Hence, convergent sea ice drift is associated with increasing SIC and the other way round for divergent drift, which is an expected behaviour.

SIC in the eastern coast shows mainly a negative correlation with sea ice drift speeds. Only next to the Fimbul Ice Shelf, coefficients change their sign in autumn and in July. In spring and summer, anti-correlation indicates that higher ice drift removes the sea ice in this region faster and neither gradually refreezing, nor ice transport from the

East Antarctic sea ice zone can replace the exported sea ice. Hence, SIC decrease when wind velocities increase. Also in winter, this anti-correlation is persistent, which is associated to the generally divergent drift pattern in this region. Strong offshore winds decrease regularly the SIC, while weaker wind velocities keep the ice coverage closed. The positive correlation between sea ice drift velocities and SIC in autumn is quite unexpected. As mentioned before, the correlation between divergence and SIC does not result in an interpretable result.

5.3 Model simulations

5.3.1 Comparison of model results with buoy data

In the following, monthly mean FESOM sea ice drift simulations are compared to monthly mean buoy-based sea ice motion for the period from 1989 till 2005 to identify the biases of the model. Differences and correlation coefficients between buoy-derived and modelled sea ice drift were analyzed regarding their seasonal and regional behaviour. For the comparison only those vectors were considered, which exist in both data sets. Sea ice drift vectors from the model were taken, when SIC is at

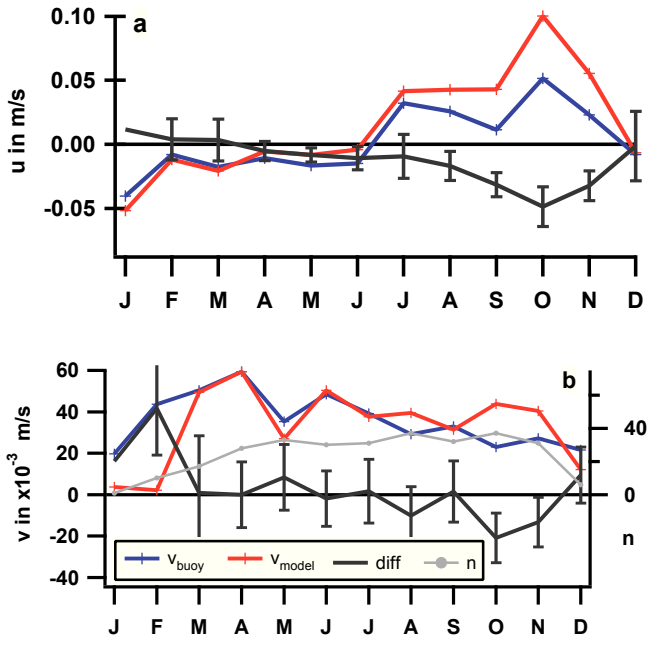

Fig. 5.22: *Monthly mean a) zonal and b) meridional sea ice drift components derived from buoy data (blue) and model simulations (red), differences between both data sets (dark gray) with attached 95 % confidence interval and number of corresponding drift vector pairs (n, light gray, only in b) in the Weddell Sea.*

least 15% at the respective grid point. If not, the buoy-derived sea ice drift velocity was also excluded from the study. Differences were afterwards calculated by subtraction of the simulated from the buoy-derived drift components. The buoy-derived curves for monthly mean zonal and meridional components differ slightly from those shown in Fig. 5.7, since the averages were not necessarily calculated from the same coincident drift vector pairs as have been used for the satellite-based drift. This is due to the fact that the satellite-derived data have only drift data for regions with more than 50% SIC, while in model simulations, a threshold of 15% SIC was used.

Regarding the zonal component (Fig. 5.22a), the overall mean sea ice motion is represented well by FESOM. The general tendencies are comparable and also the change of direction in sea ice drift between June and July from westward to eastward drift, discussed in Section 5.2.2, is reproduced in the model simulation. In contrast to the satellite-derived velocities described in Section 5.2, which mainly underestimate sea ice drift, modelled zonal sea ice velocities overestimate sea ice drift in most months. This overestimation is statistically significant between August and November. As for the comparison between buoy- and satellite-derived sea ice drift, differences between modelled and buoy-derived zonal velocities are the highest in October. In this month, FESOM overestimates zonal velocities by about 100%.

The meridional drift follows the buoy derived distribution in general and movements have a strong northward component from March until November in both data sets. From March through September, differences are quite low and not significantly different from zero (indicated by the vertical bars, which show the confidence interval). In January and February, the meridional sea ice drift is underestimated by FESOM, whereas October and November values are significantly overestimated.

The mean sea ice drift velocities for the compared monthly mean vectors are 6.21 ($\pm$ 4.0) cm/s for buoys and 8.25 ($\pm$ 5.2) cm/s for the model simulation, which results in a difference of -2.04 ($\pm$ 4.27) cm/s. Hence, the overestimation of simulated sea ice drift vectors is statistically not significant.

Monthly correlation coefficients between modelled and buoy-derived sea ice drift components lie generally between 0.5 and nearly 1, with few exceptions. From April till November, correlation coefficients are significantly different from zero for both sea ice drift components. Besides the statistical significance, which in fact only relies on the number of coincident vector pairs, there is barely evidence that the degree of correlation depends on the season. For the zonal component, coefficients are the lowest from February till April, but the meridional component shows high variations all over the year. The fact, that there is only one coincident drift vector pair for January reveals the underestimation of sea ice of FESOM in summer.

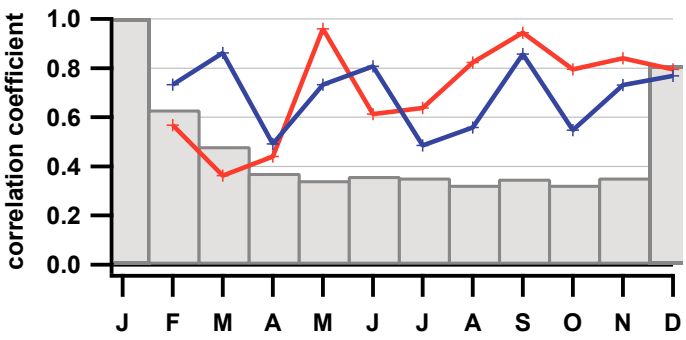

Fig. 5.23: *Correlation (r) between buoy-derived and modelled zonal (red) and meridional (blue) sea ice drift components. Gray bars indicate the regions of less than 95 % confidence for the correlation coefficients.*

In addition to the seasonal dependency of the correlation, a regional analysis was performed. The considered sub-regions are listed in Table 5.1 at page 96. However, since there are mostly less than 15 data points per region per month, a meaningful study of the regional dependency is not possible. Results vary between totally correlated to totally anti-correlated, but none of the anti-correlated results are statistically significant. Whether there is a regional dependency for the correlation between buoy-derived and modelled sea ice drift velocity components cannot be answered, because of the lack of sufficient data.

Results indicate that the agreement between both data sets is generally quite good. Since the mean correlation is relatively high, it seems to be appropriate to use the model simulations for an analysis of sea ice drift trends in the Weddell Sea.

5.3.2 Sea ice drift variability from model results

For the analysis of sea ice drift changes, the same time periods as for the satellite-based sea ice motion are discussed and compared in this section.

Figure 5.24 displays the mean sea ice drift field, its trends and their significance for the period from 1988 till 2006, derived from monthly mean model results. Along the eastern coast in the inflow region as well as in the outflow region along the Antarctic Peninsula high drift velocities occur. Furthermore, the near-marginal sea ice zone exhibits fast sea ice motion from the tip of the Antarctic Peninsula to the Greenwich Meridian. The general drift direction shows a well established c-shape. The sea ice displays the well-known Weddell Gyre circulation: In the east, it flows into the Weddell Sea, follows the coast along the Antarctic Peninsula, where the drift is northward, and is finally deflected to the east.

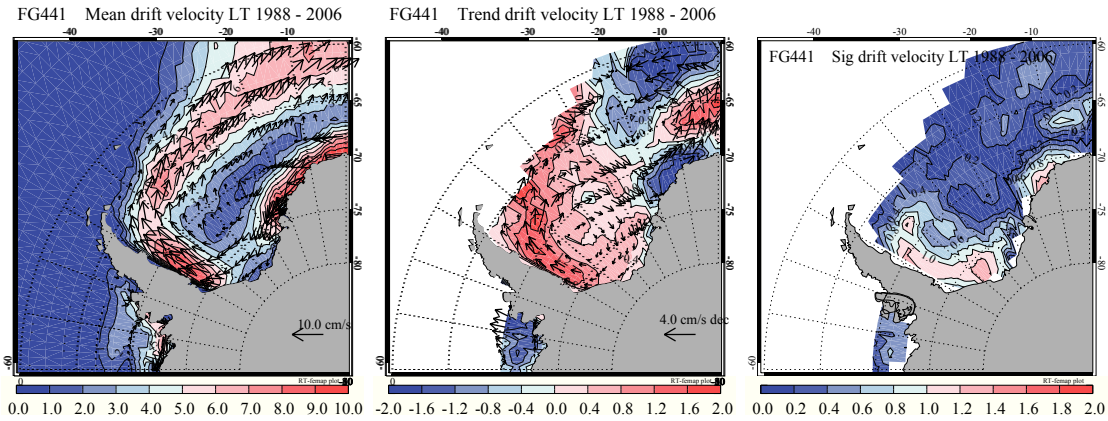

Fig. 5.24: *Modelled distribution of monthly a) mean sea ice drift in cm/s, b) drift trends in cm/s per decade, and c) relative significance of drift trends from January 1988 till December 2006.*

In the central basin, sea ice also follows this circulation, but velocities are much smaller here than in the coastal and near-marginal sea ice zones.

The central and western Weddell Sea exhibit increased drift velocities, with the highest acceleration occurring for the region near the Antarctic Peninsula. In the north-east as well as for some coastal regions in the inflow area, modelled sea ice motion decreases over the study periods. The trends of the NCEP winds are clearly visible in the modelled ice drift. Statistical significance is only given for the positive trends along the south-western coast and for the decreasing sea ice motion in some parts along the eastern coast.

The positive trends in the south-western Weddell Sea become smaller for shorter, more recent time periods, while the negative trends in the eastern Weddell Sea as well as the positive trends in the north-western and north-central Weddell Sea are intensified. This behaviour will be shown later on by time series analysis, as was done in Section 5.2.3 for satellite-derived sea ice drift velocities. Before, the monthly distributed mean sea ice drift and its trend from 1988 through 2006 are discussed (Fig. 5.25).

All over the year, the highest drift velocities with 4 cm/s (in summer) up to more than 10 cm/s (in winter) occur along the eastern and western coasts, and in winter also in the marginal sea ice zone. In a small band in the central to eastern Weddell Sea, sea ice drift is comparatively low with 1 cm/s up to 5 cm/s. Sea ice follows mainly the c-shape described before and velocities near the coast remain fairly high year-round. The summer months show generally lower drift velocities than the winter months. While this is consistent with findings obtained from satellite-based drift, the general dynamics of the sea ice differs from satellite-based observations, which show rather slow velocities along the coast and higher velocities in the central basin.

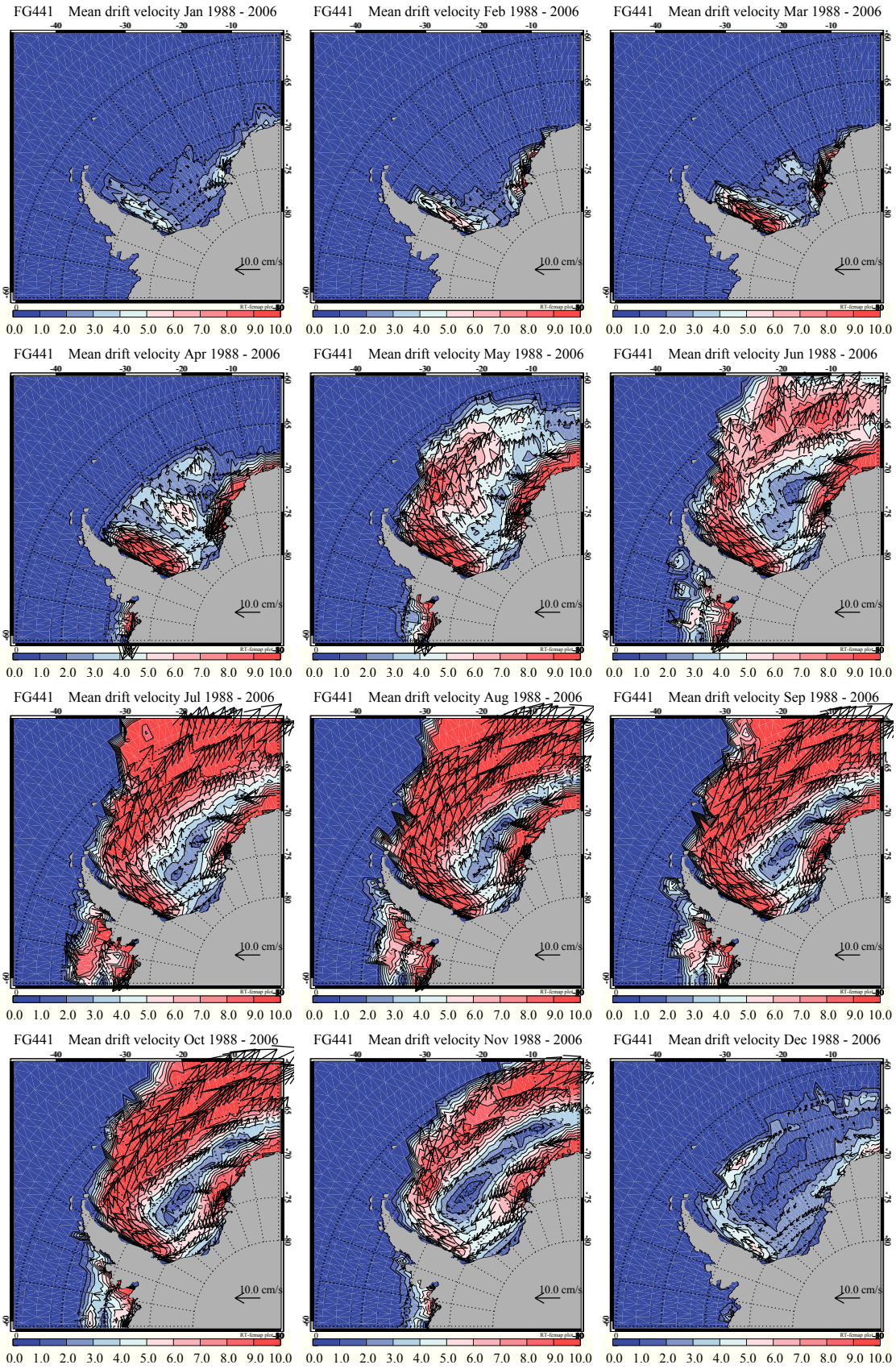

Fig. 5.25: *Modelled monthly mean sea ice drift velocities in cm/s for 1988 through 2006.*

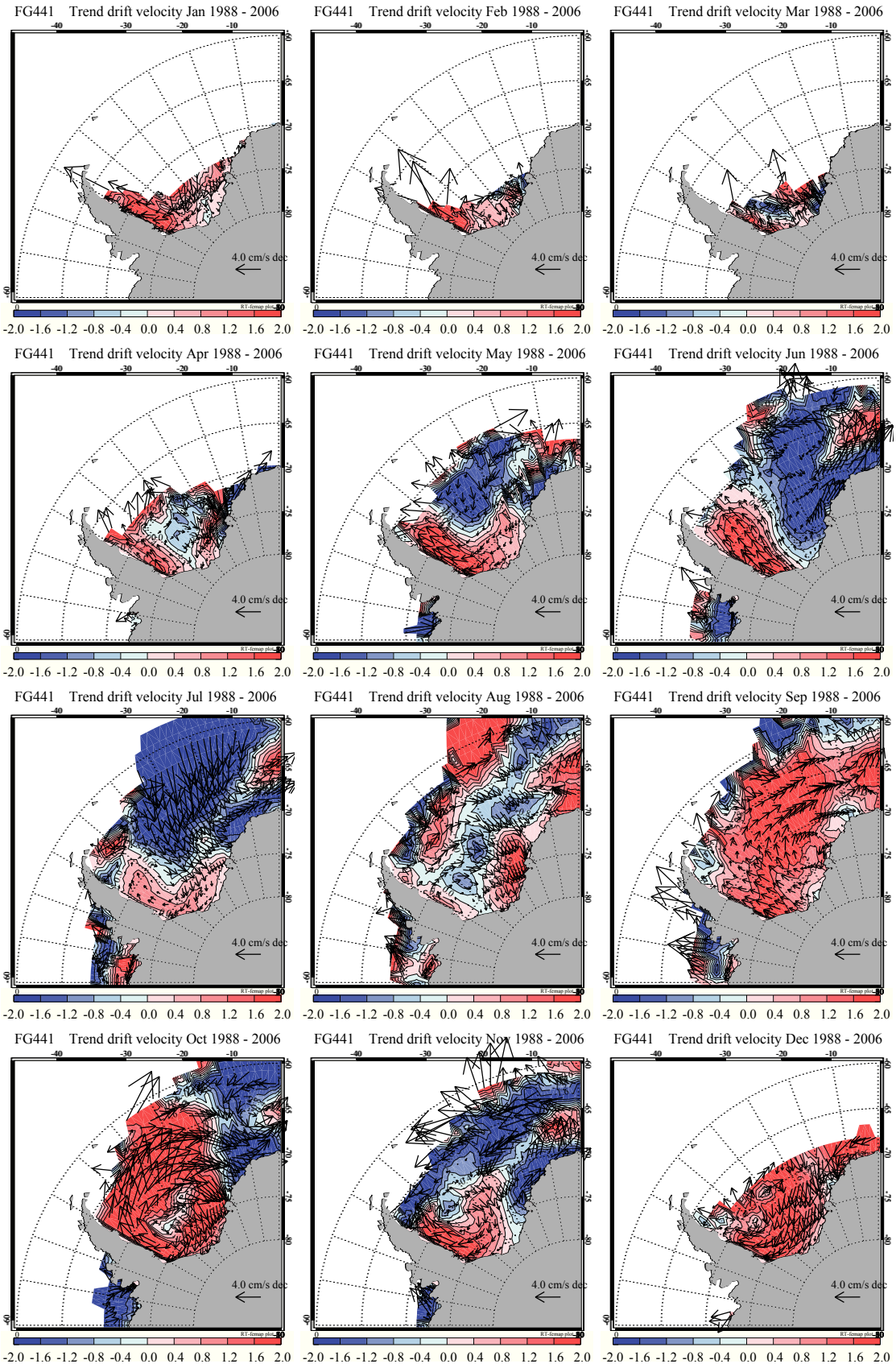

Fig. 5.26: *Sea ice drift trends in cm/s per decade from model simulations for 1988 through 2006.*

Trend analysis of the sea ice motion illustrates that during summer, modelled sea ice motion is accelerated in most parts of the Weddell Sea. However, as for the satellite data, summer results of the model have high inaccuracies and these trends might not be reliable, especially since they are statistically insignificant. In the central Weddell Sea, mostly negative trends establish and trends of the drift direction vary strongly over the year. In some months, the Gyre circulation strengthened (e.g. August, October), whereas in some other months (e.g. June and September), sea ice drift had a stronger northward component, especially in the central Weddell basin. However, in most months, sea ice drift in the central Weddell basin exhibits a decreasing meridional component. The near-coastal region along the Antarctic Peninsula generally represents accelerated drift, except for a small region at the northern tip of the Antarctic Peninsula, as was already described for the (geostrophic) wind field in Chapter 2 for this region. Along the east-coast, the mean westward drift decreases. Apart from the decreased sea ice drift in the central Weddell basin in May, only few of the calculated trends are statistically significant at the 95 % interval.

For the same coordinates as in Section 5.2.3 (see Fig. 5.16), time series were analyzed to reveal the interannual and decadal changes of modelled sea ice drift. Figure 5.27a and b show examples for the inflow current of sea ice in the eastern Weddell Sea. In this region, sea ice velocities lie between about 5 cm/s and up to about 30 cm/s. Except for the period from 1996 till 2006, Figure 5.27a illustrates accelerated sea ice drift for nearly every period, with the longest time series showing statistically significant trends (indicated by solid lines). However, towards the west, at position 2, the prevailing drift patterns look quite differently. Sea ice motion at position 2 and 3 is generally lower and decreases for all periods. The interannual variability of modelled sea ice drift in this region is relatively high for all 3 positions. For the western Weddell Sea, represented by position 5 in Figure 5.27c, the mean sea ice drift velocities lie generally between 0 and 15 cm/s. Trends of up to 0.12 cm/s per year are positive in the model simulation for all periods. In this region, sea ice is on average slower compared to the eastern region, which is consistent with findings from satellite-derived sea ice drift. Trends for position 4 (north-western Weddell Sea) are difficult to interpret, since the model underestimates sea ice extent in this region so that there are many data gaps. In the central Weddell Sea, exemplarily shown by position 6 in Figure 5.27d, sea ice motion is generally low. For position 6, the slightly positive trends for the different periods are generally statistically insignificant, while for position 8, the positive trends are higher and mostly significant. Compared to the satellite-derived sea ice drift, there are pronounced differences. Except for position 1, which shows very similar features, trends differ generally in sign. That this is not only due to the fact that single grid points were selected for the time series analysis,

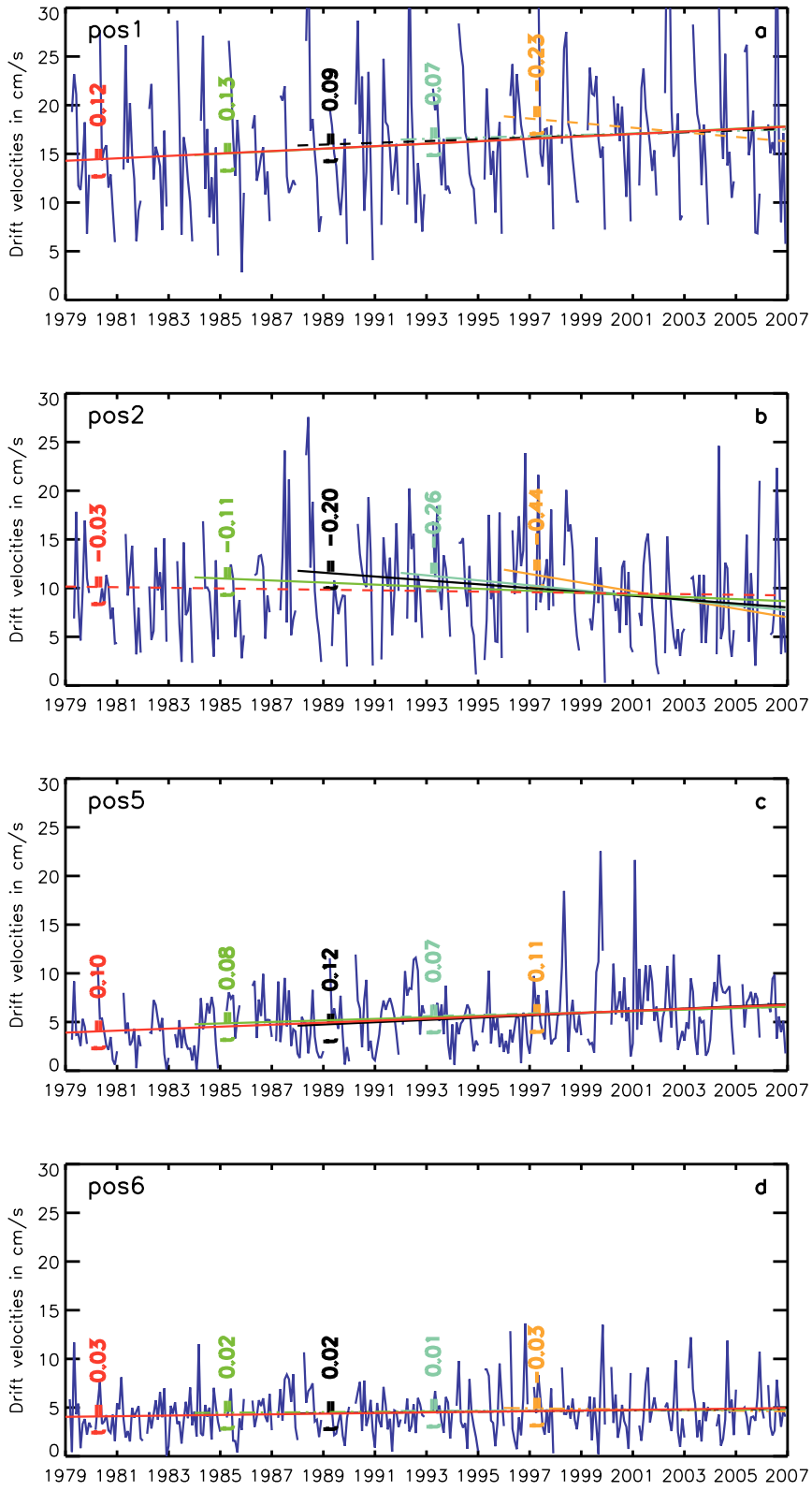

Fig. 5.27: *Time series of sea ice drift velocities and their trends for specified positions according to Figure 5.16.*

which is supported by, e.g., the maps of long-term trends of sea ice drift for both data sets (see e.g. Fig. 5.13 for satellite- based sea ice drift and Fig. 5.24 for results from FESOM). To find out, which parameter might be responsible for the apparent differences between model simulations and observational data, a sensitivity study based on the free drift model was performed.

5.3.3 Sensitivity studies with the free drift model

The last section showed that modelled sea ice drift is partly overestimated and differs from the satellite-based sea ice drift product from the NSIDC. Therefore, a sensitivity study was performed to reveal the origin of inaccuracies in the model. This study is based on a free drift model, since the simplified approach allows for an easy treatment of the sea ice and for an easy performance of a parameter study.

The free drift model considers the momentum balance (Eq. B.37) including the wind and water stresses, the Coriolis and the pressure gradient forces, but neglects the internal stresses given by $\vec{F}$ and the net acceleration ($m\partial\vec{u}/\partial t$) (*Rothrock*, 1975b; *Thorndike & Colony*, 1982; *Connolley et al.*, 2004). This approach is suitable for ice coverage with ice concentration less than 80$\%$ (e.g. *McPhee*, 1980) and in regions far away from coastal boundaries[2].

To keep results as close as possible to those of the standard run in FESOM, 10-m wind speeds from NCEP and ocean currents derived from FESOM are used for the calculation of the free drift. Results from this simplified model are compared to buoy-derived sea ice motion to reveal the impact of different parameters on the agreement between observations and model results. Therefore, sea ice thicknesses are varied between 0.5 m and 3 m in different realizations. The respective value is used over all grid cells (the same sea ice thickness for all grid points), because the actual sea ice thickness distribution in the Weddell Sea is not well known and the free drift model does not need sea ice thickness gradients but only its absolute value. Additionally, this simplified calculation allows to study the impact of different sea ice thicknesses on the sea ice drift and hence to estimate the impact of erroneous sea ice thicknesses in the model simulations on the sea ice drift. Results from various model realizations with ocean currents taken from the uppermost level (0 m) are shown in Figure 5.28 for the zonal (a) and meridional (c) sea ice drift components in comparison with buoy data (black curve). The free drift overestimates the sea ice motion nearly throughout the year for both the zonal and meridional components. Increasing the

[2] *Thorndike & Colony* (1982) found that the stability index r^2 between sea ice drift and wind falls from 0.85-0.95 down to 0.5 for regions with less than 400 km distance from the coast in the Arctic.

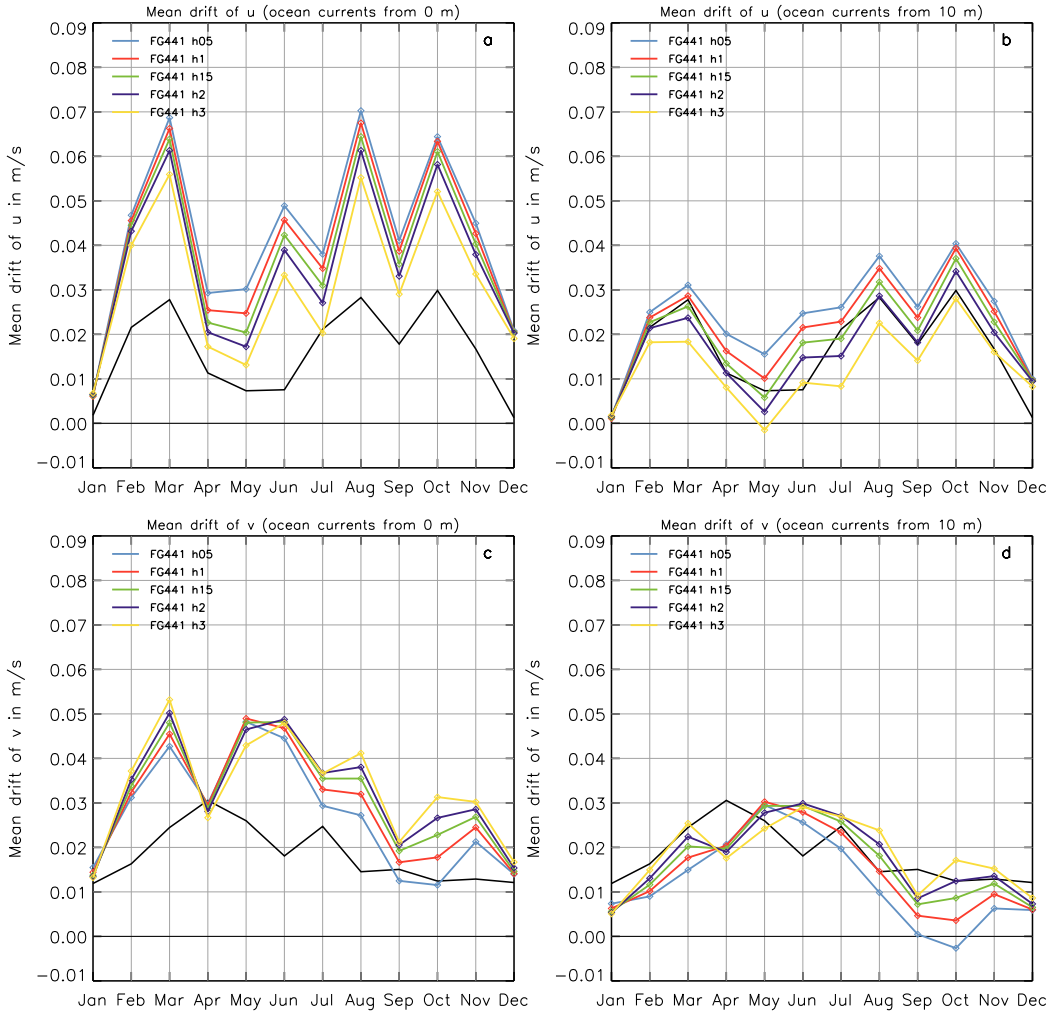

Fig. 5.28: *Comparison between free sea ice drift (coloured curves) and in-situ buoy drift (black curve) for the zonal (a, b) and meridional (c, d) sea ice drift components for the period 1989 through 2005. Data on the left side were calculated with ocean currents from FESOM in a depth of 0 m and those of the right side from a depth of 10 m.*

sea ice thickness results only in a small improvement; changes of 50 cm more (less) ice result mostly in only approximately 0.2 cm/s more (less) sea ice drift in zonal or meridional direction and in an absolute maximum difference of about 0.6 cm/s. For the zonal drift, velocities decrease with increasing sea ice thickness. For the meridional component this relation does not hold, in most cases the thicker sea ice moves faster than the thinnest ice. This is quite unexpected and needs further investigation in future work.

In addition to varying sea ice thicknesses, also a different set of ocean currents was used. On the one hand, ocean currents from level 2 (10 m depth) have been tested. Results are shown in Figure 5.28b and 5.28d for both sea ice drift components and again for varying sea ice thicknesses. The relation, that increasing sea ice thicknesses results in reduced sea ice motion in zonal, but mostly increased drift in meridional

directions holds here, too. Furthermore, results agree remarkably well with buoy observation for both drift components. Hence, changing the level from which ocean currents are taken results in a significant improvement of the modelled sea ice drift, while the impact of the sea ice thickness is less strong. In a second application of ocean currents, time-invariant climatologies were used for the simulation of the free drift. Results are shown in Figure 5.29 for the zonal (a) and meridional (b) drift component, modelled with ocean currents from level 2. Changes between both ocean current realizations are comparatively low. The most pronounced differences occur in May and June for the meridional drift component.

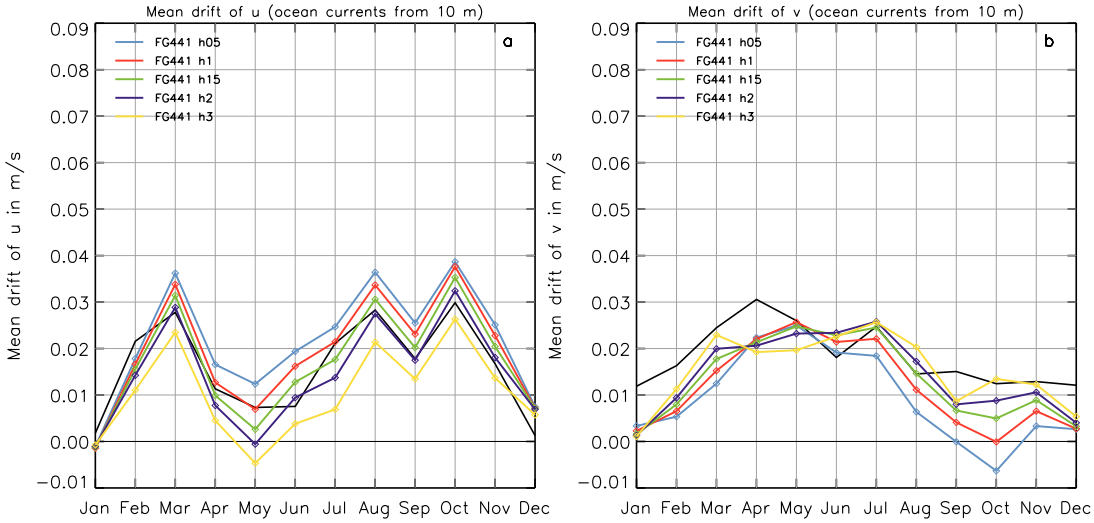

Fig. 5.29: *Comparison between free sea ice drift (coloured curves) and in-situ buoy drift (black curve) for the zonal (a) and meridional (b) sea ice drift components by using time-invariant climatological ocean currents from a depth of 10 m.*

In addition, another test was performed to assess the impact of stresses which act on the sea ice. For the standard model run, atmospheric and ocean stresses suggested by *Timmermann et al.* (2009) were used with the drag coefficients $c_{d,ai} = 1.32 \cdot 10^{-3}$ for the atmospheric and $c_{d,oi} = 3.0 \cdot 10^{-3}$ for the ocean stresses. In a second realization, stresses suggested by *Harder & Fischer* (1999) with $c_{d,ai} = 1.6 \cdot 10^{-3}$ and $c_{d,oi} = 4.5 \cdot 10^{-3}$ were used in the free drift model. The ratio between both coefficients, which is expected to have a stronger influence on sea ice drift than the individual drag coefficients (e.g. *McPhee*, 1980; *Harder & Fischer*, 1999), changes from 0.44 in the standard model run to 0.36 in the test model run. For the zonal drift component, changing drag coefficients result mostly in a decrease of sea ice drift velocities. Differences between mean sea ice motion from the standard model run and the test run have a maximum of about 2 cm/s for the respective sea ice thickness. For the meridional component, a variation of drag coefficients results in fluctuations between lower and higher sea ice drift without any relationship to the prevailing drift

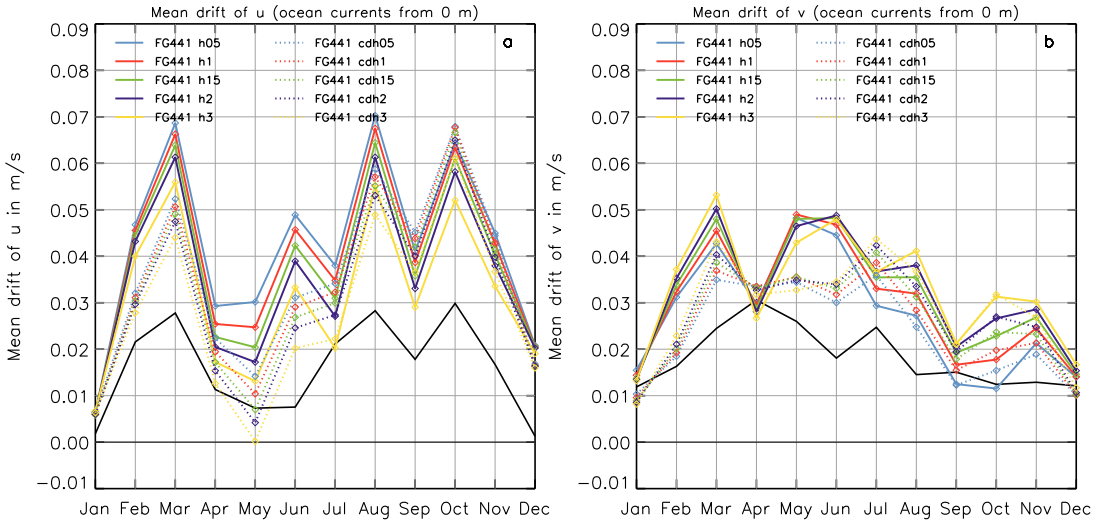

Fig. 5.30: *Comparison between free sea ice drift and in-situ buoy drift for the zonal (a) and meridional (b) sea ice drift components. Solid lines show results from the standard model run with drag coefficients suggested by (Timmermann et al., 2009). Dotted lines show the respective drift calculated with drag coefficients suggested by (Harder & Fischer, 1999).*

velocity[3]. The largest discrepancies are approximately 1.5 cm/s for the meridional sea ice velocity. Hence, the adequate selection of drag coefficients has a stronger impact on modelled sea ice drift than reasonable sea ice thickness variations. Nevertheless, the highest impact on sea ice drift is still given by the selection of the ocean level, which determines the bottom stress. Compared to sea ice drift calculated from buoys, free drift calculated with currents from ocean level 1 (0 m) overestimates buoy drift by up to 4 cm/s for the zonal and up to about 3 cm/s for the meridional component. Such a strong overestimation was also calculated from the comparison of FESOM-based sea ice drift with buoy data. Neither varying the sea ice thickness in an adequate range, nor changing the drag coefficients results in a higher agreement than a change from ocean level 1 to ocean level 2. Results from a calculation with ocean currents from level 2 (10 m depth) with drag coefficients suggested by *Timmermann et al.* (2009) show the highest agreement with buoy data. With few exceptions, drift velocities from this realization with varying sea ice thicknesses fluctuate by about $\pm$ 1 cm/s around the buoy-based drift, depending on the selected mean sea ice thickness.

Figure 5.31 illustrates the mean sea ice drift field derived from the free drift model with ocean currents from level 1 and a mean sea ice thickness of 1.5 m. As was found for the modelled sea ice drift from FESOM (as well as for the 10-m wind speeds), sea ice drift in the northern Weddell Sea is basically fairly high and eastward directed. In the

[3] i.e. whether the difference between sea ice drift from the standard model run and the sea ice drift considering the *Harder & Fischer* (1999) coefficients is positive or negative does not depend on the mean drift velocities.

central basin, sea ice drift is lower. The coastal regions show slightly higher sea ice velocities than the central Weddell basin. In general, sea ice drifts slightly faster than in the standard run of FESOM. Sea ice drift trends are also in general the same.

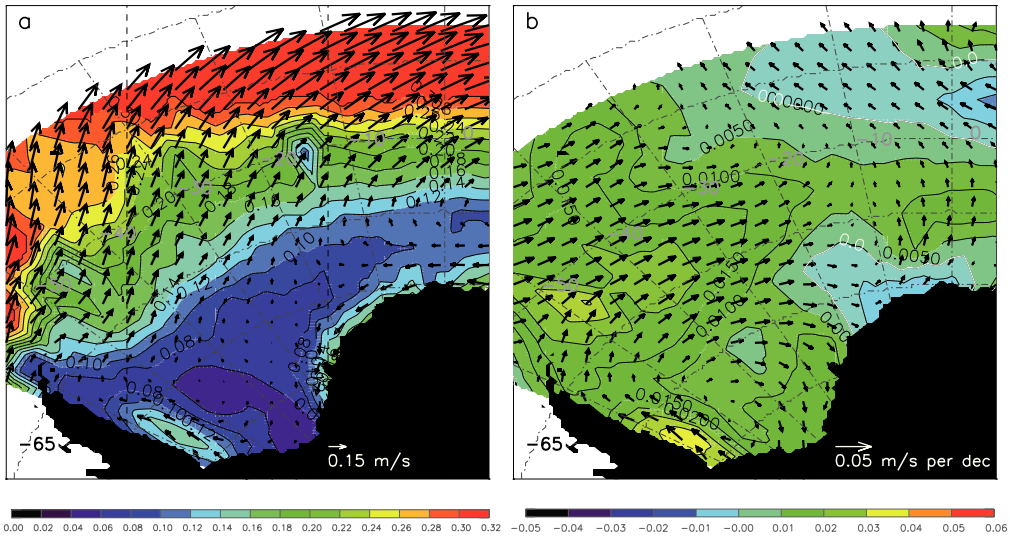

Fig. 5.31: *Mean sea ice drift in m/s (a) and its trends in m/s per decade (b) for the period 1979 through 2006, derived from the free drift model by using FESOM time-variant ocean currents from level 1, 10-m NCEP wind speeds and a mean sea ice thickness of 1.5 m.*

To assess, how much of the observed trends in modelled sea ice drift are due to changes in the atmospheric forcing and how much the ocean contributes to them, trends of the free drift with climatologies of 10-m wind speeds from NCEP were calculated. Figure 5.32 illustrates the mean sea ice drift field gained by the combination of wind climatologies and time-variant ocean currents from level 1 (5.32a,b) and level 2 (5.32c,d). Both fields were calculated with a mean sea ice thickness of 1.5 m and drag coefficients suggested by *Timmermann et al.* (2009), since this model realization agrees best with the buoy observations when ocean currents from level 2 are considered. The mean drift field derived with level 1 ocean currents (5.32a) shows a very similar pattern as for the mean drift derived with time-variant 10-m winds. That the sea ice motion from time-invariant wind fields (Fig. 5.32) is lower than that calculated from time-variant wind fields (Fig. 5.31) is due to the quadratic impact of wind velocities on the sea ice drift given in $\vec{\tau}_{ai}$. First averaging of the winds and then calculating the mean drift fields results therefore in a lower sea ice drift than first deriving sea ice drift and performing the averaging afterwards. Due to this treatment, trends are also slightly lower for this calculation. Ocean currents at the surface are strongly related to the wind forcing. Therefore, trends in the ocean surface current field are very similar to those in the 10-m wind field. Hence, to account for possible trends in the interior ocean that are not directly

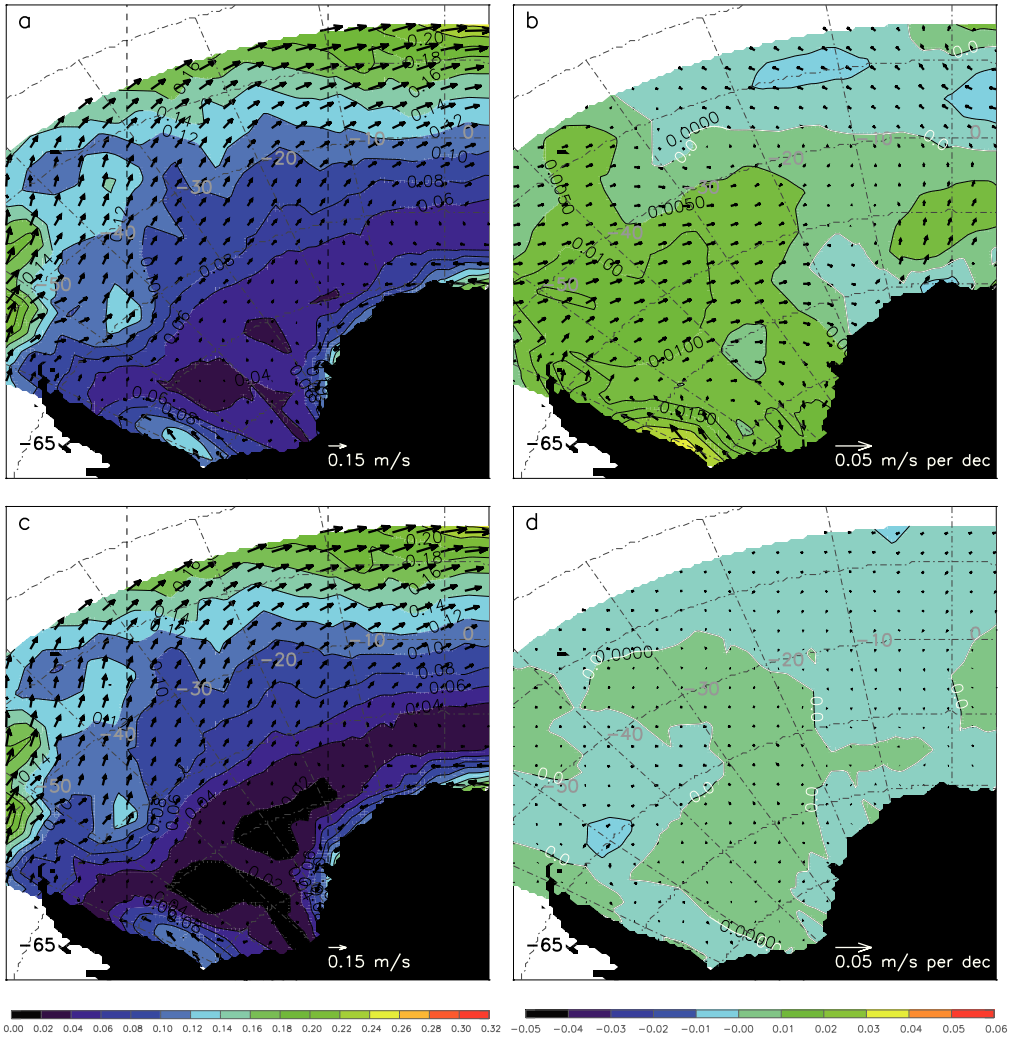

Fig. 5.32: *Mean sea ice drift in m/s and trends in m/s per decade for the period from 1979 till 2006, derived from the free drift model by using FESOM time-variant ocean currents from level 1 (a,b) and level 2 (c,d), 10-m NCEP wind speed climatologies and a mean sea ice thickness of 1.5 m.*

driven by wind forcing variability, the ice-ocean stress was computed using ocean velocities from 10 m depth. It is illustrated in Figure 5.32, that the mean sea ice drift describes nearly the same features, but with slightly lower velocities. Trends are very low and show barely the same structures as calculations with ocean currents from level 1. This induces the conclusion that most of the observed trends in the sea ice drift field modelled with the free drift approach as well as in FESOM, result from the atmospheric forcing that is prescribed by NCEP data.

To depict, whether inaccurate sea ice thickness simulations in FESOM have an impact on the sea ice drift in the model, Figure 5.33 shows the modelled mean sea ice drift fields and their trends for two examples: one realization was done with a mean sea ice thickness of 0.5 m and the other one with a mean sea ice thickness of 2 m.

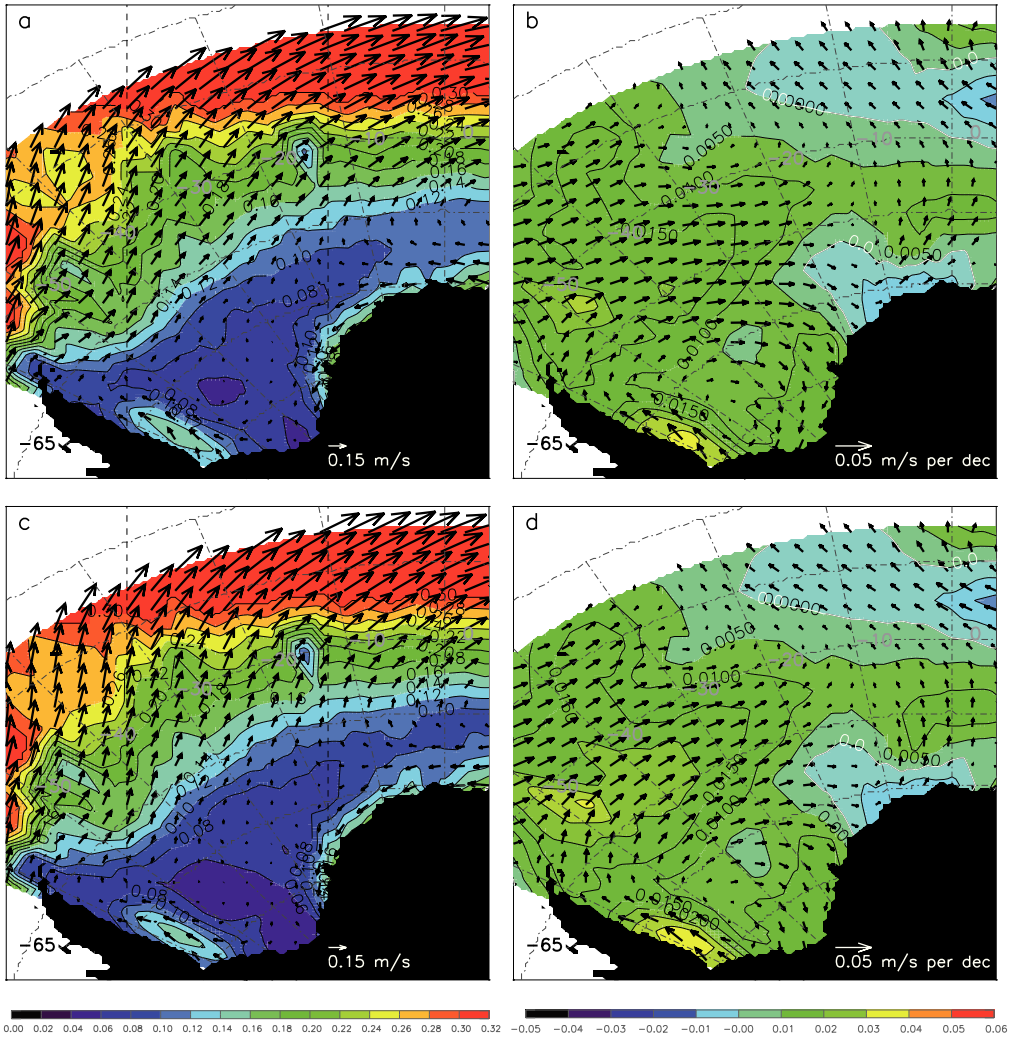

Fig. 5.33: *Mean sea ice drift in m/s and its trends in m/s per decade derived from the free drift model for the period 1979 through 2006. Mean sea ice thickness was fixed at 0.5 m (a,b) and 2 m (c,d). Ocean currents were derived by FESOM in 0 m depths. Drag coefficients are those suggested by Timmermann et al. (2009).*

These fields were derived with time-variant ocean currents at level 1 (0 m), which are used in the standard model run of FESOM, and with atmospheric and oceanic drag coefficients suggested by *Timmermann et al.* (2009). The general patterns of the mean sea ice drift field as well as for the trend distribution do barely change. Some of the trends are slightly (but not considerably) lower in the north-western Weddell Sea for an ice thickness of 0.5 m. Only the direction of the mean drift and the related trends change a bit. Both are slightly deflected to the left for the thicker ice (2 m). Hence, the biased simulation of sea ice thicknesses in FESOM has certainly an influence on regional drift directions. Nevertheless, the impact is not very strong: neither trends, nor the mean sea ice drift velocity are affected strongly. The largest impact on results for the standard model run from FESOM is expected to occur near the northern part of the Antarctic Peninsula, where sea ice thicknesses are especially

underestimated. Hence, modelled sea ice motion is potentially slightly higher because of the comparatively low sea ice thicknesses and might have a bias to lower meridional velocities. However, this impact is less pronounced than the impact that the selection of the ocean level and the influence of the NCEP forcing has on the sea ice drift. With an improved model version, that is coupled with ocean currents from level 2, the sea ice thickness distribution might agree much better with observations, and hence, the influence of an underestimation of sea ice thicknesses might be insignificant. However, this requires an adequate description of the atmospheric field, since the model would otherwise not be able to simulate representative sea ice properties, in any case.

5.4 Discussion

The analysis of satellite-based and modelled sea ice drift fields and their trends revealed for both data sets that sea ice drift velocities are generally lower in summer compared to the other seasons. In addition, also the very high mean sea ice drift in September and its trend over the study period are depicted in both data sets. However, satellite-based and simulated mean sea ice drift also differ in some regions and show partly opposite trends as, e.g., next to the Antarctic Peninsula. In this region, satellite-based data indicate that sea ice drift is very slow and shows a further decreasing trend over the study period. Model simulations, on the other hand, exhibit very high sea ice motion in this region with further increasing drift velocities. Furthermore, also in the inflow area, trends are not consistently the same. The analysis of time series for specific grid points near the coast of the eastern Weddell Sea showed that trends at the easternmost grid point are comparable in both data sets, but further to the west, next to the Brunt Ice Shelf, trends generally differ in sign. While satellite-based sea ice motion increased in this region, model simulations show decreasing trends. The determination of sea ice motion near the coastal boundaries is overall challenging, since both observations as well as model simulations have generally higher uncertainties in these regions. Satellite data, on the one hand, cannot resolve strong deformation processes and might therefore only detect low sea ice motion, which does not cause heavy deformation. FESOM, on the other hand, might not be able to resolve a small band with low drift velocities next to the coast due to its coarse resolution. Nevertheless, there are also differences in the drift regimes off the coastal boundaries in both data sets, such as the increase of mean sea ice drift velocities from the western Weddell Sea towards the eastern Weddell Sea in the satellite-based data set, while the model simulations from FESOM show the lowest

mean drift velocities in the central Weddell Sea.

Studies from, e.g., *Kottmeier & Sellmann* (1996) and *Emery et al.* (1997) indicate, that the near coastal drift velocities at the Antarctic Peninsula are actually slightly lower than further offshore. *Emery et al.* (1997) also used year-round averaged satellite-based drift vectors from the 85.5 GHz SSM/I channel and might therefore have similar sources for uncertainties as the satellite-based sea ice motion utilized in this study, but *Kottmeier & Sellmann* (1996) calculated sea ice drift from independent *in-situ* data such as drifting buoys and ship-based measurements. According to *Kottmeier & Sellmann* (1996), low drift velocities appear also in the central Weddell Sea between 10^{o}W and 30^{o}W. In the satellite-based sea ice drift fields this feature is barely present. FESOM instead simulates low drift velocities in the central Weddell Sea, although this feature is spatially overestimated, since low sea ice motion occurs as far as 50^{o}W. However, *Kottmeier & Sellmann* (1996) did not calculate year-round or long-term averages and hence the compared features are not derived for the same time periods.

The fact that satellite-based as well as simulated sea ice drift suffer from inaccuracies is shown in a comparison with buoy data for the period 1989 through 2005. This study indicates that satellite-based sea ice motion is mostly underestimated in the Weddell Sea, while model simulations rather overestimate buoy-derived drift velocities. The origin of this overestimation in model simulations was investigated by sensitivity studies from a free drift model. The free drift model showed that trends in the sea ice drift are mainly forced by the wind stress provided by NCEP, since ocean currents barely show any trends. Hence, discrepancies between modelled and satellite-based trends in sea ice motion are certainly partly due to the atmospheric data. Comparing the wind fields with satellite-based sea ice drift for the period from 1988 till 2006 revealed that there are large differences between trends of both data sets and that there are only few agreements for individual regions (mostly far from coastal boundaries and the marginal sea ice zone) in some months (e.g. March, July, September, not shown). Since data coverage in the Southern Ocean is sparse, NCEP data might be predominantly based on model simulations, especially in winter, when *in-situ* data from ships are rarely available. On the other hand, also buoy and satellite data are included in the assimilation system of the reanalysis product and additionally, coastal regions are covered by automated weather stations which measure the atmospheric components regularly throughout the year. Hence, near-coastal NCEP data might be based stronger on observations compared to other parts of the Weddell Sea. Therefore, they may be more accurate in these regions. Nevertheless, especially in the coastal regions, agreements between free drift and satellite-based sea ice drift trends are low. Indeed, one has to keep in mind that

the free drift model is not applicable in the near-coastal regions. Thus, the relation between wind speeds and sea ice drift might be low since internal stresses affect the sea ice drift strongly in these locations. However, comparable to the free drift model also FESOM simulates strong sea ice drift velocities next to the coast, indicating that internal stresses in the model do not change the sea ice drift enough to simulate drift fields in better agreement to the Polar Pathfinder sea ice motion.

From a comparison of buoy-derived and modelled sea ice drift using the free drift model, it was found that modelled ocean currents from level 1 are strongly affected by wind stresses and might impose a too strong feedback between the ocean and the sea ice. The modelled drift velocities might be improved significantly when the coupling between the sea ice and the ocean in the model is done by using modelled ocean currents from level 2, i.e. in 10 m depth. At a first guess, this might also improve the sea ice thickness distribution. The general overestimation of drift velocities in the current model version might introduce a strong redistribution of sea ice with a large export of thick, deformed sea ice and a production of much thin sea ice in leads, which would open up due to strong divergent drift. This could bias the total mean sea ice thickness to lower values. This would be an explanation for the especially low October mean sea ice thickness in the model simulation, compared to the ICESat mean sea ice thickness (see Section 4.3.2), because sea ice drift is strongly overestimated especially in this month. Since the remaining thin sea ice can be melted much faster than thick sea ice (that has been exported), summer SIE, SIC and thicknesses are expected to be underestimated in the model simulations. During the summer months, much more heat is stored in the water column because of the missing sea ice and, therefore, winter sea ice growth would start late. However, testing the sea ice thickness distribution in a new model version, which uses ocean currents from level 2 for the sea ice-ocean coupling, does not fulfill these expectations. SIE near the Antarctic Peninsula is often lower in the new realization and the distribution of thin and thick ice does not change satisfactorily.

Throughout this work it was discussed, that the NCEP reanalysis forcing used for FESOM simulations might not adequately describe the atmospheric field, especially near the Antarctic Peninsula and that some of the inaccuracies in FESOM might originate from inaccuracies in the NCEP data. Therefore, it would be meaningful to make a more detailed comparison between reanalysis and *in-situ* data. This might answer the question how accurate NCEP data are in the Weddell Sea and therefore, whether model biases originate from the reanalysis data. Unfortunately, the majority of drift buoys did not measure the wind speeds, but most of them measured at least the sea level pressure regularly, from which geostrophic winds can be determined. In addition, automated weather stations collect data at the

shores year-round. Nevertheless, for a comparison between NCEP reanalysis and *in-situ* data, one has to consider that the NCEP data are not independent of most of these observations, since they are most likely used in the reanalysis assimilation. A comparison between different reanalysis products, such as NCEP and ECMWF might also indicate some weaknesses in the individual atmospheric forcing data sets.

A weakness of the evaluation of large-scale sea ice drift data products with small-scale, high resolution buoy data is the difficulty that buoys describe more or less the movement of a single floe. Large-scale products identify, on the other hand, the sea ice drift of an array of sea ice floes. *Heil et al.* (2001) argued that in regions with prevailing convergent sea ice drift, single floes describe more or less the velocities of large-scale arrays. They further state that large parts of the Weddell Sea underlie convergent sea ice drift conditions. The NCEP reanalysis data indicate that 10-m wind fields are mainly convergent in the Weddell Sea, but satellite-based sea ice drift data show that large parts of the central Weddell Sea exhibit divergent sea ice drift. This finding is supported by different small scale studies, in which divergent drift was observed on average in different parts of the Weddell Sea (*Wadhams et al.*, 1989; *Vihma et al.*, 1996; *Heil et al.*, 2008). This would imply that the evaluation of sea ice drift from large-scale products might not be representative by using individual daily buoy data. One problem is that daily buoy-derived drift may include small-scale sea ice drift changes, which satellite data cannot identify. Therefore, satellite-derived sea ice drift might underestimate buoy-derived drift velocities. Additionally, the lowest detectable daily satellite-based drift velocity is bonded to the spatial resolution of the data product (*Emery et al.*, 1997). If sea ice displacements are much lower than the horizontal resolution of the used grid, they cannot be detected. Moreover, very fast daily sea ice motion might also not be detected by the CCM using satellite data, since detectable structures would rapidly change in the backscatter signals. For comparisons between *in-situ* data and large-scale products, monthly mean sea ice drift might be more usable, because small turbulences on daily basis, such as frequent direction changes due to, e.g., tides or storm activities, would be smoothed in the buoy data sets. This is also supported by the fact that buoy-tracks of monthly data averages show similar features as are indicated by monthly mean satellite data. Whether large-scale products can actually be evaluated by small-scale and high resolution buoy data in an adequate way, could be identified by an analysis of the errors, which are made when comparing both data sets. One could prove, for example, whether single floes deviate strongly from the group velocity of sea ice, by comparing the centroid velocity of a buoy array with the drift velocities of the individual buoys. Such an analysis would need arrays of buoys, like those, which were deployed during the ISPOL campaign in 2004 (see e.g. *Heil et al.*, 2008). The calculation could be

made for several arrays with different diameter to detect the influence that the spatial resolution of the used data products has. Additionally, different sea ice and boundary conditions, like the influence of the continental shelf or different time-scales (e.g. daily and monthly sea ice drift), could be tested. *Heil et al.* (2008) found for the western Weddell Sea in austral summer that sea ice drift from buoys within a separation length of up to 70 km is coherent. This would correspond to about three grid cells in the satellite-based sea ice drift data set, but less than one grid cell in model simulations. Furthermore, they found that correlation between the zonal as well as the meridional velocities of buoys have coefficients of more than 0.8 within an array of 60 km length for hourly drift velocities. For future work, the study of *Heil et al.* (2008) could be expanded to different time scales, such as daily, weekly or monthly averages, and can be performed for much more buoy arrays using data from former buoy deployments (see Fig. 5.2). Moreover, a comparison of single floes as well as group velocities of buoy arrays with satellite-derived sea ice drift would indicate, whether there is a need for improving the comparison scheme, i.e. comparing only sea ice velocities from arrays with large-scale drift products instead of using single buoy data, like it was done in this study.

Chapter 6

Sea ice volume fluxes

The major component of the freshwater budget in the Weddell Sea is the net sea ice mass flux (*Harms et al.*, 2001), next to the net precipitation (the difference between precipitation and evaporation) and the basal melting of the ice shelves. Changes in the freshwater budget have the potential to modify the characteristics of water masses (*Timmermann et al.*, 2001). A net freshwater export due to freezing and sea ice drift, results in a salinity enrichment, due to the fact that only a small amount of the sea water's salt is included in the crystal structure during sea ice formation. The remaining salt is injected into the ocean and increases the density of the water, leading to convection. Melting of the ice results in a freshening, and therefore, in a stabilization of the water column, but due to advection, sea ice is not necessarily melted in the region of its formation, and so, might not be available for a compensation of the exported freshwater. The effects of sea ice mass transport and a related salt release are believed to be of special importance in the Weddell Sea (*Harder & Fischer*, 1999) and may contribute to the thermohaline ocean circulation. Hence, knowledge about the freshwater fluxes is important to obtain a realistic description of the ocean in climate models.

In this chapter, the net sea ice and salt export out of the Weddell Sea basin are analyzed across a flux gate between Kapp Norvegia and Joinville Island. Model simulations from FESOM are used to quantify this net sea ice export and results are compared to fluxes gained by the sporadically observed sea ice thicknesses from ULS-moorings in combination with satellite-based sea ice drift. Additionally, simulated fluxes are compared to results of former studies.

6.1 Calculation of sea ice volume fluxes

For the calculation of sea ice transport, a flux gate between Joinville Island in the west and Kapp Norvegia in the east of the Weddell Sea was defined, whose transects

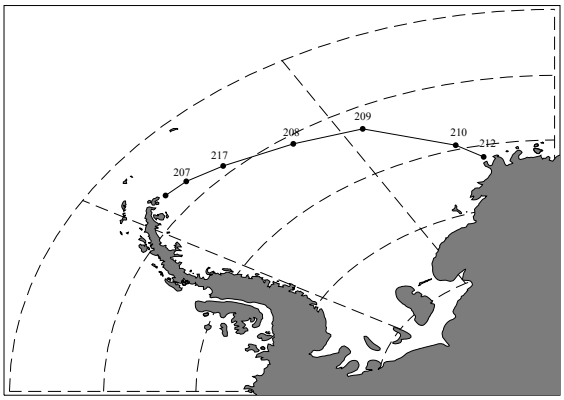

Fig. 6.1: *Flux gate for the calculation of net sea ice volume export from the Weddell Sea. The single transects cross the ULS-mooring positions.*

cross the AWI-ULS mooring sites in the Weddell Sea basin (Fig. 6.1). The transport was calculated using the flux normal to the respective transects of the flux gate. Perpendicular drift velocities ($|\vec{v_p}|$) and sea ice thicknesses (h_i) were determined approximately every 20 km. From both sea ice parameters, the volume flux was derived over all points along a transect from Eq. 6.1 (after *Kwok & Rothrock*, 1999):

$$V_i = \sum_{x_0}^{x_i} |\vec{v_{p_i}}| \cdot \Delta x \cdot h_i. \tag{6.1}$$

V_i	:	sea ice volume flux
$|\vec{v_p}|$	:	sea ice drift normal to the transect
x_0,x_i	:	positions along the respective transect
Δx	:	distances between the x_i
h_i	:	sea ice thickness

Related to the sea ice volume export, and hence the freshwater export, salt included in the ice crystal structure is exported from the Weddell Sea. According to *Harms et al.* (2001) a thickness dependent salinity of sea ice was assumed in this study to account for the fact that the salinity of sea ice decreases because of the continuous desalination after sea ice formation (*Harms et al.*, 2001):

$$S_i = \begin{cases} 7.286 - 1.776 \cdot h_i & \text{for } h_i \leq \text{ 1.85 m,} \\ 4.0 & \text{for } h_i > \text{ 1.85 m.} \end{cases} \tag{6.2}$$

The salt content that is exported out of the Weddell Sea with the sea ice transport is then given by

$$S_e = S_i \cdot \rho_i \cdot V_i \tag{6.3}$$

Nevertheless, the amount of exported salt is small compared to the amount that is released due to sea ice formation, which is assessed by Eq. 6.4:

$$S_r = (S_0 - S_i) \cdot \rho_i \cdot V_i. \tag{6.4}$$

S_0 is the reference salinity of the ocean. It is set to 34.1 psu in this study, a mean value calculated from the Winter Water (34.4 psu) and summer (33.8 psu) salinities (see, e.g., *Harms et al.*, 2001).

6.2 Sea ice volume and salt transport

For each transect of the flux gate, the monthly sea ice volume transport was calculated from i) model simulations and ii) ULS-based sea ice thicknesses combined with the Polar Pathfinder sea ice motion vectors for the deployment phases of the ULS, when both moorings enclosing a respective transect were operated during the same time period. ULS-based sea ice thicknesses and sea ice drift velocities are interpolated onto the same positions from which model results were used. Since sea ice thickness measurements in the Weddell Sea are sparse and the flux gate was never covered entirely for the same time by all moorings, the calculation of the net export across the flux gate from observations was rather done for individual transects than for the entire gate. For the calculation of the volume transport, the sea ice thicknesses of both moorings were linearly interpolated onto the same positions along the transect from which the modelled sea ice thicknesses were taken. These export rates across individual transects were then compared to modelled sea ice fluxes.

Figure 6.2 shows the simulated sea ice volume transport over all transects in the Weddell Sea (blue). Additionally, the red curves illustrate the transport calculated from ULS data and satellite-based sea ice drift velocities (hereinafter referred to as observation-based sea ice volume transport). To calculate the sea ice export between the coast and ULS 207, an additional location was chosen to close the flux gate in

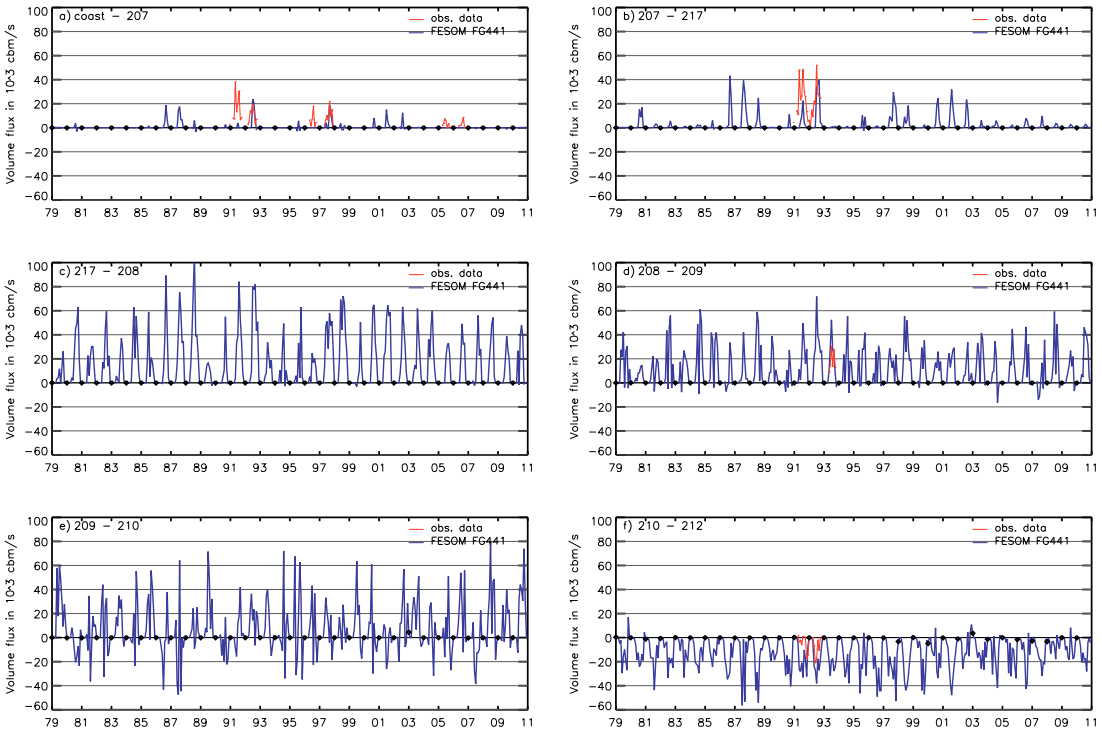

Fig. 6.2: *Monthly sea ice transport in 10^3 m^3/s across the individual transects of the flux gate shown in Figure 6.1 for 1979 through 2010. Blue curves show FESOM results, red curves indicate transport rates gained by observational data. Black dots depict the January of the respective year.*

the west. For the observation-based sea ice export, sea ice thicknesses measured at ULS 207 were projected onto this near-coastal position, i.e. sea ice thicknesses at ULS 207 and the near-coastal position are the same.

The monthly transport rates in FESOM are fairly variable: sea ice export of up to 100 x 10^3 m^3/s, but also negative rates of as much as -60 x 10^3 m^3/s are simulated. Negative rates indicate an import and positive rates an export of sea ice across the transects. The western Weddell Sea is dominated by sea ice export; rates are rarely negative between the tip of the Antarctic Peninsula and ULS 208. For these three transects, the sea ice export increases from the western to the central Weddell Sea (Fig. 6.2a-c). Between ULS 208 and ULS 209, export rates are also mostly positive but slightly lower compared to the transect between ULS 217 and ULS 208. Further to the east, the sea ice transport becomes frequently negative between ULS 209 and ULS 210 and shows nearly always an import of sea ice between ULS 210 and ULS 212. Model simulations agree in some occasions fairly well with the sparse observational data (red curve in 6.2a,b,d,f). Nevertheless, in the western Weddell Sea, sea ice transports seem to be underestimated in the simulations, potentially due to the high underestimation of sea ice thicknesses shown in Chapter 4. In the central Weddell Sea and the eastern inflow

area, on the other hand, sea ice transport is mostly overestimated, certainly an effect of the overestimation of sea ice drift.

Harms et al. (2001) derived sea ice volume export and import rates from ULS data combined with drift velocities from the free drift model according to *Kottmeier & Sellmann* (1996) and found an export of (78 $\pm$ 10) x 10^3 m^3/s for the western Weddell Sea and an import rate of (28 $\pm$ 5) x 10^3 m^3/s for the eastern inflow area. Averaging ice export rates for the same sub-regions over the study period from FESOM results in an export of (37 $\pm$ 50) x 10^3 m^3/s and an import of (15 $\pm$ 19) x 10^3 m^3/s. Hence, both simulated rates are lower than the rates calculated by *Harms et al.* (2001). Data in *Harms et al.* (2001) are averages over different observation periods for the different transects, but an adaption of the average periods for FESOM sea ice transport does not yield other findings. Moreover, the distribution of export rates between the transects differs between both studies. According to *Harms et al.* (2001) and contrary to this study, the export rates in the western Weddell Sea decrease from the west to the central Weddell Sea.

The yearly net sea ice export across the flux gate between Joinville Island in the west and Kapp Norvegia in the east of the Weddell Sea is illustrated in Figure 6.3a, together with results from previous studies. The net export shows high variability over the years. Export rates between -10 and 60 x 10^3 m^3/s are simulated by FESOM but in most years the net export is positive. The mean net sea ice export over the period January 1979 through December 2010 is 22 x 10^3 m^3/s resulting in a mean salt export of 12 x 10^4 kg/s. However, the main part of the salt, about 6 x 10^5 kg/s is rejected during sea ice formation and remains in the Weddell Sea (Fig. 6.3b) with the potential to modify the density structure of the ocean. Since the standard model run does not include shelf ice melting, only the net precipitation accounts for replacing the freshwater export by sea ice volume fluxes. According to *Timmermann et al.* (2001), net precipitation amounts to 19 x 10^3 m^3/s. Therefore, about 3 x 10^3 m^3/s of freshwater are not replaced, resulting in a salinification of the ocean, when no other freshwater is advected into the Weddell Sea.

In Figure 6.3, the yearly averaged sea ice export gained by model simulations is compared to various studies. *Harms et al.* (2001) calculated the export rates by an empirical relation between the length of the sea ice season and the respective mean sea ice thickness combined with drift velocities from a free drift model forced by ECMWF data for the period from 1979 till 1998 (red curve). They found an interannual variability between about 30 and 60 x 10^3 m^3/s, resulting in a mean net sea ice export of 46 x 10^3 m^3/s for the period 1979 through 1998, which is more than two times larger than the ice export simulated by FESOM. The results from *Harms et al.* (2001) are

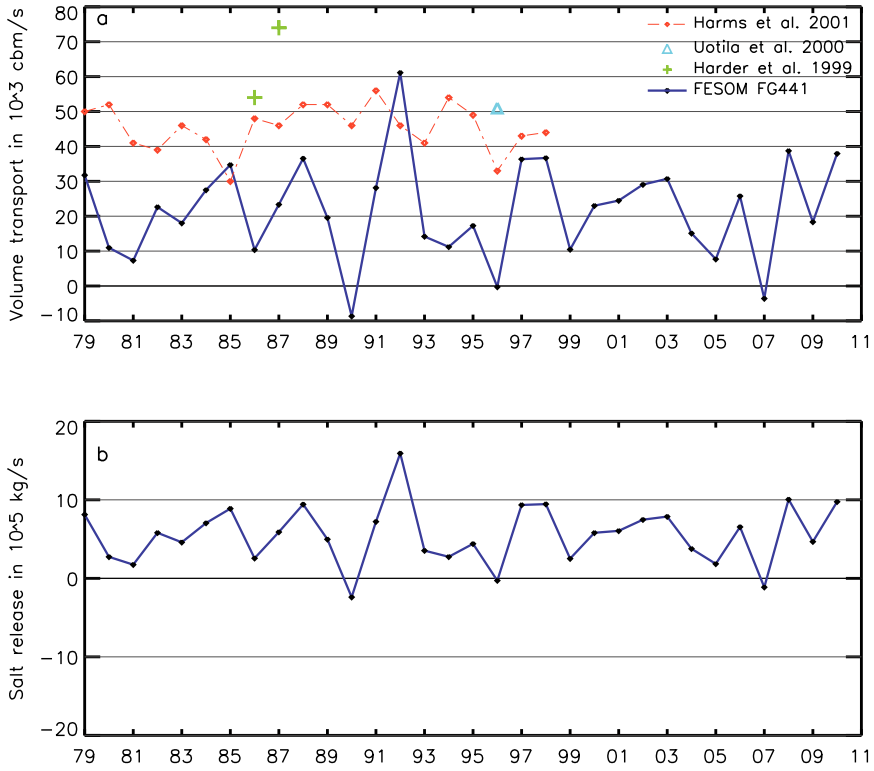

Fig. 6.3: *Yearly net sea ice export (a, in 10^3 m^3/s) across the flux gate between Joinville Island and Kapp Norvegia and salt release (b, in 10^5 kg/s) into the Weddell Sea from 1979 till 2010 (blue).*

comparable to studies of *Uotila et al.* (2000), who found a net export rate of 51 x 10^3 m^3/s in 1996 (blue triangle), combining ULS-based sea ice thickness measurements from 1991/1992 and drift velocities from the free drift model forced by ECMWF data. *Harder & Fischer* (1999) also calculated comparable fluxes of 54 x 10^3 m^3/s and 74 x 10^3 m^3/s across a transect along 68.75°S for 1986 and 1987 with their model simulations (green crosses). The sea ice transport simulations with BRIOS yielded a net mean sea ice volume flux of (42 $\pm$ 26) x 10^3 m^3/s for the period from 1985 till 1993 (*Timmermann et al.*, 2001, not shown). According to the aforementioned studies, based on both observational data as well as model simulations, sea ice volume fluxes from FESOM are mostly underestimated and the interannual variability seems to be overestimated.

Related to the underestimation of sea ice volume export is an underestimation of the net amount of salt released into the ocean. Salt release in the Weddell Sea is the main driver for water mass modification in this region; with less salt release a weaker salinification is expected. However, net precipitation is still lower than the ice-related export of freshwater and other freshwater sources such as ice shelf melting are not considered in the model. As a result, the net freshwater budget of the south-western

Weddell Sea remains negative in FESOM, so that salinification and bottom water formation still occur.

As already mentioned before, the much too low modelled sea ice thicknesses in the west certainly lead to an underestimation of sea ice export in this part of the Weddell Sea. This finding is supported by the comparison with observational-based sea ice volume fluxes as well as from a comparison with export rates from the western Weddell Sea found by *Harms et al.* (2001). Since the underestimation of sea ice thicknesses is very strong, not even the overestimation of drift velocities found in Chapter 5 can compensate for them. In the eastern inflow region on the other hand, sea ice thicknesses are in most cases only slightly underestimated. Since drift velocities are on the other hand overestimated, the import of sea ice might also be overestimated, as is indicated by the comparison with observation-based sea ice volume fluxes, although higher import rates found by *Harms et al.* (2001) oppose this assumption. Nevertheless, in both cases the net sea ice volume and salt export across the entire flux gate would be underestimated: An overestimation of imported sea ice in the east would reduce the net Weddell Sea ice export; but an underestimation of ice import would not compensate entirely for the strong underestimation of the sea ice export in the western Weddell Sea. In addition, the low summer sea ice coverage in the model accounts for low sea ice transports, because the sea ice cover does not reach the flux gate in summer and the transport of sea ice across the flux gate vanishes during these months. For the west Antarctic, this disappearance of sea ice fluxes might also occur throughout summer, since sea ice in FESOM often reach the ULS positions in this region only during winter (see Fig. 4.13, AWI-ULS 207 and 217 for instance). A better realization of sea ice drift velocities in FESOM might adjust the sea ice transport in some regions, but since the coarse resolution as well as the atmospheric forcing potentially prevent a reliable representation of sea ice thicknesses in the coastal regions and in the western Weddell Sea, the model might not be able to calculate adequate transport rates within the here presented realization.

Chapter 7

Summary

The aim of this study was to assess the interannual and decadal variability of sea ice drift, thickness and concentration in the Weddell Sea and their connection with each other. Large-scale data products were validated with small-scale *in-situ* data and were finally used to gain the temporal changes in SIC and drift. A second goal was to validate the Finite Element Sea ice-Ocean Model (FESOM) and to use the model simulations for filling the gaps of observational data, especially regarding the sea ice thickness distribution.

From an analysis of the atmospheric fields provided by NCEP, it was revealed that air temperatures generally increased in the central Weddell Sea throughout the year. Only in summer a cooling can be observed. In addition, the northern parts of the Weddell Sea frequently show a cooling. Wind speeds increased for large parts of the Weddell Sea on a year-round basis. Few exceptions arise in the eastern Weddell Sea: The westward wind along the eastern coast, next to the Fimbul Ice Shelf and the eastward wind in the north-eastern Weddell Sea decreased. It was expected, that these changes in the atmospheric state have an impact on the SIC and the sea ice drift.

It was found that SIE and ice covered area increased in the Weddell Sea by about 0.5 % and 1 % per decade over the period from 1979 till 2006, respectively. The strongest trends were found in summer and autumn and are a combination of increasing ice extent in the central and eastern Weddell Sea and a strong decrease in the western Weddell Sea. These findings are supported by trends in the SIC, which decreased at the Antarctic Peninsula and increased in the east, mostly in the marginal sea ice zone, on a year-round basis. The pack ice zone in the central Weddell Sea underlies only small trends, except for summer, when the marginal sea ice and the central Weddell Sea pack ice zone fall together. Considering the atmospheric changes from NCEP data, correlation between air temperatures and SIC is highly negative in the

marginal sea ice zone, indicating that both variables are strongly connected to each other. On the other hand, in the central Weddell Sea both parameters are positively correlated, especially in winter. It was suggested that increasing northerly winds might force a redistribution of sea ice from the west into the central and eastern Weddell Sea. This redistribution would decrease the SIC in the western Weddell Sea and might increase those in the central Weddell Sea. At the same time, these northerly winds transport warmer air masses into the central Weddell Sea (*Stammerjohn et al.*, 2008). Therefore, enhanced northerly winds in the west, as have been found to occur frequently throughout the year in the NCEP reanalysis data, might force a coincident increase in air temperatures and SIC in the central Weddell Sea. In fact, wind speeds and SIC are anti-correlated at the tip of the Antarctic Peninsula and positively correlated in the central basin. This connection becomes strongest during winter months, when correlation coefficients fall below -0.7 and the positive correlation between air temperatures and SIC in the central Weddell Sea is most pronounced. In the coastal regions in the eastern Weddell Sea, decreasing wind speeds are connected to higher SIC in summer and autumn, indicating that the decreased transport of sea ice results in higher SIC. In winter, on the contrary, both parameters are positively correlated, i.e. increased wind speeds certainly force sea ice to be more compact. This study indicates that most of the SIC changes seem to be reasonably connected to changes in the atmospheric fields.

To analyze changes in the sea ice thickness distribution on large scales, it was tested, whether sea ice class distribution, gained from scatterometer data, can be used as proxy for the sea ice thickness distribution. However, time series are very short (2000 - 2007) and it was not possible to hindcast the sea ice class distribution with model simulations, since it was not possible to connect the sea ice classes FYI and SYI with the sea ice age distribution assessed by BRIOS. The analysis of the short term data set from QuikSCAT indicated that FYI coverage increased during winter, while SYI decreased for the same time. A possible conclusion might be that the mean sea ice thickness over the Weddell Sea decreased in winter, since the impact of the relatively thin first year ice becomes stronger, compared to the impact of the relatively thick SYI. Nevertheless, there was no evidence, that the mean sea ice thickness or volume decreased.

The dynamical changes in the Weddell Sea were analyzed using sea ice drift fields retrieved from satellite derived sea ice motion vectors, which are provided by the NSIDC. The large scale sea ice drift fields were compared to the Lagrangian drift tracks of sea ice buoys, which have been deployed on top of the sea ice for several years until 2005. The comparison revealed that sea ice motion from satellites is mostly too low, especially when the prevailing sea ice motion is high. Furthermore, sea ice

drift fields in the beginning of the satellite observations are optimally interpolated based on only few data points, and therefore, the sea ice drift in large areas in the Weddell Sea is a product of the interpolation of only sparsely or sporadically occurring data. With the launch of the SSM/I in austral winter 1987, data coverage became much higher and sea ice drift fields are found to be more reliable. From satellite observations, the mean distribution of sea ice drift velocities and their trends were derived. The mean sea ice drift velocities are low near the coast and increase towards the central Weddell Sea and the marginal sea ice zone. From both buoy and satellite-derived sea ice drift it was found that the mean velocities increase from the western to the eastern Weddell Sea. Except for spring and for the eastern coastal inflow area, most parts of the Weddell Sea show a prevailing decreasing trend in sea ice motion, especially along the Antarctic Peninsula. These findings contradict the expectations made based on changes in the atmospheric fields from NCEP reanalysis, since these data show basically increased wind speeds in the coastal regions. It was discussed, that increased convergent sea ice drift at the western Weddell Sea might explain the contrary behaviour of sea ice drift and wind speed trends in this region. However, also *Schmitt* (2005) found decreased sea ice drift velocities in the Weddell Sea in her study based on another satellite-derived sea ice drift product.

The correlation between SIC and sea ice drift was difficult to interpret since coefficients barely follow any robust relationship. The correlation in the central Weddell Sea is the most robust one. Except for January and November, sea ice drift and concentrations are mainly anti-correlated. Hence, strong sea ice drift generally reduces the SIC in all seasons and vice versa for slow sea ice drift, which was associated to the predominantly divergent sea ice motion. In fact, enhanced northerly winds would reduce the prevailing north-eastward sea ice drift in the central Weddell Sea, and therefore, would result in an anti-correlation between sea ice drift and concentration.

SIC, drift and particularly sea ice thicknesses were also analyzed using model simulations from FESOM. It was demonstrated in comparisons with satellite based SIC and upward looking sonar data as well as from the few satellite-based sea ice thickness data from ICESat that the distribution of sea ice in FESOM differs from that indicated by observations. In the simulations, the most compact and thickest sea ice is situated in the south-eastern Weddell Sea instead along the Antarctic Peninsula. Both SIC as well as sea ice thicknesses are generally underestimated, but long-term trends especially for SIE and SIC are overestimated in FESOM. The best agreement with observational data is gained in the eastern Weddell Sea. In coastal regions, especially the simulation of the sea ice thickness distribution is restricted by the coarse resolution

of the model that prevents an adequate simulation of deformation processes on small scales. Furthermore, an adequate simulation of sea ice thicknesses is limited by the quality of the atmospheric forcing.

The simulated mean sea ice thickness and the sea ice volume increased slightly for the period from 1979 till 2006. The strongest increase in sea ice thickness occurs thereby at the coast and in the eastern Weddell Sea. Sea ice thickness changes show basically the same tendencies as SIC changes. The comparison of the sea ice volume trends gained from FESOM simulations and from ICESat data show a fairly good agreement.

Regarding the sea ice drift, model simulations were compared to buoy data to gain the model's accuracies. This comparison indicated that sea ice motion in FESOM is generally too high. Throughout the year, but especially in winter, the zonal sea ice drift component is overestimated. In addition, the monthly mean sea ice drift fields and their trends differ from the satellite-based data. In FESOM, the highest drift velocities occur at the coasts and the marginal sea ice zone and the lowest in the central Weddell Sea. Trends are also the highest next to the coasts and the marginal sea ice zone and the lowest in the central Weddell Sea, indicating that the sea ice drift fields in FESOM follow the wind fields from NCEP data. The best agreement between simulations and observations is the consistent increase of sea ice drift in September, while the largest discrepancy occurs in summer, when satellite-based sea ice drift decreases and FESOM reveals increasing sea ice motion.

A sensitivity study based on the free drift model was used to test the impact, which the atmospheric data have on model simulations and to find out, whether, e.g., other drag coefficients or an inaccurate representation of sea ice thicknesses might force the differences compared to observed sea ice drift. It was shown, that the agreement between buoy data and free drift is remarkably improved, when the 10-m winds are coupled to FESOM-based ocean currents gained in 10-m depth instead of using ocean currents from a depth of 0-m. Furthermore, trends in the free drift, and therefore those for drift simulated by FESOM, are basically driven by the atmospheric forcing, since ocean currents do not show strong changes.

Despite the overestimation of sea ice drift in model simulations, sea ice volume transport in FESOM is underestimated, potentially due to the strong underestimation of sea ice thicknesses in the western Weddell Sea. FESOM's simulated net sea ice export rate of about 22 x 10^3 m^3/s is about half of the export rates calculated in previous studies. This sea ice export is to a large amount compensated by net precipitation; only 3 x 10^3 m^3 of sea ice volume are not replaced by other freshwater fluxes in the model.

An improvement of FESOM is necessary, to simulate the state and the changes of the sea ice cover regarding its extent, concentration, thickness and motion and the associated sea ice volume transport rates in an adequate way. Parallel to this study, FESOM has been improved to some extent, major changes include an implementation of ice shelves and a modified realization of lateral melting. New simulations with atmospheric fields from both NCEP reanalysis as well as from HadCM3 (Hadley Centre Coupled Model) have been performed and they look promising: The sea ice distribution seems to be more realistic. The thickest sea ice moves further to the west, closely to the Antarctic Peninsula and also the SIE looks more realistic, although the realization of a realistic SIE at the tip of the Antarctic Peninsula is still a challenge (R. Timmermann, *personal communication*, 2011). Therefore, it seems meaningful to evaluate the atmospheric fields from NCEP by, e.g., studying the variability and trends from data of automated weather stations as well as from drifting buoys. In addition, a comparison between NCEP data and atmospheric fields from the ECMWF might reveal, whether both data sets show the same features or whether the higher resolution in ECMWF data leads to a better representation of sea ice in model simulations, especially in the western Weddell Sea.

It would also be interesting to reveal, whether atmospheric oscillations have a regionally or seasonal dependent influence on the sea ice, since the analysis of the complete time series did not indicate strong connections between these oscillation patterns (such as SAM) and the sea ice drift. Especially the decreased SIC in the western Weddell Sea might correlate well with the non-annular component of the SAM, since this component forces stronger northerly winds at the northern Antarctic Peninsula (*Lefebvre et al.*, 2004), which were expected to decrease the SIC in this region.

Appendices

A SIC from passive microwave brightness temperature data

The data set used for this study is a combination of observations from the Scanning Multichannel Microwave Radiometer (SMMR) on-board the Nimbus-7 satellite and the three Special Sensor Microwave/Imager (SSM/I) sensors of the Defense Meteorological Satellite Program's (DSMP) F08, F11 and F13 satellites (*Comiso*, 1999). SMMR data are available every other day from frequencies of 6.6, 10.7, 18, 21, and 37 GHz, both horizontally and vertically polarized (*Comiso et al.*, 1997). Dual polarized data at 19, 37 and 85 GHz as well as vertically polarized data at 22 GHz are available from SSM/I for each day since September 1987. The latter frequency is used as open ocean mask in the SSM/I data (*Comiso et al.*, 1997). The received signal, the brightness temperatures, is influenced by different physical properties such as surface temperature and emissivity as well as atmospheric scattering and is generally described by the following equation (*Swift & Cavalieri*, 1985):

$$T_B = \epsilon T_S e^{(-\tau)} + \underbrace{T_U + (1-\epsilon)T_D e^{(-\tau)} + (1-\epsilon)T_c e^{(-2\tau)}}_{atmospheric\ correction} \tag{A.1}$$

ϵ	:	surface emissivity
T_S	:	surface physical temperature
τ	:	atmospheric opacity
T_U	:	atmospheric upward radiation (in K)
T_D	:	atmospheric downward radiation (in K)
T_c	:	cosmic background component (in K)

According to Eq. A.1, the brightness temperature is the sum of the surface emission, given by the surface emissivity, the surface temperature in Kelvin[1] and the atmospheric absorption, plus the atmospheric correction term. The latter includes the influence of the reflected emission from space and from the upwelling and reflected downwelling atmospheric radiation (*Swift & Cavalieri*, 1985).

There are different algorithms for the translation of the received brightness temperatures into SIC. Widely used are SIC derived from the bootstrap and the NASA Team algorithms. Here, both are briefly described.

[1] $T(K) = T(^0C) + 273.16$

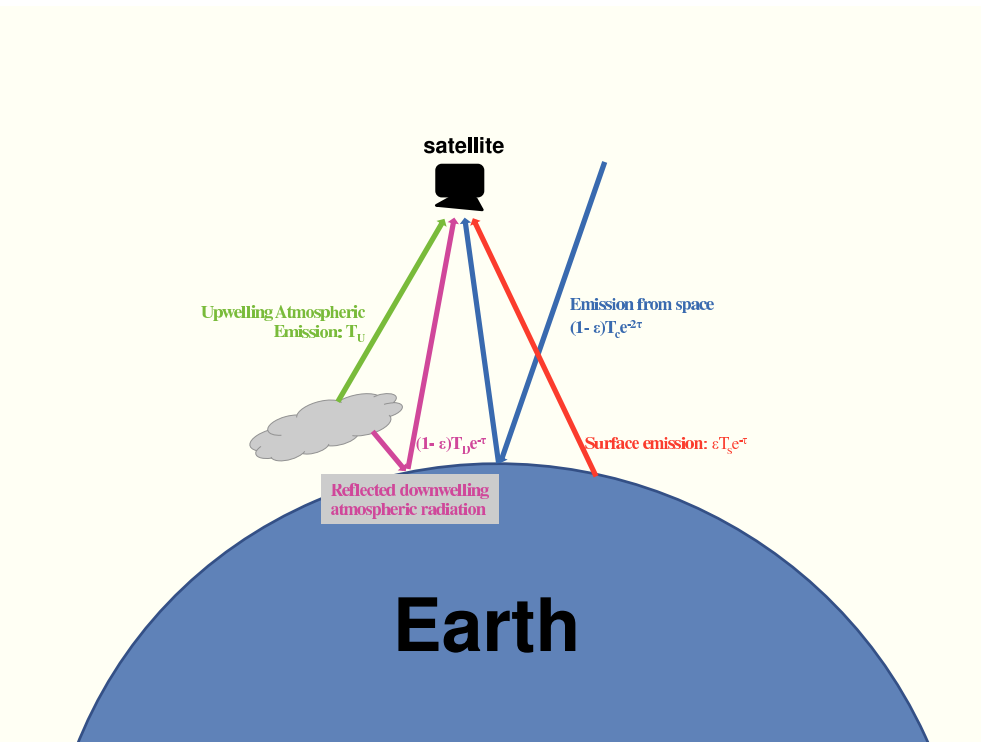

Fig. A.1: *Scheme of radiative transfer that influences measured brightness temperatures from microwave radiometer data. Redraw based on Swift & Cavalieri (1985).*

The bootstrap algorithm has been described in detail in *Comiso* (1995) and *Comiso et al.* (1997). It uses the ability of satellites to observe the Earth's surface with different frequencies and polarizations. From comparisons with observational data, the brightness temperatures from the vertically polarized 19 and 37 GHz channels have been found to be the most representative ones for the determination of SIC in the Antarctic (*Comiso et al.*, 1997). From these channels, reference brightness temperatures for open water (T_O) and sea ice (T_I) are calculated. The determination of these reference brightness temperatures is based on a relation of brightness temperatures measured with the 19 GHz and 37 GHz V-Pol channels and is described in detail in *Comiso et al.* (1997). The bootstrap algorithm derives the total SIC A in a grid cell by:

$$A = \frac{(T_B - T_O)}{(T_I - T_O)}, \tag{A.2}$$

where T_B is the observed brightness temperature.

Another method to calculate SIC from passive microwave data is provided by the NASA Team algorithm (e.g. *Cavalieri et al.*, 1991). Here, different channel combinations, techniques, weather filters and reference brightness temperatures are used (*Comiso et al.*, 1997). Contrary to the bootstrap algorithm, the Team algorithm

distinguishes between two sea ice types, namely first and second year ice, and open water in a grid cell. Then the total SIC is calculated as the sum of the percentages of both sea ice types. The percentages are calculated using the polarization ratio (PR) and the spectral gradient ratio (GR), defined by the 19 GHz and 37 GHz horizontally and vertically polarized brightness temperatures:

$$PR(19) = \frac{T_B(19V) - T_B(19H)}{T_B(19V) + T_B(19H)} \tag{A.3}$$

$$GR(37V/19V) = \frac{T_B(37V) - T_B(19V)}{T_B(37V) + T_B(19V)} \tag{A.4}$$

These ratios are used to calculate the concentrations (A_{IC1} and A_{IC2}) of each ice class:

$$A_{IC1} = \frac{(a_0 + a_1 PR + a_2 GR + a_3 PR \cdot GR)}{c_0 + c_1 PR + c_2 GR + c_3 PR \cdot GR)} \tag{A.5}$$

$$A_{IC2} = \frac{(b_0 + b_1 PR + b_2 GR + b_3 PR \cdot GR)}{c_0 + c_1 PR + c_2 GR + c_3 PR \cdot GR)} \tag{A.6}$$

and the sum of both gives the total sea ice concentration. The contributions of the polarization and the spectral gradient ratio are weighted based on the algorithms tie points, described by the coefficients a_i, b_i and c_i (*Comiso et al.*, 1997). These tie points are based on radiances that were measured for each of the three SSM/I channels for open ocean and both ice classes during winter (*Comiso et al.*, 1997).

Bootstrap and NASA Team SIC have been compared in different studies to assess, which one best matches the observed sea ice conditions. In a comparison of SIC of both algorithms for data in 1992, *Comiso et al.* (1997) showed that there are differences for the derived SIC, which lead to higher ice covered areas for the bootstrap algorithm but barely affect the SIE over the seasonal cycle. SIC in summer were nearly the same in both algorithms with almost normally distributed differences within $\pm$ 7.5 $\%$. However, in winter, the bootstrap SIC are generally higher than those of the NASA Team. Additionally, *Worby & Comiso* (2004) found in a comparison of both algorithms with ship based *in-situ* data, that the location of the sea ice edge as well the SIC at these locations are better represented by using the bootstrap

algorithm. Although bootstrap data show generally higher SIC at the sea ice edge compared to NASA team, even bootstrap data underestimate the SIC observed by high resolution satellite images (*Worby & Comiso*, 2004). Thus, SIC data derived by the bootstrap algorithm seem to be better adapted for this study than the NASA Team algorithm. The processed data are provided by the National Snow and Ice Data Center (NSIDC) on a regularly spaced 25 x 25 km^2 polar stereographic grid, starting in November 1978. Temporal resolution has been daily since August 1987, and before it was two-daily. These data provide a unique possibility to study the climatic response of the Southern Ocean's sea ice because of its consistent time series and large-scale coverage (*Worby & Comiso*, 2004).

B Description of the Finite Element Sea ice - Ocean Model

The ocean component

The Finite Element Sea ice-Ocean Model (FESOM), described in *Timmermann et al.* (2009), combines a modified version of the Finite Element Ocean Model (FEOM, *Danilov et al.*, 2004) with a dynamic-thermodynamic sea ice model. The model mesh is an unstructured surface triangular grid, which has 26 vertical z-levels. Grid nodes in the interior ocean are aligned under the surface nodes so that the 3-D mesh consists of tetrahedra. Bottom node elements can deviate from z-levels to approximate bathymetry in a smooth way (*Timmermann et al.*, 2009).

The prognostic variables of the model component are the components of the horizontal velocity (u, v), the potential temperature (Θ) and the salinity (S) of the sea water. The equations of momentum are:

$$\frac{\partial u}{\partial t} + \vec{u} \cdot \nabla u - fv = -\frac{1}{\rho_0}\frac{\partial p}{\partial x} + F_u + D_u \tag{B.7}$$

$$\frac{\partial v}{\partial t} + \vec{u} \cdot \nabla v - fu = -\frac{1}{\rho_0}\frac{\partial p}{\partial y} + F_v + D_v \tag{B.8}$$

$$0 = -\frac{1}{\rho_0}\frac{\partial p}{\partial z} - \frac{\rho g}{\rho_0} \tag{B.9}$$

with the equation of continuity:

$$\frac{\partial u}{\partial x} + \frac{\partial v}{\partial y} + \frac{\partial w}{\partial z} = 0 \tag{B.10}$$

and the temporal evolution of Θ and S given by:

$$\frac{\partial \Theta}{\partial t} + \vec{u} \cdot \nabla \Theta = F_\Theta + D_\Theta \tag{B.11}$$

$$\frac{\partial S}{\partial t} + \vec{u} \cdot \nabla S = F_S + D_S \tag{B.12}$$

(B.13)

f	Coriolis force, $f = 4\pi/86400 \cdot \Phi$, whit Φ = geographical latitude
g	acceleration due to gravity
ρ_0	mean (sea) water density = 1000 kg/m^3
p	pressure
D_χ	divergence of turbulent fluxes
F_χ	forcing term
χ	stands for either Θ, S, u, or v
ρ	non-linear equation of state, $\rho = \rho(\Theta, S, z)$
w	vertical velocity

Lateral and vertical contributions of the divergence of turbulent fluxes (D_χ) are derived from a harmonical mixing approach:

$$D_\chi = \nabla(\nu_\chi \nabla \chi) \tag{B.14}$$

with

$$\nu_{u,v} = 10^{-5} s^{-1} \Delta_i \tag{B.15}$$

$$\nu_{\Theta,S} = 0.04 \cdot \nu_{u,v} \tag{B.16}$$

$\Delta_{\vec{x}}$ is the element area. For the lateral mixing, a rotated Redi (*Redi*, 1982) and Gent-McWilliams (*Gent & McWilliams*, 1990; *Gent et al.*, 1995) scheme is used in FESOM. The rotational approach of *Redi* (1982) is applied to the horizontal tracer distribution to account for subgrid-scale processes. For the vertical mixing, a Pacanowski-Philander (*Pacanowski & Philander*, 1981) type vertical mixing scheme ensures that a weakening stratification of the ocean leads to gradually increased vertical mixing of temperature and salinity, with a maximum diffusivity of 0.01 m^2/s. The vertical viscosity is constant with $2 \cdot 10^{-3} m^2/s$.

As coastal boundary conditions, a no-slip approach was chosen and the calculation of surface stress and buoyancy fluxes is done by the ice-ocean coupling.

The sea ice component

FESOM includes a dynamic-thermodynamic sea ice model, in detail described in *Timmermann et al.* (2009) and briefly summarized here. The thermodynamic part uses the equations of *Parkinson & Washington* (1979), extended with a prognostic snow layer after *Owens & Lemke* (1990) and with the assumption that the temperature profile in the sea ice and snow layers is linear with negligible heat storage in sea ice

and snow, as was suggested by *Semtner* (1976). The effect of snow-ice conversion due to flooding is treated after *Leppäranta* (1983) and *Fischer* (1995).

The model computes the volume per unit area of ice and snow, i.e. mean sea ice as well as mean snow thickness, the sea ice concentration and the drift velocity. The temporal evolution of the prognostic variables sea ice and snow thickness (h, h_s) as well as sea ice concentration (A) is given by

$$\frac{\partial h}{\partial t} + \nabla \cdot \vec{u}_i h = S_h \tag{B.17}$$

$$\frac{\partial h_s}{\partial t} + \nabla \cdot \vec{u}_i h_s = S_s \tag{B.18}$$

$$\frac{\partial A}{\partial t} + \nabla \cdot \vec{u}_i A = S_A \tag{B.19}$$

with the left side describing the local, temporal changes of the prognostic variables and the changes due to advection. The right-hand side of Eq. B.19 expresses the source and sink terms of the thermodynamic changes of sea ice.

Energy balance

According to *Parkinson & Washington* (1979), the energy balance of the sea ice is given by

$$Q_{ai} + Q_{oi} + \rho_i L_i \left(\frac{\partial h}{\partial t} + \frac{\rho_{sn}}{\rho_i} \cdot \frac{\partial h_s}{\partial h_t} \right) = 0 \tag{B.20}$$

under the assumption that the heat storage in sea ice and snow can be neglected. The heat fluxes between sea ice and the atmosphere (Q_{ai}) and the ocean (Q_{oi}) are calculated by adding up the short- and longwave radiation and sensible and latent heat fluxes, with positive values indicating fluxes into the sea ice.

The incoming short wave radiation is calculated according to *Zillman* (1972) in combination with the cloud correction suggested by *Laevastu* (1960). The outgoing shortwave radiation is then the albedo-dependent reflected part of the incoming shortwave radiation. The incoming longwave radiation depends on the air temperature and cloudiness, and the outgoing longwave radiation is a function of the surface temperature:

$$Q_{LW}^{\downarrow} = \epsilon_a \sigma T_a^4 \tag{B.21}$$

$$Q_{LW}^{\uparrow} = \epsilon_s \sigma T_s^4 \tag{B.22}$$

The Stefan-Boltzmann constant is $\sigma = 5.67 \cdot 10^{-8} \frac{W}{m^2 K^4}$ and ϵ_a describes the emissivity of the atmosphere, given by

$$\epsilon = 0.765 + 0.22 \cdot c^3 \tag{B.23}$$

according to the empirical equation after *König-Langlo & Augstein* (1994)), with c as cloud coverage (ranging from 0 to 1). The emissivity of sea ice and water in the longwave part of the spectrum is a constant value ($\epsilon_s = 0.97$). The sensible and latent heat fluxes are described as

$$Q_s = \rho_a c_p C_s |\vec{u}_{10}|(T_a - T_s) \tag{B.24}$$

$$Q_l = \rho_a L C_l |\vec{u}_{10}|(q_a - q_s). \tag{B.25}$$

The specific heat capacity c_p is 1004 $\frac{J}{kgK}$, the latent heat of evaporation of water and sublimation of sea ice (L) amount to 2.5 $\cdot 10^6 \frac{J}{kg}$ and 2.834 $\cdot 10^6 \frac{J}{kg}$, respectively and the heat transfer coefficients for sensible and latent heat are according to *Maykut* (1971) and *Parkinson & Washington* (1979) $C_s = C_l = 1.75 \cdot 10^{-3}$. The specific humidity of air (q_a) as well as the 10-m wind speed ($\vec{u}_{10}$) and the 2-m SAT (T_a) are given by the forcing data.

The conductive heat flux through the sea ice cover and the snow layer,

$$Q_c = \frac{\kappa_i (T_b - T_s)}{h_i^*} \tag{B.26}$$

described by *Semtner* (1976), is included in the energy budgets at the interfaces between the atmosphere and sea ice as well as the sea ice and ocean:

$$Q_{ai} + Q_c + \rho_i L_i \left(\frac{\partial h}{\partial t} \right)_a = 0 \tag{B.27}$$

$$Q_{oi} - Q_c + \rho_i L_i \left(\frac{\partial h}{\partial t} \right)_0 = 0 \tag{B.28}$$

with the heat conductivities for ice ($\kappa_i = 2.17 \frac{W}{mK}$) and snow ($\kappa_s = 0.31 \frac{W}{mK}$) and

$$h_i^* = h_i + h_{sn} \frac{\kappa_i}{\kappa_s}. \tag{B.29}$$

The temperature at the bottom (T_b) is assumed to be equal to the freezing temperature of sea water.

Lateral sea ice growth and lead formation

The thermodynamic sea ice growth is the area weighted sum of the growth rates at the top (only melt or snow-ice conversion) and the bottom of the sea ice, and the new formation of sea ice in the open ocean:

$$S_h = \underbrace{A \cdot \left(\frac{\partial h}{\partial t}\right)_t}_{surface} + \underbrace{A \cdot \left(\frac{\partial h}{\partial t}\right)_b}_{bottom} + \underbrace{(1-A) \cdot \left(\frac{\partial h}{\partial t}\right)_{ow}}_{open\ ocean} \tag{B.30}$$

At the sea ice surface, the rate of sea ice thickness change is given by

$$\left(\frac{\partial h}{\partial t}\right)_t = -\frac{Q_{ai} + Q_c}{\rho_i L_i} - \frac{\partial h_s}{\partial t}. \tag{B.31}$$

The second term of the right-hand side describes the growth rate/ melt rate of snow

$$\frac{\partial h_s}{\partial t} = -\frac{Q_{ai} + Q_c}{\rho_{sn} L_i}. \tag{B.32}$$

At the bottom, changes of the sea ice thickness are described by

$$\frac{\partial h}{\partial t}_b = -\frac{Q_{oi} - Q_c}{\rho_i L_i}, \tag{B.33}$$

and under ice free conditions, freezing is given by

$$\frac{\partial h}{\partial t}_{ow} = -\frac{Q_{oa}}{\rho_i L_i} \tag{B.34}$$

as soon as the ocean surface is at the freezing point. The source term of the temporal evolution of snow (S_s) includes the accumulation of snow in ice covered regions. When air temperatures are higher, the snow cover starts to melt. It is assumed, that the snow surface has to melt completely before the sea ice thickness changes due to atmospheric heat fluxes. In case that the snow load on top of sea ice is high enough to suppress the sea ice surface below the sea surface, snow convertion into meteoric ice is calculated according to *Leppäranta* (1983).

Changes in the sea ice concentration are associated with the thermodynamic growth using the empirical relationship suggested by *Hibler III* (1979): During freezing, the ice covered area grows proportional to the area of the ice-free ocean

$$S_A = \frac{1-A}{h_0} \left(\frac{\partial h}{\partial t}\right)_{ow,freeze}. \tag{B.35}$$

h_0 is the lead closing parameter, which determines the closing rate of the ice coverage. In the standard model run used in this study, h_0 is set to 1 m. During melting events, the sea ice coverage shrinks proportionally to the decrease of the sea ice volume in a grid cell:

$$S_A = \frac{A}{2h}\left(\frac{\partial h}{\partial t}\right)_{melt}. \tag{B.36}$$

The factor $A/2h$ results from the assumption that the sea ice thickness is uniformly distributed between 0 and $2h/A$ within a grid cell. A ridging-term as described by, e.g., *Rothrock* (1975a) is not included in this model.

Momentum equation

The dynamical part of the model uses the elastic-viscous-plastic rheology described in *Hunke & Dukowicz* (1997). Sea surface tilt is derived from the ocean component. The model solves the momentum equation:

$$m\left(\frac{\partial}{\partial t} + f\vec{k}\times\right)\vec{u} = A(\vec{\tau_{ai}} - \vec{\tau}_{oi}) + \vec{F} - mg\nabla\eta \tag{B.37}$$

m	:	ice + snow mass per unit area
$\vec{\tau_{ai}}$	:	wind stress
$\vec{\tau_{oi}}$	:	ice-ocean stress
$\vec{F}$	:	impact from stresses within the ice

The atmospheric and oceanic surface stresses are calculated with the sea ice-ocean and the atmospheric drag coefficients ($c_{d,io}$, $c_{d,ia}$) according to:

$$\vec{\tau}_{ai} = \rho_a c_{d,ai}|\vec{u}_{10}|\vec{u}_{10} \tag{B.38}$$

$$\vec{\tau}_{oi} = c_{d,io}\rho_o(\vec{u} - \vec{u_w})|\vec{u} - \vec{u_w}| \tag{B.39}$$

and are scaled with the sea ice concentration A, as was suggested by *Connolley et al.* (2004). The 10-m wind speeds are described by $\vec{u}_{10}$ and ocean velocities are given by $\vec{u}_w$. ρ_a and ρ_o are the densities for air and sea water, respectively.

The internal stresses $\vec{F}$ are given by

$$F_j = \sum \frac{\partial \sigma_{ij}}{\partial x_i} \tag{B.40}$$

(*Hibler III*, 1979), which include the strain rate $\dot{\epsilon}_{ij}$, the nonlinear bulk and shear viscosities and the ice strength

$$P = P^* h e^{-C(1-A)} \tag{B.41}$$

in the two dimensional stress tensor σ_{ij}.

Values for model parameters are 20000 N/m^2 for the ice strength parameter P^*, $3.0 \cdot 10^{-3}$ for the ice-ocean drag coefficient ($c_{d,io}$) and 1.32$\cdot 10^{-3}$ for the wind stress ($c_{d,ia}$).

Coupling of sea ice and ocean

The coupling between the ocean and the sea ice component is similar to the BRIOS (Bremerhaven Regional Ice Ocean Simulations, *Timmermann et al.*, 2002) model and is basically described in *Timmermann et al.* (2009). Between the sea ice bottom and the ocean, heat fluxes are parameterized as

$$Q_{oi} = \rho_w c_{p,w} c_{h,io} u_* (T_o - T_f) \tag{B.42}$$

with the density ρ_w and heat capacity $c_{p,w}$ of sea water at constant pressure and a transfer coefficient of $c_{h,io} = 0.012$. With the ocean surface velocity $\vec{u}_w$, the sea ice velocity $\vec{u}$ and an oceanic drag coefficient of $c_{d,io} = 3 \times 10^{-3}$, the friction velocity u_* is given by

$$u_* = \sqrt{c_{d,io}} |\vec{u} - \vec{u}_w|. \tag{B.43}$$

T_o in Eq. B.42 denotes the ocean's surface temperature. The freezing temperature T_f is a function of the surface salinity S_0 and is calculated after an equation of *Millero* (1978).

Ocean surface heat flux,

$$Q_o = (1 - A) Q_{ow} - A Q_{oi} \tag{B.44}$$

is a combination of the heat flux in open water parts, derived from the balance described in *Parkinson & Washington* (1979), and heat exchanged with the sea ice.

The total salt flux is a combination of net input from melting and freezing ($F_{S,i}$) as well as from net precipitation ($F_{S,ow}$):

$$F_S = F_{S,i} + F_{S,ow} \tag{B.45}$$

with the first part expressed as

$$F_{S,i} = (S_0 - S_i)\frac{\rho_i}{\rho_w}\left(\frac{\partial h_i}{\partial t}\right)_{th} + S_0\frac{\rho_{sn}}{\rho_w}\left(\frac{\partial h_s n}{\partial t}\right)_{th}. \tag{B.46}$$

Only thermodynamic sea ice and snow volume changes contribute to this salt flux (indicated by $_{th}$, *Timmermann et al.*, 2009). The salinity of the uppermost ocean layer (S_0) is set to a constant value of 34 psu to ensure a global conservation of salt. Sea ice salinity (S_i) is set to 5 psu, that of snow to 0 psu. Densities are $\rho_i = 910$ kg/m^3 for sea ice and $\rho_{sn} = 290$ kg/m^3 for snow. The other contribution to the total salt flux is given by net precipitation. For temperatures above 0 ^oC, precipitation is assumed to be rain that runs completely into the ocean. Below the surface freezing point, net precipitation accumulates as snow on top of sea ice, but runs to the ocean in ice free regions.

$$F_{S,ow} = S_o \begin{cases} (P-E) & \text{for } T_a \geq 0^oC \\ (1-A)(P-E) & \text{for } T_a < 0^oC \end{cases} \tag{B.47}$$

Using the bulk formulars

$$\tau_{io} = \rho_w c_{d,io}|\vec{u}_i - \vec{u}_w|(\vec{u}_i - \vec{u}_w) \tag{B.48}$$

$$\tau_{ao} = \rho_a c_{d,ao}|\vec{u}_{10}|\vec{u}_{10} \tag{B.49}$$

the ice-ocean and the ocean-atmosphere stresses are derived with the ocean-surface velocity ($\vec{u}_w$) and the wind speed at 10-m height. The total ocean surface stress is the area-weighted sum of the ice-ocean and ocean-atmosphere stresses:

$$\tau_o = A \cdot \tau_{io} + (1-A) \cdot \tau_{ao} \tag{B.50}$$

Model initialization

To initialize the model simulations, temperature and salinity derived from the World Ocean Atlas (WOA01) January mean data set are prescribed. For regions with an initial sea surface temperature below -1 ^{o}C, an initial sea ice thickness of 1 m with a snow layer of 0.1 m and a sea ice concentration of 0.9 are prescribed. For the simulations, daily atmospheric fields are taken from the NCEP/NCAR reanalysis. Forcing variables are the 10-m wind speeds, the 2-m air temperature, the specific humidity, the total cloudiness and the net precipitation. The grid resolution is 1.5^o and the time-step is 2 hours. Neither restoring nor flux correction are applied. For more details on the model refer to *Timmermann et al.* (2009) and *Danilov et al.* (2004).

C Modelled sea ice age in comparison with observations

In Chapter 4.1, the sea ice classes FYI and SYI were analyzed using the QuikSCAT scatterometer data for the period 2000 through 2007. Since this data set is not available for longer time periods, a hindcast in model simulations might help to assess interannual and interdecadal variability in a reliable way. Furthermore, model simulations might help to evaluate whether changes in the sea ice class distribution occur in the Weddell Sea. The model used for this individual study is the Bremerhaven Regional Ice Ocean Simulations (BRIOS) model, since it already contains a sea ice age routine after *Harder* (1996). As FESOM, BRIOS is forced by NCEP reanalysis data and has a similar grid resolution with (1.5^o x 1.5^o)$cos\phi$, but it is formulated using finite differences. A detailed description of BRIOS and its validation can be found in, e.g., *Timmermann et al.* (2002), *Timmermann & Beckmann* (2004), and *Assmann et al.* (2005).

To assess a reliable prediction of the sea ice class distribution in the Weddell Sea, an adequate representation of the ice extent in model simulations is the first criterion. For a comparison between model simulations and QuikSCAT data, SIE was simulated for the same period for which the scatterometer data are available. Modelled SIE and its anomalies from BRIOS are illustrated in Figure C.2, in comparison with the observations for the Weddell Sea. Figure C.2a clearly shows that the model

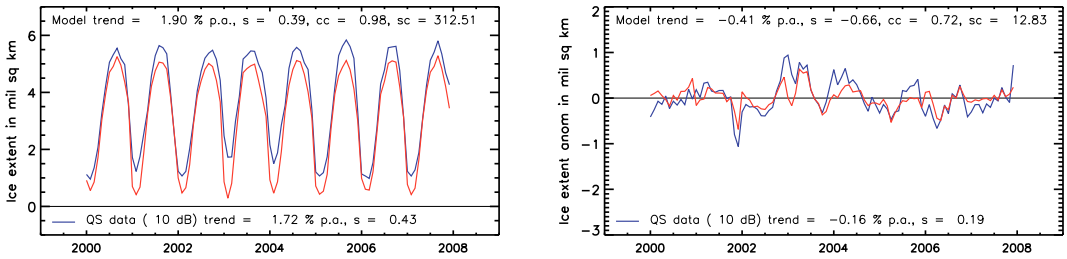

Fig. C.2: *Monthly mean SIE (left) and anomalies of SIE (right) in million km^2 from QuikSCAT data (blue) and model simulations (red) for the period 2000 through 2007. cc = correlation coefficient, s/sc = relative significance*

(red) underestimates the yearly summer minima and winter maxima in SIE in all years. Furthermore, the interannual variability of SIE is slightly underestimated. Nevertheless, the variability of monthly anomalies is well reproduced by the model simulation. Trends of SIE anomalies are -0.41 $\%$ per year for model simulation (red) and -0.16 $\%$ per year for observations, respectively (shown in Figure C.2b). The correlation between both anomaly curves is 0.72. The high correlation between

simulated and observed SIE implies that the general tendencies of the variability can be simulated fairly well, and therefore, the first criterion for an adequate representation of the sea ice is fulfilled by the model.

For the comparison between observations and model simulation, the age of sea ice is calculated in BRIOS with a routine after *Harder* (1996), which is briefly explained in the following. When sea ice starts to grow in a grid cell, it has an initial age of zero days. Every time step Δt, the total sea ice layer becomes older by Δt, when no other thermodynamical or dynamical processes influence the sea ice volume of the respective grid cell. When freezing occurs at the sea ice bottom, the thin layer of new formed sea ice has again an age of zero days. The age of the total sea ice layer is then the volume weighted average over both sea ice ages in the respective grid cell. Hence, in the new time step, the total sea ice layer becomes less than Δt older, since the averaged age contains all the ice (new as well as old) in one grid cell. The temporal evolution in the age of sea ice is given by

$$\frac{\partial a}{\partial t} = \frac{1}{h}\frac{\partial (ha)}{\partial t} - \frac{a}{h}\frac{\partial h}{\partial t} \tag{C.51}$$

where a is the volume averaged age of the sea ice and h the respective sea ice volume per unit area, i.e. the sea ice thickness. The prognostic equation for (ha) is

$$\frac{\partial (ha)}{\partial t} + \underbrace{\nabla \cdot (\vec{u} ha)}_{advection\ term} = \underbrace{h}_{source} + \underbrace{a M_h}_{sink}. \tag{C.52}$$

Without source and sink terms, the product (ha) would only depend on the horizontal advection, i.e. the age of the sea ice would be a volume weighted mean over the actual present and the advected ice in a grid cell (*Harder*, 1996).

The right-hand side of Eq. C.52 describes the aging over the integration period (source) and the changes in age connected to the thermodynamical changes in sea ice volume (sink). The source term h (i.e. the aging over the integration period) is given by

$$\frac{\partial (ha)}{\partial t} = h. \tag{C.53}$$

The sea ice thickness h does not change by the aging process ($\partial h/\partial t = 0$) and hence, Eq. C.51 results with Eq. C.53 in an aging rate of 1. The sink of the term in Eq. C.52 is connected to the melt rate M_h. In the case that melting occurs, $M_h = \partial h/\partial t < 0$ and the temporal evolution of the age due to melting is

$$\frac{\partial a}{\partial t} = 0 \tag{C.54}$$

with applying

$$\frac{\partial(ha)}{\partial t} = a\frac{\partial h}{\partial t} \tag{C.55}$$

in EQ. C.51. It is assumed that the volume loss during melting phases is distributed to all sea ice layers equally. Hence, each sea ice layer with a respective age loses the same percentage of volume. Therefore, the averaged age of the total sea ice layer does not change due to melting.

In case that freezing occurs, the melt rate is $M_h = 0$ and $\partial h/\partial t > 0$, resulting in a reduced aging of the sea ice layer according to

$$\frac{1}{a}\frac{\partial(ha)}{\partial t} = -\frac{1}{h}\frac{\partial h}{\partial t} \tag{C.56}$$

due to the thermodynamical increase of the sea ice volume in the respective grid cell.

The simulated distribution of sea ice age is illustrated in Figure C.3, exemplarily for the same months as QuikSCAT backscatter coefficients have been shown (Fig. 4.2). Large parts of the Weddell Sea are covered by relatively young sea ice. The oldest sea ice is located in the south-central Weddell Sea, next to the Filchner Ice Shelf. The age of up to 400 days in May and June implies that this sea ice was formed during spring the year before. Also the QuikSCAT data show a small area of SYI in this region. However, BRIOS simulates the highest amount of older sea ice in the central Weddell Sea, while QuikSCAT-based sea ice classes indicate the main occurrence of SYI in the north-western Weddell Sea, next to the tip of the Antarctic Peninsula. Hence, the general distribution of sea ice classes is not the same for both data sets.

For a comparison between the actually prevailing total areas of the respective ice classes, it is necessary to define a relation between the variables sea ice class and sea ice age. The age of the sea ice cannot be directly translated into a sea ice class. While the changes of sea ice age due to horizontal advection can be seen in satellite-based data as well as in model simulations, the changes in the mean age of a sea ice layer due to freezing at the sea ice bottom are not detectable by satellites. The satellites can only see the oldest layer, which the model cannot resolve. Of course, modelled sea ice with a comparatively old surface layer in a grid cell is also older on average, and hence, SYI derived from satellite observations is connected to the older sea ice in model simulations. To transfer the simulated age of the sea ice into the respective sea ice class, three different criteria were tested. In the first case, any sea ice that is older than a minimum age of 0, 30 or 60 days in February is treated as SYI. This was done because of the assumptions that the minimum SIE is generally

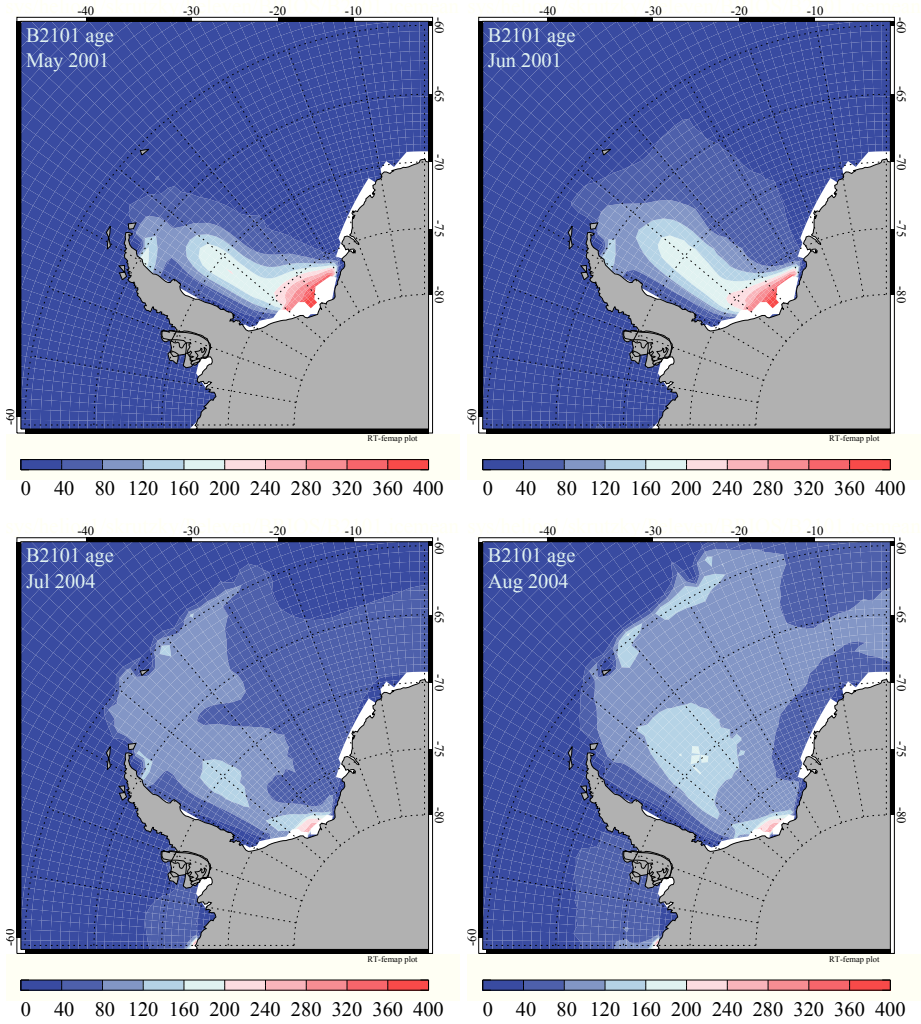

Fig. C.3: *Age of sea ice in days for May and June 2001 (top) and July and August 2004 (bottom) simulated with BRIOS.*

reached in February, no freezing takes place during this month and all the sea ice that is persistent in this month is sea ice that survived the summer melt period. The variation between 0, 30 and 60 days minimum age in February allows for excluding newly formed sea ice in the case that freezing actually does take place during January and February. Every month, the minimum age increases by one month and sea ice has to fulfill this criterion to be defined again as SYI. Every sea ice covered grid cell that is not defined as SYI is considered as FYI.

In the case of freezing, the averaged age of the sea ice becomes younger in the model, i.e. the respective age would increase by only a fraction of an entire month. Therefore, sea ice might fail the specification made in case 1, even though it might have been classified as SYI in February. Hence, the second case takes into consideration that the averaged sea ice age decreases in the model, when freezing

takes place. Sea ice is defined as SYI when

$$age \geq \frac{3}{4} * minimum\ age \tag{C.57}$$

and when it is thicker than 1 m (January-April), 1.5 m (May-June) and 2 m (July-December), respectively. In this case, younger sea ice can be classified as SYI but it has to have a mean sea ice thickness that is reasonable for modelled SYI thicknesses in the respective season.

The third case considers additionally that the model's resolution is much coarser than that of the satellite observations. Sea ice is treated as SYI when

$$age\_factor = \frac{(simulated\ age)}{(minimum\ age)} \geq 0.5 \tag{C.58}$$

with the additional conditions for sea ice thickness as described for case 2. In addition, only the area $grid\ cell * age\_factor$ counts as SYI area. The other part, $1-(grid\ cell * age\_factor)$ contains the FYI. All three cases were computed for a minimum age of 0, 30 and 60 days in February.

Figure C.4 shows time series of the anomalies for the different simulated sea ice class areas in comparison with satellite observations for case 3, considering different backscatter coefficients as a threshold between both sea ice classes. It can be seen that FYI is simulated in reasonable agreement with observations and also trends are of the same order of magnitude for both sources, although none of the trends are statistically significant. Changes are generally small between the three cases, with differences between case 1 and case 2 (not shown) being stronger than those between case 2 and case 3.

For the SYI, time series of model simulations are all negatively correlated with QuikSCAT observations, and as Figure C.4 (bottom) displays, there is little agreement between both data sets. The magnitudes of the trends decrease from case 1 to case 3 as well as those from minimum age of 0 to 30 days in February, but none of the trends is statistically significant.

The main reason for the model's inability to detect the SYI coverage reasonably is probably the fact that the vertically averaged age of sea ice decreases in a grid cell, while sea ice is growing at the bottom. Indeed, satellites cannot see this growing; they distinguish the sea ice classes only regarding surface properties. At first thought, it could be helpful, if the reduction of the age of sea ice during freezing is switched off in a new simulation. The resulting "maximum age", however, cannot be treated with an advection equation in the shape of Eq. C.52, which is defined

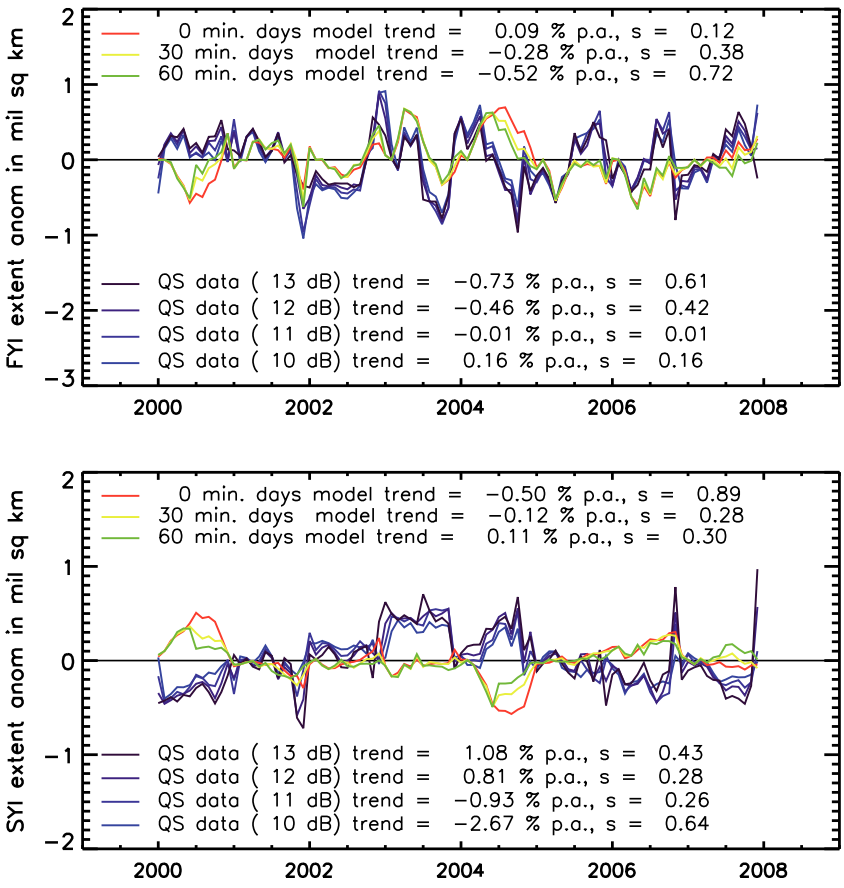

Fig. C.4: *Monthly anomalies of FYI (top) and SYI (bottom) extent in million km^2 for different backscatter coefficients in comparison with BRIOS model results. Blue/ purple curves show QuikSCAT anomalies and red, green and yellow curves are from model simulations with zero, 30 and 60 minimum days needed for SYI as initial age in February. s denotes the relative significance of the respective trend. Here, the results from case 3 are shown (for case description see text).*

for extensive quantities [2]. Hence, the treatment of a "maximum age" as intensive quantity requires a completely different numerical treatment. Another problem is that summer SIE is underestimated in model simulations and only little sea ice remains in summer and becomes second year ice (*Timmermann et al.*, 2009). This is a big issue when comparing simulations to observations. However, the detection of SYI with scatterometer data can also be challenging. Wrong detection of SYI may occur due to two processes:

1. If a satellite pixel consists of SYI, FYI and water, the backscatter power is a

[2]The extensive quantities are proportional to the mass of the respective body (here the sea ice). In the formal way, intensive quantities (independent of the mass of a body) are translated into extensive ones for a treatment in a prognostic equation, as was done here by the product of ha or as is done, e.g., in the oceanography for the calculation of the salt content (*Harder*, 1996).

combination of high values from the SYI and low values for FYI and water. Hence, mean backscatter might be too low for a detection of SYI and the FYI fraction in the entire Weddell Sea might be overestimated.

2. Melt processes influence the optical, thermal and microwave properties of snow irreversibly (*Willmes et al.*, 2006; *Nicolaus et al.*, 2009; *L. Kaleschke, personal communication, 2010*). Due to melting, refreezing or flooding, backscatter signals are biased towards higher values (*Willmes et al.*, 2006), and therefore, any sea ice that is affected by these processes might be classified spuriously as SYI.

The second point mainly influences the summer results, when temperatures rise frequently above 0 ^{o}C. Nevertheless, in the western Weddell Sea, low pressure systems with high air temperatures can appear in winter in the pack ice zone too (*Massom et al.*, 1997; *Worby et al.*, 1998). It was found that temperatures from NCEP can exceed 0 ^{o}C even in winter, which persists sometimes over days. Hence, melt processes may start and certainly influence the backscatter signals. Since this feature appears in regions where the SYI is normally detected by the QuikSCAT data, this yields another uncertainty in the calculation of the area of SYI from these data.

A completely different approach for the calculation of the sea ice age would be to calculate backward drift trajectories of "virtual" sea ice floes in the model. This would allow for a simulation of a sea ice age, which is comparable to the ice class distribution detected by satellites (and can indeed be compared to backward trajectories obtained from observed sea ice drift). However, this would require an accurate representation of sea ice drift as well as sea ice distribution throughout the year, including summer results.

D Comparability of mean and modal sea ice thicknesses

To estimate the uncertainty that arises when mean sea ice thicknesses modelled by FESOM are compared to the ULS measurements, which are expected to represent modal sea ice drafts (*Strass & Fahrbach*, 1998), a test was performed using airborne laser altimeter measurements[3]. These data were collected across a transect with a length of approximately 150 km in the western Weddell Sea (56^{o}W/ 66^{o}S) in February 2010. To gain the surface elevation relative to the ocean surface, the mean height over a 1.5 km transect was subtracted from the individual measurements. The profiles have been adjusted so that the lowest values are coincident with a height of 0.0 m above the ocean.

From these data, which have a footprint of about 0.035 m, mean and modal surface elevations were averaged over transects of approximately 5 m to achieve a correspondence to ULS measurements, which have a footprint of about 5 m. It is assumed here that the distribution of sails on top of the sea ice is to some extent the same as the distribution of keels at the ice's underside so that the relation between mean and modal surface elevations is representative for sea ice thicknesses as well. To visualize this relationship, a linear regression was performed between mean and modal surface elevations. Two examples of this test study are shown in Figure D.5.

In the first case, a surface elevation of 0.08 m was selected to be the upper bound for individual measurements. All the other data with elevations higher than 0.08 m were not considered for the calculation of mean and modal values. Under the assumption that the surface elevation is the same as the total freeboard (snow + sea ice)[4], this value represents sea ice of up to about 4 m according to the relation between ice draft and sea ice thickness after *Harms et al.* (2001). This relation was transformed into a relation between sea ice thickness and freeboard:

$$h_i = \frac{1.012F - 0.028}{0.012}. \tag{D.59}$$

A second test took all surface elevations lower than 1 m into consideration, since this

[3]Measurements were conducted by Polar-5 surveys during the Jasper campaign in 2010 and have been processed and provided by Dr. J. Hartmann from the Alfred Wegener Institute.

[4]This assumption is justified if the lowest surface elevations represent open water or very thin sea ice. In case that the lowest elevations have been measured above sea ice, the freeboard and the related sea ice thicknesses are underestimated. However, this will potentially not change results in this study.

is the threshold that *Zwally et al.* (2008) and *Yi et al.* (2011) considered in their studies from ICESat laser altimeter measurements.

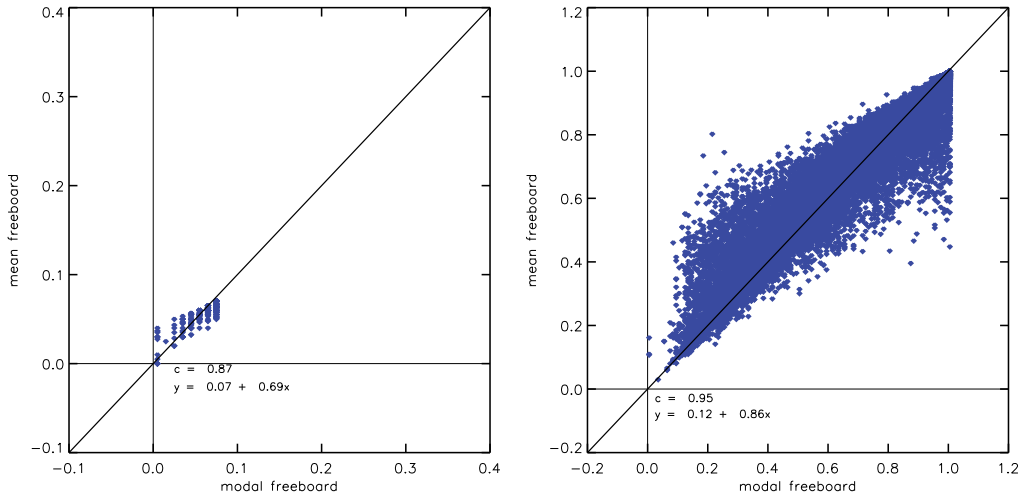

Fig. D.5: *Comparison between mean and modal sea ice freeboard from laser measurements performed in the western Weddell Sea in February 2010. Left: Freeboards limited to 0.08 m, right: Freeboards limited to 1 m. The black line indicates a slope of 1.*

In both test cases, the mean surface elevation overestimates the modal one for the lower two-third of the data. Above 0.05 m in the first case and 0.66 for the second example, mean freeboards are on average lower than the respective modal ones.

Related to the surface elevations in case 1, modal sea ice thicknesses above 2.5 m overestimate the mean sea ice thicknesses, below 2.5 m one can expect, that mean values are higher than the modal ones. In the western Weddell Sea, ULS based measurements indicate frequently the occurrence of sea ice thicknesses above 2.5 m in winter, hence, an overestimation of mean sea ice thicknesses in these months is most likely. Nevertheless, sea ice thicknesses are up to 90% underestimated by FESOM at ULS 207, for example, which cannot be fully explained by the inaccuracies from comparing modal with mean sea ice thicknesses. In addition, when modal sea ice thicknesses are below 2.5 m, the above shown relation would result in an overestimation of FESOM simulated sea ice thicknesses, which is rarely the case. Except for some ULS measurements along the Greenwich Meridian, mean modelled sea ice thicknesses underestimate the ULS measurements.

E Statistics

Significance for any trends, correlations or differences was calculated by using the students t-test (e.g. *Press et al.*, 2007). The statistical significance (te) for a linear trend

$$\hat{y}(x) = a + bx. \tag{E.60}$$

was derived by dividing the trend by its standard deviation

$$te = \frac{b}{\sigma_y} \quad \text{with} \tag{E.61}$$

$$\sigma_y = \sqrt{\frac{1}{n-2}\frac{\sum(y_i - \hat{y}(x))^2}{(x_i - \overline{x})^2}} \tag{E.62}$$

For differences $x_d = x - y$, the significance is calculated by:

$$te = \frac{\bar{x} - \bar{y}}{\sqrt{(\sigma_x^2 + \sigma_y^2)/n}}. \tag{E.63}$$

The standard deviation of this difference is revealed from Eq. E.64

$$\sigma_d = \sqrt{(\sigma_x^2 + \sigma_y^2)} = \sqrt{\frac{1}{n-1}\sum (x_{i,d} - \overline{x}_d)^2} \tag{E.64}$$

The correlation coefficients between two variables were derived according to Eq. E.65

$$r = \frac{\sum (x_i - \overline{x})(y_i - \overline{y})}{\sqrt{\sum (x_i - \overline{x})^2 \sum (y_i - \overline{y})^2}} \tag{E.65}$$

and its statistical significance was assessed by:

$$te = \frac{r\sqrt{n-2}}{\sqrt{1-r^2}}, \tag{E.66}$$

whereby for the correlation r holds:

$$-\sqrt{\frac{te^2}{n-2+te^2}} < r < \sqrt{\frac{te^2}{n-2+te^2}}. \tag{E.67}$$

Whether a correlation coefficient is statistically significant or not depends only on the degrees of freedoms (F = n - m - 1, with n = number of data points, m = number of independent variables).

Statistical significance was calculated for the 95% level throughout this study and is usually given in terms of a relative significance. That means that the critical value te was divided by the value that is necessary for the given number of degrees of freedom to be statistically significant at the 95% level (te_{soll}):

$$te_{rel} = \frac{te}{te_{soll}}. \tag{E.68}$$

A relative significance of 1 or more describes a statistically significant result. For a time period of n = 28 years (1979-2006), i.e. 26 degrees of freedom, te_{soll} is 2.056, and for a period of n = 19 years (1988-2006) it is 2.11 for a two-sided t-test in case that the tested time series are not autocorrelated.

F Glossary

AAO - Antarctic Oscillation
ACC - Antarctic Circumpolar Current
AMSR-E - Advanced Microwave Scanning Radiometer for Earth Observing System
AVHRR - Advanced Very High Resolution Radiometer
BRIOS - Bremerhaven Regional Ice Ocean Simulations
CCM - Cross Correlation Method
CERSAT - Centre ERS d'Archivage et de Traitement
DJF - December, January, February: summer
DMSP - Defense Meteorological Satellite Program
ECMWF - European Centre for Medium-Range Weather Forecasts
ENSO - El Niño-Southern Oscillation
FEOM - Finite Element Ocean Model
FESOM - Finite Element Sea ice-Ocean Model
FFT - Fast Fourier Transformation
FYI - First Year Ice
GLAS - Geoscience Laser Altimeter System
GPS - Geographic Information System
HadCM3 - Hadley Centre Coupled Model
H-pol - Horizontal-polarization
ICESat -Ice, Cloud, and Land Elevation Satellite
IPAB - International Programme for Antarctic Buoys
JJA - June, July, August: winter
MAM - March, April, May: autumn
MYI - Multi Year Ice
NCEP - National Center for Environmental Predictions
NSIDC - National Snow and Ice Data Center
OI - Optimal Interpolation/ optimally interpolated
PCA - Principal Component Analysis
SAM - Southern Annular Mode
SAT - Surface Air Temperature
SIC - Sea Ice Concentration
SIE - Sea Ice Extent
SST - Sea Surface Temperature
SMMR - Scanning Multichannel Microwave Radiometer
SO - Southern Oscillation
SON - September, October, November: spring

SSM/I - Special Sensor Microwave/Imager

SYI - Second Year Ice

ULS - Upward Looking Sonars

V-pol - Vertical polarization

WOA - World Ocean Atlas

List of Figures

Bibliography

Ackley, S., K. R. Buck, & S. Taguchi, Standing crop of algae in the sea ice of the Weddell Sea region, *Deep-Sea Research*, *26A*, 269–281, 1979.

Agnew, T. A., H. Le, & T. Hirose, Estimation of large-scale sea-ice motion from SSM/I 85.5 GHz imagery, *Annals of Glaciology*, *25*, 305–311, 1997.

Arblaster, J. M., & G. A. Meehl, Contributions of external forcings to Southern Annular Mode trends, *Journal of Climate*, *19*, 2896–2905, 2006.

Argos Collect Localisation Satellites Company, *Argos user's manual*, 2008, Toulouse, France.

Assmann, K. M., H. H. Hellmer, & S. S. Jacobs, Amundsen sea ice production and transport, *Journal of Geophysical Research*, *110*, 2005, doi:10.1029/2004JC002797.

Atkinson, A., V. Siegel, E. Pakhomov, & P. Rothery, Long-term decline in krill stock and increase in salps within the Southern Ocean, *Nature*, *432*, 100–103, 2004.

Barreira, S., & R. H. Compagnucci, Spatial fields of Antarctic sea-ice concentration anomalies for summer-autumn and their relationship to Southern Hemisphere atmospheric circulation during the period 1979-2009, *Annals of Glaciology*, *52(57)*, 140–150, 2011.

Bracegirdle, T. J., W. M. Connolley, & J. Turner, Antarctic climate change over the twenty first century, *Journal of Geophysical Research*, *113*, 2008, doi:10.1029/2007JD008933.

Brennecke, W., Die ozeanographischen Arbeiten der Deutschen Antarktischen Expedition 1911-1912, *in Arch. Dtsch. Seewarte*, *39*, 216 pp., 1921.

Cavalieri, D. J., & C. L. Parkinson, Antarctic sea ice variability and trends, 1979-2006, *Journal of Geophysical Research*, *113*, 2008, doi:10.1029/2007JC004564.

Cavalieri, D. J., J. P. Crawford, M. R. Drinkwater, D. T. Eppler, L. D. Farmer, R. R. Jentz, & C. C. Wackerman, Aircraft active and passive microwave validation of sea ice concentration from the Defense Meteorological Satellite Program Special Sensor Microwave Imager, *Journal of Geophysical Research*, *96*, 21,989–22,008, 1991.

Cavalieri, D. J., P. Gloersen, C. L. Parkinson, J. C. Comiso, & H. J. Zwally, Observed hemispheric asymetry in global sea ice changes, *Science*, *278*, 1997, doi:10.1126/science.278.5340.1104.

Cavalieri, D. J., C. L. Parkinson, & K. Y. Vinnikov, 30-Year satellite record reveals contrasting Arctic and Antarctic decadal sea ice variability, *Geophysical Research Letters*, *30*, 2003, doi:10.1029/2003GL018031.

Comiso, J. C., SSM/I sea ice concentrations using the Bootstrap algorithm, *NASA Reference Publication*, *1380*, 49 pp., 1995.

Comiso, J. C., *Bootstrap sea ice concentrations from Nimbus-7 SMMR and DMSP SSM/I, 1979-2006.*, Boulder, Colorado USA: National Snow and Ice Data Center. Digital media, 1999, updated 2008.

Comiso, J. C., D. J. Cavalieri, C. L. Parkinson, & P. Gloersen, Passive microwave algorithms for sea ice concentration: A comparison of two techniques, *Remote Sensing Environment*, *60*, 60,357–384, 1997.

Comiso, J. C., D. J. Cavalieri, & T. Markus, Sea-ice concentration, ice temperature, and snow depth using AMSR-E data, *IEEE Geoscience and Remote Sensing*, *41(2)*, 243–252, 2003.

Connolley, W. M., J. M. Gregory, E. Hunke, & A. J. McLaren, Notes and Correspondence: On the consistent scaling of terms in the sea-ice dynamic equation, *Journal of Physical Oceanography*, *34*, 2004.

Danilov, S., G. Kivman, & J. Schröter, A finite-element ocean model: principles and evaluation, *Ocean Modelling*, *6*, 125–150, 2004.

Drinkwater, M. R., X. Liu, & S. Harms, Combined satellite- and ULS-derived sea-ice flux in the Weddell Sea, Antarctica, *Annals of Glaciology*, *33*, 125–132, 2001.

Emery, W. J., A. C. Thomas, M. J. Collins, W. R. Crawford, & D. L. Mackas, An objective method for computing advective surface velocities from sequential infrared satellite images, *Journal of Geophysical Research*, *91*, 12,865–12,878, 1986.

Emery, W. J., C. W. Fowler, J. Hawkins, & R. H. Preller, Fram Strait satellite image-derived ice motions, *Journal of Geophysical Research*, *96*, 4751–4768, 1991.

Emery, W. J., C. W. Fowler, & J. A. Maslanik, Satellite-derived maps of Arctic and Antarctic sea ice motion: 1988 to 1994, *Geophysical Research Letters*, *24*, 897–900, 1997.

Ezraty, R., & J. F. Piollé, SeaWinds on QuikSCAT Polar Sea Ice Grids User Manual, 2001, ftp://ftp.ifremer.fr/pub/ifremer/cersat/manuels/mutp01.pdf.

Ferguson, S. H., M. K. Taylor, & F. Messier, Influence of sea ice dynamics on habitat selection by polar bears, *Ecology*, *81(3)*, 761–772, 2000.

Fetterer, F., K. Knowles, W. Meier, & M. Savoie, *Sea ice index*, Boulder, Colorado USA: National Snow and Ice Data Center. Digital media, 2002, updated 2009.

Fichefet, T., B. Tartinville, & H. Goosse, Antarctic sea ice variability during 1958-1999: A simulation with a global ice-ocean model, *Journal of Geophysical Research*, *108(C3)*, 2006, doi:10.1029/2001JC001148.

Fischer, H., Vergleichende Untersuchungen eines optimierten dynamisch-thermodynamischen Meereismodells mit Beobachtungen im Weddellmeer, *Berichte zur Polarforschung 166*, Alfred-Wegener-Institut für Polar- und Meeresforschung, 1995.

Fogt, R. L., & D. H. Bromwich, Decadal variability of the ENSO teleconnection to the High-Latitude South Pacific governed by coupling with the Southern Annular Mode, *Journal of Climate*, *19*, 979–997, 2006.

Foldvik, A., T. Gammelsrød, & T. Tørresen, Circulation and water masses on the southern Weddell Sea shelf, *Antarctic Research Series*, *43*, 5–20, 1985, Washington, DC: AGU.

Foster, T. D., & E. C. Carmack, Frontal zone mixing and Antarctic bottom water formation in the southern Weddell Sea, *Deep-Sea Research*, *23*, 301–317, 1976.

Fowler, C., *Polar Pathfinder Daily 25 km EASE-Grid Sea Ice Motion Vectors*, Boulder, Colorado USA: National Snow and Ice Data Center. Digital media, 2003, updated 2007.

Fowler, C. W., W. J. Emery, & J. A. Maslanik, Twenty three years of Antarctic sea ice motion from microwave satellite imagery, *Proceedings of International Geoscience and Remote Sensing Symposium IGARSS '01, July 9-13, Sydney*, *Vol. 1*, 157–159, 2001, doi:10.1109/IGARSS.2001.976088.

Friedlaender, A. S., W. R. Fraser, D. Patterson, S. S. Qian, & P. N. Halpin, The effects of prey demography on humpback whale (Megaptera novaeangliae) abundance around Anvers Island, Antarctica, *Polar Biology*, *31*, 1217–1224, 2008.

Geiger, C. A., W. D. Hibler III, & S. F. Ackley, Large-scale sea ice drift and deformation: Comparison between models and observations in the western Weddell Sea during 1992, *Journal of Geophysical Research*, *103*, 21,893–21,913, 1998.

Gent, P. R., & J. C. McWilliams, Isopycnal mixing in ocean circualtion models, *Journal of Physical Oceanography*, *20*, 150–155, 1990.

Gent, P. R., J. Willebrand, T. J. McDougall, & J. C. McWilliams, Parameterizing eddy-induced tracer transports in ocean circulation models, *Journal of Physical Oceanography*, *25(6)*, 1365, 1995.

Gong, D., & S. Wang, Definition of Antarctic oscillation index, *Geophysical Research Letters*, *26*, 459–462, 1999.

Goosse, H., & H. Renssen, A two-phase response of the Southern Ocean to an increase in greenhouse gas concentrations, *Geophysical Research Letters*, *28(18)*, 3469–3472, 2001.

Haas, C., & C. Kottmeier, *Contributions to the International Arctic and Antarctic Buoy Programmes IABP/IPAB*, Alfred Wegener Institute for Polar and Marine Research Bremerhaven, 2003.

Harder, M., Dynamik, Rauhigkeit und Alter des Meereises in der Arktis - Numerische Untersuchungen mit einem großskaligen Modell, *Berichte zur Polarforschung / Reports on polar research, 203*, Alfred-Wegener-Institut für Polar- und Meeresforschung, 1996.

Harder, M., & H. Fischer, Sea ice dynamics in the Weddell Sea simulated with an optimized model, *Journal of Geophysical Research*, *104*, 11,151–11,162, 1999.

Harms, S., E. Fahrbach, & V. Strass, Sea ice transport in the Weddell Sea, *Journal of Geophysical Research*, *106*, 9057–9073, 2001.

Heil, P., C. Fowler, J. Maslanik, W. Emery, & I. Allison, A comparison of East Antarctic sea-ice motion derived using drifting buoys and remote sensing, *Annals of Glaciology*, *33*, 139–144, 2001.

Heil, P., J. Hutchings, A. Worby, M. Johansson, J. Launiainen, C. Haas, & W. Hibler III, Tidal forcing on sea-ice drift and deformation in the western Weddell Sea in early austral summer, 2004, *Deep-Sea Research II*, *55*, 943–962, 2008.

Hibler III, W. D., A dynamic thermodynamic sea ice model, *Journal of Physical Oceanography*, *9*, 815–846, 1979.

Hoeber, H., & M. Gube-Lehnhardt, The Eastern Weddell Sea Drifting Buoy Data Set of the Winter Weddell Sea Project (WWSP) 1986, *Berichte zur Polarforschung / Reports on polar research, 37*, Alfred-Wegener-Institut für Polar- und Meeresforschung, 1987.

Hunke, E. C., & J. K. Dukowicz, An elastic-viscous-plastic model for sea ice dynamics, *Journal of Physical Oceanography*, *27*, 1849–1867, 1997.

Johannessen, O. M., E. V. Shalina, & M. W. Miles, Satellite evidence for an Arctic sea ice cover in transformation, *Science*, *286(5446)*, 1937–1939, 1999.

Kalnay, E., M. Kanamitsu, R. Kistler, W. Collins, D. Deaven, L. Gandin, M. Iredell, S. Saha, G. White, J. Woollen, Y. Zhu, M. Chelliah, W. Ebisuzaki, W. Higgins, J. Janowiak, K. C. Mo, C. Ropelewski, J. Wang, A. Leetmaa, R. Reynolds, R. Jenne, & D. Joseph, The NCEP/NCAR 40-Year Reanalysis Project, *Bulletin of the American Meteorological Society*, *77(3)*, 437–471, 1996.

Kottmeier, C., & D. Engelbart, Generation and atmospheric heat exchange of costal polynyas in the Weddell Sea, *Boundary-Layer Meteorology*, *60*, 207–234, 1992.

Kottmeier, C., & R. Hartig, Winter observation of the atmosphere over Antarctic sea ice, *Journal of Geophysical Research*, *95*, 16,551–16,560, 1990.

Kottmeier, C., & L. Sellmann, Atmospheric and oceanic forcing of Weddell Sea ice motion, *Journal of Geophysical Research*, *101*, 20,809–20,824, 1996.

Kottmeier, C., S. Ackley, E. Andreas, D. Crane, H. Hoeber, J. King, J. Launiainen, D. Limbert, D. Martinson, R. Roth, L. Sellmann, P. Wadhams, & T. Vihma, Wind, temperature and ice motion statistics in the Weddell Sea, 1996, WMO/ICSU/IOC. World Climate Research Programme (WCRP), International Programme for Antarctic Buoys (IPAB).

Kwok, R., & J. C. Comiso, Spatial patterns of variability in Antarctic surface temperature: Connection to the Southern Hemisphere Annular Mode and the Southern Oscillation, *Geophysical Research Letters*, *29*, 2002a.

Kwok, R., & J. C. Comiso, Southern Ocean climate and sea ice anomalies associated with the Southern Oscillation, *Journal of Climate*, *15*, 487–501, 2002b.

Kwok, R., & D. A. Rothrock, Variability of Fram Strait ice flux and North Atlantic Oscillation, *Journal of Geophysical Research*, *104*, 5177–5190, 1999.

Kwok, R., A. Schweiger, D. A. Rothrock, S. Pang, & C. Kottmeier, Sea ice motion from satellite passive microwave imagery assessed with ERS SAR and buoy motions, *Journal of Geophysical Research*, *103*, 8191 – 8214, 1998.

König-Langlo, G., & E. Augstein, Parameterization of the downward long-wave radiation at the Earth's surface in polar regions, *Meteorologische Zeitschrift*, *3(6)*, 343–347, 1994.

Laevastu, T., Factors affecting the temperature of the surface layer of the sea ice, *Commentationes Physico-Mathematicae*, *25(1)*, 1960.

Lange, M. A., & H. Eicken, The sea ice thickness distribution in the northwestern Weddell Sea, *Journal of Geophysical Research*, *96*, 4821–4837, 1991.

Large, W. G., & S. G. Yeager, The global climatology of an interannually varying air-sea flux data set, *Climate Dynamics*, *33*, 341–364, 2008, doi:10.1007/s00382-008-0441-3.

Lefebvre, W., & H. Goosse, Analysis of the projected regional sea-ice changes in the Southern Ocean during the twenty-first century, *Climate Dynamics*, *30*, 59–76, 2008, doi:10.1007/s00382-007-0273-6.

Lefebvre, W., H. Goosse, R. Timmermann, & T. Fichefet, Influence of the Southern Annular Mode on sea ice-ocean system, *Journal of Geophysical Research*, *109*, 2004.

Leppäranta, M., A growth model for black ice, snow ice and snow thickness in subarctic basins, *Nordic Hydrology*, *14*, 5970, 1983.

Liu, J., J. A. Curry, & D. G. Martinson, Interpretation of recent Antarctic sea ice variability, *Geophysical Research Letters*, *31*, 2004, doi:10.1029/2003GL018732.

Loeb, V., V. Siegel, O. Holm-Hansen, R. Hewitt, F. W., W. Trivelpiece, & S. Trivelpiece, Effects of sea-ice extent and krill or salp dominance on the Antarctic food web, *Nature*, *387*, 897–900, 1997.

Markus, T., & D. J. Cavalieri, Snow depth distribution over sea ice in the Southern Ocean from satellite passive microwave data, in *Antarctic sea ice: Physical Processes, Interactions and Variability*, vol. 74 of *Antarctic Research Series*, pp. 19–39, In M. O. Jeffries (Ed.), 1998, Washington, DC: AGU.

Marshall, G. J., Trends in the southern annular mode from observations and reanalyses, *Journal of Climate*, *16*, 4134–4143, 2003.

Marshall, G. J., A. Orr, N. P. M. van Lipzig, & J. C. King, The impact of a changing Southern Hemisphere Annular Mode on Antarctic Peninsula summer temperatures, *Journal of Climate*, *19*, 5388–5404, 2006.

Maslanik, J. A., C. Fowler, J. Stroeve, S. Drobot, J. Zwally, D. Yi, & W. Emery, A younger, thinner Arctic ice cover: Increased potential for rapid, extensive sea-ice loss, *Geophysical Research Letters*, *34*, 2007, doi:10.1029/2007GL032043.

Massom, R. A., Observing the advection of sea ice in the Weddell Sea using buoy and satellite passive microwave data, *Journal of Geophysical Research*, *97*, 15,559–15,572, 1992.

Massom, R. A., M. R. Drinkwater, & C. Haas, Winter snow cover on sea ice in the Weddell Sea, *Journal of Geophysical Research*, *102*, 1101–1117, 1997.

Maykut, G. A., Estimates of the regional heat and mass balance of the ice cover, in *A Symposium on Sea Ice Processes and Models*, vol. 1, pp. 65–74, University of Washington, Seattle, 1971.

McPhee, M. G., *An analysis of pack ice drift in summer*, pp. 62–75, in Sea Ice Processes and Model, edited by R. S. Pritchard, 1980, University of Washington Press, Seattle.

Millero, F. J., Freezing point of sea water, *In: Eighth Report of the Joint Panel of Oceanographic Tables and Standards, UNESCO Technical Papers in Marine Science*, *28*, 29–31, 1978.

Mosby, H., The water of the Atlantic Ocean, *in Scientific Results of the Norwegian Antarctic Expedition*, *1*, 1–131, 1934.

Nicolaus, M., C. Haas, & S. Willmes, Evolution of first-year and second-year snow properties on sea ice in the Weddell Sea during spring-summer transition, *Journal of Geophysical Research*, *114*, 2009, doi:10.1029/2008JD011227.

Ninnis, R. M., W. J. Emery, & M. J. Còllins, Automated extraction of pack ice motion from Advanced Very High Resolution Radiometer imagery, *Journal of Geophysical Research*, *91*, 10,725–10,734, 1986.

Owens, W. B., & P. Lemke, Sensitivity studies with a sea ice-mixed layer-pycnocline model in the Weddell Sea, *Journal of Geophysical Research*, *95*, 9527–9538, 1990.

Pacanowski, R. C., & S. G. H. Philander, Parameterization of vertical mixing in numerical models of the tropical oceans, *Journal of Physical Oceanography*, *11*, 1443–1451, 1981.

Parkinson, C. L., & D. J. Cavalieri, A 21 year record of Arctic sea-ice extents and their regional, seasonal and monthly variability and trends, *Annals of Glociology*, *34*, 441–446, 2002.

Parkinson, C. L., & W. M. Washington, A large-scale numerical model of sea ice, *Journal of Geophysical Research*, *84*, 311–337, 1979.

Parkinson, C. L., K. Y. Vinnikov, & D. J. Cavalieri, Evaluation of the simulation of the annual cycle of the Arctic and Antarctic sea-ice coverage by 11 major global climate models, *Journal of Geophysical Research*, *111*, 2006, doi:10.1029/2005JC003408.

Perovich, D. K., C. S. Roesler, & W. S. Pegau, Variability in Arctic sea ice optical properties, *Journal of Geophysical Research*, *103*, 1193–1208, 1998.

Press, W. H., S. A. Teukolsky, W. T. Vetterling, & B. P. Flannery, *Numerical Recipes: the art of scientific computing. Third edition.*, Cambridge, etc., Cambridge University Press, 727-730, 2007.

Redi, M. H., Oceanic isopycnal mixing by coordinate rotation, *Journal of Physical Oceanography*, *12*, 1154–1158, 1982.

Renner, A. H. H., & V. Lytle, Sea-ice thickness in the Weddell Sea, Antarctica: a comparison of model and upward-looking sonar data, *Annals of Glaciology*, *46*, 419–427, 2007.

Renwick, J. A., Trends in the Southern Hemisphere polar vortex in NCEP and ECMWF reanalyses, *Geophysical Research Letters*, *31*, 2004, doi:10.1029/2003GL019302.

Rigor, I. G., R. L. Colony, & S. Martin, Variations in surface air temperature observations in the Arctic, 1979-97, *Journal of Climate*, *13*, 896–914, 2000.

Rothrock, D. A., The energetics of the plastic deformation of pack ice by ridging, *Journal of Geophysical Research*, *80(30)*, 4514–4519, 1975a.

Rothrock, D. A., The steady drift of an incompressible Arctic ice cover, *Journal of Geophysical Research*, *80*, 387–397, 1975b.

Rothrock, D. A., Y. Yu, & G. A. Maykut, Thinning of the Arctic sea-ice cover, *Geophysical Research Letters*, *26*, 3469–3472, 1999.

Schmitt, C., Interannual variability in Antarctic sea ice motion, Ph.D. thesis, University of Karlsruhe (TH), Germany, 2005.

Schnack-Schiel, S. B., G. S. Dieckmann, R. Gradinger, I. A. Melnikov, M. Spindler, & D. N. Thomas, Meiofauna in sea ice of the Weddell Sea (Antarctica), *Polar Biology*, *24*, 724–728, 2001.

Schwegmann, S., C. Haas, C. Fowler, & R. Gerdes, A comparison of satellite-derived sea ice motion with drifting buoy data in the Weddell Sea, *Annals of Glociology*, *52(57)*, 2011.

Semtner, A. J., A model for the thermodynamic growth of sea ice in numerical investigations of climate, *Journal of Physical Oceanography*, *6*, 379–389, 1976.

Serreze, M. C., R. G. Barry, & A. S. McLaren, Seasonal Variations in sea ice motion and effects in sea ice concentration in the Canada Basin, *Journal of Geophysical Research*, *95*, 10,955–10,970, 1989.

Serreze, M. C., M. M. Holland, & J. Stroeve, Perspectives on the Arctic's shrinking sea-ice cover, *Science*, *315*, 1533–1536, 2007, doi:10.1126/science.1139426.

Spencer, M. W., C. Wu, & D. G. Long, Improved resolution backscatter measurements with SeaWinds pencil-beam scatterometer, *IEEE Transactions on Geoscience and Remote Sensing*, *38*, 89–104, 2000.

Stammerjohn, S. E., D. G. Martinson, R. C. Smith, & X. Yuan, Trends in the Antarctic annual sea ice retreat and advance and their relation to El Niño-Southern Oscillation and Southern Annual Mode variability, *Journal of Geophysical Research*, *113*, 2008, doi:10.1029/2007JC004269.

Strass, V. H., Measuring sea ice draft and coverage with moored upward looking sonars, *Deep-Sea Research I*, *45*, 795–818, 1998.

Strass, V. H., & E. Fahrbach, Temporal and regional variation of sea ice draft and coverage in the Weddell Sea obtained from upward looking sonars, *Antarctic Research Series*, *74*, 123–139, 1998, in: Jeffries, M.O. (Ed.), Antarctic sea ice: Physical Processes, Interactions and Variability.

Stroeve, J. C., M. C. Serreze, F. Fetterer, T. Arbetter, W. Meier, J. Maslanik, & K. Knowles, Tracking the Arctic's shrinking ice cover: Another extreme September minimum in 2004, *Geophysical Research Letters*, *32*, 2005, doi:10.1029/2004GL021810.

Swift, C. T., & D. J. Cavalieri, Passive microwave remote sensing for sea ice research, *EOS*, *66(49)*, 1210–1212, 1985.

Thompson, D. W. J., & S. Solomon, Interpretation of recent southern hemisphere climate change, *Science*, *296*, 895–899, 202.

Thorndike, A. S., & R. Colony, Sea ice motion in response to geostrophic winds, *Journal of Geophysical Research*, *87*, 5845–5852, 1982.

Timmermann, R., & A. Beckmann, Parameterization of vertical mixing in the Weddell Sea, *Ocean Modelling*, *6*, 83–100, 2004, doi:10.1016/S1463-5003(02)00061-6.

Timmermann, R., P. Lemke, & C. Kottmeier, Formation and maintenance of a polynya in the Weddell Sea, *Journal of Physical Oceanography*, *29(6)*, 1251–1264, 1999.

Timmermann, R., A. Beckmann, & H. H. Hellmer, The role of sea ice in the fresh water budget of the Weddell Sea, Antarctica, *Annals of Glaciology*, *33*, 419–424, 2001.

Timmermann, R., A. Beckmann, & H. H. Hellmer, Simulations of ice-ocean dynamics in the Weddell Sea 1. Model configuration and validation, *Journal of Geophysical Research*, *107*, 2002, doi:10.1029/2000JC000741.

Timmermann, R., H. Goosse, G. Madec, T. Fichefet, C. Ethe, & V. Dulière, On the representation of high latitude processes in the ORCA-LIM global coupled sea ice-ocean model, *Ocean Modelling*, *8*, 175–201, 2005, doi:10.1016/j.ocemod.2003.12.009.

Timmermann, R., S. Danilov, J. Schröter, C. Böning, D. Sidorenko, & K. Rollenhagen, Ocean circulation and sea ice distribution in a finite element global sea ice-ocean model, *Ocean Modelling*, *27*, 114–129, 2009.

Tipler, P. A., *Physik*, Spektrum Akademischer Verlag, 2000.

Turner, J., Review - The El Niño-Southern Oscillation and Antarctica, *International Journal of Climatology*, *24*, 1–31, 2004, doi:10.1002/joc.965.

Turner, J., A. S. Harangozo, G. J. Marshall, J. C. King, & S. R. Colwell, Anomalous atmospheric circulation over the Weddell Sea, Antarctica during austral summer of 2001/02 resulting in extreme sea ice conditions, *Geophysical research letters*, *29(24)*, 2002, doi:10.1029/2002GL015565.

Turner, J., S. R. Colwell, G. J. Marshall, & T. A. Lachlan-Cope, Antarctic climate change during the last 50 years, *International Journal of Climatology*, *25*, 279–294, 2005, doi:10.1002/joc.1130.

Turner, J., J. C. Comiso, G. J. Marshall, T. A. Lachlan-Cope, T. Bracegirdle, T. Maksym, M. P. Meredith, Z. Wang, & A. Orr, Non-annular atmospheric circulation change induced by stratospheric ozone depletion and its role in the recent increase of Antarctic sea ice extent, *Geophysical Research Letters*, *36*, 2009, doi:10.1029/2009GL037524.

Uotila, J., T. Vihma, & J. Launiainen, Response of the Weddell Sea pack ice to wind forcing, *Journal of Geophysical Research*, *105*, 1135–1151, 2000.

van den Broeke, M., The semi-annual oscillation and Antarctic climate. Part 3: The role of near-surface wind speed and cloudiness, *International Journal of Climatology*, *20*, 2000.

Venegas, S. A., & M. R. Drinkwater, Sea ice, atmosphere and upper ocean variability in the Weddell Sea, *Journal of Geophysical Research*, *106*, 16,747–16,765, 2001.

Vihma, T., J. Launiainen, & J. Uotila, Weddell Sea ice drift: Kinematics and wind forcing, *Journal of Geophysical Research*, *101*, 18,279–18,296, 1996.

Wadhams, P., C. B. Sear, D. R. Crane, M. A. Rowe, S. J. Morrison, & D. W. S. Limbert, Basin-scale ice motion and deformation in the Weddell Sea during winter, *Annals of Glaciology*, *12*, 1989.

Willmes, S., J. Bareiss, C. Haas, & M. Nicolaus, The importance of diurnal processes for the seasonal cycle of sea-ice microwave brightness temperature during early summer in the Weddell Sea, Antarctica, *Annals of Glociology*, 2006.

Willmes, S., C. Haas, M. Nicolaus, & J. Bareiss, Satellite microwave observations of the interannual variability of snowmelt on sea ice in the Southern Ocean, *Journal of Geophysical Research*, *114*, 2009, doi:10.1029/2008JC004919.

Wilson, P. R., D. G. Ainley, N. Nur, S. S. Jacobs, K. J. Barton, G. Ballard, & J. C. Comiso, Adélie penguin population change in the pacific sector of Antarctica: relation to sea ice extent and the Antarctic Circumpolar Current, *Marine Ecology Progress Series*, *213*, 301–309, 2001.

Windmüller, M., Untersuchung von atmosphärischen Reanalysedaten im Weddellmeer und Anwendung auf ein dynamisch thermodynamisches Meereismodell., 1997, Diplomarbeit am Institut für Meereskunde an der Christian-Albrechts-Universität, Kiel, Germany. 65 pp.

Worby, A. P., & J. C. Comiso, Studies of the Antarctic sea ice edge and ice extent from satellite and ship observations, *Remote Sensing of Environment*, *92*, 98–111, 2004, doi:10.1016/j.rse.2004.05.007.

Worby, A. P., R. A. Massom, I. Allison, V. I. Lytle, & P. Heil, East Antarctic sea ice: A review of its structure, properties and drift, in *Antarctic sea ice: Physical Processes, Interactions and Variability*, vol. 74 of *Antarctic Research Series*, pp. 41–67, In M. O. Jeffries (Ed.), 1998, Washington, DC: AGU.

Worby, A. P., C. A. Geiger, M. J. Paget, M. L. Van Woert, S. F. Ackley, & T. L. DeLiberty, Thickness distribution of Antarctic sea ice, *Journal of Geophysical Research*, *113*, 2008, doi:10.1029/2007JC004254.

Yi, D., H. J. Zwally, & J. W. Robbins, ICESat observations of seasonal and interannual variations of sea-ice freeboard and estimated thickness in the Weddell Sea, Antarctica (2003-2009), *Annals of Glaciology*, *52(57)*, 43–51, 2011.

Zhang, J., Increasing Antarctic sea ice under warming atmosphere and oceanic conditions, *Journal of Climate*, *20*, 2515–2529, 2007, doi:10.1175/JCLI4136.1.

Zillman, J. W., A study of some aspects of the radiation and heat budgets of the southern hemisphere oceans, in *Meteorological Study*, vol. 26, p. 526, Dept. of the Interior, Canberra, Australia, 1972.

Zwally, H. J., J. C. Comiso, C. L. Parkinson, D. J. Cavalieri, & P. Gloersen, Variability of Antarctic sea ice 1979-1998, *Journal of Geophysical Research*, *107*, 2002a, doi:10.1029/2000JC000733.

Zwally, H. J., R. Schutz, W. Abdalati, J. Abshire, C. Bentley, A. Brenner, J. Bufton, J. Dezio, D. Hancock, D. Harding, T. Herring, B. Minster, K. Quinn, S. Palm, J. Spinhirne, & R. Thomas, ICESat's laser measurements of polar ice, atmosphere, ocean, and land, *Journal of Geodynamics*, *34*, 405–445, 2002b.

Zwally, H. J., R. Schutz, C. Bentley, J. Bufton, T. Herring, J. Minster, J. Spinhirne, & R. Thomas, *GLAS/ICESat L2 Antarctic and Greenland Ice Sheet Altimetry Data V001.*, Boulder, Colorado USA: National Snow and Ice Data Center. Digital media, 2003.

Zwally, H. J., D. Yi, R. Kwok, & Y. Zhao, ICESat measurements of sea ice freeboard and estimates of sea ice thickness in the Weddell Sea, *Journal of Geophysical Research*, *113*, 2008, doi:10.1029/2007JC004284.

Acknowledgements

I would like to thank Prof. Peter Lemke and Prof. Rüdiger Gerdes for the discussions and advice during my doctorate and for reviewing this thesis. Special thanks go to Dr. Ralph Timmermann, who introduced me to FESOM and took always his time to answer my questions and to lead inspiring discussions. Another special thanks goes to Prof. Christian Haas for his support, inspiring discussions and for giving me the opportunity to spend some months abroad and to make first experiences with the EM-bird.

This work was only possible due to several freely available data sets. In this context I would particularly like to thank the NSIDC (Boulder, USA), the CERSAT at IFREMER (Plouzané, France) and the NCEP (Boulder, USA). Further, I would like to thank Hannelore Witte, Wolfgang Dierking and Jörg Hartmann for providing me processed ULS and airborne laser altimeter data.

I would also like to thank Dr. Eberhard Fahrbach, who gave me the opportunity to participate in the ANT-XXVII/2 cruise to Antarctica.

All ESSReS participants and especially Klaus Grosfeld I would like to thank for the fruitful discussions and the enjoyable time during the seminars, lectures and soft skill courses and the support in challenging situations.

Big thanks go to Annette Bombosch for helping me to improve the style of this thesis.

Thanks go also to all colleagues at AWI for answering all my questions, for the discussions, their support and for the good working atmosphere.

Finally, I would like to thank my family and friends for their support during the last years and for always believing in me.

This work was written in the Sea Ice Physics group at the Alfred Wegener Institute for Polar and Marine Research and was funded by the Earth System Science Research School (ESSReS), an initiative of the Helmholtz Association of German research centres (HGF) at the Alfred Wegener Institute for Polar and Marine Research. Parts of this work were also funded by the German Exchange Service (DAAD).